Exciton Dynamics in Lead Halide Perovskite Nanocrystals: Recombination, Dephasing and Diffusion

Bernhard Johann Bohn

München, 2019

Exciton Dynamics in Lead Halide Perovskite Nanocrystals: Recombination, Dephasing and Diffusion

Dissertation

zur Erlangung des Doktorgrades der Naturwissenschaften (Dr. rer. nat.)

an der Fakultät für Physik

der Ludwig-Maximilians-Universität München

vorgelegt von

Bernhard Johann Bohn

aus Augsburg

München, 26. November 2019

Promotionskommission

Erstgutachter:	Prof. Dr. Jochen Feldmann
Zweitgutachter:	Prof. Dr. Michael Thorwart
Vorsitzender:	Prof. Dr. Jan Lipfert
Beisitzer:	Prof. Dr. Emiliano Cortés
Tag der mündlichen Prüfung:	14. Januar 2020

dedicated to my parents

Publications, Conferences and Awards

Scientific Publications of Results Presented in This Work

- B. J. Bohn, T. Simon, M. Gramlich, A. F. Richter, L. Polavarapu, A. S. Urban, J. Feldmann
  Dephasing and quantum beating of excitons in methylammonium lead iodide perovskite nanoplatelets
  ACS Photonics 5(2): 648-654 (2017)

- B. J. Bohn, Y. Tong, M. Gramlich, M. L. Lai, M. Döblinger, K. Wang, R. L. Z. Hoye, P. Müller-Buschbaum, S. D. Stranks, A. S. Urban, L. Polavarapu, J. Feldmann
  Boosting tunable blue luminescence of halide perovskite nanoplatelets through postsynthetic surface trap repair
  Nano Letters 18(8): 5231-5238 (2018)

- E.-P. Yao, B. J. Bohn, Y. Tong, H. Huang, L. Polavarapu, J. Feldmann
  Exciton diffusion length and dissociation rate in $CsPbBr_3$ perovskite nanocrystal-PCBM composites: Layer-by-layer vs blend structures
  Advanced Optical Materials 7(8): 1801776 (2019)

- M. Gramlich, B. J. Bohn, Y. Tong, L. Polavarapu, J. Feldmann, A. S. Urban
  Exciton-exciton annihilation in strongly quantum confined perovskite nanoplatelets
  Nano Letters under review (2020)

Additional Publications of My Time as a PhD Student

- B. J. Bohn, M. Schnell, M. A. Kats, F. Aieta, R. Hillenbrand, F. Capasso
  Near-field imaging of phased array metasurfaces
  Nano Letters 15(6): 3851-3858 (2015)

- K. J. Mohler, B. J. Bohn, M. Yan, G. Mélen, T. W. Hänsch, N. Picqué
  Dual-comb coherent Raman spectroscopy with lasers of 1-GHz pulse repetition frequency
  Optics Letters 42(2): 318-321 (2017)

- Y. Tong, B. J. Bohn, E. Bladt, K. Wang, P. Müller-Buschbaum, S. Bals, A. S. Urban, L. Polavarapu, J. Feldmann
  From precursor powders to $CsPbX_3$ perovskite nanowires: one-pot synthesis, growth mechanism, and oriented self-assembly
  Angewandte Chemie International Edition 56(44): 13887-13892 (2017)

- C. M. Wolff, P. D. Frischmann, M. Schulze, B. J. Bohn, R. Wein, P. Livadas, M. T. Carlson, F. Jäckel, J. Feldmann, F. Würthner, J. K. Stolarczyk
  All-in-one visible-light-driven water splitting by combining nanoparticulate and molecular co-catalysts on CdS nanorods
  Nature Energy 3(10): 862-869 (2018)

- A. Mähringer, A. C. Jakowetz, J. M. Rotter, B. J. Bohn, J. K. Stolarczyk, J. Feldmann, T. Bein, D. D. Medina
  Oriented thin films of electroactive triphenylene catecholate-based 2D metal-organic frameworks
  ACS Nano 13(6): 6711-6719 (2019)

- S. Rieger, B. J. Bohn, M. Döblinger, A. F. Richter, Y. Tong, K. Wang, P. Müller-Buschbaum, L. Polavarapu, L. Leppert, J. K. Stolarczyk, J. Feldmann
  Excitons and narrow bands determine the optical properties of cesium bismuth halides
  Physical Review B 100(20): 201404 (2019)

- A. F. Richter, M. Binder, B. J. Bohn, N. Grumbach, S. Neyshtadt, A. S. Urban, J. Feldmann
  Fast electron and slow hole relaxation in InP-based colloidal quantum dots
  ACS Nano 13(12): 14408-14415 (2019)

- S. Strohmair, A. Dey, Y. Tong, L. Polavarapu, B. J. Bohn, J. Feldmann
  Spin polarization dynamics of free charge carriers in $CsPbI_3$ nanocrystals
  Nano Letters under review (2020)

Conferences and Workshops

- *Workshop on Photonics and Optoelectronics with New Materials* (Talk)
  Lenggries, Germany, July 2016

- *CeNS Workshop Venice 2016: Nanoscale Matter – Novel Concepts and Functions* (Poster)
  Venice, Italy, September 2016

- *Workshop on Optical Spectroscopy of New Materials* (Talk)
  Syracuse, Italy, March 2017

- *International WE-Heraeus-Physics School on Exciting Nanostructures: Probing and Tuning the Electronic Properties of Confined Systems* (Poster)
  Bad Honnef, Germany, July 2017

- *Nanophotonics of 2D Materials, N2D 2017* (Talk)
  San Sebastian, Spain, August 2017

- *6th International SolTech Conference* (Poster)
  Munich, Germany, October 2017

- *SPIE. Photonics West: Ultrafast Phenomena and Nanophotonics XXII* (Talk)
  San Francisco, USA, January 2018

- *MRS Spring Meeting 2018* (Talk)
  Phoenix, USA, April 2018

- *34th International Conference on the Physics of Semiconductors: ICPS 2018* (Poster)
  Montpellier, France, August 2018

- *CeNS Workshop Venice 2018: Celebrating NanoScience* (Poster)
  Venice, Italy, September 2018

- *7th International SolTech Conference* (Poster)
  Würzburg, Germany, October 2018
- *Workshop on Optical Spectroscopy of New Materials 2019* (Talk)
  Haigerloch, Germany, March 2019
- *EMRS Spring Meeting 2019* (Talk)
  Nice, France, May 2019
- *Sino-German Bilateral Symposium "Nano-Photonics and Nano-Optoelectronics"* (Invited Talk)
  Changsha, China, November 2019

Awards

- **Best Poster Award**
  International WE-Heraeus-Physics School on Exciting Nanostructures: Probing and Tuning the Electronic Properties of Confined Systems (Poster)
  Bad Honnef, Germany, July 2017
- **CeNS Publication Award, Best Interdisciplinary Publication 2017**
  for *"From precursor powders to $CsPbX_3$ perovskite nanowires: one-pot synthesis, growth mechanism, and oriented self-assembly"* in "Angewandte Chemie International Edition"
  Munich, Germany, December 2017
- **Best Student Paper Award**
  SPIE. Photonics West: Ultrafast Phenomena and Nanophotonics XXII (Talk)
  San Francisco, USA, January 2018
- **Fellowship Under a Marie Skłodowska-Curie Grant**
  for my research stay in the Molecular Foundry at the Lawrence Berkeley National Laboratory as part of the COMPASS project from the European Union's Horizon 2020 research and innovation programme (agreement No. 691185)
  Berkeley, USA, March - June 2018
- **CeNS Travel Award**
  34th International Conference on the Physics of Semiconductors: ICPS 2018 (Poster)
  Montpellier, France, August 2018
- **Best Poster Award**
  7th International SolTech Conference (Poster)
  Würzburg, Germany, October 2018
- **CeNS Publication Award, Scientific Breakthrough 2018**
  for *"All-in-one visible-light-driven water splitting by combining nanoparticulate and molecular co-catalysts on CdS nanorods"* in "Nature Energy"
  Munich, Germany, November 2018

Zusammenfassung

Ein beispielloser Anstieg der Effizienz von Solarzellen während den vergangenen zehn Jahren führte zur Renaissance von Perowskit-Materialien. Großes Interesse wurde in der Photovoltaik-Community geweckt, da diese rasante Entwicklung durch kosteneffiziente Bauelemente auf der Basis von massiven Filmen aus Bleihalogenid-Perowskiten erzielt werden konnte. Danach verging nicht viel Zeit, bis sich Nanokristalle dieses Perowskit-Typs als vielversprechendes Material für lichtemittierende und andere optoelektronische Anwendungen erwiesen. Im Rahmen dieser Arbeit wurden verschiedene Nanokristall-Zusammensetzungen und -Morphologien untersucht, indem stationäre und zeitaufgelöste optische Spektroskopie an Ensembles von Nanokristallen durchgeführt wurden.

Exzitonen, d. h. gebundene Elektron-Loch-Paare, spielen in solchen Halbleiter-Nanostrukturen bekanntlich auch bei Raumtemperatur eine wichtige Rolle. Dies liegt an ihren geringen physikalischen Abmessungen und der daraus resultierenden Quantenbeschränkung, die unter anderem zu stark erhöhten Exzitonen-Bindungsenergien führt, die weitaus größer sind als die thermische Energie von Elektronen. Um Bauelemente zu verstehen, die auf Bleihalogenid-Perowskit-Nanokristallen basieren, muss daher zunächst die Dynamik der Exzitonen in solchen Kristallen und deren Anordnungen verstanden werden. Diese herausfordernde Aufgabe bildet die Hauptmotivation für diese Arbeit.

Dementsprechend wurden drei entscheidende Prozesse untersucht, bei denen Exzitonen in Bleihalogenid-Perowskit-Nanokristallen involviert sind:

(i) Die Rekombination von Exzitonen, die ihre Lebensdauer bestimmt,
(ii) Die Dephasierung von Exzitonen, die mit der spektralen Verbreiterung des entsprechenden Übergangs zusammenhängt,
(iii) Die Diffusion von Exzitonen, die das Transportverhalten von Exzitonen in Nanokristallen oder deren Ansammlungen beschreibt.

Die Rekombination wurde an quantenbeschränkten $CsPbBr_3$ Nanoplättchen untersucht, deren präzise Dickenkontrolle eine Abstimmbarkeit der Emissionswellenlänge im grünen bis blauen Spektralbereich ermöglichte. Ein postsynthetischer Reparaturprozess für Oberflächendefekte führte zu hohen Photolumineszenzquantenausbeuten von bis zu 73 %. Differentialtransmissionsspektroskopie wurde eingesetzt, um die dickenabhängigen Raten für die Exziton-Exziton-Annihilation sowie für die monomolekulare Rekombination zu bestimmen.

Die Dephasierung wurde anhand von dicken $MAPbI_3$ Nanoplättchen untersucht. Vierwellenmischen bei niedrigen Temperaturen ergab eine Exzitonen-Dephasierungszeit im Bereich von mehreren hundert Femtosekunden. Zusätzliche temperaturabhängige Absorptionsspektroskopie ermöglichte die Unterscheidung zwischen dem homogenen und dem inhomogenen Beitrag zur totalen Verbreiterung des exzitonischen Übergangs. Darüber hinaus wurden Quantenschwebungen für die gleichzeitige Anregung von Exzitonen und freien Elektron-Loch-Paaren beobachtet. Damit konnte die Exzitonen-Bindungsenergie bestimmt werden, für die ein Wert von 25 meV ermittelt wurde.

Die Diffusion von Exzitonen wurde für Anordnungen von $CsPbBr_3$ Nanowürfeln und Nanodrähten mittels Photo-lumineszenz-Intensitätsprofilen und Photolumineszenz-Abschwächung gemessen. Resultierende Diffusionslängen im Bereich 200–400 nm wurden extrahiert.

Abstract

An unprecedented rise in solar cell efficiencies during the past ten years led to the renaissance of perovskite materials. Great interest arose within the photovoltaics community, as this rapid development could be achieved through cost-efficient devices based on bulk films of lead halide perovskites. Not much time passed afterwards until nanocrystals of this material emerged with huge potential mainly for light-emitting but also for other optoelectronic applications. In the course of this thesis, several nanocrystal compositions and morphologies were investigated by applying steady-state and time-resolved optical spectroscopy on ensembles of nanocrystals.

Excitons, i.e., bound electron-hole pairs, are known to play an important role in such semiconductor nanostructures even at room temperature. This is due to their small physical dimensions, and the resulting quantum confinement leading, among other things, to strongly increased exciton binding energies, far larger than the thermal energy of electrons. Therefore, in order to understand devices based on lead halide perovskite nanocrystals, first, the dynamics of excitons within such crystals and arrangements of them must be understood. This challenging task forms the main motivation for this thesis.

Accordingly, three crucial processes involving excitons within lead halide perovskite nanocrystals were examined:

(i) The recombination of excitons, which determines their lifetime,
(ii) The dephasing of excitons, which is related to the spectral broadening of the respective transition,
(iii) The diffusion of excitons, which describes the transport behavior of excitons within nanocrystals or assemblies of them.

Recombination was studied on quantum confined $CsPbBr_3$ nanoplatelets, whose precise thickness control enabled an emission wavelength tunability in the green to blue spectral range. A postsynthetic surface trap repair process led to high photoluminescence quantum yields of up to 73 %. Differential transmission spectroscopy was employed to determine the thickness-dependent rates for exciton-exciton annihilation as well as for monomolecular recombination.

Dephasing was investigated using bulk-like $MAPbI_3$ nanoplatelets. Four-wave mixing revealed an exciton dephasing time in the range of several hundreds of femtoseconds at low temperatures. Additional temperature-dependent absorption spectroscopy enabled a differentiation between the homogeneous and inhomogeneous contributions to the total broadening of the excitonic transition. Furthermore, quantum beats were observed for the simultaneous excitation of excitonic and continuum states. This enabled a determination of the exciton binding energy, for which a value of 25 meV was obtained.

Diffusion was measured for assemblies of $CsPbBr_3$ nanocubes and nanowires by means of photoluminescence mapping and photoluminescence quenching experiments. Resulting exciton diffusion lengths in the range 200–400 nm were extracted.

Table of Contents

1 Introduction

"What is perovskite?"

> *"The term perovskite refers to crystals with a very specific crystal structure of the form ABX_3.[1] Many different atoms or molecules can form such a structure.[2] For example, most of the Earth's mantle consists of the perovskite $MgSiO_3$, largely to be found in depths of 700-2700 km since it requires a high-pressure environment to be stable.[3] The original perovskite was first discovered in the form of $CaTiO_3$ on the Earth's surface in 1839 by the mineralogist Gustav Rose.[4]"*

"Oh, I see. So you study these minerals?"

> *"Not quite. To be precise, I investigate so-called lead halide perovskites."*

"That sounds very specific. I guess not many people are working on them?"

> *"You'd be surprised! Just look it up on Google Scholar. While you'll find only around 500 articles on this topic up until 2008, the number has exploded since. In the past ten years more than 12 000 articles have been published. Do you want to know what happened in 2009?"*

The above is in essence a typical dialogue I had many times during the past three years when talking about my work with people outside of my research community. What I want to point out here, is the substantial increase of interest that lead halide perovskites (LHPs) have gained throughout the last decade. It started with the successful implementation of LHPs in a solar cell,[5] paving the way for a whole new topic at the forefront of current research — the development of photovoltaics based on LHP.[6] Recently, for the first time, the efficiency of a purely LHP-based solar cell surpassed 25 %.[7] Despite these impressive advances, awareness in the general population is still only minimal.

LHPs are classified as semiconductors and in general are an interesting material for optical applications. The rapid advances regarding the photovoltaic efficiencies of LHPs are based on bulk thin films of this material.[8–10] However, compared to bulk films, the main focus of this thesis lies on a quite different form of LHPs. Here, so-called nanocrystals (NCs) are examined.[11–13] In contrast to bulk films, NCs usually exhibit significantly stronger photoluminescence (PL) and with emission in the visible spectrum could thus be suitable candidates for use in light-emitting diodes (LEDs).[14–16] Colloidal chemistry allows for quick and reliable synthesis of such NCs which can be shrunk down to only a few unit cells in all directions.[17,18] Notably, going to these extreme length scales of only a few nanometers or even less has a dramatic impact on the optical properties such as the emission wavelength of the NCs as quantum confinement starts playing a role.[19,20] Additionally, the shape, size, and arrangement of the NCs can be tuned and also influence important properties like the polarization behavior, charge carrier diffusion or the coupling between NCs.[21–23] Using variations within the synthesis routine leads to completely different NC morphologies,[18] such as platelets, cubes, supercrystals, wires and rods.[20,24,25]

As its title already reveals, this thesis studies exciton dynamics within individual LHP NCs as well as larger arrangements of them.

> *"What is an exciton?"*
>
> > *"An exciton is a quasiparticle, comprising an electron and a hole bound together through the Coulomb interaction between them.[26–28]"*

In the scope of this work, the time-integrated as well as the time-resolved behavior of excitons are examined by means of optical spectroscopy. Accordingly, Chapter 2 introduces the relevant basics of general semiconductor physics before turning to the specific case of LHP semiconductors and the role NCs play in this material. The detailed description of the methods in Chapter 3 then explains the various laser light sources used for optical excitation of the LHP samples. Moreover, the spectroscopy techniques that were employed to gather stationary or time-resolved information on the exciton population are explained. Based thereon, three exciton processes are then examined in greater detail. Each process is also the main topic of one of the three results chapters. The first process described in Chapter 4 is recombination, taking into account the various pathways through which an exciton may be extinguished. Next, Chapter 5 studies the process of dephasing. It describes the loss of coherence for an exciton ensemble and is related to the spectral broadening of the exciton transition. Finally, the process of diffusion is investigated in Chapter 6. This relates to the transport of excitons within a single or across several adjacent NCs. Each of these chapters starts with an individual, concise introduction including more information on …

> *"Why was this done?"*

2

Fundamentals

This chapter introduces the fundamental concepts regarding semiconductors and highlights the role of excitons within this material class. First, the main focus will be on optical absorption in general and the effect of quantum confinement, based on which spectral broadening and the influence of temperature will be discussed. Subsequently, these general rules will be applied to the more specific case of semiconductor nanocrystals in the form of lead halide perovskites. Eventually, the theory of the excitonic processes of recombination, dephasing and diffusion will be explained on this basis.

2.1 Excitons in Semiconductors

Lead halide perovskites exhibit peculiar properties, rendering them distinctly different from classical semiconductors like gallium arsenide (GaAs), silicon (Si) or cadmium sulfide (CdS). Nevertheless, they are also semiconductors and the same basic principles apply equally to all of the aforementioned materials. For this reason, a general background including the concepts of semiconductors, excitons and their related processes will be introduced first and independent of the exact material type.

2.1.1 Semiconductor Basics

Almost 100 years ago, renowned physicists like Arnold Sommerfeld,[29] Felix Bloch[30] and Alan Herries Wilson[31] laid the foundation for the band structure model of electrons in crystalline solids. Not surprisingly, the birth of the term semiconductor for a solid material in which the number of free electrons strongly depends on temperature also falls into this time period.[32] Semiconductor heterostructures enabled the invention of the pn diode[33] as well as the transistor[34] at the Bell Telephone Laboratories and essentially form the basis of all modern electronics.

In an ideal crystal lattice the sum of potentials induced by all individual atomic cores results in a periodic effective potential for the electrons

$$V(\mathbf{r}) = V(\mathbf{r} + \mathbf{R})\,. \tag{2.1}$$

Here, $\mathbf{R} = n_1\mathbf{a}_1 + n_2\mathbf{a}_2 + n_3\mathbf{a}_3$ denotes the translation vector of the underlying Bravais lattice in real space with the integers n_i and the primitive vectors of the lattice $\mathbf{a}_\mathrm{i}$.[32,35] Instead of treating all of the about 10^{23} outer electrons per cubic centimeter one uses a so-called one-electron approximation in which one electron in a unit cell is described. Due to the periodicity of the crystal and the usually low density of free electrons of less than $10^{19}\,\mathrm{cm}^{-3}$ this is a particularly suitable approach to reliably describe semiconductors.[32] Noninteracting electrons within a periodic potential $V(\mathbf{r})$ as given by Equation 2.1 obey the time-independent Schrödinger equation

$$\left[\frac{\mathbf{p}^2}{2\,m_\mathrm{e}} + V(\mathbf{r})\right]\psi_{\mathrm{n},\mathbf{k}}(\mathbf{r}) = E_\mathrm{n}(\mathbf{k})\,\psi_{\mathrm{n},\mathbf{k}}(\mathbf{r}) \tag{2.2}$$

with the momentum operator $\mathbf{p} = -i\hbar\nabla$, the electron mass m_e and the discrete band index n.[36,37] This equation may be solved using Bloch's theorem,[38] yielding wavefunctions of the form

$$\psi_{\mathrm{n},\mathbf{k}}(\mathbf{r}) = e^{i\mathbf{k}\mathbf{r}} \cdot u_{\mathrm{n},\mathbf{k}}(\mathbf{r}) \tag{2.3}$$

which essentially represents a plane wave $e^{i\mathbf{k}\mathbf{r}}$ that is modified by the periodic function

$$u_{\mathrm{n},\mathbf{k}}(\mathbf{r}) = u_{\mathrm{n},\mathbf{k}}(\mathbf{r} + \mathbf{R})\,. \tag{2.4}$$

Importantly, $u_{\mathrm{n},\mathbf{k}}(\mathbf{r})$ exhibits the same periodicity as the crystal lattice itself.[30] Each of the wavefunctions $\psi_{\mathrm{n},\mathbf{k}}(\mathbf{r})$ is associated with an energy eigenstate $E_\mathrm{n}(\mathbf{k})$ and consequently the periodicity also leads to a probability density function for the observed electron

$$\left|\psi_{\mathrm{n},\mathbf{k}}(\mathbf{r})\right|^2 = \left|\psi_{\mathrm{n},\mathbf{k}}(\mathbf{r}+\mathbf{R})\right|^2 \tag{2.5}$$

that is accordingly the same for all unit cells of the crystal. Reciprocal space (k-space) is connected to the real space via a Fourier transformation.[31] Therefore, the eigenvalues $E_\mathrm{n}(\mathbf{k})$ of Equation 2.2 need to be studied only within the first Brillouin zone in k-space since the whole crystal can then be described via

$$E_\mathrm{n}(\mathbf{k}) = E_\mathrm{n}(\mathbf{k}+\mathbf{G}) \tag{2.6}$$

wherein $\mathbf{G} = m_1\mathbf{b}_1 + m_2\mathbf{b}_2 + m_3\mathbf{b}_3$ is a linear combination of the reciprocal primitive lattice vectors $\mathbf{b}_\mathrm{i}$.[35] $E_\mathrm{n}(\mathbf{k})$ is also referred to as the dispersion relation and is one of the most significant properties when it comes to the physical understanding of a certain semiconductor material. The crystal's periodicity enforces a symmetry at the boundaries of the Brillouin zone where

$$\frac{\mathrm{d}E_\mathrm{n}(\mathbf{k})}{\mathrm{d}\mathbf{k}} = 0 \tag{2.7}$$

has to be fulfilled. This is also consistent with the non-crossing rule.[39] These flattened out regions in the dispersion relation $E_\mathrm{n}(\mathbf{k})$ at the zone boundaries lead to the fact that there are energy intervals within the first Brillouin zone — and thus the whole crystal — that cannot be accessed by any k-value.[40] Moreover, extrema of the energy bands tend to be at the center of the first Brillouin zone, the so-called Γ-point, or at the borders of the zone. Usually, these maxima or minima can be approximated fairly well assuming a parabolic dispersion relation for k-values in their vicinity. Generally, it may be noted that electrons in a periodic potential arrange in energy bands of a certain width, which can be separated by energy gaps in which no stationary eigenstates exist.[32] Of course, all of this does not necessarily imply that all of these bands $E_\mathrm{n}(\mathbf{k})$ are actually filled with electrons. Rather, bands only describe all possible states that may be occupied by electrons. If one is only interested in the overall energy E of possible electron states, the information of all bands can be summarized in the density of states (DOS)

$$D(E) = \frac{1}{V}\sum_{\mathrm{n},\mathbf{k}} \delta(E - E_\mathrm{n}(\mathbf{k})) \tag{2.8}$$

where V is the volume of the crystal. The quantity $D(E)\mathrm{d}E$ determines how many quantum states lie in the energy interval $[E, E+\mathrm{d}E]$ which is normalized with respect to the volume.[41] In this context, the Fermi energy E_F is an important quantity defining the highest energy value an electron could reach in the ground state of a system at 0 K.[42] Generally speaking, one may distinguish two different energetic positions of E_F. If it lies within an energetic band, i.e., $D(E_\mathrm{F}) \neq 0$, then the material is defined as a metal. However, if E_F lies in one of the above mentioned energy gaps, i.e., $D(E_\mathrm{F}) = 0$, one refers to the material either as an insulator or a semiconductor. In the latter case all of the bands with an energy less than E_F are called valence band (VB), whereas all of the bands above the gap with an energy larger than E_F are named conduction band (CB). Effectively, the magnitude of the so-called energy band gap E_G between CB and VB has to be taken into account in order to distinguish between insulators and semiconductors. Usually, a semiconductor is defined by the range $0\,\mathrm{eV} < E_\mathrm{G} < 4\,\mathrm{eV}$, whereas

insulators exhibit even larger band gaps. However, the upper limit of 4 eV is not a strict border and there is a rather smooth transition region in which insulators and semiconductors coexist according to this definition.[32]

The results so far determine the energies at which electrons can occupy states and the density of these states, however, one also needs to know how these states are actually occupied by electrons. Electrons are fermions and consequently obey Fermi-Dirac statistics, having the distribution function

$$f(E,T) = \frac{1}{\exp\left(\frac{E-E_\mathrm{F}}{k_\mathrm{B}T}\right)+1} \tag{2.9}$$

with the Boltzmann constant k_B and the temperature T.[43,44] This function gives the occupation probability for a certain energy value E. For $T = 0\,\mathrm{K}$ it is a step function meaning that all of the states in the VB are filled by electrons whereas all of the states in the CB remain empty. For $T > 0\,\mathrm{K}$ the distribution "smears out" and some of the electrons possess enough thermal energy to overcome the energy band gap E_G. Then, they reside in the CB where they contribute to the conductivity of the semiconductor and are considered to be free or quasi-free depending on the notation. The actual probability to find an electron at a certain energy is then given by the product $D(E) \cdot f(E,T)$.[32]

2.1.2 Excitons Versus Free Electron-Hole Pairs

So far, the basics have been introduced by describing only electrons and their properties within a periodic crystal. However, in order to understand those processes occurring in semiconductor materials that are relevant to us, the respective counterparts of electrons need to be considered, as well, which are the so-called holes.

Equation 2.9 shows how the temperature T influences the electron distribution in a semiconductor. With increasing temperature more and more electrons accumulate in the conduction band. This thermal excitation, lifting an electron up into the energetically higher CB, simultaneously results in an empty space in the VB which is referred to as a hole. Generally, this process is called electron-hole (e-h) pair generation. Consequently, with respect to an initial equilibrium, the amount of electrons and holes is the same. Holes are quasiparticles representing the lack of an electron within a semiconductor and therefore carry the positive elementary charge $+e$.

Usually, electrons in the CB assemble at the energetically favorable conduction band minimum (CBM) at the energy E_CBM. Conversely, holes in the VB tend to gather at the valence band maximum (VBM) at E_VBM. Consequently, the band gap energy may be calculated via $E_\mathrm{G} = E_\mathrm{CBM} - E_\mathrm{VBM}$. It was already mentioned in the previous subsection that the region close to these extrema in the energy bands can be approximated fairly well by a parabolic function, which leads to

$$E_\mathrm{CB}(\mathbf{k}) = E_\mathrm{CBM} + \frac{\hbar^2}{2\,m_\mathrm{e}^*}\left(\mathbf{k}-\mathbf{k}_\mathrm{CBM}\right)^2 , \qquad E_\mathrm{VB}(\mathbf{k}) = E_\mathrm{VBM} - \frac{\hbar^2}{2\,m_\mathrm{h}^*}\left(\mathbf{k}-\mathbf{k}_\mathrm{VBM}\right)^2 \tag{2.10}$$

for electrons and holes, respectively.[40] Here, $\mathbf{k}_\mathrm{CBM}$ and $\mathbf{k}_\mathrm{VBM}$ denote the k-vectors at which the respective extremum occurs. If $\mathbf{k}_\mathrm{CBM} = \mathbf{k}_\mathrm{VBM}$, one speaks of a direct band gap for the investigated semiconductor. Otherwise it is referred to as an indirect band gap. Differentiating Equation 2.10 twice with respect to $\mathbf{k}$ leads to

$$\frac{1}{m_\mathrm{e}^*} = \frac{1}{\hbar^2}\frac{\mathrm{d}^2 E_\mathrm{CB}(\mathbf{k})}{\mathrm{d}\mathbf{k}^2}\,, \qquad \frac{1}{m_\mathrm{h}^*} = -\frac{1}{\hbar^2}\frac{\mathrm{d}^2 E_\mathrm{VB}(\mathbf{k})}{\mathrm{d}\mathbf{k}^2} \tag{2.11}$$

which shows that the effective masses of the electron m_e^* and hole m_h^* are related to the curvature of the respective energy band. In solid state physics these effective masses are the mass an electron or hole within the crystal lattice seems to have when responding to external forces caused, e.g., by an electric field.

Besides the aforementioned thermal excitation, other ways to generate e-h pairs are impact ionization,[45] charge carrier injection into the respective material[46] or photoexcitation. The latter — also referred to as optical excitation — is the main process for e-h pair generation within this thesis and served as the quintessential initial step in most of the experiments. Therefore, the following part shall cover the underlying process of photon absorption and interrelated e-h pair generation within a semiconductor. A certain energy

$$E = h\nu = \hbar\omega \tag{2.12}$$

may be ascribed to each photon, depending only on its frequency, either in the form of ν or — in case of angular notation — in the form of $\omega = 2\pi\nu$. In vacuum the wavelength of these photons is $\lambda = c/\nu$ which is also an accurate approximation for light waves traveling in air. The spectroscopic experiments conducted for this thesis spanned the wavelength region from the near ultraviolet (NUV) to the near infrared (NIR), including the whole visible range (VIS) in between. In terms of photon energy E, this presents the range of about 1.3 eV to 3.5 eV. When being absorbed in a semiconductor, a photon is annihilated and transfers its energy to an electron which in turn is lifted to an energetically higher band, leaving a hole behind in its original band. Keeping in mind the previous subsection, the mentioned span of photon energies relates well to the definition of a semiconductor material, whose band gap energy E_G per definition lies in a comparable range.

Naturally, the probability for a photoinduced electron transition benefits from an initial situation with many electrons in the ground state and only few electrons in the final state of the respective transition. In thermal equilibrium and at moderate temperatures the states of the VB are almost completely filled with electrons while the CB remains mostly empty in accordance with Equation 2.9 representing the Fermi-Dirac statistics. Even though intraband transitions of electrons — for example just within the CB — might occur as well, this suggests that the by far most probable type of optically induced transitions are so-called interband transitions, i.e., the ones in which an electron from the VB is lifted into the CB. It goes without saying that such transitions require a photon energy $E \geq E_\mathrm{G}$ to overcome the energy gap between the involved bands. Generally, Fermi's golden rule[47,48] is used to describe the rate, i.e., the probability per time, for a given transition

$$\Gamma_{\mathrm{m}\to\mathrm{n}} = \frac{2\,\pi}{\hbar} \cdot |\langle n|H'|m\rangle|^2 \cdot D_\mathrm{j}\,(\hbar\omega) \tag{2.13}$$

from an initial state $|m\rangle$ to a final state $|n\rangle$. H' is the perturbation causing the transition, in this case an electric field in the form of incident photons. $\langle n|H'|m\rangle$ is the so-called matrix element and determines the probability of a given transition, thus it also states if a transition is possible at all. The term $D_\mathrm{j}\,(\hbar\omega)$ is the so-called joint density of states (JDOS) which is defined as

$$D_{\mathrm{j}}(\hbar\omega) = \frac{2}{8\,\pi^3} \int \delta[E_{\mathrm{n}}(\mathbf{k}) - E_{\mathrm{m}}(\mathbf{k}) - \hbar\omega]\,\mathrm{d}^3\mathbf{k}\,. \tag{2.14}$$

The delta function basically represents the conservation of energy and thereby indicates that only those transitions need to be taken into account for which the energy of the absorbed photon $E = \hbar\omega$ is equal to the energy difference of the final and initial state of the electron $E_{\mathrm{n}}(\mathbf{k}) - E_{\mathrm{m}}(\mathbf{k})$. In general, photon absorption processes do not only require the conservation of energy, but also of momentum. The linear dispersion relation of photons $E(\mathbf{k}) = \hbar\omega(\mathbf{k}) = \hbar c|\mathbf{k}|$ is extremely steep compared to typical dispersion relations of electrons in a periodic lattice as introduced in Equation 2.6 (i.e., 2-3 orders of magnitude steeper). Thus, when exciting an electron transition, a photon mainly transfers energy to the respective electron while barely influencing its momentum. Transitions requiring a larger change in momentum need the additional interaction with phonons within this process.[32]

Despite the requirement $E = \hbar\omega \geq E_{\mathrm{G}}$ for interband transitions, absorption spectra often exhibit features below the band gap energy E_{G} where the semiconductor would be expected to be transparent. This may be explained by the Coulomb potential

$$V(\mathbf{r}_{\mathrm{e}}, \mathbf{r}_{\mathrm{h}}) = \frac{e^2}{4\,\pi\epsilon_0\epsilon_{\mathrm{r}}|\mathbf{r}_{\mathrm{e}} - \mathbf{r}_{\mathrm{h}}|} \tag{2.15}$$

acting between electrons and holes; an effect that has been neglected so far.[40] This potential leads to bound states of the negatively charged electron and the positively charged hole, both of which carry the elementary charge e as their absolute charge. Such a bound quasiparticle is referred to as an exciton. The surrounding material is taken into account via the permittivity $\epsilon = \epsilon_{\mathrm{r}}\epsilon_0$ consisting of the dielectric function of the semiconductor ϵ_{r} and the vacuum permittivity ϵ_0. Besides that, $\mathbf{r}_{\mathrm{e}}$ and $\mathbf{r}_{\mathrm{h}}$ denote the positions of the electron and hole within the crystal, respectively. In bulk crystals, the potential $V(\mathbf{r}_{\mathrm{e}}, \mathbf{r}_{\mathrm{h}})$ results in a constant mean value for the distance between the bound electron and hole of an exciton which is referred to as the exciton Bohr radius $a_{\mathrm{ex}} = |\mathbf{r}_{\mathrm{e}} - \mathbf{r}_{\mathrm{h}}|$ for the energetically lowest excitonic state.

Generally speaking, there are two types of excitons, the Frenkel exciton as well as the Wannier-Mott exciton. On the one hand, Frenkel excitons are strongly bound. In this case, the e-h pair is located near a single atom or molecule within the lattice, meaning that $a_{\mathrm{ex}} \leq a$, where a denotes the lattice constant of the investigated semiconductor crystal. On the other hand, Wannier-Mott excitons conversely represent weakly bound e-h pairs in which the exciton Bohr radius a_{ex} for the bulk crystal is larger than the lattice spacing a. The exciton type for a certain semiconductor is basically given by the dielectric function ϵ_{r} which is reported to be relatively large in LHP semiconductors.[49,50] In accordance with Equation 2.15, this leads to a strongly reduced Coulombic potential due to electric field screening.[51,52] Consequently, excitons in LHP crystals are only weakly bound and there is common agreement that these are excitons of the Wannier-Mott type.[53,54] Therefore, only the relevant theory for Wannier-Mott excitons will be discussed in the following.

Figure 2.1 a shows a graphical representation of a Wannier-Mott exciton within a bulk crystal. The distance between the bound electron and hole spans across several unit cells, leading to a screening of the Coulomb potential which is taken into account via the dielectric function of the material ϵ_{r}.

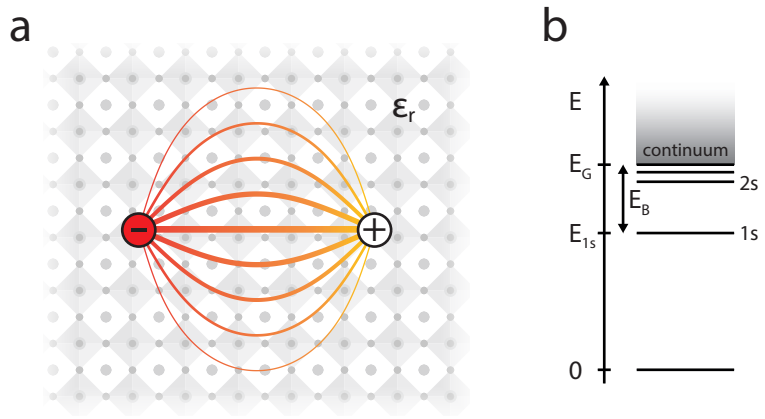

Figure 2.1: Wannier-Mott Exciton. (a) Illustration of a of Wannier-Mott exciton within a bulk semiconductor crystal. The bound electron and hole attract each other due to the Coulomb potential. **(b)** Theoretical model of the electronic energy levels of a semiconductor in the two-particle picture representing possible transitions: ground state, excitonic levels (1s, 2s, 2p, ...) and continuum onset at the band gap energy E_G. The difference between E_G and the 1s excitonic state E_{1s} is the exciton binding energy E_B.

In order to obtain the energy eigenvalues E_{ex} for this two-particle system one has to solve the Schrödinger equation including the Coulomb potential in the Hamiltonian.[55]

$$\left[\frac{\mathbf{p}_e^2}{2\,m_e^*} + \frac{\mathbf{p}_h^2}{2\,m_h^*} - \frac{e^2}{4\,\pi\epsilon_0\epsilon_r|\mathbf{r}_e - \mathbf{r}_h|}\right]\psi_{ex}(\mathbf{r}) = E_{ex}\,\psi_{ex}(\mathbf{r}) \tag{2.16}$$

This is also referred to as the Wannier equation and resembles a problem similar to the theoretical model of the hydrogen atom.[38,56] Hence, a reduced mass m_{ex} and total k-vector $\mathbf{K}$ may be assigned to the exciton:

$$m_{ex} = \left[\frac{1}{m_e^*} + \frac{1}{m_h^*}\right]^{-1}, \tag{2.17}$$

$$\mathbf{K} = \mathbf{k}_e + \mathbf{k}_h\,. \tag{2.18}$$

Taking this into account, the solution of Equation 2.16 yields the total energy of an exciton

$$E_{ex} = E_{n,\mathbf{K}} = E_n + \frac{\hbar^2}{2\,(m_e^* + m_h^*)}\mathbf{K}^2\,. \tag{2.19}$$

While the latter summand describes the overall motion of the exciton, the first part E_n represents the energy stored within the Coulomb bond of the exciton. Explicitly, this may be calculated via

$$E_n = \frac{m_{ex}e^4}{8\,h^2\epsilon_0^2\epsilon_r^2}\frac{1}{n^2}\,, \tag{2.20}$$

wherein, similar to the mathematical model for the hydrogen atom, the integer $n \geq 1$ may be used to label the different solutions and the associated energy values. For $n = 1$ this expression yields the so-called exciton binding energy

$$E_{\mathrm{B}} = E_{\mathrm{n=1}} = \frac{\hbar^2}{2\,{a_{\mathrm{ex}}}^2 m_{\mathrm{ex}}}\,, \tag{2.21}$$

which is the maximum amount of energy that may be stored in the Coulomb bond of an exciton. Here, the formula for the aforementioned exciton Bohr radius

$$a_{\mathrm{ex}} = \frac{4\,\pi\epsilon_0\epsilon_{\mathrm{r}}\hbar^2}{m_{\mathrm{ex}}e^2} \tag{2.22}$$

is introduced. It reveals the typical distance between an electron and a hole comprising an exciton ($n = 1$) within a bulk crystal. Summing up, the preceding equations explain why photons with an energy below the band gap

$$\hbar\omega = E_{\mathrm{G}} - \frac{E_{\mathrm{B}}}{n^2} \tag{2.23}$$

may be absorbed in a semiconductor and result in the excitation of bound e-h pairs. Figure 2.1 b depicts the exciton energy levels in the two-particle picture which shows the possibility of transitions in accordance with Equation 2.23. As in the model for the hydrogen atom, the excitonic transitions — or, put differently, the orbital hybridizations — are named 1s, 2s, 2p and so forth. Yet, it is important to note and crucial for this work that the 1s exciton with $n = 1$ is the predominant transition as the strength of the excitonic transitions is strongly reduced with increasing n. Further explanation on this will follow in the next subsection.

There are three additional possible mechanisms for absorption of photons with energies below the band gap E_{G}. The first one is the nonlinear process of multiphoton absorption in which several photons with an energy $\hbar\omega < E_{\mathrm{G}}$ interact to surpass the band gap energy E_{G}, thereby enabling absorption.[57–59] In the context of this work, the excitation densities were kept sufficiently low to rule out a relevant occurrence of such effects. A second mechanism is the excitation of intraband transitions, for example of electrons within the CB. Given the range of excitation densities and wavelengths used in this work, this effect may be neglected, as well. Put simply, this is due to the modest amount of electrons in the CB compared to the amount of electrons in the VB which are potential candidates for interband transitions, effectively making this the dominant observed type of transition. Lastly, the presence of crystal defects or dopants within the semiconductor crystal may lead to energetic states in the originally forbidden band gap region.[41] Interestingly, LHP crystals exhibit a strong defect tolerance, rendering this effect negligible, as well.[60,61] Therefore, within the context of this thesis excitons are the dominant cause for sub-band gap absorption, such that according features in this wavelength region, especially in proximity to the continuum onset, may be attributed to them.

In the final part of this subsection the importance of the exciton binding energy and its influence on the semiconductor will be discussed. Absorption of photons with $\hbar\omega \geq E_{\mathrm{G}}$ is represented by the continuum region in Figure 2.1 b. There, the generated electrons as well as holes are considered to be free and are named accordingly. These free electrons and holes form the complement to bound e-h pairs below the band gap E_{G}. Usually, everyday devices are operated at room temperature; naturally, this was also the condition for many of our experiments. However, at room temperature ($T = 293\,\mathrm{K}$) the thermal energy of electrons E_{th} may play a non-negligible role.

E_{th} is distributed according to Maxwell–Boltzmann statistics and the average thermal energy per electron may be calculated via

$$E_{\mathrm{th}} = f \cdot \frac{1}{2} k_{\mathrm{B}} T \tag{2.24}$$

with the Boltzmann constant k_{B} and the temperature T.[62] The factor f denotes the number of degrees of freedom, i.e., for a bulk crystal $f = 3$. Yet, often only $k_{\mathrm{B}}T$ is used to approximate the thermal energy of an electron population. At room temperature (20 °C) this amounts to 25 meV. This explains why the exciton binding energy E_{B} is of importance. If E_{B} lies in the same range or is even smaller than E_{th}, the thermal energy may be sufficient to overcome the barrier towards the continuum. In other words, the thermal energy may ionize an exciton and lead to a free electron and a free hole. So, due to thermal broadening, the changeover between an exciton and an e-h pair is not as strict as it may appear at first glance in Figure 2.1 b. Under thermodynamic equilibrium, excitons and free e-h pairs coexist with an ongoing interchange between both species.[22] The fraction of the exciton species compared to the overall number of excited charge carriers not only depends on the exciton binding energy, but also on the excitation density, which influences the probability that electrons and holes meet and thereby possibly form an exciton.[63]

Since the exciton binding energy influences the percentage of free electrons and holes, it is also an important parameter for semiconductor devices. In solar cell applications, small values for E_{B} are favorable as they effectively enable an easier separation of electrons and holes within the device due to the greater proportion of free electrons and holes. In contrast, LEDs require effective radiative recombination of electrons and holes such that bound e-h pairs with a larger E_{B} may be advantageous. This makes LHP an interesting candidate for both types of devices since E_{B} can be adjusted via the composition and geometry.

2.1.3 The Elliott Model

For the present work, dynamic processes involving excitons were studied using several spectroscopic techniques. The Elliott model for optical absorption in semiconductors[26] can serve to explain the shape of these spectra with a special focus on excitons arising at the absorption onset and shall hence be discussed in the following subsection.

According to the Elliot model, the absorption behavior of a semiconductor can be described as

$$\begin{aligned}\alpha_{\mathrm{3D}}(\hbar\omega) = & \underbrace{A_{\mathrm{ex}} \sum_{n=1}^{\infty} \frac{4\pi}{n^3}\, \delta\left(\hbar\omega - E_{\mathrm{G}} + \frac{E_{\mathrm{B}}}{n^2}\right)}_{\text{excitons}} + \\ & \underbrace{A_{\mathrm{c}}\, \Theta(\hbar\omega - E_{\mathrm{G}})\, D_{\mathrm{j}}(\hbar\omega)\, \frac{\pi \exp\left(\pi(\hbar\omega - E_{\mathrm{G}})^{-\frac{1}{2}}\right)}{\sinh\left(\pi(\hbar\omega - E_{\mathrm{G}})^{-\frac{1}{2}}\right)}}_{\text{continuum}}\end{aligned} \tag{2.25}$$

around its onset. Therein, and as highlighted, the first part describes the contribution of excitons to the overall absorption whereas the second part is used to predict the spectrum of the continuum.[38,64] A_{ex} and A_c are factors ascribed to the respective amplitude of both terms. The exciton series ($n \geq 1$) comprises a delta function which has the energetic position of the respective exciton level, as already introduced in Equation 2.23, in its argument. At the same time, the amplitude of the distinct exciton levels scales with n^{-3}. This explains why the 1s exciton ($n = 1$) yields the dominant contribution of the excitons whereas higher orders ($n \geq 2$) only play a minor role (see Figure 2.2). Accordingly, I mainly refer to the 1s exciton when talking about excitons in general. The second part of Equation 2.25 — and in particular the JDOS term $D_j(\hbar\omega)$ — represents the contribution of continuum transitions. The Heaviside step function $\Theta(\hbar\omega - E_G)$ ensures that this part of the equation does not contribute to the energy range below E_G. The Elliott model as introduced here assumes a bulk semiconductor with a direct band gap. Therefore, $D_j(\hbar\omega)$ exhibits a square root dependence with respect to the photon energy starting from E_G. The Elliot model is especially suitable for the absorption onset and does not take into account higher bands in the continuum. Additionally, this term is modified by the so-called Sommerfeld or Coulomb enhancement factor, rendering the Coulomb interaction not only responsible for the presence of excitons below the continuum, but also for absorption above the onset.[38]

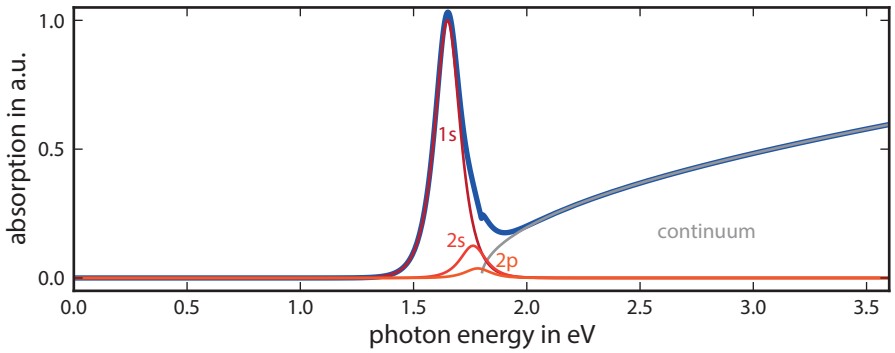

Figure 2.2: Elliott Model for the Absorption Onset. The blue curve shows the calculated absorption onset for a semiconductor with a band gap energy $E_G = 1.8$ eV and an exciton binding energy $E_B = 150$ meV. In this theoretical model the underlying contributions of the first three excitonic levels and the continuum are highlighted in shades of red and grey, respectively. The remaining parameters are $A_{ex} = 0.0125$, $A_c = 0.07$ and $\Gamma = 50$ meV.

In real experiments as well as in the modeling of experimental data, the theoretical concept of the delta function fails and a broadening term Γ has to be introduced instead. To this end, the delta function $\delta(x)$ is replaced by a term of the form $1/[\pi\Gamma\cosh(x/\Gamma)]$. Figure 2.2 shows what an absorption spectrum modeled according to Equation 2.25 looks like when considering the mentioned broadening effect.

2.1.4 Confined Systems

So far, the theory of charge carriers within semiconductors has been discussed for bulk crystals, i.e., for a three-dimensional (3D) material. However, in this work semiconductor nanocrystals were studied, whose dimensions were limited to length scales of only a few nanometers in at least one direction. In many textbooks, such length scales even serve as the definition of the size at which quantum effects become important.[35,65,66]

The particular problem underlying this definition is known as “particle in a box” which is a well-established concept of quantum mechanics.[67] In this gedankenexperiment, an electron is no longer

free to propagate as in the bulk crystal, but restricted to a finite region of space with the shape of a cuboid. Essentially, the nanocrystals examined in this work may as well be approximated by cuboids. Due to their minute size, the so-called effect of quantum confinement may have to be taken into account. Depending on the exact nanocrystal morphology determined by the three edge lengths of the cuboid, quantum confinement may be negligible or play a role in up to all three dimensions. Table 2.1 displays this context and also lists how the energy dependence of the DOS, and therefore of the JDOS, as well, changes in case of quantum confinement.

Table 2.1: Quantum Confinement. Listing of the four basic types of confinement from the bulk 3D crystal down to the quantum dot representing a 0D structure.[65] The reduced dimensionality also influences the energetic dependence of the density of states.

structure	quantum confinement	# of free dimensions	density of states
bulk	none	3	$\propto E^{1/2}$
quantum well	1D	2	$\propto E^{0}$
quantum wire	2D	1	$\propto E^{-1/2}$
quantum dot	3D	0	discrete

One of the more important nanocrystal types studied in the course of this work exhibits a platelet shape, hence being a two-dimensional structure exhibiting quantum confinement in one direction. The theoretical equivalent to such a platelet is a quantum well with an infinite size in both unconfined dimensions. Accordingly, this particular model shall be introduced in the following, representative of confinement more generally.

In a quantum well, an electron is free to propagate in x- and y-directions, however, in z-direction it is trapped in a potential well, i.e., between two infinitely high energetic barriers. The potential is given by

$$V(z) = \begin{cases} \infty & z < 0 \\ 0 & 0 \leq z \leq L \\ \infty & L < z \end{cases} \tag{2.26}$$

wherein L denotes the width of the structure represented by the potential well.[67] Boundary conditions dictate $\psi_\mathrm{n}(z = 0) = \psi_\mathrm{n}(z = L) = 0$, and solving the Schrödinger equation accordingly yields

$$\psi_\mathrm{n}(z) = A_\mathrm{n} \sin\left(\frac{n\pi z}{L}\right) \tag{2.27}$$

and the respective energies

$$E_\mathrm{n}(L) = \frac{\hbar^2 \pi^2 n^2}{2\, m_\mathrm{e} L^2}\,. \tag{2.28}$$

The integer n is the so-called quantum number labeling the states. The boundary conditions cause a quantization along the z-dimension with a restriction on the allowed energies, whereas the energies for the other dimensions are those of a free electron. The same applies to a hole in the VB. Accordingly, the exciton consisting of both also is confined in such structures. From Equation 2.28 it can be gathered that $E_\mathrm{n}(L) \propto L^{-2}$, implying that the size along the confined dimension has a strong influence on the

magnitude of the effect. The length L at which confinement becomes non-negligible may be defined by $E_n(L) \geq E_{th}$.[65] When considering e-h pairs, the axis length along which confinement occurs is commonly divided into two regimes: the weak confinement region with $L \geq a_{ex}$ and the strong confinement region with $L < a_{ex}$.[20] Irrespective of the definition of such a length, it is important to note that the transition between no discernible confinement and strong effects is rather smooth. Therefore, an assignment of a certain nanocrystal to one of the structures listed in Table 2.1 is not always straightforward.

Ultimately, the infinitely deep potential well is an oversimplification for the perovskite platelets. In fact, more sophisticated models are needed to model these nanocrystals with a layer of ligands around them.[19] In order to keep it simple, the following paragraphs feature a qualitative analysis of the reduction in thickness of a bulk-like nanocrystal. Specifically, they will focus on how the properties of a nanocrystal change when transitioning from a 3D towards a 2D material. The three most conspicuous consequences of this analysis are shown schematically in Figure 2.3 and will be highlighted one by one in the following:

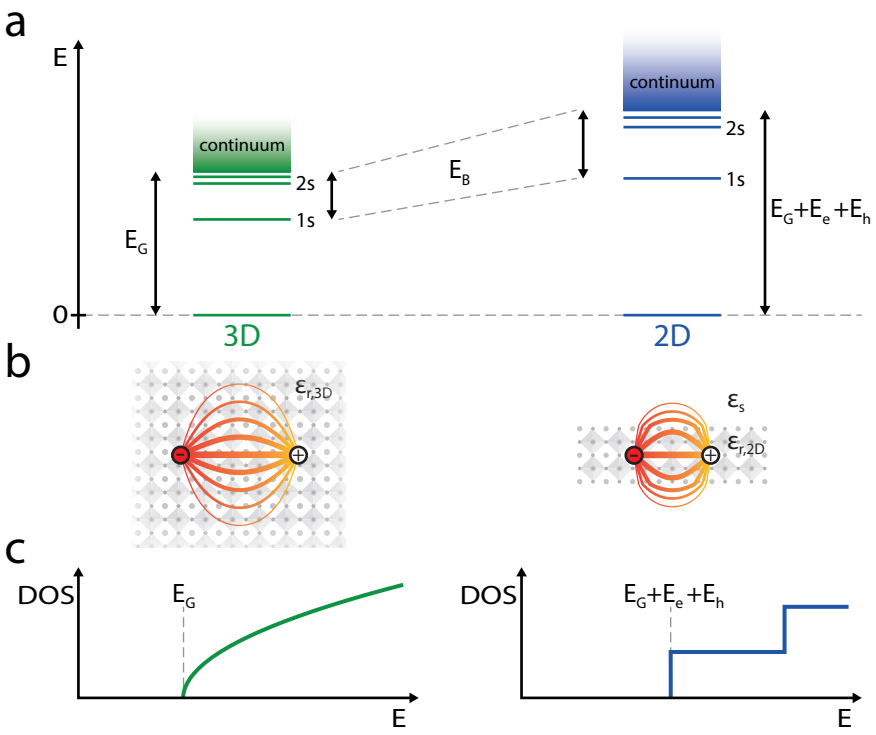

Figure 2.3: Effect of Quantum Confinement (3D to 2D). (a) Reducing the size of a bulk-like 3D semiconductor down to the confinement regime along one dimension will lead to an increase in the continuum onset $E_C = E_G + E_e + E_h$ and a larger exciton binding energy E_B. **(b)** The schemes of excitons within 3D and 2D crystals show how the reduced screening in the latter case leads to a stronger binding between the electron and hole. **(c)** Consequently, the density of states exhibits a modified onset and moreover becomes a step function which eventually alters the shape of the absorption spectra in the continuum region.

- **Continuum Onset**

  In bulk 3D crystals the continuum onset E_C occurs at E_G as shown in Figure 2.3 a. When confinement is introduced, the continuum is blue-shifted to $E_C = E_G + E_e + E_h$ due to the confinement of electrons in the CB ($+E_e$) and holes in the VB ($+E_h$).

- **Exciton Binding Energy**
  Equation 2.21 shows that $E_B \propto a_{ex}^{-2}$. When confined due to a platelet thickness $L < a_{ex}$, the exciton no longer has the option to fully extend up to its original value a_{ex} associated with bulk crystals. This reduction in the effective radius leads to an increase of the exciton binding energy E_B within 2D structures. Another effect of importance that leads to an even further enhanced exciton binding energy E_B is the reduced screening of the Coulomb interaction between the electron and the hole in thin 2D structures.[52] This has two reasons. First, the nanoplatelets themselves present a different dielectric environment for excitons with a deviant dielectric function as compared to a 3D structure. Second, and even more importantly, the surrounding material around the platelet with a significantly lower dielectric function ($\epsilon_s < \epsilon_{r,2D}$) comes into play. The electric field in this specific region outside of the platelet is not screened as efficiently as within the crystal, leading to an overall stronger interaction between the electron and the hole of an exciton. Figure 2.3 b illustrates this context and Figure 2.3 a shows the concomitant increase of E_B in the energy diagram. In atomically thin materials, this strong enhancement of electron-hole interaction is generally ubiquitous.[68]

- **Density of States**
  Table 2.1 comprises an overview on the energy dependence of the density of states for different degrees of confinement. When reducing the thickness of a bulk crystal, the square root dependence of the 3D material $\sqrt{E}$ will vanish and the absorption spectrum in the continuum will accordingly flatten out, adopting the shape of a step-like density of states function for 2D materials (see Figure 2.3 c).

2.1.5 Broadening of Optical Transitions

Given that the ground and excited states of an electron are assigned to a fixed energy value, one may be tempted to assume that absorption and emission spectra exhibit sharp lines. However, in reality every transition possesses a certain line width, i.e., there is always some spread around a mean energy value. This subsection shall introduce the main reasons for such spectral broadening of transitions in semiconductor nanocrystals.

Natural Line Width

Even a single emitter at a temperature of 0 K exhibits a Lorentzian shaped intensity distribution

$$I(E) = \frac{A_0}{(E - E_0)^2 + \left(\frac{\gamma}{2}\right)^2} \tag{2.29}$$

centered around the transition energy E_0.[69] The constant A_0 is determined such that the intensity profile $I(E)$ fulfills the normalization condition $\int_0^\infty I(E)\mathrm{d}E = 1$. In this representation of the distribution function the full width at half maximum (FWHM) of the Lorentzian profile $\gamma = \Delta E$ is referred to as the natural line width γ. This value is given by the uncertainty principle $\Delta E \cdot T_1 \geq \hbar$ where T_1 denotes the lifetime of the excited state. These properties are linked to each other via a Fourier transformation, which leads to a Lorentzian function when being applied on a single exponential decay.

As the name suggests, the natural line width is an inherent property of each and every transition. However, usually it is not directly observable since other, stronger broadening effects are superimposed onto this rather weak effect. Generally speaking, all broadening effects are divided into two categories: homogeneous and inhomogeneous. The natural line width as described above is an example for homogeneous broadening, but both of these categories will be specified in the following.

Homogeneous Broadening

We will start with homogeneous broadening and turn to inhomogeneous effects later on before concluding with the resulting consequences for the total broadening. First, we want to juxtapose both fundamental types of broadening and highlight their differences in Table 2.2. Therein, we limit ourselves to broadening mechanisms occurring in semiconductors.

Table 2.2: Homogeneous and Inhomogeneous Broadening. The two types of broadening are due to fundamentally different mechanisms and therefore also exhibit a varied behavior in terms of temperature-dependence and spectral line shape.

	homogeneous broadening Γ_{hom}	inhomogeneous broadening Γ_{inhom}
origin	scattering processes (carrier-phonon, carrier-carrier), natural line width	deviations within the sample (size, shape, defects, surface, dielectric environment)
temperature-dependence	yes, $\longrightarrow \Gamma_{\mathrm{hom}}(T)$	no, $\longrightarrow \Gamma_{\mathrm{inhom}}$ = constant
shape	Lorentzian $f_{\mathrm{L}}(x) = a\,\frac{c^2}{(x-b)^2+c^2}$	Gaussian $f_{\mathrm{G}}(x) = a\exp\left(\frac{-(x-b)^2}{2\,c^2}\right)$

Generally speaking, homogeneous broadening refers to mechanisms increasing the optical line width of an electronic transition by equally affecting different absorbing or radiating locations within the investigated semiconductor.[70] Therefore, in a purely homogeneously broadened sample the spectral profile of transitions originating from all of the possible different sample locations is equal and given by a Lorentzian distribution. Besides the aforementioned natural line width, this type of broadening can be attributed mainly to scattering events in the semiconductor (see Table 2.2). Here, the expression "carrier" shall represent charge carriers in general, i.e., electrons or holes, which might occur in their free form or bound as excitons. The probability for these scattering events depends on the sample temperature since an increased temperature leads to increased movement of carriers and the lattice. Eventually, such movement leads to a slight uncertainty in the absolute position of the energetic bands in the semiconductor, thereby causing broadened transitions. At room temperature, the natural line width is small compared to the contribution stemming from scattering. Moreover, within the confines of the relevant measurements that studied broadening effects in this thesis, the excitation density was kept relatively low and constant, therefore suppressing carrier-carrier scattering to a small amount. This leaves carrier-phonon processes as the dominant source for homogeneous broadening.[71]

Phonons are quasiparticles describing the collective excitation in the elastic, periodic arrangement of atoms or molecules within a semiconductor crystal, i.e., they represent the vibrational motion of the lattice.[65] A distinction between acoustic and optical phonons is made for solids containing more

than one atom in their smallest unit cell. Acoustic phonons describe movements in which all atoms of a unit cell move coherently in the same direction. Conversely, optical phonons denote out of phase movements between neighboring atoms or molecules within the same unit cell. Without going into further detail, acoustic phonon modes typically lie energetically lower than their optical counterparts as can be gathered from the respective dispersion curves.[40] The naming can be easily understood given that the optical branch with its respective phonons possessing a dipole moment may be excited by light. In contrast, this is not possible for acoustic phonons, which get their name for their ability to propagate like sound waves.

Recapitulatory, the total amount of homogeneous broadening may be defined as

$$\Gamma_{\mathrm{hom}}(T) = \Gamma_{\mathrm{hom,rest}} + \Gamma_{\mathrm{ac}}(T) + \Gamma_{\mathrm{op}}(T) = \Gamma_{\mathrm{hom,rest}} + \gamma_{\mathrm{ac}} T + \frac{\gamma_{\mathrm{op}}}{\exp\left(E_{\mathrm{op}}/k_{\mathrm{B}}T\right) - 1} \,. \tag{2.30}$$

Here, the term $\Gamma_{\mathrm{hom,rest}}$ accounts for the small contribution stemming from the natural line width γ and carrier-carrier scattering. Due to its small magnitude compared to the broadening caused by phonons, this term is often neglected in literature.[72,73] However, in Equation 2.30 a more precise definition of $\Gamma_{\mathrm{hom}}(T)$ is carried out. In principle, the temperature T also has a slight influence on $\Gamma_{\mathrm{hom,rest}}$, however, this effect is insignificant. The dominant temperature-dependent phonon contribution is described by the remaining terms, where $\Gamma_{\mathrm{ac}}(T)$ and $\Gamma_{\mathrm{op}}(T)$ account for the respective contributions of acoustic and optical phonons.[72,74,75] The broadening caused by acoustic phonons scales linearly with the temperature T and the dependency is determined by the coupling strength γ_{ac}. Due to this correlation they mainly play a role at low temperatures. Optical phonons follow Bose-Einstein statistics and therefore gain in importance at elevated temperatures. Their scattering strength is described by the Fröhlich coupling constant γ_{op} and the average optical phonon energy E_{op} within this model.[76]

While Equation 2.30 suggests that $\Gamma_{\mathrm{ac}}(T)$ and $\Gamma_{\mathrm{op}}(T)$ vanish completely for temperatures close to 0 K, this is not entirely true. Even at low finite temperatures, acoustic phonons still contribute to $\Gamma_{\mathrm{hom}}(T)$ due to scattering with charge carriers.[77,78] Moreover, the broadening term $\Gamma_{\mathrm{hom,rest}}$ gains in importance in the low temperature regime as carrier-carrier scattering will be present for each temperature due to a given finite excitation density. Finally, it shall be mentioned that the correlation between homogeneous broadening Γ_{hom} and dephasing time T_2 represents an important cornerstone in the present work and will be dealt with in Section 2.4.

Inhomogeneous Broadening

This mechanism is essentially rooted in simple geometry. The examined volume within a spectroscopy measurement is not infinitesimally small. Therefore, deviations within the sample volume might occur. For larger structures, these may for example be variations in the layer thickness within heterostructures, and in the case of nanocrystals or other forms of clusters this simply refers to different sizes or shapes of the respective constituents inside the examined volume.[79,80] Additionally, inhomogeneous broadening may also stem from impurities, strain inhomogeneities or different dielectric environments. All of these deviations have a slight influence on the energy bands within the structure and thereby lead to an increased transition line width, also known as inhomogeneous broadening. Clearly, these geometric properties are inherent to the material and hence do not strongly change with temperature, making Γ_{inhom} a constant with respect to temperature. Moreover, crystal size or defect distributions should be

described by a Gaussian function. This in turn is reflected by the respective spectral line shape of the inhomogeneous broadening which can be approximated by such a function.

In closing, it shall be explained how the total broadening $\Gamma_{\text{total}}(T)$ of a transition may be calculated. The mathematically correct way to determine $\Gamma_{\text{total}}(T)$ is to calculate the convolution of the Gaussian-shaped inhomogeneous broadening and the Lorentzian-shaped homogeneous broadening resulting in a so-called Voigt profile.[69] However, this is usually not needed and it is sufficient to determine the total broadening as the sum of both fundamental mechanisms via

$$\Gamma_{\text{total}}(T) = \Gamma_{\text{hom}}(T) + \Gamma_{\text{inhom}} \,. \tag{2.31}$$

2.1.6 Influence of Temperature

The influence of temperature on spectral broadening through phonons has been described above. Here, in the last part of the present section, three additional temperature-driven effects in semiconductors shall be highlighted briefly.

Accessibility of Defect States

Earlier, semiconductors were introduced as a perfect periodic structure of a repeated unit cell. However, in reality defects (impurities, voids or interstitials) may be present within a semiconductor or on its surface, causing so-called trap states.[81] These states are named after their potential ability to trap excited charge carriers in their vicinity. Like a potential well they feature a certain energetic depth and, depending on this value, they may be classified either as shallow or deep traps. Usually, in contrast to their counterparts, shallow traps will not capture charge carriers at room temperature due to their sufficiently large thermal energy allowing them to overcome this quite small barrier in the potential. However, shallow traps gain in importance as the temperature of the semiconductor is reduced.[82]

Shift of the Band Gap

Not only confinement, also the temperature can lead to a shift of the band gap E_{G}. This is mainly governed by two separate mechanisms.[83] First, the band gap is a result of the potential given by the crystal structure and its periodicity. Consequently, a temperature-dependent dilatation of the lattice leads to a shift of the VB and CB with respect to each other. Moreover, the electron-phonon interaction is also influenced by the temperature and may lead to similar shifts.

Studying these temperature-dependent effects for several semiconductors, Varshni developed his famous empirical expression

$$E_{\text{G}}(T) = E_{\text{G}}(T = 0\,\text{K}) - \frac{\alpha T^2}{T + \beta} \,. \tag{2.32}$$

Therein, the material dependent parameters α and β enable a convenient description of the correlation between the band gap E_{G} and the temperature T of a semiconductor.

Change of the Crystal Phase

In some semiconductors, a change in temperature may lead to different orientations of subunits within the given crystal structure.[84] For example, the perfect cubic phase might not always be the energetically most favorable one. As a consequence, subunits of the crystal can realign with respect to each other, forming a stable phase for a given crystal composition at a certain temperature. This effect will be shown in detail in the next section for the case of perovskite crystals.

2.2 Lead Halide Perovskite Nanocrystals

The renaissance of lead halide perovskite (LHP) was initiated with its successful implementation in a solar cell in 2009,[5] paving the way for a whole new topic at the forefront of current research — the development of photovoltaics based on the highly efficient sunlight absorbing semiconductor LHP.[6] However, LHPs have not only proven to be advantageous for applications based on charge separation, but also for the opposite process in which charges are brought together to emit light. Hence, they are also interesting candidates for LEDs.[18] Bulk films of this material exhibit limitations regarding their photoluminescence quantum yields, but the emergence of colloidal synthesis yielding perovskite NCs has been beneficial to solve this problem. Strongly luminescent LHP NCs were the samples investigated for this thesis. In the following section, this novel class of material will be introduced.

2.2.1 Structure, Compositions and Morphologies

Structure

Originally, the term perovskite only referred to the mineral calcium titanate $CaTiO_3$, but now it is generally used for all compounds exhibiting an identical crystal structure ABX_3. For the LHPs studied in this work, this stoichiometry typically consists of a monovalent A-cation, a divalent B-cation and a monovalent X-anion. Consequently, these compounds are mostly held together by ionic bonds, which is also a reason why their synthesis is possible at relatively low temperatures[85] and why ion exchanges may be easily carried out.[21,86,87]

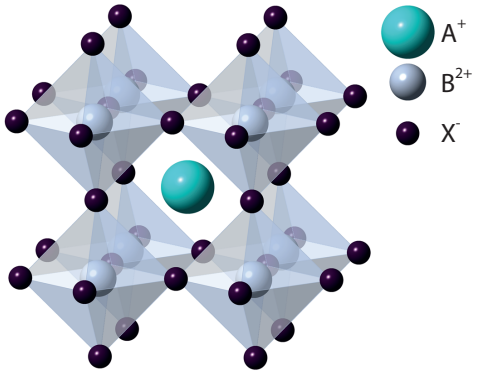

Figure 2.4: Perovskite Crystal Structure. Representation of the cubic perovskite structure with the cations A^+, B^{2+} and the anion X^-. A unit cell of this structure contains exactly one centered BX_6^{4-} octahedron with eight A^+ cations at the corners. In the tetragonal and orthogonal phase, the octahedra are tilted against each other which leads to slightly different sizes of the unit cells for these three crystal phases.

Figure 2.4 depicts the perovskite crystal structure with its characteristic corner-sharing octahedra in the cubic phase and the A^+ ions in between them. With decreasing temperature, the crystal may also exhibit the tetragonal or orthogonal phase.[88] Then, the octahedra are tilted against each other, causing a different arrangement of the ions within the unit cell and hence leading to changed optical properties such as a different energy band gap. That is, the correlation of energy band gap versus temperature can experience discontinuities at theses phase transitions,[72,76] and Varshni's heuristic formula[83] (Equation 2.32) can be applied to only one of these crystal phases at a time.

Compositions

The name lead halide perovskite already suggests some of the material's constituents. In the examined NCs the B-site cation was always lead (Pb^{2+}) and the halide X-site anion was either chloride (Cl^-), bromide (Br^-), or iodide (I^-). Thanks to the well-known technique of halide ion exchange it is also possible to synthesize mixed perovskites with the stoichiometry $APbCl_xBr_{3-x}$ or $APbBr_xI_{3-x}$ where $0 < x < 3$.[17,89] Beyond the work of this thesis, lead was also replaced with the nontoxic alternative bismuth.[90] Lastly, the A-site is either occupied by methylammonium ($CH_3NH_3^+$, MA^+) or cesium (Cs^+).

Whether a given composition is stable and hence actually capable of forming a perovskite crystal structure with corner-sharing octahedra is usually determined by the tolerance factor t_G proposed by Goldschmidt in 1926.[1]

$$t_G = \frac{r_A + r_X}{\sqrt{2}(r_B + r_X)} \tag{2.33}$$

The variables r_A, r_B and r_X represent the respective ionic radii of the cations and anions of the crystal lattice. Their values can be obtained from the literature.[91,92] In principle, Equation 2.33 determines how densely/efficiently the space of the lattice is filled. It acts as a measure for the overall stability of the respective structure. Usually, if t_G assumes a value between 0.8 and 1, a stable perovskite structures is to be expected. Outside of this range other structures are generally energetically more favorable.[93]

Table 2.3: Goldschmidt Tolerance Factor. The stability of a perovskite composition can be evaluated with the Goldschmidt tolerance factor t_G. The table shows the respective values for all compositions examined in the course of this thesis which have the common formula $APbX_3$ with A = MA^+ or Cs^+ and X = Cl^-, Br^- or I^-.

	Cl^-	Br^-	I^-
MA^+	0.936	0.927	0.912
Cs^+	0.819	0.815	0.807

As can be seen in Table 2.3, all of the perovskite crystals examined within the course of this thesis lie within this range of t_G values that indicate a stable perovskite crystal structure. For the organic-inorganic $MAPbX_3$ perovskite crystals, the ionic radius of the MA^+ molecule is an effective value and amounts to 217 pm.[91] The overall smaller values of t_G for fully inorganic $CsPbX_3$ perovskites stem from the smaller ionic radius of Cs^+ = 167 pm. Consequently, the Cs^+ ions do not occupy as much space between the octahedra as the protonated amine MA^+. This has an influence on the aforementioned crystal phase specifically concerning the octahedral tilt angle. Cs-based perovskites usually occur in the orthorhombic phase at room temperature and transitions to the tetragonal and cubic phases only happen at elevated temperatures.[94,95] In contrast, MA-based perovskites appear in the cubic or tetragonal phase at room temperature and exhibit phase transitions when cooling down.[72,76,96]

Morphologies

Not only the composition, but also the morphology and crystal size, determine the crystal phase and other properties.[97,98] This leads us to one of the unique and most notable features of the material this work focuses on. Bulk perovskite films are not the subject of interest here, as nanocrystals (NCs) of

various perovskite compositions were investigated. Generally speaking, one talks about a NC when the size of the crystal in at least one dimension induces quantum confinement (cf. Subsection 2.1.4). Thinking in terms of the unit cell of the crystal, this means that such crystals only consist at maximum of a few tens of unit cells in the confined dimension(s). As already mentioned, LHP NCs usually exhibit the shape of cuboids. At their surface all of the A-site positions are assumed by organic ligands instead of MA^+ or Cs^+. Usually, these ligands are long-chained molecules like octylammonium ($C_8H_{17}NH_3^+$) or oleylamine ($C_{18}H_{35}NH_2^+$) which passivate the surface of the NC and prevent further growth thereof.[18,19] Figure 2.5 shows a scheme of a NC with its surrounding ligands for the example of a $CsPbBr_3$ nanoplatelet.

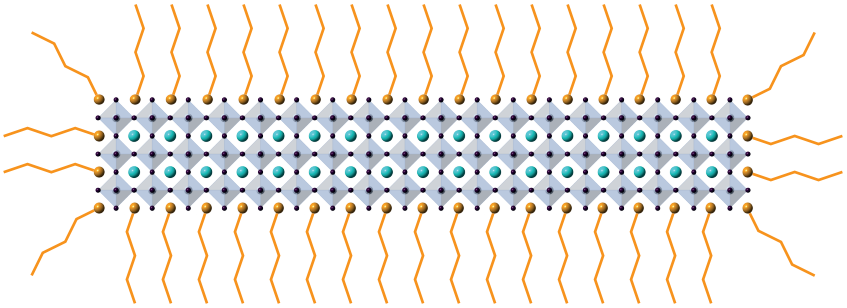

Figure 2.5: Perovskite Nanocrystals. The above scheme shows a side view of a $CsPbBr_3$ nanoplatelet. This 2D structure is represented in its typical size with a lateral length of around 10 nm and a thickness of only three unit cells (1.8 nm). The surface is protected by ligands anchoring at the A-site lattice positions.

Although having the same crystal structure as bulk films of perovskite, these NCs may exhibit different optical and electronic properties. The dimensionality of the structures is of importance, but as adumbrated before, an explicit assignment to the degree of quantum confinement is not always possible. Just as an example, $CsPbX_3$ nanowires (X = I, Br, Cl) fall into the weak confinement regime along their two transversal dimensions and do not show any form of quantum confinement along the third, longitudinal axis.[21] Property-wise, these structures show mixed evidence of 3D and 1D materials. Their absorption characteristics are similar to those of a bulk material, but their diffusion and polarization behavior indicate a 1D structure. Other properties that are strongly dictated by the NC morphology are for instance the band gap, emission wavelength,[12,19] photoluminescence quantum yield, influence of surface defects,[20] exciton binding energy or carrier cooling rates.[52]

2.2.2 Electronic Band Structure

The formation of energy bands was already explained earlier in this chapter for semiconductors in general. Here, we drill down on this issue and describe the electronic band structure for the specific case of LHPs. The computational modeling method density-functional theory (DFT) is a common choice for band structure calculations and has already extensively aided in the study of the optical properties of LHPs.[99–101] Theoretical modeling like this is quite complex. Several complementary techniques are required for an accurate reflection of experimental findings within these semiconductors. For example, it has been found that the tilting of the octahedra within LHPs has a strong influence on the electronic band structure.[102,103] In this context, it is a common mistake to rely on merely one unit cell using periodic boundary conditions to represent the perovskite crystal. LHPs are said to be polymorphous and in order to take into account the different crystal phases and varying tilting

angles of the octahedra due to thermal disorder, a larger volume of the crystal must be modeled to obtain realistic results for the energy bands.[104] Despite the ongoing efforts of a large community of researchers working on LHPs for the last few years, some effects of this intriguing material still remain elusive.[105] The properties requiring further studies include, for example, the exact role of the organic cation or the dynamic disorder of the lattice. Nevertheless, there is vast agreement among scholars on the rough electronic band structure of LHPs and how it is related to some of the material properties. This shall be explained on the basis of Figure 2.6.

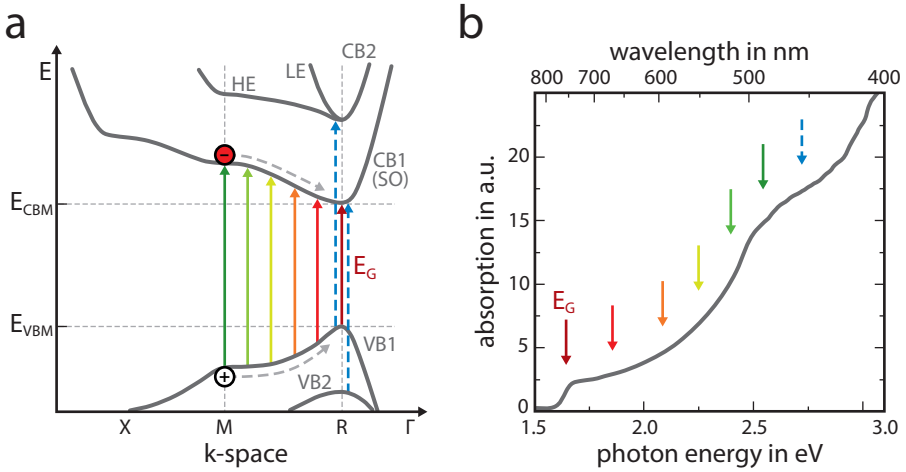

Figure 2.6: Electronic Band Structure of Lead Halide Perovskites. **(a)** Scheme of a typical band structure representing bulk LHPs based on DFT calculations by Even et al.[106,107] The bands CB1 and VB1 determine the band gap energy E_G and enable a strong absorption over the visible range. Allowed photoinduced transitions are marked by the colored solid arrows pointing upwards between those two bands. Moreover, the dashed blue arrows represent partly dipole-allowed transitions at the R point involving lower or higher bands ("VB2 to CB1" or "VB1 to CB2"). **(b)** Arrows with the same color coding indicate where the transitions marked in (a) can be observed in the actual absorption spectrum for the case of $MAPbI_3$. [adapted from Reference [53]]

A schematic representation of the calculated band structure at room temperature is shown in Figure 2.6 a. This computational calculation is based on the composition $MAPbI_3$, however, it provides a good qualitative representation for other compositions as well. The energetically highest VB, i.e., VB1 determining the VBM, is mainly s-like due to the strong contribution of lead,[18,108] but its energetic position may be shifted by the halide component, which is also the reason for the band gap tunability via halide ion exchange.[109] In contrast to VB1, the CB is almost exclusively p-like. The heavy lead and halide ions induce significant spin-orbit coupling, therefore causing a lower split-off band (CB1) within the CB which contains the CBM relevant for band edge absorption.[53,110] Both, the VBM as well as the CBM are located at the R point, therefore making LHPs a direct band gap material with a steep absorption onset at the band gap energy E_G. In contrast, to the typical direct band gap semiconductor GaAs, the character of the bands at the band edge (i.e., s- or p-like) is flipped.[111] As a consequence, a situation similar to GaAs with heavy and light holes at the VBM is avoided in LHPs. Instead, as shown in Figure 2.6 a the energetically higher CB2 consists ot two bands describing heavy and light electrons (HE and LE). Notably, this makes LHP an particularly nice material for the study of optical properties at the absorption onset, as both bands may be described reasonably well by a single parabola around the R point. Moreover, the bands around the VBM and CBM even exhibit a similar band curvature.[18]

As shown in Figure 2.6 a, dipole-allowed photoinduced transitions close to this band edge between the R and M point in k-space are indicated by solid lines. The bands in this region are also the reason

why LHPs exhibit such high absorption cross sections in the visible range. Interband transitions involving the lower (higher) VB2 (CB2) are only partly dipole-allowed and exhibit a lower oscillator strength compared to transitions of the type "VB1 to CB1".[106,107] The relation between the band diagram (Figure 2.6 a) and the actual absorption spectrum is presented in Figure 2.6 b for a $MAPbI_3$ LHP. The respective arrows of the same color indicate the highlighted transitions spanning over a broad wavelength range in the visible region. This also shows that $MAPbI_3$ is an efficient absorber in this spectral range, one of the reasons why it is such an interesting material for light-harvesting applications.

Finally, two additional issues in conjunction with the electronic band structure of LHPs shall be addressed — the defect tolerance and the Rashba effect. It is astonishing that perovskite films or NCs that are synthesized at room temperature using relatively basic chemistry have the potential to outperform other semiconductor materials regarding their device efficiency, for example in solar cells or LEDs. This is the case despite the much higher defect density within LHPs compared to traditional semiconductor materials like silicon or gallium arsenide.[82] The respective inherent attribute of LHPs is called defect tolerance and describes the material's ability to retain the electronic band structure of the pristine crystal even in the case of large defect concentrations.[18,61] First-principles DFT calculations reveal that defect states within LHPs are located close to or within the energy bands.[112] Furthermore, these are mainly shallow defects and therefore — especially at room temperature — they have no strong influence on the material, such that it maintains its electronic band structure.[113]

In closing, we will quickly discuss the Rashba effect in LHPs, a topic that has gained much attention recently. The luminescence of LHP NCs is known to be strong and reported to originate from excitons. However, it is still a matter of debate whether the ground state of these excitons is of bright or dark character. Symmetry analysis without consideration of the Rashba effect predicts an optically inactive dark ground exciton singlet below a bright exciton triplet state.[114] Under the assumption of relaxation to the lowest state, this would be a contradiction to the bright emission of such NCs. Therefore, it has been suggested that a weak contribution of the Rashba effect may reverse the ordering of the bright and dark levels, which would also lead to a slightly indirect band gap.[115] In contrast to that, a recent study posits in theory as well as experiment that the Rashba effect rather plays a negligible role and that the ground exciton state is indeed a singlet dark state.[116] However, the energetic difference to the bright triplet state is only in the order of a few meV. Therefore, and due to an extremely reduced bright-to-dark phonon-assisted relaxation, LHPs display an intense luminescence nevertheless. As a consequence, the Rashba effect will not be discussed further within this thesis.

2.2.3 Single Nanocrystals Versus Ensembles

The smallest laser spot diameter used for probing optical properties of NCs within this thesis was approximately 300 nm wide. Even for a thin film consisting of only one layer of densely packed perovskite nanocubes, this already leaves about 500 NCs within the focal spot. However, the diameter of the probe volume typically was in the range of around 100 µm. This rough comparison of the illuminated probe volume to the size of a single NC implies that thousands of NCs are easily observed simultaneously; and exactly this is the case for the measurements discussed in the following unless otherwise stated. Single nanocrystal measurements are also possible,[117,118] yet they require precise

microscopy as well as highly diluted samples and a careful sample preparation in order to avoid stacking or clustering of the investigated NCs.

Consequently, it is important to note that experimentally observed perovskite samples in this work consisted of an ensemble of many NCs. An individual small NC may be considered as a single emitter and therefore usually only exhibits homogeneous broadening.[119] However, looking at the whole ensemble one has to understand that these NCs are not perfectly identical. Therefore, besides homogeneous transition broadening of each individual crystal within the ensemble, inhomogeneous broadening will be present in the spectroscopy studies. The line broadening contribution Γ_{inhom} may also be taken as a measure for the homogeneity of the NCs within the sample.

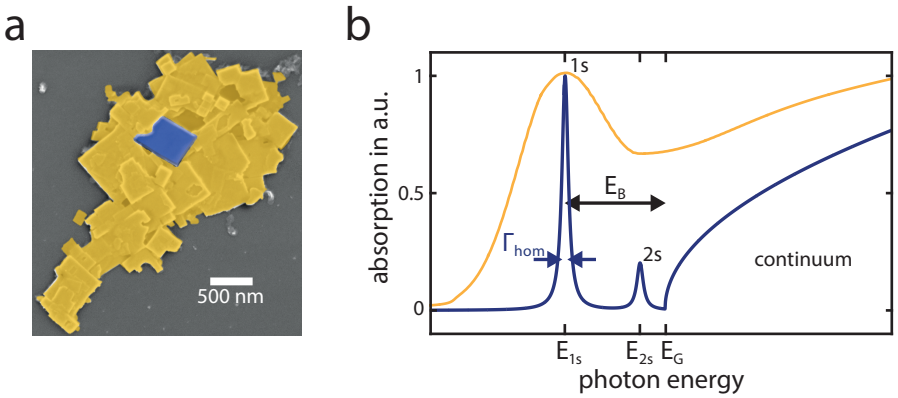

Figure 2.7: Nanocrystal Ensembles and Spectral Broadening. (a) SEM image of a small aggregate of bulk-like $MAPbI_3$ nanoplatelets on a substrate. False coloring has been applied to highlight a single nanocrystal in a blue shade whereas the whole ensemble is accentuated with a yellow tint. **(b)** Scheme showing the absorption spectra of an individual NC (blue curve) and the whole ensemble (yellow curve). Due to inhomogeneous broadening, information on the broadening contributions or the exciton binding energy E_B cannot be directly accessed from the linear absorption spectrum of the ensemble.

With the help of Figure 2.7 we may discuss how this context has an impact on optical spectra — here specifically on an absorption spectrum. Figure 2.7 a shows an SEM image of $MAPbI_3$ nanoplatelets that exhibit a wide range of sizes and tend to form aggregates on the substrate.[76] Therefore, an investigation of individual nanoplatelets is not easily feasible and optical properties must be experimentally derived from the whole ensemble. Respective schematic absorption spectra for this scenario are illustrated in Figure 2.7 b. Therein, the blue curve represents the absorption of an individual nanoplatelet as highlighted in blue in the SEM image. In this ideal case, the linear absorption spectrum displays sharp peaks corresponding to excitonic transitions and a well defined band-to-band continuum onset. This allows for a precise determination of the excitonic levels, the exciton binding energy E_B, and the homogeneous broadening Γ_{hom}. Note that this is a schematic representation and that relatively large nanoplatelets like the ones shown in Figure 2.7 a may also exhibit small inhomogeneous broadening by themselves. However, in actual experiments, the absorption spectrum is measured for a whole ensemble at once. This is indicated by the yellow curve in Figure 2.7 b representing the absorption of all nanoplatelets shown in Figure 2.7 a. Within this ensemble, the absorption spectrum may differ for each NC, leading to a distribution of optical transitions, i.e., to inhomogeneous broadening. In the broadened spectrum of the ensemble, information on the homogeneous broadening or the exciton binding energy E_B can no longer be extracted as easily. Summing up, one has to be aware that the spectroscopic studies of the thesis at hand are performed on NC ensembles consisting of not necessarily perfectly identical NCs.

2.3 Recombination

The previous two sections established the fundamental basis needed to put my optical studies on perovskite nanocrystals into context. After this common background with relevance for all of the results chapters, the remaining three sections of this chapter each specifically address one topic that is directly related to a chapter with experimental results. First, this section lays the theoretical base for Chapter 4, which deals with the recombination of electrons and holes.

2.3.1 Relaxation Regimes

As explained before, a free e-h pair or an exciton may be generated via absorption of a photon. Here, we will take a more detailed look at this absorption and especially the relaxation processes following the initial generation of an e-h pair. In order to resolve such processes temporally, one has to apply laser pulses that are at least as short as the interactions that should be observed. Therefore, a laser amplifier system emitting ultrashort pulses was employed in most experiments (see Subsection 3.2.1).

Besides the short pulse length enabled by this amplifier system, lasers generally — and advantageously — emit monochromatic and coherent light. Thereby, the systematic coherent excitation of certain electronic transitions may be precisely controlled and only the central wavelength of the laser with a narrow spectral distribution around it determines which transitions can be induced. Accordingly, a photon with an energy $E = E_C - E_B$ has the potential to excite the exciton transition resonantly, thereby creating a bound e-h pair. For photons with energies above the continuum onset, i.e., $E > E_C$, there is a continuous range of possible transitions. Free e-h pairs generated in this range possess an excess energy relative to E_C and therefore usually relax down to the energetically favorable band edge through several scattering processes. Ultimately, the band edge is the typical energetic location where electrons and holes accumulate and from where they tend to recombine, thereby reestablishing the original thermodynamic equilibrium before the excitation, i.e., with the afore excited electron back in the VB.[120]

Generally, the processes following an initial excitation with a short laser pulse can be divided into the four temporal regimes presented in Table 2.4. The first three (coherent, non-thermal, and hot-excitation regime) are ascribed to intraband processes in which the electron stays within the CB. Only the final (isothermal) regime involves interband transitions in which the electrons fall back into the holes of the VB. Table 2.4 also assigns time scales to the respective regimes, but it should be noted that all of these regimes may overlap temporally since many e-h pairs are excited simultaneously. The represented time scales rather serve as a rough orientation and indicate statistically averaged values for the involved processes at room temperature. In the following, the regimes and the physical interactions involved therein will be addressed individually.

The coherent regime is of particular interest for this thesis and describes the oscillations of free e-h pairs or excitons, which are all in phase directly after their excitation with an ultrashort laser pulse. This coherence decays extremely fast since the first instance of scattering of a single e-h pair already leads to the loss of its coherent behavior. This decay process is referred to as dephasing. The theory for coherent polarization oscillations and their decay in semiconductors will be explored in Section 2.4, while the results obtained for the dephasing time of excitons in LHPs are presented in Chapter 5.

Table 2.4: Relaxation Regimes after Photoexcitation. The four temporally-overlapping relaxation regimes following an initial photoexcitation with an ultrashort laser pulse in a semiconductor.[120] The listed time scale and respective interactions for each regime describe the path of an excited electron in the CB back to its initial position in the VB.

$t = 0.0\,\text{ps}$	**excitation:** "e-h pair generation" • absorption of incident ultrashort fs-pulse • electron transition "VB to CB"
$t \leq 0.2\,\text{ps}$	**coherent regime:** "time until first collision" • momentum scattering • carrier-carrier scattering • intervalley scattering
$t \leq 2\,\text{ps}$	**non-thermal regime:** "equilibrium among carriers" • carrier-carrier scattering • intervalley scattering • carrier-optical phonon scattering
$t \leq 100\,\text{ps}$	**hot-excitation regime:** "equilibrium with the lattice" • hot-carrier-phonon scattering • decay of optical phonons • carrier-acoustic phonon scattering
$50\,\text{ps} \leq t$	**isothermal regime:** "e-h pair recombination" • carrier recombination • electron transition "CB to VB"

Both the non-thermal and the hot-excitation regimes mainly involve scattering processes through which excited electrons relax towards the CBM. These interactions and their temporal decay have been studied extensively by my former colleague Dr. Verena Hintermayr within bulk and 2D LHP nanoplatelets.[52,121] Therefore, time-resolved studies of these effects are not included in this thesis, however, the interaction with phonons will be examined as a cause for spectral broadening of transitions.

The reverse process to absorption — in a sense that electrons and holes recombine — finally takes place in the so-called isothermal regime. Recombination will represent the main focus of the remainder of this section and will hence be explained in greater detail in the following subsection.

As a final remark it shall be noted that e-h pairs can diffuse within the crystal or even to adjacent NCs before their recombination. Longer lifetimes of e-h pairs enhance the probability for these processes. Moreover, even charge extraction after e-h pair dissociation may occur at an interface with an adjacent material. This will be examined in Chapter 6, while the respective theoretical background will be laid out in Section 2.5.

2.3.2 Radiative and Nonradiative Recombination

Generally, e-h recombination either occurs via a radiative or a nonradiative mechanism. All of the interband relaxation paths observed in the context of the present work may be assigned to one of three different categories which will be highlighted below. For the description of these processes one needs to distinguish between the recombination of free e-h pairs and that of excitons.

Radiative Recombination

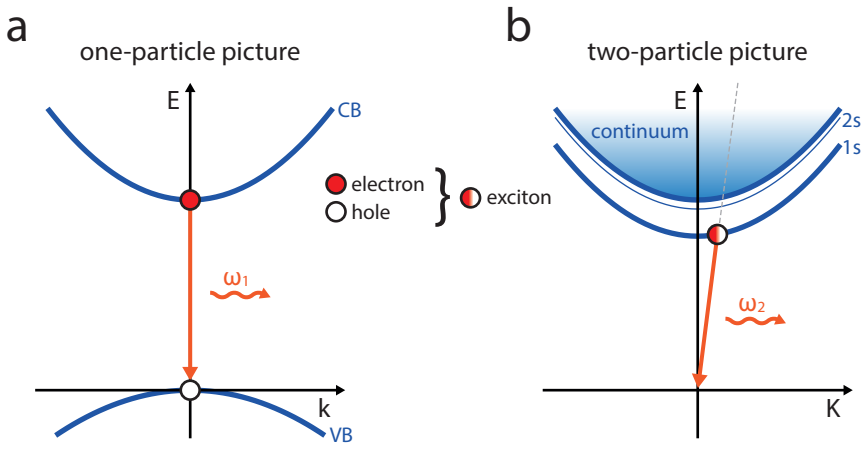

Figure 2.8: Radiative Recombination. (a) Radiative recombination of free e-h pairs mainly occurs at the relaxed state ("CBM to VBM"). Thereby an excited electron falls back into the VB and a photon with the respective energy is emitted. **(b)** The two-particle picture is needed to represent the same context for excitons.

As the name suggests, this type of recombination involves the emission of photons, resulting in photoluminescence (PL). Consequently, this is the sought-after process within LHP NCs that are destined for efficient light emission. More details on PL and its efficiency will be explained in Subsection 3.3.3. Here, this effect is solely introduced and compared to the respective nonradiative mechanisms.

Figure 2.8 a shows the process of radiative recombination for free e-h pairs in the so-called one-particle picture based on a schematic illustration of the electronic band structure around the direct band gap. Here, the electron and hole are highlighted as red and white circles in the CB and VB, respectively. Usually, intraband relaxation to the CBM or VBM is a much faster process compared to interband recombination. Therefore, most instances of the latter process mainly involve electrons that relax from the CBM to the VBM as illustrated in the scheme for the direct band gap of LHPs. Due to the negligible change in momentum compared to the energy difference, such transitions are drawn as vertical lines. In this process, the electron transfers the resulting energy difference to a photon that is consequently emitted. In contrast, the energy levels of excitons cannot be represented using the one-particle picture. Instead, the two-particle picture must be applied, which illustrates the excitonic states with respect to the continuum (see Figure 2.8 b).[56] In this picture, radiative recombination may only occur along the linear dispersion function of light, which is indicated by the grey dashed line in the scheme. This process is similar to free e-h recombination, however, it experiences different dynamics and exhibits the emission of a slightly red-shifted photon compared to the other process.

Trap-Assisted Recombination

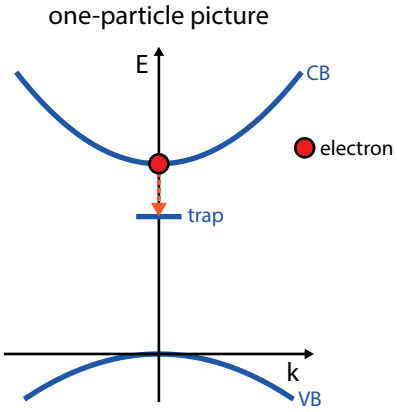

Figure 2.9: Trap-assisted Recombination. This scheme illustrates the nonradiative monomolecular process which involves the capture of an electron (or hole) into a specific trap state.

Subsection 2.2.2 already introduced the term "defect tolerance" as a property of LHPs. Trap states in LHPs are usually located close to the edge of energy bands or even within them.[82] Moreover, many defects exhibit a shallow character, meaning that the thermal energy of electrons is sufficient for them to leave the trap. Still, these traps open up relaxation channels, leading to nonradiative recombination via phonon interactions. The respective scheme for this mechanism is shown in Figure 2.9. For excitons this is more complex and cannot be depicted properly, yet the effect itself also exists for bound e-h pairs.

Auger Recombination and Exciton-Exciton Annihilation

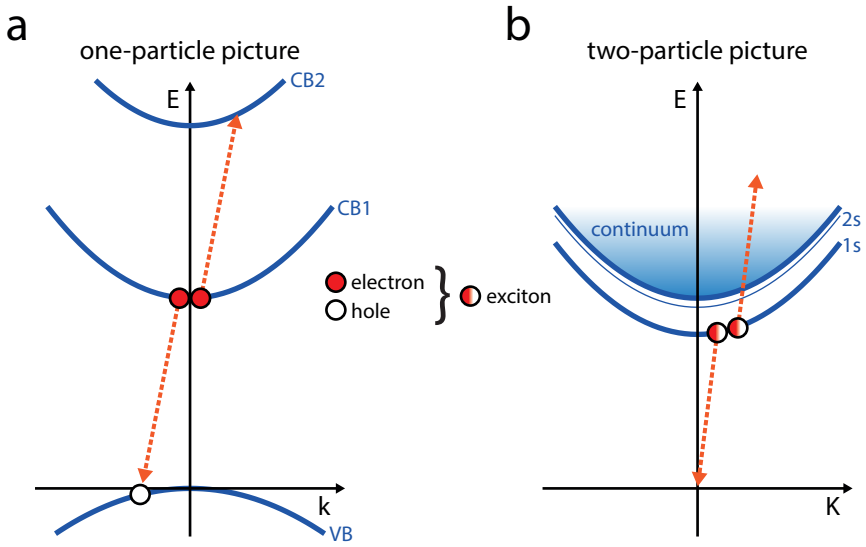

Figure 2.10: Auger Recombination and Exciton-Exciton Annihilation. (a) At least three particles are involved in higher-order Auger processes. In the course of its interband transition to the VB, the energy of an electron is transferred to another electron in the CB which is lifted to a higher conduction band CB2 in response. Via interaction with phonons, it could end up at a higher energy on the same band CB1, as well. Note that, conversely, the reverse process is possible for holes in the VB. **(b)** The counterpart interaction for excitons in the two-particle picture is the so-call exciton-exciton annihilation. While falling back to the ground state, an exciton transfers its energy to another nearby exciton which is thereby lifted into the continuum.

In all recombination processes, energy and momentum conservation must be satisfied. While both mechanisms introduced so far rely on an energy transfer to a photon or to phonons, respectively, we finally turn to another effect in which energy is transferred to another carrier (electron, hole or exciton). This phenomenon is referred to as Auger recombination for free e-h pairs and as exciton-exciton annihilation for excitons. Free e-h pairs may also transfer their energy to another nearby electron in the CB or a hole in the VB instead of emitting a photon via radiative recombination. This third charge carrier is promoted into an energetically higher band, while the other two free charge carriers are annihilated. Of course, and as depicted in Figure 2.10 a, this is a three-particle process. It may therefore only be observed for sufficiently high charge carrier densities.[122] Again, the two-particle picture is needed to explain the related process for excitons (see Figure 2.10 b). In exciton-exciton annihilation, the released energy of an exciton is transferred to another exciton.[123] Usually, this energy exceeds the exciton binding energy E_B, such that the exciton absorbing this energy is lifted into the continuum where it persists as a free e-h pair. However, via the aforementioned fast intraband relaxation channels, this free e-h pair often quickly relaxes back to its original excitonic state via phonon scattering. The exciton-exciton annihilation process in thin LHP nanoplatelets is studied within this work. Therefore, this effect shall be discussed in greater detail in the following subsection.

2.3.3 Exciton-Exciton Annihilation

As mentioned above, exciton-exciton annihilation is a nonradiative multiparticle process known to be strongly dependent on the excitation density since increased exciton densities enhance the probability for such events to occur.[123,124] With this in mind and only referring to excitons, the process of exciton-exciton annihilation represents the exact opposite to so-called monomolecular exciton recombination in which only a single exciton recombines either radiatively emitting a photon or nonradiatively via traps. Therefore, exciton-exciton annihilation needs to be considered one of the limiting factors for luminescent LHP NCs. A purpose of this work was to understand how this mechanism is affected by the size of NCs. Nanoplatelets (NPls) with variable thickness in the confined dimension are a suitable material for this purpose and were accordingly utilized as samples. These confined systems exhibit high exciton binding energies much smaller than the thermal energy of electrons. Therefore, we could assume for our experiments conducted at room temperature that all excited e-h pairs exist as excitons after a fast initial intraband relaxation.[20]

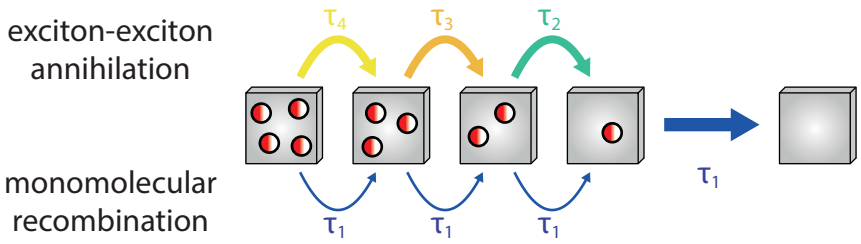

Figure 2.11: Scheme of an Interband Relaxation Pathway for a Single Nanoplatelet. A single NPl initially containing four excitons predominantly undergoes exciton-exciton annihilation processes until only one exciton remains. Due to the higher exciton density, the annihilation processes described by the lifetimes τ_4 and τ_3 occur even faster than those described by τ_2. During the first tens of picoseconds monomolecular recombination (τ_1) plays a negligible role as indicated by the thin arrows.

First, the possible recombination processes shall only be illustrated for one single NPl. This is shown in Figure 2.11 where the initial photoexcitation led to the generation of four excitons within the NPl. From this starting point, the exciton population may either decay via exciton-exciton annihilation (τ_4, τ_3, τ_2) or via monomolecular recombination (τ_1). As reported by Klimov et al., recombination rates are quantized within small NCs, such that the resulting recombination rate of an individual NPl depends on the exact amount of excitons the respective NPl contains.[123] Generally, the relaxation from N to $N-1$ excitons slows down with decreasing N as the carrier density within the equally sized NPls is accordingly reduced. For the population decay shown in Figure 2.11, this means that the lifetimes increase gradually, i.e., $\tau_4 < \tau_3 < \tau_2 < \tau_1$. In the colloidal CdSe NCs studied by Klimov et al., τ_2 turned out to be more than one order of magnitude smaller than τ_1. Here, I already want to reveal, that this difference in magnitude between τ_2 and τ_1 even surpasses two orders of magnitude for the case of the $CsPbBr_3$ NPls studied in this thesis. Due to this drastic difference, the process described by τ_2 occurs at a much faster timescale and, therefore, it is a reasonable assumption that exciton-exciton annihilation is the dominant recombination process for all NPls containing more than one exciton. This is also the reason why the less likely monomolecular recombination process is indicated by thinner arrows in Figure 2.11.

On this basis, the actual exciton-exciton annihilation experiment shall be explained. As already stated in Subsection 2.2.3 the experiments within this thesis are not conducted on single NCs as illustrated in Figure 2.11. Therefore, in the next step, an ensemble of many NPls has to be considered. Regarding the model used to analyze the experiment, it is important that excitons in different NPls of the illuminated ensemble do not interact with each other. In particular, excitons within a distinct NPl should not have the possibility to transfer to a nearby NPl. Therefore, the NPls were dispersed in hexane, such that no NPl had direct contact to other NPls due to their low concentration within the cuvette.

Against this backdrop, Figure 2.12 describes how exciton-exciton annihilation processes can be observed experimentally. Initially, all NPls are in thermal equilibrium and no NPl contains excitons (the amount of thermally excited charge carriers can be neglected). An ultrashort laser pulse excites an ensemble of NPls promoting electrons from the VB to the CB, thereby initially creating free e-h pairs. The subsequent intraband relaxation processes within these thin 2D structures occur so fast that already after around 1 ps all excited e-h pairs can be assumed to have formed excitons. This situation is defined as $t = 0$ in the scheme of Figure 2.12. The yellow panel illustrates that some NPls of the ensemble do not contain any exciton, whereas other NPls may possess several. In fact, those are the ones of interest for the process of exciton-exciton annihilation since at least two excitons are needed within a single NPl to observe this effect. This annihilation between excitons happens on a short time scale, such that it can be assumed that after several tens of picoseconds all of the NPls initially containing more than one exciton, reduce this amount to exactly one remaining exciton (cf. "$t = t_1$" in Figure 2.12). Then, slower monomolecular recombination becomes the dominant process with lifetimes in the nanosecond regime. The cycle of this experimental scheme repeats itself only once every 2 ms, starting with the next excitation pulse. Due to this long pause it can be assumed that thermal equilibrium — i.e., a state with no excitons in the NPls (cf. "$t = t_2$" in Figure 2.12) — is reached easily each time before the next excitation pulse arrives on the sample.

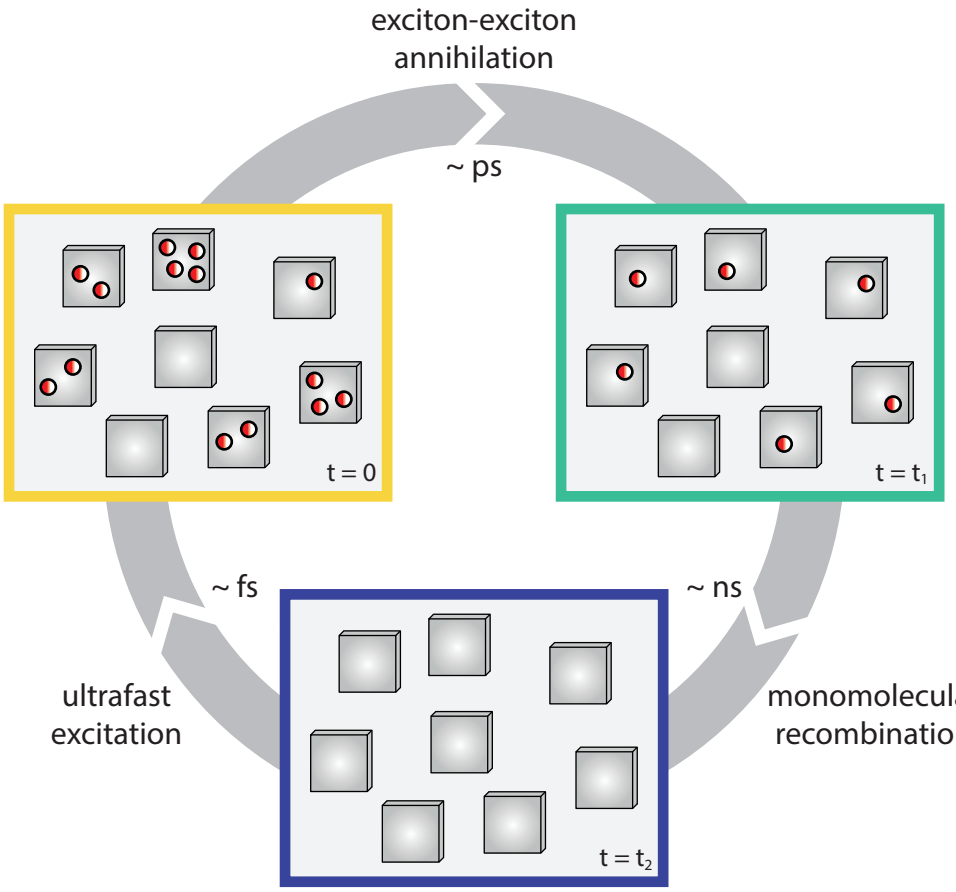

Figure 2.12: Time Sequence of the Exciton-Exciton Annihilation Experiment. Initially, excitation is caused using an ultrashort laser pulse. Already after ~ 1 ps, all of the excited e-h pairs relax down to the exciton level, establishing a Poisson distribution over the observed NPls ($t = 0$, which — by exception — does not define the exact moment of the excitation here, but the moment approximately 1 ps thereafter). Exciton-exciton annihilation with lifetimes in the low ps-regime is a much faster process compared to excitonic or trap-assisted recombination. Therefore, it may be assumed that all of the exciton-exciton annihilation processes occur before monomolecular recombination — involving only one exciton per NPl — becomes the dominant contribution to the overall interband relaxation process ($t = t_1$). The latter mechanism takes place within several nanoseconds after, while the ultrafast excitation is only initiated once every 2 ms. Therefore, it is a safe assumption that no NPl contains an exciton before the next excitation-relaxation cycle starts ($t = t_2$).

In order to describe exciton-exciton annihilation mathematically, the following definitions shall be introduced:

$$\begin{aligned} n_{\text{total}} &\mathrel{\hat{=}} \text{“total number of observed NPls”} \\ N_{\text{total}} &\mathrel{\hat{=}} \text{“total number of excitons at } t = 0\text{”} \\ N &\mathrel{\hat{=}} \text{“number of excitons within an individual NPl at } t = 0\text{”} \\ n(N) &\mathrel{\hat{=}} \text{“number of NPls with N excitons at } t = 0\text{”} \\ \langle N \rangle = N_{\text{total}} / n_{\text{total}} &\mathrel{\hat{=}} \text{“average number of excitons per NPl at } t = 0\text{”} \end{aligned} \tag{2.34}$$

An exemplary set of these values can be extracted from Figure 2.12, from which one obtains $n_{\text{total}} = 8$, $N_{\text{total}} = 14$, and $\langle N \rangle = 1.75$. Furthermore, there are three NPls containing exactly two excitons at $t = 0$,

translating to $n(N = 2) = 3$. Adding up all NPls in groups like this with the same amount of excitons will always yield the total number of NPls, i.e.,

$$\sum_{N=0}^{N_{\text{total}}} n(N) = n_{\text{total}} \,. \tag{2.35}$$

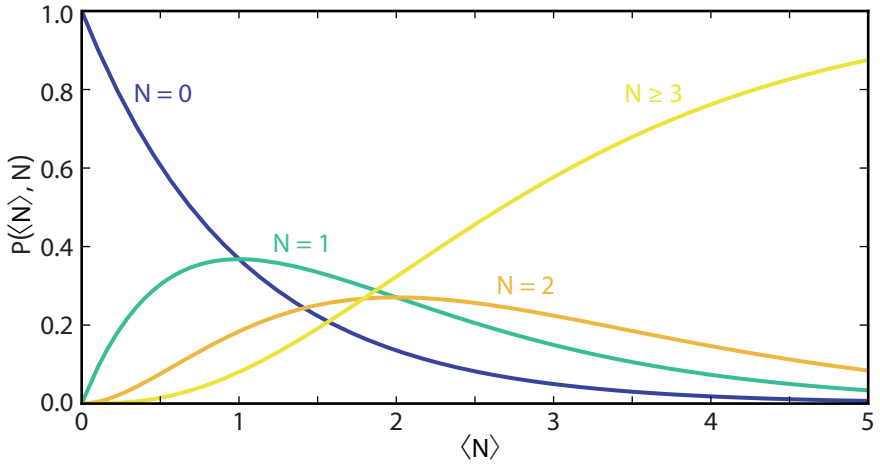

Figure 2.13: Poisson Distribution. At $t = 0$, excitons are distributed across all observed NPls according to Poisson statistics. In the experiment, the average number of excitons per NPl $\langle N \rangle$ is controlled via the pump power which determines how many photons arrive at the excitation volume that contains a fixed number of observed NPls n_{total}. Equation 2.36 is plotted here as a function of $\langle N \rangle$ for the cases $N = 0$, $N = 1$, $N = 2$, and $N \geq 3$. This way, for a fixed $\langle N \rangle$, one may look up the percentage of NPls that contain zero, one, two, or more NPls at $t = 0$, respectively.

While this holds true in general, we can be more precise for the mentioned experiment. The excitons generated in the NPls at $t = 0$ are Poisson distributed within the range of the employed excitation densities.[123] The Poisson distribution function

$$P(\langle N \rangle, N) = \frac{\langle N \rangle^N}{N!} e^{-\langle N \rangle} \tag{2.36}$$

reveals the probability for a NPl to contain N excitons given a fixed value for $\langle N \rangle$ (see Figure 2.13). As explained in Subsection 2.2.3, the ensemble of NPls contains a high number of individual elements and therefore the law of large numbers may be considered, such that statistics apply to describe this system. Then, the Poisson distribution $P(\langle N \rangle, N)$ reflects the percentage of NPls containing N excitons as compared to the whole ensemble of n_{total} NPls. Therefore, Equation 2.35 can be rewritten as

$$\sum_{N=0}^{N_{\text{total}}} P(\langle N \rangle, N) \cdot n_{\text{total}} = n_{\text{total}} \,. \tag{2.37}$$

For the sake of simplicity, in this thesis only the annihilation process $N = 2$ to $N = 1$ shall be compared for different NPl thicknesses, i.e., the exciton-exciton annihilation lifetime τ_2 shall be measured. To this end, only measurements for which $0.3 < \langle N \rangle < 0.4$ will be used for the analysis of this exciton-exciton annihilation process. For values of $\langle N \rangle$ in this range, around 4.3 % of all NPls contain exactly two excitons at $t = 0$, whereas only around 0.6 % of all NPls contain more excitons than that, thereby rendering this a good starting point for the determination of τ_2 (see Figure 2.13).

2.4 Dephasing

Earlier, the coherent regime, corresponding roughly to the time interval occurring right after the excitation of an e-h pair with an ultrashort laser pulse, was introduced (see Subsection 2.3.1). In the present section, coherent dynamics of excitons in this time regime shall be explained and their connection to spectral transition broadening will be elucidated. The optical Bloch equations will be introduced as the respective theoretical framework. Moreover, the measurement technique for the observation of ultrafast coherence decay, so-called four-wave mixing, will be explained. Comprising an additional description of photon echos and quantum beating, this section forms the background for Chapter 5.

2.4.1 Coherence of Exciton Polarization Oscillations

When employing an ultrafast coherent laser pulse for the optical excitation of a semiconductor, its electric field generates a polarization in the sample oscillating with the frequency of the incident light pulse ω_{ex}. If photons of this light pulse excite the exciton transition resonantly, their energy is absorbed completely and the induced polarization within the sample continues to oscillate with ω_{ex}, carrying the initial phase ϕ_i which is inverted to the phase of the laser pulse.[125] As long as the ensemble of excited excitons maintains this phase value, the system is said to be coherent. Generally, excitons may lose their coherence via scattering or recombination. This loss of coherence is referred to as dephasing.

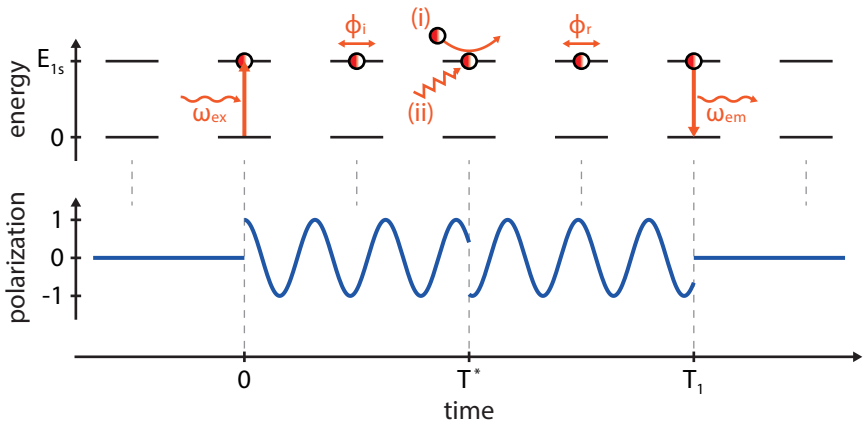

Figure 2.14: Polarization Decay for a Single Exciton. At $t = 0$, an ultrashort light pulse (ω_{ex}) resonantly excites an exciton. The absorbed photon causes an oscillating polarization for the generated exciton with the frequency ω_{ex}. Thereby, the incident coherent laser pulse determines the initial phase ϕ_i of the polarization oscillation which actually carries the inverted phase of the laser pulse. A single exciton maintains this phase until the first scattering event occurs at time $t = T^*$, either with (i) another exciton (carrier-carrier scattering) or with (ii) a phonon (carrier-phonon scattering). Afterwards, the exciton's phase relation with respect to the initial laser pulse is lost, but the polarization of the exciton continues to oscillate with random phase ϕ_r. Eventually, the exciton recombines at $t = T_1$, indicated schematically above in the form of radiative recombination involving an emitted photon with the frequency ω_{em}.

In a first step, this process is illustrated in Figure 2.14 for a single exciton. Directly following the initial resonant optical excitation with ω_{ex}, the polarization of the exciton oscillates with the same frequency and the phase ϕ_i until the first scattering or recombination event occurs. Scattering can either involve another exciton or a phonon. The corresponding time scale, on which the exciton loses its coherence but continues to exist, is given by the so-called pure dephasing time T^*. In contrast, recombination

— and therefore extinction — of an exciton is described by the lifetime of the exciton population T_1. Generally, $T^* \ll T_1$ and after the first scattering incidence, the exciton oscillates with a random phase ϕ_r until its recombination occurs.

In the next step, we take a look at an ensemble of many excitons excited resonantly at $t = 0$. In this case, T^* and T_1 are time constants reflecting the overall decay of coherence for the whole exciton ensemble via the aforementioned processes of scattering and recombination.[63] Although less likely, it is possible that a recombination process after the time T_1 is the first interaction of an exciton, causing it to lose its initial phase ϕ_i. However, it is more probable that an exciton experiences several scattering events prior to its recombination. Either way, only the first event causing a loss of coherence matters here. The whole process of coherence decay of the ensemble may then be described by the dephasing time T_2[126–128] given by

$$\frac{1}{T_2} = \frac{1}{2\,T_1} + \frac{1}{T^*}\,. \tag{2.38}$$

However, as mentioned above, the recombination lifetime T_1 is much larger than the time of pure dephasing T^*. Therefore, the dephasing time T_2 is assumed to be almost identical to the pure dephasing T^*, i.e.,

$$T_1 \gg T^* \quad \Longrightarrow \quad T_2 \approx T^*\,. \tag{2.39}$$

Accordingly, the process of dephasing is almost exclusively caused by scattering events that randomize the initial phase ϕ_i of the excitons. As indicated in Figure 2.14, scattering with other excitons (or charge carriers in general) or phonons is the likeliest event. Both processes shall be highlighted briefly in the following.

- **Carrier-Carrier Scattering**
  Naturally, exciton-exciton scattering is an excitation density-dependent process, growing more probable with an increasing amount of excitons within the excitation volume. This means that the dephasing time T_2 is reduced when using stronger laser intensities since more absorbed photons lead to more excitons. Of course, exciton-exciton scattering is also present at low excitation densities, though, mainly caused by dipole interaction. Usually, a resonant excitation at the electronic exciton transition is chosen for dephasing experiments in order to avoid additional scattering through intraband relaxation mechanisms. Still, in some cases, free carriers also play a role, not only when the exciton binding energy is in the range of the thermal energy of an electron E_{th}, but also when the excitation pulse exhibits a certain spectral width. The bare charge of free carriers leads to a longer ranging Coulomb field compared to the dipole interaction between excitons, such that free carriers are even more prone to carrier-carrier scattering events.[120] Both cases — exciton-exciton as well as exciton-free carrier scattering — cause so-called excitation-induced dephasing.

- **Carrier-Phonon Scattering**
  However, when keeping the excitation density reasonably low, the effective reason for the coherence decay of excitons is scattering with phonons. At low temperatures, acoustic phonons are the dominant source of dephasing. However, with increasing temperature, optical phonons

gain in importance. The influence of phonons on the homogeneous broadening Γ_{hom} of a transition has already been explained in Subsection 2.1.5.

Furthermore, excitons may also scatter at lattice defects or the crystal boundary. However, generally speaking, this effect is rather small and can be neglected for our studies.[72,76]

Figure 2.15 illustrates how the overall polarization of an exciton ensemble decays via the above mentioned mechanisms. In this scheme, a purely homogeneously broadened ensemble is assumed, meaning that all involved excitons exhibit an identical transition frequency, ω_{ex}, with which the induced polarization oscillates. The corresponding oscillation period T_{p} is so short that in an experiment only the exponential envelope function $f(t) = \exp(-t/T_2)$ may be used to describe the loss of coherence, the dephasing time T_2 being the lifetime of this so-called free polarization decay.

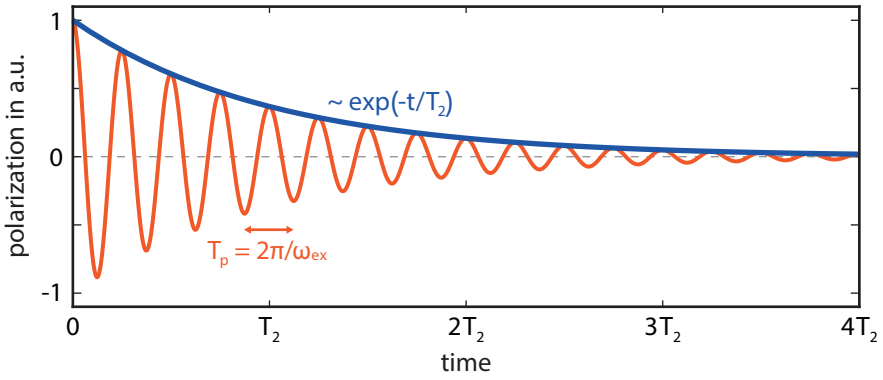

Figure 2.15: Free Polarization Decay of an Exciton Ensemble. Translating the scheme in Figure 2.14 to an exciton ensemble in which all excitons possess an identical transition energy $\hbar\omega_{\mathrm{ex}}$, i.e., an ensemble with $\Gamma_{\mathrm{inhom}} = 0$, one speaks of free polarization decay as the decay of the overall polarization of the ensemble. Single excitons within the ensemble may lose their coherence either by scattering (T^*) or recombination (T_1). The exponential free polarization decay as shown here is then described by the dephasing time T_2 as given by Equation 2.38. For wavelengths in the visible range, the period of the exciton oscillation $T_{\mathrm{p}} = 2\pi/\omega_{\mathrm{ex}}$ is less than 2.6 fs which is significantly shorter than typical values for T_2. Therefore, the envelope function (blue curve) describes the coherence decay reasonably well and hence represents the population of excitons still carrying the initial phase ϕ_{i}.

In Subsection 2.1.5 we learned that the natural line width γ of a transition is given by the natural population decay of the excited state T_1 and contributes to homogeneous broadening Γ_{hom}. Moreover, Equation 2.38 shows that the dephasing time T_2 already includes both decay time constants T^* and T_1. Generally, the bandwidth of optical spectra is related to decay constants via a Fourier transform.[69,129] Hence, the shorter time $T^* \ll T_1$, denoting pure dephasing, represents the dominant contribution to the overall homogeneous bandwidth. In summary, T_2 is the quantity that determines the homogeneous broadening of an exciton transition[130] in accordance with

$$\Gamma_{\mathrm{hom}} = \frac{2\,\hbar}{T_2}\,. \tag{2.40}$$

In linear spectroscopy, homogeneous and inhomogeneous broadening of an exciton ensemble cannot be distinguished completely. The aforementioned correlation, however, enables an experimental extraction of Γ_{hom} within such an exciton ensemble via the measurement of T_2.[130,131]

2.4.2 Optical Bloch Equations

Before introducing the technique capable of measuring T_2, the underlying theoretical concept —the optical Bloch equations — shall be explained. In the simplest theoretical approximation, each exciton within a semiconductor crystal can be considered as a two-level system having a ground state $|a\rangle$ at energy E_a and an excited state $|b\rangle$ at energy E_b.[120,132,133] As shown in Figure 2.16, the exciton therefore either exists (after an excitation) or it does not (before excitation or after recombination).

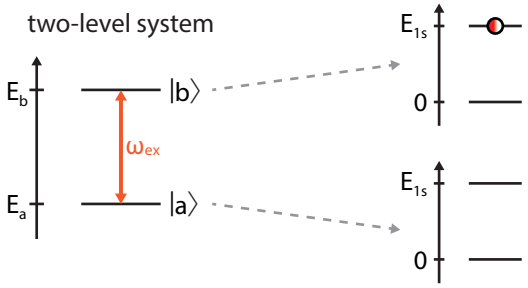

Figure 2.16: Two-Level System Describing an Exciton. Schematic of a two-level system having a ground state $|a\rangle$ and an excited state $|b\rangle$ which may be used to describe an exciton. Photons fulfilling the condition $\hbar\omega_{ex} = E_b - E_a$ may excite the transition between both states resonantly.

The coherent phenomena studied within this work are always analyzed for a whole ensemble of excitons. From the theory point of view, all of these excitons may be represented by an ensemble of independent two-level systems that is described by the wave functions

$$\left|\psi_j(t)\right\rangle = c_{aj}(t)\,|a\rangle + c_{bj}(t)\,|b\rangle \ , \tag{2.41}$$

wherein j denotes the integer referring to the j-th exciton within the ensemble.[120] In this model $\left|c_{aj}(t)\right|^2 + \left|c_{bj}(t)\right|^2 = 1$ is fulfilled. In an independent two-level model it has to be ascertained that photons with frequency ω_{ex} are resonant with the exciton transition between E_a and E_b and off-resonance with respect to other possible transitions within the semiconductor. The transition may exhibit purely homogeneous, but also additional inhomogeneous broadening.

As mentioned above, we are interested in the whole ensemble. Instead of dealing with all of the individual bilinear combinations shown in Equation 2.41, the density matrix formalism may be relied on to facilitate the treatment of interacting quantum systems.[134] Interestingly, within this approach, the individual wave functions $\left|\psi_j(t)\right\rangle$ are not generally known, but certain statistical properties of the whole ensemble may be extracted. Conveniently, this manifests in the density matrix operator

$$\rho(t) = \sum_j P_j(t)\left|\psi_j(t)\right\rangle\left\langle\psi_j(t)\right| \ , \tag{2.42}$$

wherein $P_j(t)$ denotes the fraction of systems with the state vector $\left|\psi_j(t)\right\rangle$. For the two-level model the density matrix operator may be expressed as

$$\rho(t) = \begin{bmatrix} \rho_{bb}(t) & \rho_{ba}(t) \\ \rho_{ab}(t) & \rho_{aa}(t) \end{bmatrix} = \begin{bmatrix} n(t) & p(t) \\ p^*(t) & 1-n(t) \end{bmatrix} . \tag{2.43}$$

The diagonal elements $\rho_{bb}(t)$, $\rho_{aa}(t)$ and the off-diagonal elements $\rho_{ba}(t)$, $\rho_{ab}(t)$ have a fundamentally different meaning for the description of the ensemble.[134] The diagonal components describe the probability for the system to be in state $|b\rangle$ or $|a\rangle$, respectively. The probability and therefore population of the excited state $|b\rangle$ is defined as $n(t) = \rho_{bb}(t)$, consequently leaving $1 - n(t) = \rho_{aa}(t)$ for the ground state $|a\rangle$. In contrast, the off-diagonal elements represent the polarization of the ensemble $p(t)$, i.e., the coherence of all involved excitons. For a random phase distribution within the exciton ensemble, these terms will amount to zero. However, as described in the previous subsection, excitation of the ensemble with a short laser pulse with frequency ω_{ex} may create coherence between the involved quantum states, leading to non-zero off-diagonal elements in the density matrix and an oscillating polarization $p(t)$ along the axis given by the linear laser excitation. In turn, this polarization will decay via the process of dephasing.

In order to obtain the time evolution of this mixed state of multiple excitons, the von Neumann equation

$$i\hbar \frac{\mathrm{d}\rho(t)}{\mathrm{d}t} = [H(t), \rho(t)] = H(t)\rho(t) - \rho(t)H(t) \tag{2.44}$$

has to be solved. Just as the Schrödinger equation describes the time evolution of pure states $\left|\psi_j(t)\right\rangle$, the von Neumann equation describes the time evolution for the density operator.[135] The Hamiltonian needed to solve this equation is given by

$$H(t) = H_0 + H_{excite}(t) + H_{relax} \,. \tag{2.45}$$

The first of these three summands H_0 is the Hamiltonian ascribed to the isolated system given by the diagonal matrix

$$H_0 = \begin{bmatrix} E_b & 0 \\ 0 & E_a \end{bmatrix} , \tag{2.46}$$

which includes the energies E_b and E_a of the excited and ground state, respectively. The second summand in Equation 2.45 describes the excitation of this two-level system via an external electric field, i.e., an incident laser pulse $\mathbf{E}(\mathbf{k}, t)$. Applying the dipole-approximation for the generation of an exciton,[134] leads to

$$H_{excite}(t) = \begin{bmatrix} 0 & -\mathbf{d}_{ba}\mathbf{E}(\mathbf{k}, t) \\ -\mathbf{d}_{ab}\mathbf{E}(\mathbf{k}, t) & 0 \end{bmatrix} , \tag{2.47}$$

in which the incident electric field interacts with the dipole momentum operator $\mathbf{d}$. Finally, H_{relax} describes processes through which the ensemble returns to thermal equilibrium after excitation.[120,125] This Hamiltonian is described via

$$[H_{relax}, \rho(t)]_{bb} = -\frac{\rho(t)_{bb}}{T_1} = -\frac{n(t)}{T_1} \quad , \quad [H_{relax}, \rho(t)]_{ba} = -\frac{\rho(t)_{ba}}{T_2} = -\frac{p(t)}{T_2} \,, \tag{2.48}$$

wherein the lifetime of the excited state T_1 and the dephasing time T_2, i.e., the lifetime of the coherence term $p(t)$, appear.[120]

Plugging the Hamiltonian H given by Equation 2.45 into Equation 2.44 leads to the differential equations

$$\frac{\mathrm{d}}{\mathrm{d}t}\, n(t) = -\frac{i}{\hbar}\left(p^*(t)\mathbf{d} - p(t)\mathbf{d}^*\right)\mathbf{E}(\mathbf{k},t) - \frac{n(t)}{T_1}\,, \tag{2.49}$$

$$\frac{\mathrm{d}}{\mathrm{d}t}\, p(t) = -\frac{i}{\hbar}(1-2\,n(t))\,\mathbf{d}\,\mathbf{E}(\mathbf{k},t) - \left(\frac{i(E_\mathrm{b}-E_\mathrm{a})}{\hbar} + \frac{1}{T_2}\right) p(t)\,. \tag{2.50}$$

These are the so-called optical Bloch equations describing the excitation dynamics in an ensemble of two-level systems, such as excitons, interacting with an electromagnetic field.[120,134] They form the theoretical basis for the characterization of coherent transient experiments by providing information on $n(t)$ as well as $p(t)$ and especially on the correlation between these quantities. The coupled differential optical Bloch equations cannot be solved analytically. Rather, a Taylor series expansion or other numerical approaches are needed to solve them. An even more sophisticated set of equations, the so-called semiconductor Bloch equations, may be derived from the basis shown above.[32] Most importantly, this more advanced theoretical model also considers many-body interactions among charge-carriers as well as their scattering with phonons.[136] However, the optical Bloch equations as presented in Equation 2.49 and Equation 2.50 are already sufficient in order to describe the four-wave mixing technique as a measure to determine the coherence decay of an exciton ensemble with reasonable accuracy.

2.4.3 Four-Wave Mixing

As mentioned earlier, four-wave mixing (FWM) — or, to be more precise, two-beam degenerate FWM, the simplest form of FWM spectroscopy — serves as the experimental technique for determining dephasing times T_2 for an ensemble of resonantly excited excitons as performed in the course of this thesis. Here, the fundamental physical background of this experiment will be discussed, whereas all of the experimental details will be covered in Subsection 3.3.4.

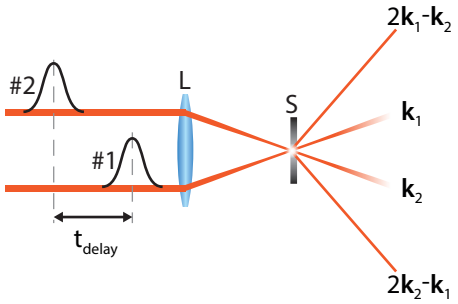

Figure 2.17: Four-Wave Mixing. Two pulses with a tunable time delay between them are focused through a lens (L) onto the sample (S) with the wave vectors $\mathbf{k}_1$ and $\mathbf{k}_2$. The amplitude of the third-order diffracted polarization emitted in directions $2\,\mathbf{k}_1 - \mathbf{k}_2$ and $2\,\mathbf{k}_2 - \mathbf{k}_1$ depends on the time delay t_{delay} and represents the FWM signal.

A schematic illustration of this technique is shown in Figure 2.17. It involves two ultrashort laser pulses with the same photon energy which in turn matches the exciton transition within the investigated sample, thereby fulfilling the condition of resonant excitation. The time delay t_{delay} between both pulses can be controlled and both beams are focused onto a sample where they overlap spatially. The pulse arriving first is referred to as the pump pulse. As already depicted in Figure 2.17, for the explanations it is assumed that pulse #1 with wave vector $\mathbf{k}_1$ is the pump pulse. When incident on the LHP semiconductor, this pump pulse #1 generates a coherent polarization of an exciton ensemble as described in Subsection 2.4.1.

The probe pulse #2 arrives with delay t_{delay} with respect to the initial excitation. As long as t_{delay} is less than or in the range of T_2, i.e., the excited polarization of the pump pulse #1 has not yet fully decayed, the radiation field of pulse #1 interferes with the subsequent pulse #2, creating a so-called interference grating with wave vector $\mathbf{k}_1 - \mathbf{k}_2$.[137] This enables self-diffraction of the probe pulse #2, resulting in a diffracted signal in the direction of $2\,\mathbf{k}_2 - \mathbf{k}_1$ (diffraction in other directions is less efficient).[32] Overall, four waves are involved in this process: the pump pulse #1 with wave vector $\mathbf{k}_1$, the probe pulse #2 with wave vector $\mathbf{k}_2$ (counted twice due to its interactions), and the emitted pulse traveling in direction $2\,\mathbf{k}_2 - \mathbf{k}_1$. Therefore, this phenomenon is referred to as four-wave mixing and the diffracted beam represents the FWM signal I_{FWM}. Therein, $I_{\text{FWM}}\left(t_{\text{delay}}\right)$ denotes the energy of the diffracted FWM light pulse of this third-order nonlinear process as a function of the pulse delay time t_{delay}.[134]

As a side note, if the order of the two pulses #1 and #2 is switched ($t_{\text{delay}} < 0$) such that pulse #2 acts as the pump pulse, the exactly analogous process will occur resulting in a diffracted signal in direction $2\,\mathbf{k}_1 - \mathbf{k}_2$. Either way, the FWM signal will always be detected in a direction different from $\mathbf{k}_1$ and $\mathbf{k}_2$, resulting in a so-called background-free detection.[32] Experimentally, this is of course favorable for the observation of the FWM signal which is weak compared to the transmitted pulses.

Using the optical Bloch equations it can be shown that the polarization of the exciton ensemble in the sample $p(t)$ actually causes the diffracted FWM signal, the electric field amplitude of which $\mathbf{E}_{\text{FWM}}(\mathbf{r}, t)$

follows the same temporal decay as $p(t)$.[130] Here, the location $\mathbf{r}$ represents any position along the diffracted beam of the FWM signal. Based on this, the polarization decay of the ensemble can be recorded by varying t_{delay} stepwise. In two-beam degenerate FWM, only one value is measured per step in t_{delay}, i.e., the energy of the output FWM light pulse $I_{\mathrm{FWM}}\left(t_{\mathrm{delay}}\right)$. This is also referred to as time-integrated FWM. The observed FWM signal is obtained via

$$I_{\mathrm{FWM}}\left(t_{\mathrm{delay}}\right) = \int_{t_{\mathrm{delay}}}^{\infty} \left|\mathbf{E}_{\mathrm{FWM}}(\mathbf{r},t)\right|^2 \mathrm{d}t \propto \int_{t_{\mathrm{delay}}}^{\infty} \left|p(t)\right|^2 \mathrm{d}t\,. \tag{2.51}$$

The time delay of the probe pulse t_{delay} basically determines the moment at which the FWM signal can be detected first. Naturally, the function $I_{\mathrm{FWM}}\left(t_{\mathrm{delay}}\right)$ will therefore also exhibit a temporal decay. In any case, the dephasing time T_2 describes the loss of coherence for the exciton ensemble, i.e., T_2 is the lifetime of $p(t)$. However, when looking at the measured quantity $I_{\mathrm{FWM}}\left(t_{\mathrm{delay}}\right)$, one has to distinguish between two fundamentally different cases. This brings us back to the question whether the exciton transitions within the ensemble are purely homogeneously or also inhomogeneously broadened.

Here, we turn to the case of pure homogeneous broadening, whereas inhomogeneous broadening will be dealt with in the following subsection. The decay of the polarization $p(t)$ after excitation with a single pump pulse arriving at $t = 0$ for this scenario has already been illustrated in Figure 2.15 and is referred to as free polarization decay. The expected exponential decay with lifetime T_2 is observed for the envelope function. A subsequent probe pulse arriving at $t = t_{\mathrm{delay}}$ yields an instantaneous FWM signal in direction $2\,\mathbf{k}_2 - \mathbf{k}_1$, while an exponential decay will be observed in the time-integrated signal $I_{\mathrm{FWM}}\left(t_{\mathrm{delay}}\right)$, as well. However, due to the relation $I_{\mathrm{FWM}}\left(t_{\mathrm{delay}}\right) \propto \left|p(t)\right|^2$ given by Equation 2.51, the lifetime T_{decay} of $I_{\mathrm{FWM}}\left(t_{\mathrm{delay}}\right)$ is actually a factor two faster as compared to the dephasing time T_2. Therefore, this paragraph may be summarized as

$$\Gamma_{\mathrm{inhom}} = 0 \quad \Longrightarrow \quad T_2 = 2 \cdot T_{\mathrm{decay}}\,, \tag{2.52}$$

meaning that in a FWM experiment on a purely homogeneously broadened exciton ensemble one first extracts the lifetime T_{decay} from the measured function $I_{\mathrm{FWM}}\left(t_{\mathrm{delay}}\right)$ before multiplying this value with a factor of two in order to obtain the dephasing time T_2 for this ensemble.

2.4.4 Photon Echo

In reality, most exciton ensembles will not only be homogeneously broadened, but will show a distribution of energies, i.e., $\Gamma_{\text{inhom}} > 0$. In this case, the exciton ensemble may be grouped into homogeneously broadened subensembles, such that a fixed frequency ω_i can be ascribed to each subensemble (see Figure 2.18 a). Due to their variation in energy, the polarizations of these components $p_i(t)$ also evolve with their respective frequency ω_i, thereby causing a quite different behavior of the FWM signal for inhomogeneously-broadened systems as compared to the free polarization decay shown in Figure 2.15. For the description of this process a picture will be employed that is similar to the one used to describe spin echos back in the 1950s.[138] A modified version of this picture is shown in Figure 2.18 b and will be addressed in the following. Moreover, the microscopic polarization of the individual subensembles $p_i(t)$, the macroscopic polarization of the whole ensemble $p(t) = \sum_i p_i(t)$, and $|p(t)|^2$ — the quantity being proportional to the FWM signal — are plotted in Figure 2.18 c-e.

- **(i): Excitation with Pump Pulse**
  The pump pulse arrives at $t = 0$ and excites all of the transitions ω_i within the inhomogeneously broadened ensemble. This is referred to as a $\pi/2$ pulse. Initially, the microscopic polarizations $p_i(0)$ belonging to the respective frequencies ω_i are all in phase. Therefore, their superposition $p(0)$ shows a strong signal, as well. In the picture of circles illustrated here, the phase of the involved polarization components $p_i(t)$ is represented by the angular position of the sketched excitons.

- **(ii): Decay of the Macroscopic Polarization and Dephasing**
  There are two reasons for the decay of the macroscopic polarization following its initial excitation. First, the components $p_i(t)$ evolve at different rates due to their different frequencies ω_i and therefore their constructive interference is quickly lost. Moreover, each exciton within the ensemble may be involved in a scattering event and thereby contribute to the overall dephasing of the ensemble which is illustrated by the decaying amplitude of $p_i(t)$.

- **(iii): Interaction with Probe Pulse**
  When the probe pulse arrives at the sample at $t = t_{\text{delay}}$, it acts as a so-called π pulse and reverses the phase evolution for all components of $p_i(t)$. In the picture of Figure 2.18 b this means that each exciton changes its direction, but continues to move with ω_i.

- **(iv): Recovery of the Macroscopic Polarization Versus Dephasing**
  Afterwards, the reverse of (ii) takes place. That is, all of the excitons, which have not yet been involved in scattering processes, start to restore their initial phase coherence. Meanwhile, dephasing proceeds as before, lowering the overall amplitude of the polarizations. Illustrating this process, circle (iv) shows that the exciton representing ω_5 has already decayed completely and the exciton corresponding to ω_2 has experienced at least one scattering event.

- **(v): Emission of a Photon Echo**
  Finally, all of the excitons that were not involved in scattering reestablish their initial phase coherence at $t = 2\,t_{\text{delay}}$ and the macroscopic polarization $p(t)$ reaches a maximum. The superposition of all these dipoles leads to the emission of a so-called photon echo[139] which is emitted in the direction of $2\,\mathbf{k}_1 - \mathbf{k}_2$ and represents the FWM signal for the inhomogeneously broadened exciton ensemble.

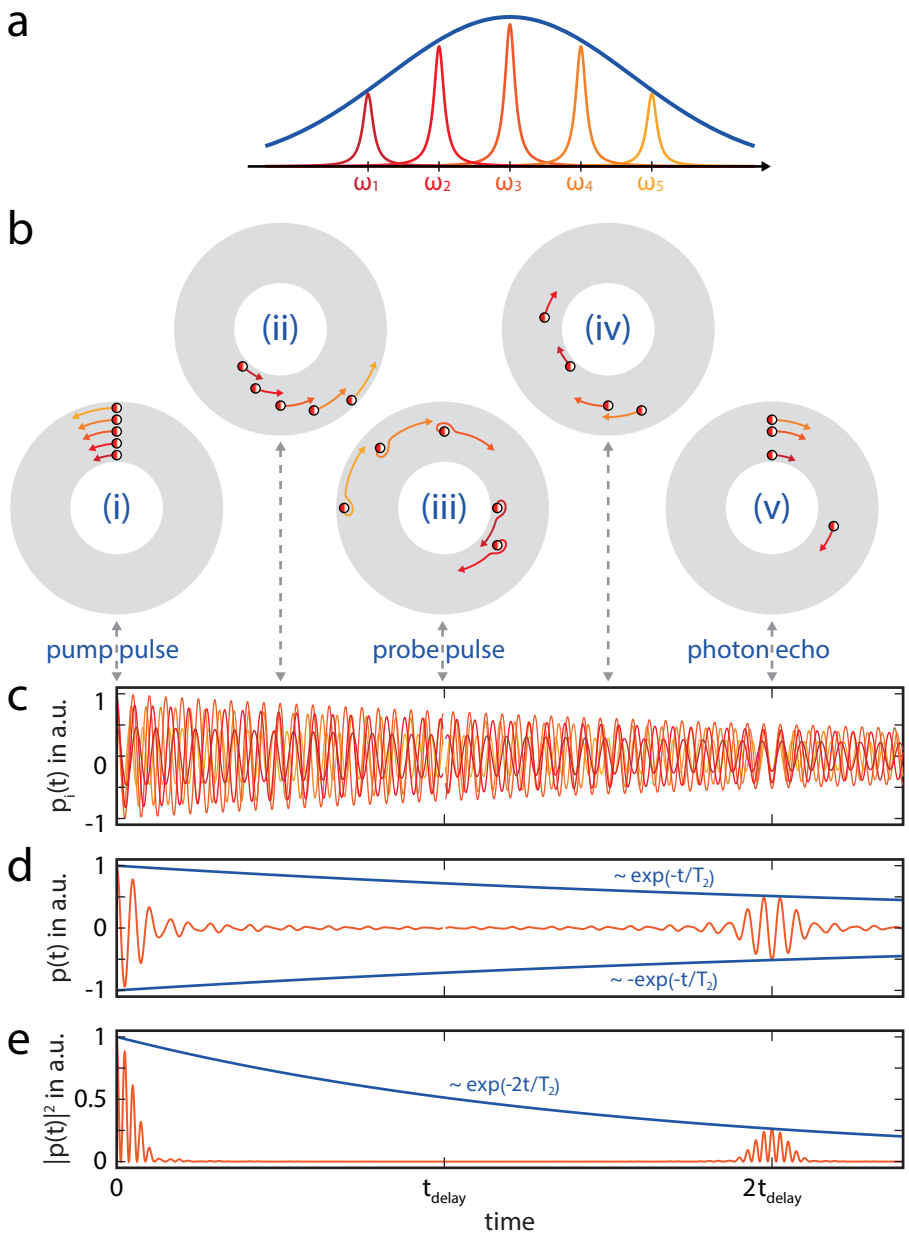

Figure 2.18: Photon Echo Generation. (a) Exciton ensembles featuring an inhomogeneously broadened transition consist of homogeneously broadened subensembles, each representing a certain fixed frequency ω_i. **(b)** When exciting such an ensemble, the pump pulse at $t = 0$ initiates polarization oscillations of the subensembles with each initially possessing the same phase. Due to the distribution of ω_i, these oscillations quickly run out of phase until the probe pulse at $t = t_{delay}$ reverses the different frequency components' phase evolution. This results in a coherent superposition of all remaining polarization components that have not experienced any scattering event until $t = 2\,t_{delay}$. This superposition results in a light pulse, the so-called photon echo. **(c)** The amplitudes of the microscopic polarizations $p_i(t)$ — each representing one homogeneously broadened subensemble of transitions corresponding to ω_i — decay through scattering events with lifetime T_2. **(d)** The macroscopic polarization of the ensemble $p(t)$, i.e., the sum of all subensemble polarizations $p_i(t)$, shows that constructive interference, in which all excitons still carry the approximately same phase, decays rapidly and is only reestablished at $t = 2\,t_{delay}$ after reversing the phase evolution via interaction with the probe pulse. **(e)** In a plot of $|p(t)|^2$ the photon echo at $t = 2\,t_{delay}$ represents the actual FWM signal $I_{FWM}\left(t_{delay}\right)$ emitted in the direction of $2\,\mathbf{k}_1 - \mathbf{k}_2$.

Figure 2.18 b-e shows the polarization dynamics of the exciton ensemble during photon echo generation for a fixed value of t_{delay} which will generate a single data point for the final time-integrated FWM curve $I_{FWM}\left(t_{delay}\right)$. For a single ensemble, the photon echo has a fixed temporal width $\Delta t \propto \hbar/\Gamma_{inhom}$.[140] Therefore, the amplitude I_{FWM} of the mentioned data point is essentially given by the amplitude of the

photon echo shown in Figure 2.18 e. So when increasing the pulse delay time starting from $t_{\mathrm{delay}} = 0$ and measuring the photon echoes, one effectively scans the blue curve of Figure 2.18 e. This plot also clarifies that, between excitation and detection of the signal, the exciton ensemble is given twice as much time for dephasing processes as the time defined by t_{delay}. Therefore, we may infer

$$\Gamma_{\mathrm{inhom}} > 0 \quad \Longrightarrow \quad T_2 = 4 \cdot T_{\mathrm{decay}} \,. \tag{2.53}$$

This means that in the case of an inhomogeneously broadened transition the decay of the FWM signal, i.e., the photon echo, is proportional to $\exp\left(-4\, t_{\mathrm{delay}}/T_2\right)$. A more detailed theoretical prediction of the time-integrated signal for the photon echo can be obtained when applying the semiconductor Bloch equations. Also involving the lifetime of the excited state T_1, the semiconductor Bloch equations lead to

$$I_{\mathrm{FWM}}\left(t_{\mathrm{delay}}\right) = \Theta\left(t_{\mathrm{delay}}\right) \cdot \left[1 + A_1 \left(1 - \exp\left(-\frac{t_{\mathrm{delay}}}{T_1}\right)\right)^2\right] \cdot A_2 \exp\left(-\frac{4\, t_{\mathrm{delay}}}{T_2}\right) \tag{2.54}$$

wherein A_1 and A_2 denote variable scaling factors.[120,141] Like most theoretical models on FWM, this equation is based on the assumption that the pump and probe pulses are infinitesimally short, delta function-like pulses.

2.4.5 Quantum Beating

The two-level system shown in Figure 2.16 is sufficiently accurate as a qualitative model for the polarization decay of resonantly excited exciton ensembles. However, to resolve fast processes like dephasing experimentally, ultrashort laser pulses have to be employed. It is an inherent property of ultrashort pulses to be spectrally broadened around a central wavelength, simply because pulse length and spectral width are coupled via a Fourier transform. With such a broadened excitation spectrum it would seem that the requirement of a resonant excitation of the observed transition is not fulfilled. To look into this problem, one must consider the energetic structure of the system with respect to the exciting laser pulse.

So far, we have assumed a resonant excitation of the 1s exciton only. However, as explained in Equation 2.23, depending on the exciton binding energy E_{B}, the excitonic transitions may lie energetically close to the absorption continuum onset. So, for LHP NCs exhibiting small values for E_{B},[53] a resonant excitation of the exciton only can be problematic, considering the spectral width of the excitation pulse necessary to achieve high temporal resolution.

A situation in which the FWHM of the excitation spectrum lies in the range of E_{B} is illustrated in Figure 2.19 a. The central wavelength of the excitation pulse is positioned in a way that excitonic and energetically lowest continuum transitions are excited at the same time. In this case, a two-level system is not a correct representation. Rather, a three-level system, as depicted in Figure 2.19 b, is a more appropriate representation. As explained in Subsection 2.1.3, higher-order excitons only play a minor role and can be neglected here. In this case $|b\rangle$ and $|c\rangle$ represent excitons and free e-h pairs, respectively. The corresponding dephasing times $T_{2,\mathrm{b}}$ and $T_{2,\mathrm{c}}$ differ strongly since scattering processes are markedly different for free e-h pairs. Therefore, the appearance of the third-order diffracted polarization, i.e., the FWM signal changes significantly.

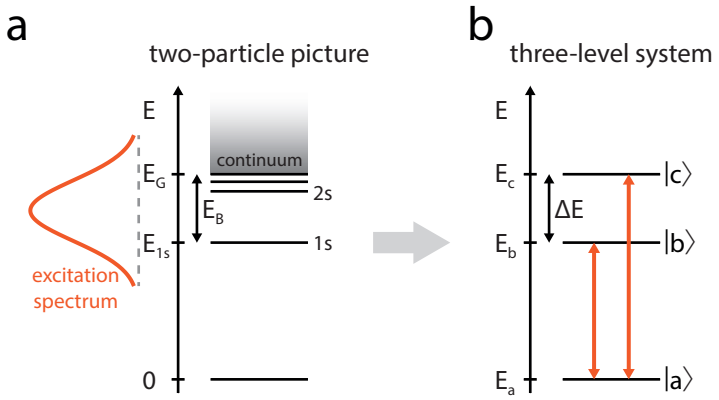

Figure 2.19: Three-Level System for Exciton and Continuum Excited States. **(a)** For small values of E_B the spectrum of an ultrashort laser pulse may cover the 1s and the continuum levels. Therefore, a simultaneous excitation of these states will occur. **(b)** This system can be simplified to a three-level system in which higher-order excitons are neglected. The energy difference ΔE between the two excited states $|c\rangle$ and $|b\rangle$ corresponds to the exciton binding energy E_B in (a).

The superposition of both (or more) excited states at the absorption onset is also referred to as an excitonic wave packet[142] and leads to so-called quantum beating.[143,144] It is possible to model the FWM signal $I_{QB}(t_{delay})$ for the three-level system with two simultaneously excited transitions. Then, one obtains

$$I_{QB}(t_{delay}) = \Theta(t_{delay}) \cdot A \cdot \left(w_b^2 \exp\left(-\frac{2\,t_{delay}}{T_{2,b}}\right) + w_c^2 \exp\left(-\frac{2\,t_{delay}}{T_{2,c}}\right) + 2\,w_b w_c \cos\left(\frac{\Delta E}{\hbar}\,t_{delay}\right) \exp\left(-\left(\frac{1}{T_{2,b}} + \frac{1}{T_{2,c}}\right) t_{delay}\right)\right) \tag{2.55}$$

with the condition $t_{delay} \geq 0$.[145] The quantities w_b and w_c denote the spectral weights of both transitions. The scaling factor A depends on $T_{2,b}$, $T_{2,c}$, w_b, w_c and ΔE, but not on t_{delay}. Therefore, it can be understood as a constant that does not change the shape of $I_{QB}(t_{delay})$.

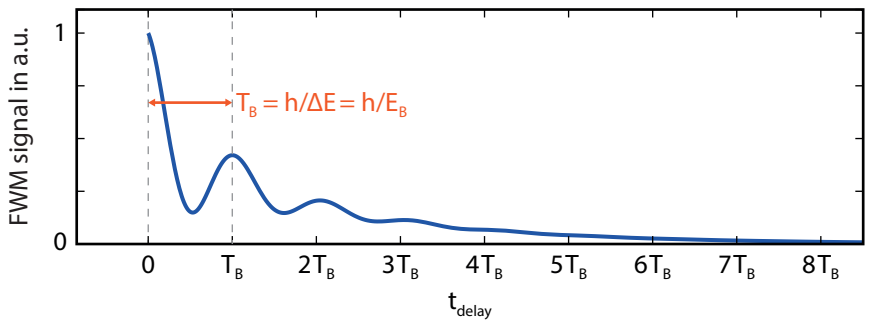

Figure 2.20: Quantum Beating for a Three-Level System. When several transitions within a sample are excited simultaneously — in this case the ones from E_a to E_b and E_c, respectively, as indicated in the three-level system in Figure 2.19 — the FWM signal exhibits a beating behavior with a periodicity T_B that relates to the energy difference of the involved states $\Delta E = E_c - E_b$. As shown here, this can be modeled as a function of the time delay t_{delay} in accordance with Equation 2.55.

The energy difference ΔE between the two excited levels influences the period of the beating signal as shown in Figure 2.20 where Equation 2.55 is plotted in order to visualize the polarization decay of a three-level system. The different frequencies of the two transitions cause the beating behavior in which

constructive and destructive superpositions alternate while the overall signal decays exponentially. The period of the beating signal is referred to as T_B and can be extracted from the plot. It is related to the energy spacing via

$$\Delta E = h/T_B \,, \tag{2.56}$$

where $\Delta E = E_B$ as shown in Figure 2.19.[146]

In Subsection 2.2.3 we discussed that the extraction of E_B might be strongly hindered with conventional methods in inhomogeneously broadened ensembles of NCs. That said, quantum beat spectroscopy (QBS) provides an alternative approach for the indirect measurement of E_B via the beating period T_B. To be even more accurate, multilevel systems could be relied on, considering higher-order excitons and taking the continuum into account as a set of closely spaced levels.[142] However, studies have shown that the three-level approach already provides a reasonably accurate representation of experimental data.[120,133,145]

2.5 Diffusion

The final section of this chapter forms the background for Chapter 6. Starting with the general laws of diffusion, the special conditions related to exciton diffusion within NCs will be derived. Based thereon, two concepts for the measurement of the exciton diffusion length will be introduced.

2.5.1 General Laws of Diffusion

Generally, diffusion denotes the movement of particles from a region of higher concentration towards a region of lower concentration.[147] This process could for example involve atoms or molecules within a closed system. The basic equations for diffusion date back to the nineteenth century and were established by Adolf Fick.[148] For the three-dimensional case, his first law states

$$\mathbf{J}(\mathbf{r}) = -D\nabla c(\mathbf{r})\,, \tag{2.57}$$

where $\mathbf{J}(\mathbf{r})$ denotes the diffusion flux vector that defines the direction and magnitude of the corresponding particle flow at position $\mathbf{r}$. Equation 2.57 shows that $\mathbf{J}(\mathbf{r})$ is directly proportional to the gradient of the concentration distribution $\nabla c(\mathbf{r})$ with a factor D which is known as the diffusion coefficient. This means that a given initial gradient in concentration is the driving force for diffusion leading to the movement of the respective particles. No external force is involved in this process, it is rather referred to as a "random walk".[149] The temporal evolution of the concentration is considered in Fick's second law which states

$$\frac{\partial c(\mathbf{r},t)}{\partial t} = D\nabla^2 c(\mathbf{r},t)\,. \tag{2.58}$$

Here and in the following, the diffusion coefficient D is assumed to be time-independent.

2.5.2 Exciton Diffusion in Nanocrystals

An important question for this work was, which role diffusion plays for excitons within individual LHP NCs or their assemblies. In contrast to other particles, excitons first have to be generated and also have a limited lifetime T_1 until their decay. Equation 2.58 has to be adapted accordingly. The corresponding following equation restricts itself to the representation of diffusion along one dimension, the z-direction in this case.

$$\frac{\partial n_{\mathrm{ex}}(z,t)}{\partial t} = \underbrace{n_0 \exp(-\alpha z)}_{\text{generation}} + \underbrace{D\frac{\partial n_{\mathrm{ex}}(z,t)}{\partial z^2}}_{\text{diffusion}} - \underbrace{\frac{n_{\mathrm{ex}}(z,t)}{T_1}}_{\text{extinction}} \tag{2.59}$$

Obviously, the equivalent to the concentration c in Equation 2.58 is the exciton density n_{ex}. Additionally, the adapted formula includes a term attributed to exciton generation which is assumed to occur instantaneously and is based on the Beer-Lambert law considering an incident light wave in z-direction.[150,151] Finally, the last term accounts for the extinction of excitons, i.e., the decay with lifetime T_1.

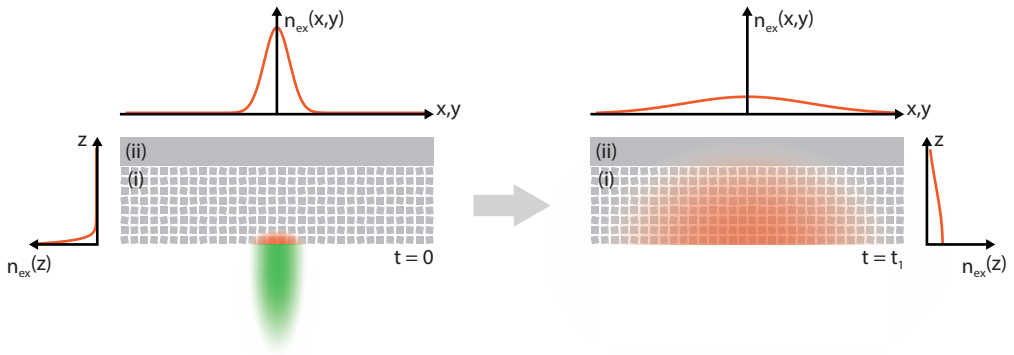

Figure 2.21: Exciton Diffusion in Nanocrystals. A laser pulse (green) hits the surface of a LHP NC film (i) at normal incidence. Excitons (red) are generated close to the surface within this film due to absorption of the photons. Therefore, the initial distribution of excitons $n_{ex}(t = 0)$ is basically determined by the Gaussian profile of the excitation beam in the xy-plane and by the exponential decay of the Beer-Lambert law along the z-axis. Through diffusion the distribution of excitons spreads out such that some excitons potentially reach the adjacent layer of material (ii) at a time $t_1 > 0$ before their decay.

Generally, one can distinguish between two types of diffusion in the NC systems investigated throughout the course of this work. The first case usually applies to NCs which are relatively large in at least one dimension, i.e., the length in this dimension should be much greater than the exciton Bohr radius a_{ex}. Within such a NC, an exciton is basically free to move in the non-confined directions as long as it is not bound to a defect. The second case plays a role for densely packed small NCs, for example a film of nanocubes. In such cases an exciton is usually confined to one NC, but has the possibility to transfer to an adjacent NC via Förster resonance energy transfer (FRET),[152] also referred to as exciton hopping in this specific case of exciton transport.[153,154]

Figure 2.21 illustrates the diffusion occurring in a NC ensemble right after the initial excitation with a laser pulse. Here, the pulse propagates towards the NC film at normal incidence. Hence, the Gaussian shaped beam profile of the excitation laser determines the initial density of excitons in the lateral directions $n_{ex}(x, y, t = 0)$. Moreover, as mentioned above, $n_{ex}(z, t = 0)$ is given by the Beer-Lambert law. Starting from this situation — depicted in the left panel of Figure 2.21 — the spreading of excitons throughout the NC film may be described by Equation 2.59 and the respective versions of this equation for the x and y direction. The right panel of the figure shows the exciton distribution after a certain time $t_1 > 0$. In agreement with the laws of diffusion, the exciton density is strongly reduced in the initial excitation spot, while excitons are distributed over a larger volume.

2.5.3 Determination of the Exciton Diffusion Length

To compare exciton diffusion within several systems, it is best to assign a value to each of these systems that determines the average distance an exciton travels during its lifetime: the exciton diffusion length, described by

$$L_D = \sqrt{2\,D\,T_1} = \sqrt{2\,\mu\,\frac{k_B T}{e}\,T_1}\,, \tag{2.60}$$

exhibiting a square-root dependence on the product of the diffusion coefficient D and the average lifetime of an exciton T_1 within the pure material of the examined film.[155,156] In some parts of the literature, the factor 2 is dropped, but here the mathematically rigorous convention is used, such that

L_D denotes the minimum net displacement achieved in one dimension by $1/e$ of the starting exciton population.[157] Moreover, Equation 2.60 reveals the proportionality of the diffusion coefficient D to the exciton mobility μ and the temperature T. Large electron-hole diffusion lengths up to around 1 µm — mainly due to long lifetimes — have been reported for bulk films of organometal trihalide perovskites at room temperature and are also one of the main reasons for the success of this material type in the recent development of solar cells.[158] In this work NC assemblies were investigated to find out how the exciton diffusion properties differ compared to a bulk film. To this end, two approaches were applied to study the exciton diffusion length in such LHP NC systems, as explained briefly in the following.

Photoluminescence Mapping

The concept of photoluminescence mapping is based on diffusion along the lateral direction parallel to the film surface. In the scheme of Figure 2.21 this corresponds to diffusion within the xy-plane. For this approach to be accurate, the film thickness should be as uniform as possible. In particular, it should not contain any empty spots void of NCs. Moreover, the supporting layer underneath the NC film — i.e., layer (ii) in Figure 2.21 — should be an exciton blocking material in this scenario.

The Gaussian profile of the exciton distribution $n_{ex}(x, y, t)$ can be studied by observing the in- and outgoing light waves from this film on a substrate. First, the ingoing wave, i.e., the excitation laser beam, determines the exciton distribution $n_{ex}(x, y, t = 0)$. Therefore, the laser beam and $n_{ex}(x, y, t = 0)$ exhibit the same Gaussian profile such that the FWHM of this distribution ($FWHM_{Laser}$) may be obtained by mapping the surface of the film while only measuring the reflected excitation beam. Then, the emitted wave shall be observed, i.e., the photoluminescence (PL) of the NC film which occurs at a longer wavelength as compared to the excitation. Not all exciton recombination processes exhibit a radiative nature, however, the magnitude of PL originating from a certain point is directly proportional to the local exciton density $n_{ex}(x, y)$. It does not even matter if the excitation light source is a pulsed or continuous wave laser when mapping a time-integrated PL distribution along the surface. The averaged PL map will represent the Gaussian profile corresponding to the average exciton lifetime T_1 such that $FWHM_{PL} = FWHM_{PL}(T_1)$ may be extracted from this distribution.[159]

Obtaining $FWHM_{Laser}$ and $FWHM_{PL}$ enables the calculation of the standard deviation for both Gaussian profiles according to

$$\sigma = \frac{FWHM}{2\sqrt{2\ \ln(2)}} \tag{2.61}$$

such that σ_{Laser} and σ_{PL} may be obtained. Finally then, the exciton diffusion length

$$L_D = \sqrt{\sigma_{PL}^2 - \sigma_{Laser}^2} \tag{2.62}$$

may be calculated using the aforementioned standard deviation values. In the above description, identical diffusion along the x and y axes has been assumed. In NCs or NC assemblies that are not fully symmetric along the xy-plane, the behavior will likely deviate. In Chapter 6 this will be shown and discussed in greater detail.

Photoluminescence Quenching

In contrast to photoluminescence mapping, the second approach to determine the exciton diffusion length L_D is based on an exciton quenching layer adjacent to the NC film. Such a quenching layer could for example consist of a fullerene such as C_{60}[155] or the fullerene derivative phenyl-C_{61}-butyric acid methyl ester (PCBM)[22] — materials that are generally known to be strong electron acceptors.[160] If an exciton reaches the interface to the adjacent layer via diffusion, the exciton will be dissociated and the resulting free electron will transfer to layer (ii) whereas the free hole stays in layer (i) (see Figure 2.21). Since this e-h pair is no longer available for radiative recombination, this method is referred to as photoluminescence quenching. This possibility of surface quenching represents an additional way for an exciton to decay.[161,162] In the previous case without a quenching layer, the only way for an exciton to decay was recombination (radiatively or nonradiatively), occuring at a rate $k_{re} = 1/T_1$ as described in the previous sections. The additional path for exciton decay is referred to as charge transfer and consists of diffusion towards the interface and subsequent exciton dissociation. Therefore, the rate for the charge transfer process is $k_{ct} = k_{diff} + k_{diss}$. Consequently, the overall exciton decay within such a system of two layers may then be described by

$$k_{total} = k_{re} + k_{ct} = \frac{1}{T_1} + \frac{1}{T_{ct}} = \frac{1}{T_{total}} . \tag{2.63}$$

Moreover, two boundary conditions may be defined for Equation 2.59.[157] All coordinates with $z = 0$ represent the surface of the NC film and the ones with $z = L$ represent the interface between layer (i) and (ii) (cf. Figure 2.21). That is, the NC film thickness is given by L. There is no exciton movement out of the surface of the film into the air at $z = 0$, therefore the first boundary condition is

$$\frac{\partial n_{ex}(z = 0, t)}{\partial z} = 0 . \tag{2.64}$$

Moreover, assuming perfect quenching, the exciton population decays completely at the interface, i.e.,

$$n_{ex}(z = L, t) = 0 . \tag{2.65}$$

Considering these boundary conditions in combination with Equation 2.59 and Equation 2.63, it can be shown that the overall exciton lifetime in the presence of a quenching layer T_{total} may be estimated as

$$T_{total} \approx T_1 \left(1 + \frac{\pi^2}{8} \left(\frac{L_D}{L} \right)^2 \right)^{-1} . \tag{2.66}$$

This estimation is reasonably accurate as long as $\alpha L < 1$, where α is the absorption coefficient of the NC film.[157] Finally, solving Equation 2.66 for the exciton diffusion length leads to

$$L_D \approx \frac{2\,L}{\pi} \sqrt{2 \left(\frac{T_1}{T_{total}} - 1 \right)} . \tag{2.67}$$

Hence, L_D may be calculated from the exciton lifetimes with and without an adjacent quenching layer (T_{total} and T_1, respectively) if the NC layer thickness L is known.

3

Materials and Methods

Having laid the ground with fundamental explanations concerning the experiments conducted in the course of this thesis, the following chapter serves the purpose of introducing the respective employed materials and methods. Firstly, a typical perovskite NC synthesis is described, followed by an introduction to the different NC compositions and morphologies that may be achieved. Next, the three lasers used most commonly in the experiments for this thesis shall be explored with special emphasis on the optical nonlinear processes occurring within these systems. It goes without saying that none of the presented work would have been possible without a well-functioning, stable and reliable light source — in this case, pulsed lasers whose maintenance and optimization represented a key part of my efforts. In the final section of this chapter, various spectroscopic experiments that were used to study the light-matter interaction in perovskite NCs will be explained in detail.

3.1 Perovskite Nanocrystal Synthesis and Variety

The synthesis of lead halide perovskite NCs used in my research was mainly performed by my colleagues Dr. Yu Tong, Dr. Lakshminarayana Polavarapu and Alexander Richter who are more experienced in the realm of chemistry. Therefore, this section will be kept rather brief, only providing a glimpse into the colloidal chemistry behind NC synthesis. To this end, the synthesis of $CsPbBr_3$ nanoplatelets (NPls) shall be explained as a particular example for the general synthetic procedure. Subsequently, other NC compositions and morphologies will be discussed.

3.1.1 Synthesis of Nanoplatelets

The beauty and special charm of the synthesis of these $CsPbBr_3$ NPls lies in the possibility to tune their thickness with atomic precision. Along their lateral dimension the platelets exhibit a square shape with an edge length of around 14 nm,[20] well above the Bohr radius a_{ex} = 7 nm that has been reported for $CsPbBr_3$.[11] This means we can expect no or, at most, only weak confinement of the charge carriers due to the lateral size. However, the NPl thickness can be effectively applied as a lever to control the confinement. Generally, as described before in Subsection 2.1.4, a reduction of the thickness down to the strong-confinement regime below the Bohr radius leads to a blue-shift of the emission wavelength. This is an effect of high interest since it enables wavelength tunability into the blue region without the usage of mixed-halide $CsPbBr_xCl_{(3-x)}$ NCs which are prone to instability.[163]

While the general formula for the bulk material is $CsPbBr_3$, this expression is often also used when referring to NCs of reduced dimensionality. Of course, this formula applies without restrictions to large crystals which are in principle an infinite repetition of the crystal's unit cell. However, this formula ceases to be accurate when the thickness of such a platelet is reduced to only a few unit cell heights which is given by the height of an $PbBr_6$ octahedron and amounts to 0.6 nm (see Figure 2.5). A single layer of unit cells is called a monolayer (ML), but for NCs the outer shell contains no Cs ions. Instead, the outermost Cs-sites serve as anchoring points for ligands that form the surface of the NC and stabilize the whole structure. Considering the consequent lack of Cs, the formula $[CsPbBr_3]_{n-1}PbBr_4$ is better suited to accurately describe the composition of a NPl with a thickness of n MLs. This shows that for each distinct platelet thickness there is a fixed ideal Cs/Pb ratio. Based thereon, it is possible to control the NPl thickness. In this NPl synthesis, two different precursors are applied, each containing only Cs or only Pb. Their ratio is chosen to yield NPls with a fixed number of MLs. The required chemicals for this synthesis were purchased from *Sigma-Aldrich* and used as received. In detail, these include Cs_2CO_3 (cesium carbonate, 99 %), $PbBr_2$ (lead(II) bromide, ≥ 98 %), $SnBr_2$ (Tin (II) bromide), NaBr (sodium bromide), KBr (potassium bromide), oleic acid (technical grade 90 %), oleylamine (technical grade 70 %), toluene (for HPLC, ≥ 99.9 %), acetone (for HPLC, ≥ 99.9 %), hexane (for HPLC, GC, ≥ 97.0 %) and ethyl acetate (ACS reagent, ≥ 99.5 %).

The procedure of this colloidal synthesis relies on two precursors which are prepared individually in the beginning. For preparation of the Cs-oleate precursor, 0.1 mmol Cs_2CO_3 powder are dissolved in 10 ml oleic acid at 100 °C under continuous stirring. The second precursor, i.e., the $PbBr_2$ precursor solution is obtained by dissolving 0.1 mmol $PbBr_2$ powder and 100 µl each of oleylamine and oleic acid in 10 ml toluene at 100 °C. The mentioned ligands help to solubilize $PbBr_2$ in toluene, while a closed reaction chamber prevents toluene from evaporating.

Table 3.1: Synthesis of $CsPbBr_3$ Nanoplatelets. Precursor and acetone amounts used to synthesize NPls of a distinct thickness.

thickness of NPls [ML]	Cs-oleate precursor [µl]	$PbBr_2$ precursor [ml]	acetone [ml]
2	150	3	2
3	150	1.5	2
4	150	1.2	2
5	200	1	2
6	250	1	2.5

Subsequently, the actual NPl synthesis is conducted at room temperature and in an ambient atmosphere. Control over the platelet thickness is achieved by tuning the ratio of the two aforementioned precursors and the amount of acetone which acts as an anti-solvent. Under vigorous stirring, the Cs-oleate precursor is added to a toluene solution containing the $PbBr_2$ precursor. After 5 s, acetone is added, initiating the formation of NPls. After an additional 60 s of stirring, the obtained NPl dispersion is centrifuged at 4000 rpm for 3 min and afterwards the precipitate is redispersed in 2 ml of hexane. The respective precursor amounts needed to achieve a certain platelet thickness given by the number of MLs are listed in Table 3.1. In the case of the 5 and 6 ML NPl samples, 0.2 ml and 0.3 ml of acetone, respectively, are injected into the Pb precursor solution prior to the whole procedure.

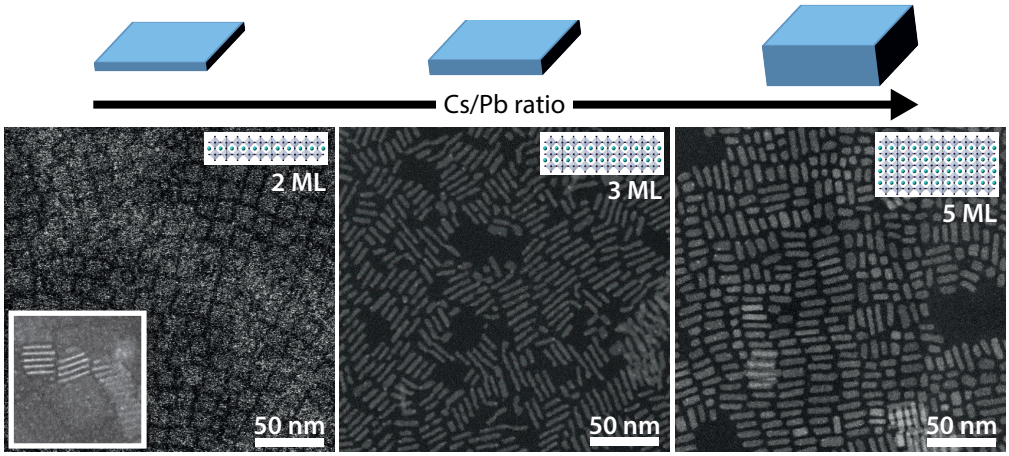

Figure 3.1: Transmission Electron Microscopy of $CsPbBr_3$ NPls. A scheme illustrating how NPl thickness is controlled via the Cs/Pb ratio. ADF-STEM images confirm that the synthesis approach results in uniform platelets with a distinct thickness which amounts to 2, 3 and 5 MLs in the three cases shown above. Usually, the NPls tend to form stacks when put on a substrate with sufficiently high NPl concentration, thus they are standing upright on their edges such that their thickness can be extracted easily (second and third panel plus inset in the first panel). Only in the first panel there are platelets lying flat on the substrate surface revealing the lateral platelet shape.

The annular dark field scanning transmission electron microscopy (ADF-STEM) images in Figure 3.1 show examples of the 2, 3, and 5 ML samples. The NPls were deposited on a substrate and all of them can be discerned individually. When these NPls are in close proximity to each other, as it may be the case when depositing them on a substrate, they tend to form stacks and thus stand on their edges. This is what can be seen in the second and third panel while they are lying down in the first panel revealing the full lateral size. Statistical evaluation of the ADF-STEM images reveals that the thickness of the NPls is indeed a multiple of the ML thickness of 0.6 nm, thereby proving that the labeling is correct. Other techniques like electron diffraction, high-resolution ADF-STEM, energy-dispersive

X-ray (EDX) spectroscopy and X-ray diffraction (XRD) give access to additional information on the crystal shape, structure, orientation and composition. Reference [20] presents these characterization techniques in great detail and gives further information on $CsPbBr_3$ NPls.

3.1.2 Different Compositions and Morphologies

Fundamentally, there are two different ways to change the optical and electronic properties of perovskite NCs. One is to alter their composition, the other is to modify their morphology. While the first possibility is also applicable to bulk films, the latter applies to NCs in particular. The following provides an insight into both of these approaches and how they have been applied within the work carried out in the context of this thesis.

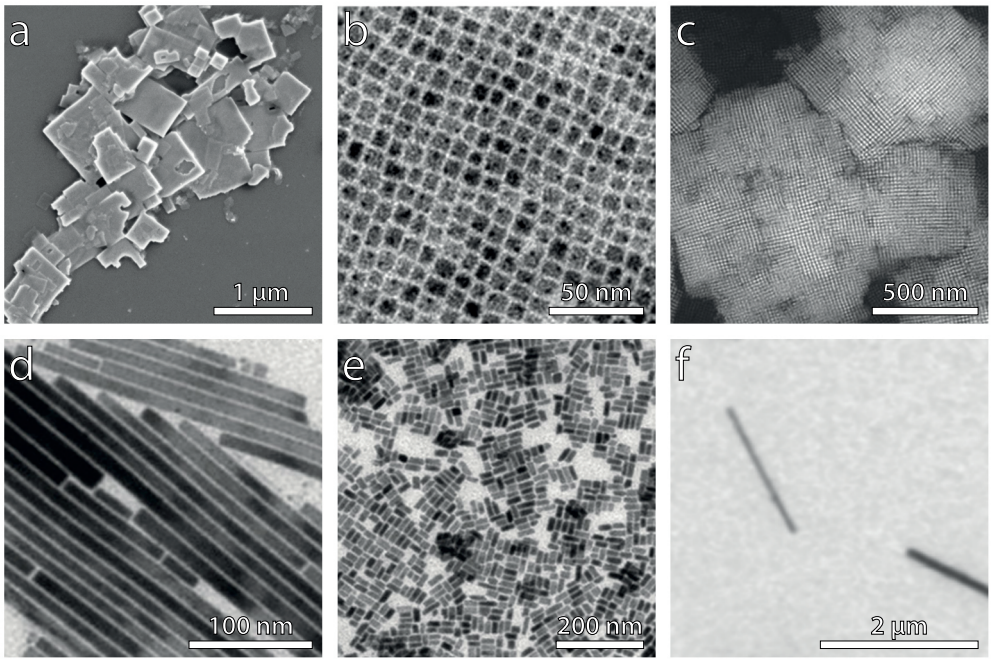

Figure 3.2: Electron Microscopy Images of Different NC Morphologies. The variety of different NC morphologies includes **(a)** $MAPbI_3$ nanoplatelets [adapted from Reference [76]], **(b)** $CsPbBr_3$ nanocubes [adapted from Reference [22]], **(c)** $CsPbBr_3$ supercrystals [adapted from Reference [23]], **(d)** $CsPbBr_3$ nanowires [adapted from Reference [21]], **(e)** $CsPbI_3$ nanorods [adapted from Reference [25]] and **(f)** larger $MAPbBr_3$ wires.

As mentioned before the general formula for bulk perovskite crystals is ABX_3. For this thesis, both organic-inorganic NCs using methylammonium (MA^+) as the A-site cation as well as fully inorganic NCs based on cesium (Cs^+) were studied. The difference between these two cations only has a minor influence on the energy band gap of the resulting perovskite crystal.[164] Within the studies for this thesis, the B-site cation was lead (Pb^{2+}) throughout, even though lead-free NCs were studied outside the scope of this work.[90] This leaves the X-site halide anion as the key component determining the band gap of lead halide perovskites, a crucial property for the emission wavelength. The halide anions iodide (I^-), bromide (Br^-) and chloride (Cl^-) are used to reach the respective red, green and blue wavelength regions for bulk-like NCs. Typically, the Br-based NCs are synthesized initially and then the halide ions are substituted by a postsynthetic anion exchange process. This enables a full or partial replacement of the halide anions, thereby also making mixed-halide NCs with a continuously tunable band gap accessible.[21,61,165]

Another way to tune the band gap — and with it the emission wavelength — is the use of different NC morphologies.[166] As explained before, reducing the size of NCs in at least one dimension leads to a corresponding confinement of electrons and holes, thus also influencing the possible energetic transitions within the NCs. However, not only the emission wavelength may be changed by the morphology. The size, shape and arrangement of NCs also influence other NC properties like the polarization behavior, charge carrier diffusion or the coupling between NCs. Using variations in synthetic procedures leads to completely different NC morphologies.[18] Figure 3.2 depicts some of the possible outcomes of such varying syntheses, with the individual panels showing platelets, cubes, supercrystals, wires and rods. Besides these morphologies, there is also a growing interest in large, extended sheets of perovskite layers in the Ruddlesden-Popper phase.[167,168] Belt-shaped NCs have been reported as well.[169] Out of this wide variety of perovskite NCs, the present work focuses on cube-, platelet- and wire-shaped NCs.

3.2 Light Sources

3.2.1 Ti:Sapphire-Based Amplifier

For most of the optical experiments conducted in the course of this thesis, an ultrafast Ti:Sapphire-based amplifier employing an integrated femtosecond oscillator and a pump laser was used. This apparatus was provided in the form of the powerful one-box solution *Libra-HE+* by *Coherent*. Figure 3.3 reveals the inside of this laser system and shows its five building blocks which all together enable the amplification of femtosecond pulses.

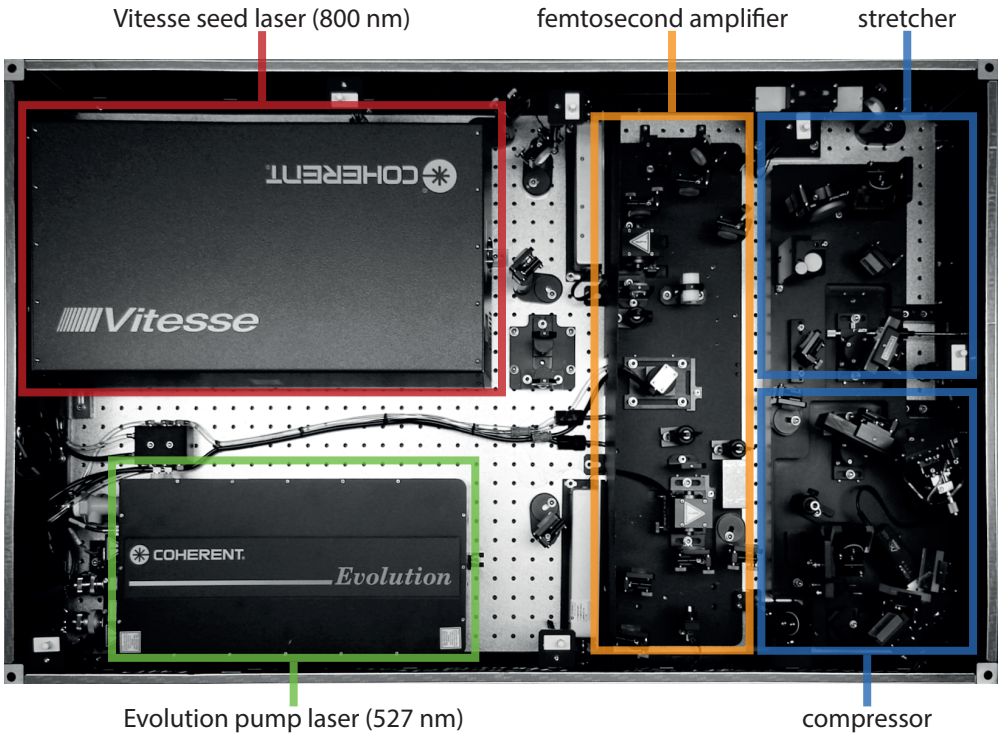

Figure 3.3: Ti:Sapphire-Based Amplifier. The one-box solution *Libra-HE+* by *Coherent* comprises all five components needed for the generation of strongly amplified femtosecond pulses. The short femtosecond seed pulses from the *Vitesse* output are guided along the edge of the box towards the stretcher where they are stretched to picoseconds in duration. In the Ti:sapphire crystal of the femtosecond amplifier these pulses are overlapped with intense pump pulses emanating from the *Evolution* laser, all in all resulting in strongly amplified pulses with a central wavelength of 800 nm and a pulse energy of about 5 mJ. Finally, these amplified pulses are compressed, achieving a pulse length of approximately 100 fs at the output of the *Libra-HE+*. [Photograph kindly provided by *Coherent*]

The actual source of the femtosecond pulses (with a wavelength of 800 nm) is the integrated *Vitesse* seed laser which comprises a Ti:sapphire oscillator pumped by a continuous-wave (CW) *Verdi* diode laser (532 nm). The name Ti:sapphire refers to the sapphire (Al_2O_3) crystal of the system that is doped with Ti^{3+} ions and acts as the gain medium. This material is widely known for its intriguing and excellent properties in the field of ultrashort pulse generation.[170] It has a large gain bandwidth with a maximum around 800 nm. Within the oscillator cavity, the continuous wave mode is suppressed by the Kerr effect inside the Ti:sapphire crystal, leading to the mode-locked pulsed operation with an ultrashort light pulse (85 fs) traveling between the two end mirrors of the cavity. One of these mirrors is semitransparent, thus releasing one pulse at each round-trip, which results in a repetition rate of 80 MHz given by the length of the cavity.

Coming from the *Vitesse* seed laser, these pulses are guided to the grating-based stretcher, where they get temporally elongated to a pulse length in the picosecond regime. This is needed to avoid damage to the crystal in the next and crucial step — the amplification. The respective region highlighted in the center of Figure 3.3 comprises another cavity with two high-speed optical switches at both ends, the so-called Pockels cells. The cell at the entrance of the cavity picks out one single pulse coming from the stretcher every millisecond meaning that only one in 80 000 pulses is used, whereas the rest of them is simply blocked. This single pulse is locked inside the cavity between both Pockels cells. Another Ti:Sapphire crystal is positioned within the cavity where the trapped oscillating pulse is overlapped with the laser beam originating from the *Evolution* diode laser. Similar to the aforementioned *Verdi*, this pump laser also has a wavelength in the green region (527 nm). However, the difference is that the *Evolution* is a pulsed source with a repetition rate of 1 kHz, matching the condition of the stretched *Vitesse* seed pulses that enter the cavity only once every millisecond. These pump pulses with a huge pulse energy of 20 mJ and a duration of around 120 ns are considerably longer than the cavity trapped seed pulses. This enables a lasting interaction between the two pulses while the seed pulse does several round trips within the cavity, getting amplified each time it passes the Ti:Sapphire crystal. After about ten cycles the seed pulse reaches the maximum possible pulse energy of around 5 mJ. Then, the second Pockels cell at the end of the cavity is activated in order to release this strongly amplified (by a factor of 10^6) pulse towards the last component of the amplifier system. This is the compressor, which essentially reverses the effects of the stretcher and compresses the pulses back to their initial length of about 85 fs.

The concept described above is known as regenerative amplification. It leads to highly reduced repetition rates (1 kHz in this case), but strongly amplified pulses with immense pulse energies while maintaining the pulse length in the femtosecond regime.

3.2.2 Optical Parametric Amplifier

Strictly speaking, the optical parametric amplifier (OPA) is not a light source per se since it uses a split off beam of the *Libra-HE+* as input and modifies these strong pulses having an initial energy of around 2.1 mJ. We employed the *OPerA Solo* built by *Light Conversion* and distributed by *Coherent* which enables a transformation of these input pulses into pulses of different wavelengths in the extensive range from 190 nm up to 12 µm at the output of the device. Depending on the desired output wavelength, a combination of several nonlinear processes needs to take place within the OPA, such as white light generation, sum/difference frequency generation or second harmonic generation.

In order to grasp the concept of optical parametric amplification and the functioning of the OPA, the essential processes occurring within the system shall be briefly explained in chronological order. Figure 3.4 shows a photograph of the inside of the system. Therein, the processes are assigned to several highlighted regions. First, the input pulses are coupled into the system and two beam splitters (1) (2) are applied to create three beams in total, two of them being pump beams while the remaining, weakest one of them serves as the origin of the OPA output pulses. The pulses of the last-mentioned beam are focused on a sapphire plate (3) where they generate a white light continuum covering the whole visible part of the spectrum and ranging into the near-infrared region. This process of supercontinuum generation is possible when high laser intensities occur within a crystal which is the case for these focused femtosecond pulses. It is not a separate phenomenon on its own, but rather

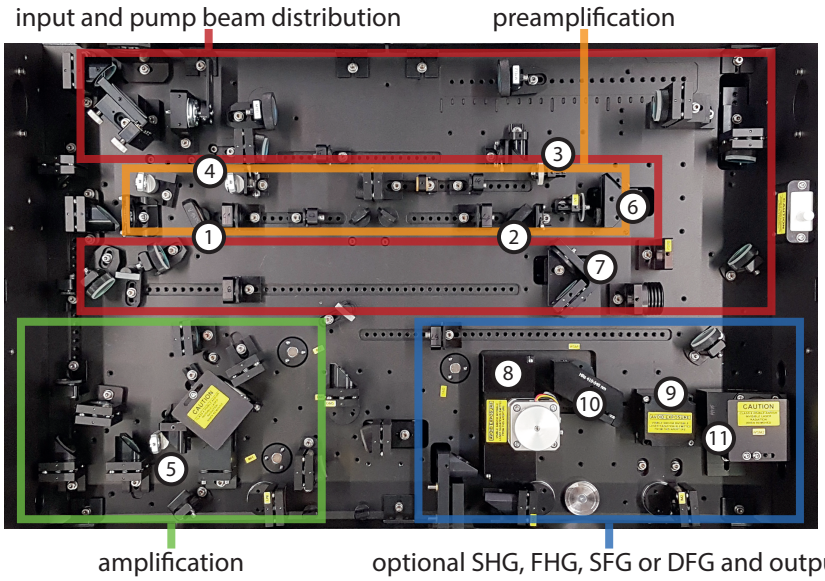

Figure 3.4: Optical Parametric Amplifier. The *OPerA Solo* includes two amplification stages and leverages several nonlinear optical processes in order to generate output pulses with a tunable wavelength in the extensive range from 190 nm up to 12 µm. The following key components are highlighted in the photograph: beam splitters for the separation of the two amplification pulses ① ②, sapphire crystal for white light generation ③, nonlinear crystals for the amplification processes ④ ⑤, time-delay stages ⑥ ⑦, mixers for second harmonic generation ⑧ ⑨ and wavelength separators ⑩ ⑪.

a fairly complex interplay of several nonlinear effects leading to spectral broadening of the input pulses.[171] The pulses are also stretched in time, with the shorter wavelength components lagging slightly behind the longer wavelengths within the pulse.

In the nonlinear crystal ④, this white light continuum and the weaker pump pulse beam are focused and overlapped non-collinearly. This is where the preamplification takes place and the corresponding process of optical parametric amplification (PA) is illustrated in the first panel of Figure 3.5 a. Strictly speaking, there are two incident photons ω_p, ω_s.

If the intensity is sufficiently high, it is possible that single pump photons ω_p are transformed into two photons with lower frequencies, where one of them is identical to the incident signal photon ω_s, effectively amounting to an amplification of this latter component. This process always obeys the conservation of energy and momentum.[172] The respective equation for the energy can be directly read out from the scheme in Figure 3.5 a and states

$$\omega_p = \omega_s + \omega_i \tag{3.1}$$

where ω_s denotes the aforementioned signal and ω_i denotes the so-called idler. The OPA comprises several computer-controlled motors that enable the correct tuning for obtaining a certain target output wavelength. For preamplification and correct choice of the initial ω_s, the delay stage ⑥ is moved in a way that a femtosecond pump pulse in the crystal ④ temporally overlaps with the part of the white light spectrum that is supposed to be amplified. Rewriting Equation 3.1 in terms of wavelengths and inserting the fixed pump wavelength $\lambda_p = 800\,\text{nm}$ yields

$$\frac{1}{800\,\text{nm}} = \frac{1}{\lambda_s} + \frac{1}{\lambda_i} \tag{3.2}$$

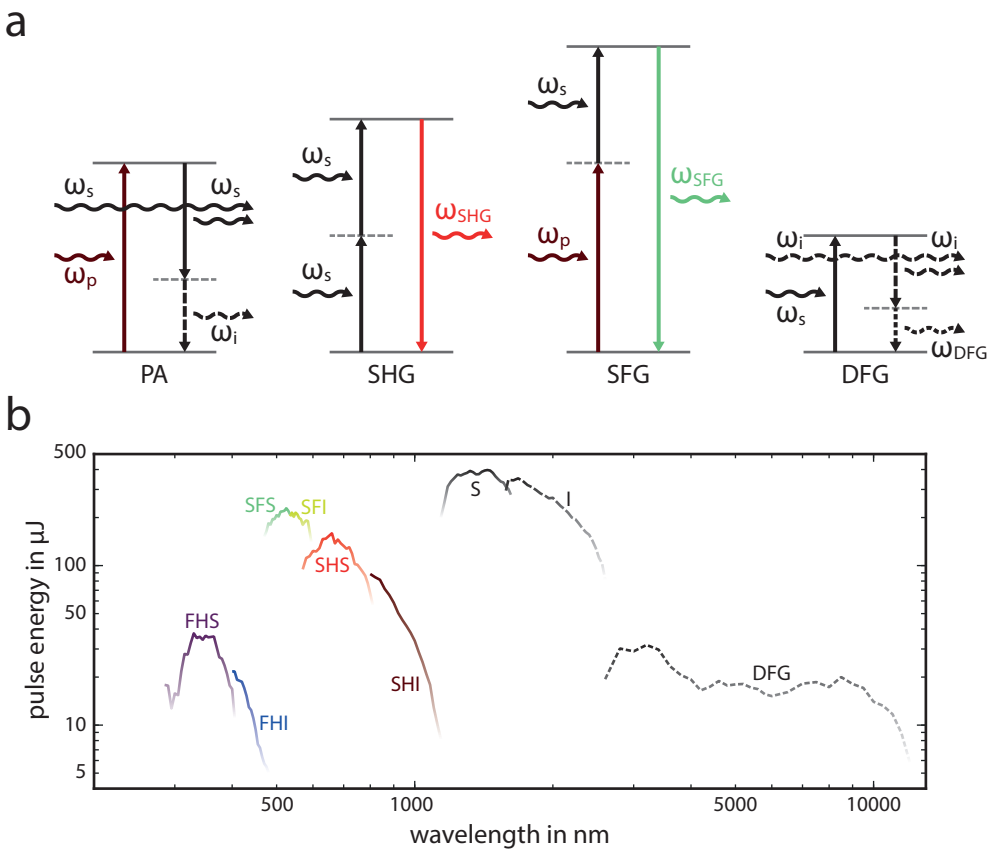

Figure 3.5: Nonlinear Processes and Tuning Curve of the OPA. (a) In order to access the broad wavelength tunability of the OPA output several nonlinear processes are needed. The above schemes illustrate parametric amplification (PA), second harmonic generation (SHG), sum frequency generation (SFG) and difference frequency generation (DFG). **(b)** The tuning curve of the OPA shows that it can be operated in nine different modes each giving access to a distinct wavelength region. The achievable output pulse energy and stability are strongly dependent on the exact desired wavelength. The color gradient within the graphs of each individual operation mode is an indicator of the stability. [Raw data for the tuning curves kindly provided by *Light Conversion*]

and one recognizes that the wavelengths of S and I fall into the near-infrared region with an achievable wavelength range for the signal λ_s from 1140 nm to 1620 nm. Similar to the pump pulses the generated pulses have a length of around 90 fs. Due to the non-collinear beam geometry, blocking the remaining residual contributions behind the crystal can easily isolate the amplified signal beam. The requirement of momentum (k-vector) conservation is assured by rotating the nonlinear crystal which enables phase matching of the involved pulses.

This signal beam is then collimated by a lens telescope and guided onto the nonlinear crystal of the amplification stage, where it overlaps with the strongest pump beam, this time in a collinear configuration. Similar as in the first stage, the PA process generates a strongly amplified signal beam and — basically as a side product — an idler wave of similar intensity. A dichroic mirror behind the crystal filters out the residual transmitted pump beam. Further optical filtering can provide the isolated use of the signal or idler as the output of the OPA.

Generally, all possible output wavelengths are displayed in the tuning curve of the OPA shown in Figure 3.5 b together with the respective pulse energies. Note that this graph also shows the seven additional operation modes of the OPA that are needed to reach other output wavelengths. However, all of them have the generation of the signal (S) and idler (I) beams in common. By using so-called

frequency mixers (8) (9) and wavelength separators (10) (11) in the last building block of the system, additional nonlinear processes can be introduced and their output can be optically filtered. For example, second harmonic generation (SHG) can be used to frequency double either S or I, resulting in SHS and SHI (see Figure 3.5). If this is done twice, it results in fourth harmonic generation (FHG), with the help of which FHS and FHI may even reach wavelengths in the ultraviolet region. The spectral gap between such modes may be closed using sum frequency generation (SFG), in which an additional split off pump beam is combined with S or I resulting in SFS and SFI. Finally, difference frequency generation (DFG) between S and I gives access to the mid-infrared region with output wavelengths of up to 12 µm. DFG is actually very similar to PA, however, here the goal is to extract the difference frequency rather than the amplified frequency. The tuning curve in Figure 3.5 b gives a complete overview of all accessible wavelengths of the OPA output and demonstrates that the pulse energy and stability of the output strongly depend on the operation mode and exact wavelength.

3.2.3 White Light Laser

For most of the steady-state and time-resolved PL measurements, a white light laser (WLL) was employed (*NKT Photonics*, *SuperK EXTREME EXR-20*). Similar to the preamplification stage of the OPA this device is based on supercontinuum generation in a highly nonlinear medium. However, in this case the respective material is not a compact, thin sapphire crystal, but a long solid core photonic

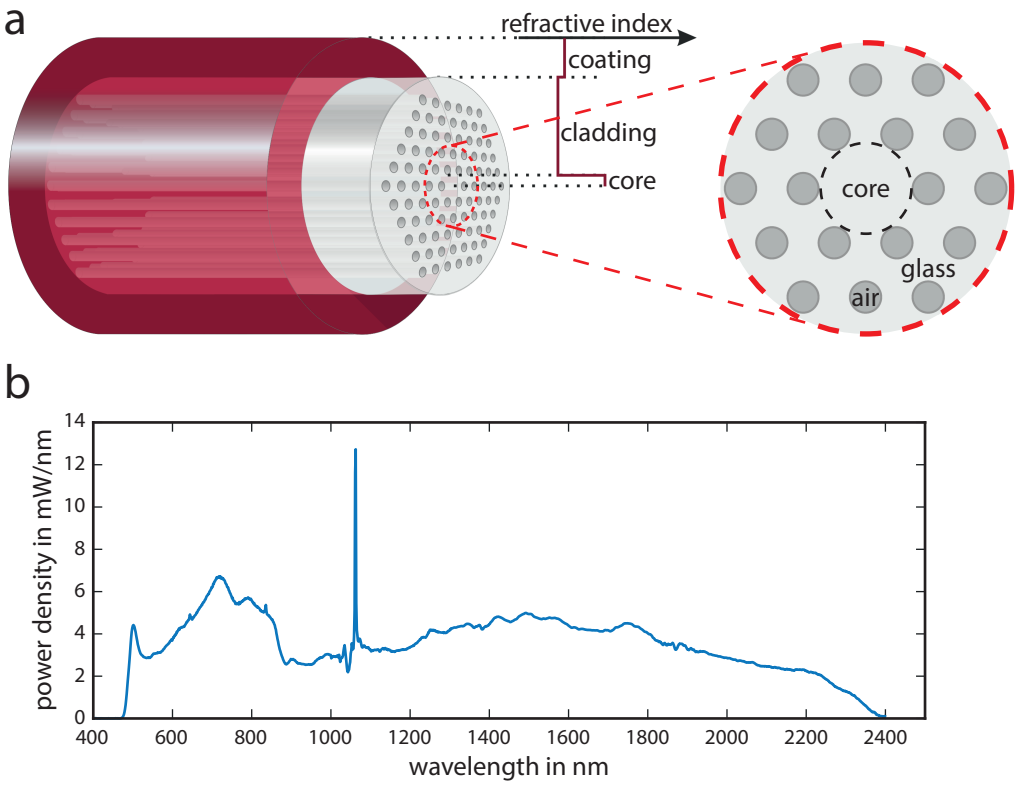

Figure 3.6: Photonic Crystal Fiber and Supercontinuum Output Spectrum. (a) Schematic structure of a solid core PCF and a transversal cross section thereof. The refractive index in the core as well as the cladding region can be controlled by varying the cross-sectional geometry of the air voids within the SiO_2 glass fiber. **(b)** The initial pump pulses with a wavelength of $\lambda_{central}$ = 1064 nm generate a broad supercontinuum in the nonlinear PCF of the *SuperK EXTREME EXR-20* giving access to nearly the whole visible and near-infrared region at the output of the laser. [3D scheme and raw data for the output spectrum kindly provided by *NKT Photonics*]

crystal fiber (PCF). Figure 3.6 a schematically depicts such a PCF and its cross section. As can be seen, it comprises highly pure SiO_2 glass with a solid core and a number of concentric arrangements of air voids hexagonally distributed around said core. By tuning the diameter and the distance of these air voids in the cladding region, the refractive index along the radial axis of the PCF can be engineered such that even over a broad spectral region the PCF only guides the fundamental Gaussian mode in its core with a high beam quality of $M^2 < 1.1$. By reducing the diameter of the core down to around 2 µm, the light is confined to a small area. This results in high laser intensities making the core a highly nonlinear medium which thus supports supercontinuum generation. A mode-locked ytterbium-doped fiber laser ($f_{rep} = 78\,\text{MHz}$, $t_{pulse} = 5\,\text{ps}$ and $\lambda_{central} = 1064\,\text{nm}$) with a power of several Watts is used as the pump laser and coupled into the PCF, where it generates a broad white light spectrum spanning from 475 nm to 2400 nm (see Figure 3.6 b).

An acousto-optic tunable filter at the output of the laser enables the selection of a single output wavelength out of the above spectrum, making it a monochromatic source again. Using the additional *SuperK EXTEND-UV* based on second-harmonic generation it is even possible to reach the ultraviolet region down to 330 nm. Furthermore, the system also includes a pulse picker that may be used to reduce the repetition rate of the pulsed laser down to 152 kHz, which is a crucial property for time-correlated single photon counting (TCSPC) experiments and will be further explained in the next section. Overall, the WLL is a versatile, stable, and user-friendly device enabling continuous tuning of the wavelength over a broad region with pulses in the tens of picoseconds range and sufficient power for simple spectroscopic excitation experiments.

3.3 Spectroscopic Experiments

3.3.1 Linear Absorption

The physical process of absorption was explained in detail in Subsection 2.1.2. To put it in a nutshell, it is the excitation of an allowed transition within a material that leads to the extinction of the absorbed photon and the generation of an e-h pair. In semiconductors this is usually only possible for photons with an energy above the band gap, but in the case of a high photon flux even below-band-gap photons can create e-h pairs through multi-photon absorption.[59] Moreover, Section 2.1 introduced the presence of excitons occurring energetically slightly below the continuum onset of the absorption.

A precise measurement of absorption is not as trivial as it might seem at first glance. In particular, the absorption behavior of the investigated semiconductor NCs can either be studied using solid films of these NCs that have been deposited on a transparent substrate or using a dispersion of the respective NCs in a cuvette. When a beam of light is incident on such a sample, several processes can possibly take place. In a simplified picture, the beam can be transmitted, reflected, absorbed or scattered. Most of the effects of reflections can be identified and subsequently subtracted by comparing the NC sample to a blank substrate or a cuvette only filled with the respective solvent of the NC dispersion. Usually, the examined NC samples used throughout this work do not exhibit strong scattering and moreover this effect was also largely suppressed by keeping the film thickness or NC concentration in dispersions low. Taking all of this into account, absorption can be studied with reasonable accuracy by measuring the transmission intensity of the incident beam. This so-called linear absorption spectroscopy was relied on when absorption values had to be determined for particular NCs.

That being said, linear absorption spectroscopy mostly only served as the first step in optical characterization of the investigated NCs and NC systems of this thesis, delivering information about the band gap and the homogeneity of the material. Moreover, the shape of linear absorption spectra reveals whether the respective semiconductor NCs are bulk-like or exhibit properties of confined systems. Usually, two different setups were applied to record these spectra. The first one is the *Cary 5000 UV-Vis-NIR* spectrophotometer, a commercial system from *Agilent Technologies* capable of fast measurements at room temperature over a large spectral range. Several broadband light sources can be used and the whole desired wavelength region is scanned by a monochromator while a collimated beam with the intensity $I_0(\lambda)$ is guided onto the sample. Detectors measure the intensity of the transmitted signal $I(\lambda)$. Via the resulting transmission $T(\lambda)$ associated with the investigated sample, the optical density (OD) at the respective wavelength $OD(\lambda)$ may be obtained as follows:

$$\begin{aligned} T(\lambda) &= \frac{I(\lambda)}{I_0(\lambda)} = 10^{-OD(\lambda)} \\ \Longrightarrow OD(\lambda) &= -\log_{10}(T(\lambda)) \end{aligned} \tag{3.3}$$

The quantity OD is used to describe the process of absorption in this thesis according to the Beer-Lambert law. Statistically, this is only valid for a single scattering process occurring in the sample per photon. Thus, throughout all experiments conducted in the course of the present thesis, the OD in the relevant spectral region was kept in a range of 0.1 to 1 by controlling the film thickness or the

concentration of the NCs within the dispersion. Additionally, the light intensity was adjusted to a reasonably low level to exclude multi-photon processes and strong emission.

Often, absorption is evaluated as a function of the photon energy E. In order to plot $OD(E)$, it is sufficient to accordingly adjust the axis values using the inverse relation between wavelength and photon energy.[173] Note that it will discussed why this is not the case for PL spectra, though, in the next subsection.

The main advantages of the *Cary 5000 UV-Vis-NIR* are its measurement speed and the fact that it actually scans the broad spectral range measuring only one wavelength at a time. Additionally, it even offers an integrating sphere for samples that exhibit stronger scattering contributions. However, the temperature-dependent absorption studies in this thesis also require spectra recorded at low temperatures which is not possible with the *Cary 5000 UV-Vis-NIR*. Rather, a custom setup employing a liquid helium cryostat was used for this purpose. Figure 3.7 displays a simplified representation of this setup.

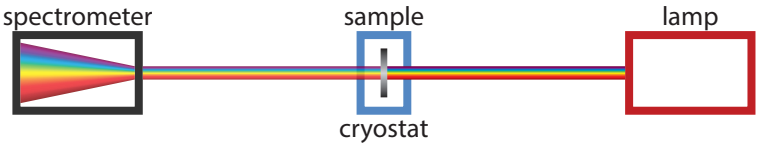

Figure 3.7: Scheme of the Absorption Setup. The substrate with the NCs is mounted in a vacuum chamber that is part of the cryostat. This way the sample can be cooled down from room temperature to around 10 K. The collimated beam of a xenon lamp is guided onto this sample and the transmitted beam is coupled into a spectrometer that records the corresponding spectrum.

First, NCs are deposited on a transparent substrate. For low-temperature measurements sapphire substrates are used for their high thermal conductivity. These substrates are then mounted inside the cryostat's vacuum chamber. Once a pressure below 10^{-4} mbar is reached, the cooling process can be initiated. Liquid helium with a temperature of around 4 K is pumped through the cryostat finger, while electric heating is used to counterbalance this effect in order to reach and then maintain a desired temperature. To this end, a proportional–integral–derivative (PID) controller monitors the temperature in proximity to the sample position and controls the valve for the helium flow and the current for the heating accordingly. A xenon short arc lamp (*Osram*, *XBO 75W/2*) illuminates the sample with a collimated light beam on a circular spot with a diameter of 5 mm. On the other side of the cryostat, the transmitted signal is coupled into a spectrometer (*Princeton Instruments*, *SpectraPro SP2300*) with which the respective spectrum is recorded on a charge-coupled device (CCD), i.e., a camera that saves the counts per bin (*Princeton Instruments*, *PIXIS 400 eXcelon*), saving the spectrum as a function $I(\lambda)$. Before or after these measurements the spectrum for an empty substrate is recorded and serves as the reference $I_0(\lambda)$. Alternatively, a correction with the room temperature spectrum recorded with the *Cary 5000 UV-Vis-NIR* can be taken to calculate $I_0(\lambda)$. Afterwards, Equation 3.3 is exploited to extract the OD spectra for the sample. For the evaluation of these data sets recorded at different temperatures a script in *MATLAB* was written.

3.3.2 Transient Absorption

Transient absorption spectroscopy (TAS) is a technique to investigate energetic levels and carrier relaxation pathways. It works by comparing the linear absorption spectrum of a sample with one after the sample has been strongly optically excited to populate excited states.[174] As a general matter, the *Libra-HE+* amplifier serves as the source of the femtosecond pulses needed for this pump-probe technique. In a nutshell this works as follows. A pump pulse with photons of sufficient energy generates e-h pairs within the semiconductor sample. Subsequently, another probe pulse is used to learn more about the energetic distribution and dynamics of these e-h pairs.

A photo of the setup used in this thesis is shown in Figure 3.8, where the individual building blocks are grouped in four regions that can be assigned to the pump beam, probe beam, sample position, and to the detection of the signal.

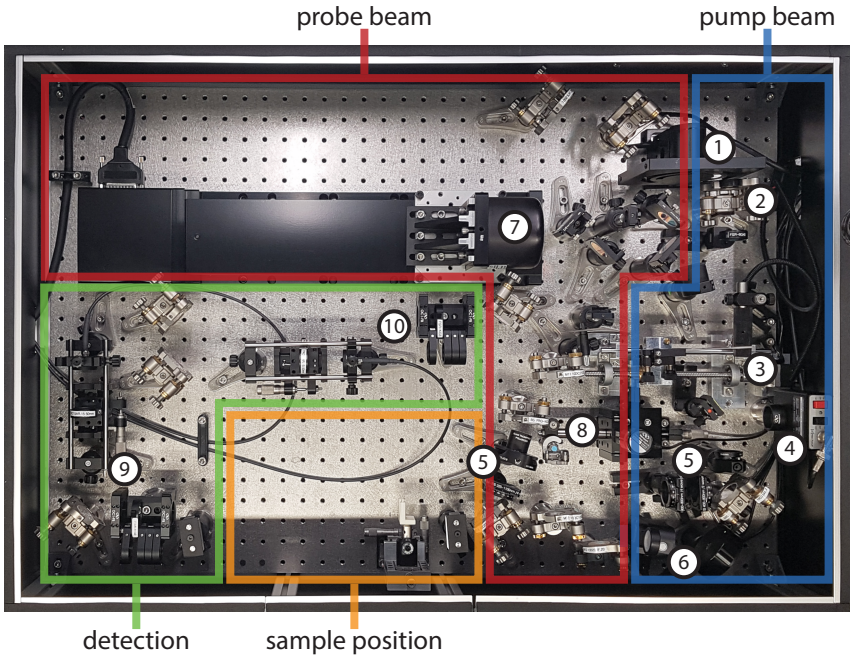

Figure 3.8: Transient Absorption Spectrometer. The *Newport TAS* system shown above has been strongly modified from its original state to cater the needs of the present work. A pump pulse optically excites the sample and a transmission spectrum of a subsequent white light probe pulse with a tunable time delay relative to the excitation is detected in a spectrometer. By running an optical chopper at half of the laser repetition rate, i.e., at 500 Hz, every second pump pulse is blocked and thus the effect of the pump pulse on the sample and the respective dynamics can be studied by comparing these two cases with and without excitation. The following key components are highlighted in the photograph: optical chopper that blocks every second pump pulse ①, BBO crystal on a flip mount for the optional use of SHG in the pump beam ②, linear variable ND filter mounted on a motorized stage to control the pump power and its stability ③, fast photodiode that monitors the amplitude of each individual pump pulse ④, polarization optics ⑤, power meter ⑥, linear delay stage ⑦, CaF_2 crystal for white light generation ⑧ and the optical filtering plus coupling into the fibers leading to the spectrometer for the probe as well as the reference channel ⑨ ⑩.

In the following paragraphs, these four regions will be addressed one by one, thereby explaining the TAS technique in detail. First, we turn to the region associated with the pump beam. There are two options for the pump pulse generation. On the one hand, it can be generated from the fundamental *Libra-HE+* amplifier pulses via SHG in a barium borate (BBO) crystal, however, this option results in a fixed excitation wavelength of 400 nm. On the other hand, tunable pumping is achieved by coupling the *OPerA Solo* OPA signal into the TAS setup. The pulse energy can then be controlled via a variable

neutral density (ND) filter. The beam is focused onto the sample, which comprises either dispersed NCs in a cuvette or deposited NCs on a substrate. Just like in the preparation for the linear absorption experiments, the concentration of NCs has been adjusted to keep the OD in the range 0.1-1, thereby also avoiding strong scattering effects.

In the second region, a fundamental amplifier pulse enters the setup via its second entrance at a similar time as the pump pulse. It travels twice through a retroreflector mounted on a linear delay stage and is then focused onto a CaF_2 crystal where it generates the probe pulse via white light generation. In principle, other crystals could be used as well, but CaF_2 is known for its output spectrum reaching into the ultraviolet (UV) region, which was necessary for the conducted measurements. On the flip side, this material can be damaged more easily than other crystals. Consequently, in order to avoid being damaged, the crystal is permanently displaced vertically by a motorized stage. Behind the crystal, the beam is collimated and guided through the NC sample where it spatially overlaps with the pump beam. The focal spot of the probe beam is smaller than that of the pump beam, which has a diameter of around 650 µm. This allows for a more uniform excitation within the probe volume and also ensures that the full probe volume is being excited. As is known from above, the repetition rate of the amplifier is 1 kHz. In the TAS setup a chopper is installed in the pump beam path and operated at half of the laser frequency, i.e., 500 Hz. Accordingly, every second pump pulse is blocked and does not reach the sample. In the case a pump pulse is blocked, only the white light probe pulse reaches the sample, which creates a situation similar to that of Figure 3.7. The transmission spectrum behind the sample $I_{\mathrm{w/o\,pump}}(\lambda)$ is coupled into an optical fiber and measured in a spectrometer. In cases where the pump pulse is not blocked, the time delay between this initial pulse and the subsequent probe pulse is critical. The exact temporal overlap of both pulses in the sample is defined as the time $t_{\mathrm{delay}} = 0$. For any effect to occur, the pump pulse must arrive first. In this case, the pump pulse generates excited e-h pairs. With excited states being populated, the transmitted signal obtained of the subsequent probe pulse $I_{\mathrm{with\,pump}}(\lambda)$ is changed with respect to the aforementioned case without excitation $I_{\mathrm{w/o\,pump}}(\lambda)$. It will also change with the time delay between the pump and probe pulses due to dynamic effects like charge carrier thermalization or recombination.

The time delay between the pump and probe pulses is tuned via a linear delay stage which changes the path length of the probe beam. The setup is built in a way that the position $t_{\mathrm{delay}} = 0$ is achieved when the movable retroreflector mirror is close to the front of the motorized stage. This way a maximum delay between pump and probe pulse of up to $t_{\mathrm{delay}} = 3$ ns can be reached when moving the retroreflector mirror toward the end of the stage. The smallest step size the stage can be moved by relates to < 1 fs and therefore is small enough for the temporal resolution of the measurement not to be determined by the stage, but only by the pulse length of the pump and probe pulses. A huge advantage of using white light probe pulses is the simultaneous measurement of the charge carrier dynamics over a whole broad wavelength range without increasing the overall measurement time. However, similar to white light generation in the OPA, the different spectral regions within the white light pulse arrive at slightly different times at the sample, rendering the exact position $t_{\mathrm{delay}}(\lambda) = 0$ a function of the probed wavelength. This is referred to as the chirp and can be corrected in the postprocessing of the measurement data. Combining all of the above information one can determine the change in absorption $\Delta OD(\lambda)$ caused by the pump pulse for each individual stage position t_{delay}. Taking into account Equation 3.3 we obtain accordingly:

$$\begin{aligned}\Delta OD(\lambda) &= OD_{\text{with pump}}(\lambda) - OD_{\text{w/o pump}}(\lambda) \\ &= \log_{10}\left(\frac{I_{\text{w/o pump}}(\lambda)}{I_0(\lambda)}\right) - \log_{10}\left(\frac{I_{\text{with pump}}(\lambda)}{I_0(\lambda)}\right) \\ &= \log_{10}\left(I_{\text{w/o pump}}(\lambda)\right) - \log_{10}\left(I_{\text{with pump}}(\lambda)\right) \\ &= \log_{10}\left(\frac{I_{\text{w/o pump}}(\lambda)}{I_{\text{with pump}}(\lambda)}\right).\end{aligned} \tag{3.4}$$

It is interesting to recognize that the initial intensity of the probe pulse before it enters the sample (I_0) cancels out such that the change in absorption can be measured exclusively in terms of the two transmission spectra measured after the sample. However, for this to be accurate, the samples must be prepared so that their OD values lie between about 0.1 to 1 in the spectral region of interest.

The value $\Delta OD(\lambda)$ is usually calculated for two consecutive pulse pairs, such that a spectrum can be obtained every 2 ms. A time between two pulses of 1 ms is sufficient to allow all of the charge carriers to return back to their initial state, which also explains why a slow repetition rate is actually favorable for this type of experiment. Spectra can also be averaged over a longer time to reduce the noise. Also, $\Delta OD(\lambda)$ can be used to calculate the relative change in transmission $\Delta T(\lambda)/T_0(\lambda)$ when exploiting Equation 3.3 and Equation 3.4.

$$\begin{aligned}\frac{\Delta T(\lambda)}{T_0(\lambda)} = \frac{T(\lambda) - T_0(\lambda)}{T_0(\lambda)} &= \frac{\dfrac{I_{\text{with pump}}(\lambda)}{I_0(\lambda)} - \dfrac{I_{\text{w/o pump}}(\lambda)}{I_0(\lambda)}}{\dfrac{I_{\text{w/o pump}}(\lambda)}{I_0(\lambda)}} \\ &= \frac{I_{\text{with pump}}(\lambda)}{I_{\text{w/o pump}}(\lambda)} - 1 = 10^{-\Delta OD(\lambda)} - 1\end{aligned} \tag{3.5}$$

Therefore, TAS may also be referred to as differential transmission spectroscopy (DTS). Usually, the values obtained for $\Delta T(\lambda)/T_0(\lambda)$ during the course of this thesis were below 10 %, effectively rendering the relative change in transmission almost proportional to $\Delta OD(\lambda)$.

As mentioned earlier, the TAS setup was heavily modified in the course of the present work to enhance signal stability, to increase flexibility, and ease of use, as well as to enable new measurement options. In terms of the four components highlighted in Figure 3.8, these changes may be summarized as follows:

- **Pump Beam**
  Flip-mounts and magnetic feet were added to the arrangement in the pump beam to allow for an easy swapping between the OPA and SHG as the pump pulse source. For accurate TAS measurements with a low noise level, the pump power adjustment must be reliable and its stability over the whole measurement time has to be guaranteed. To this end, a new power meter was inserted directly into the setup. Via a newly-added motorized flip mirror, the power may also

be checked during the measurement. This power meter (*Newport*, *919E-20U-10-20K*) is especially suitable for femtosecond pulses. Regarding pump pulse stability, it has to be differentiated between short term fluctuations from pulse to pulse and more persistent drifts in the average power that develop over the course of several minutes. Two separate mechanisms have been integrated into the system to address these two types of fluctuations on different time scales. On the one hand, a small fraction of each pump pulse is directed onto a fast photodiode and the integrated signal is calculated for each individual pulse. If this value lies outside of a preassigned stability range, the single spectrum resulting from this pulse is discarded and thus will not contribute to the overall measurement. To address the second issue of drifts in the average power over a longer time scale, a computer-controlled motorized stage system was implemented in conjunction with a linear variable ND filter. It is noted that this approach was designed and developed in collaboration with Dr. Michael Fedoruk. With a feedback loop monitoring the pulse energy the ND filter can be adjusted to guarantee a constant value for the transmitted pulse energy through the ND filter. This system also includes two automated shutters at the pump and probe beam entrance of the TAS. In combination with the other upgrades they enable remote-controlled operation of power-dependent TAS measurements.

- **Probe Beam**
  Similar to the fast pump pulse correction on a pulse to pulse basis, a stability control mechanism for the white light was implemented, which checks the spectrum of each individual pulse in the reference channel. Typically, this excludes damaged spots of the white light crystal from the measurement since these usually cause fluctuations in the white light. Additionally, polarization optics (polarizers, half-wave plates and quarter-wave plates) on flip mounts were added to the path of the pump and probe beams, allowing pumping or probing with circularly polarized light.

- **Sample Position**
  A new manual xyz-stage was designed to enable rapid switching between cuvette and substrate sample holders. Furthermore, a closed cycle helium cryostat (Advanced Research Systems) was installed and can be directly placed at the sample position inside the TAS box. This way the temperature of the sample can be controlled as an additional measurement parameter. A PID temperature controller (*Lake Shore Cryotronics*, *Model 335 Cryogenic Temperature Controller*) was used to tune the temperature of the sample mounted at the cryostat finger to values between 4 K and 350 K.

- **Detection**
  The original detection unit was completely replaced. In the modified setup, a dual optical fiber connected to a spectrometer (*Newport*, *MS260i*) with three gratings is used for detection. The white light probe beam is split into two parts, with the first part passing through the sample and its transmitted signal coupled into the first fiber. In contrast, the second beam is coupled directly into the second fiber and serves as the reference channel. Within the spectrometer these two input signals travel parallel to each other along the same path, but at different heights. Both signals are guided onto two separate CCD cameras operating in the visible range. Consequently, it can be determined whether fluctuations in the transmitted pulse spectrum stem from the white light itself or from effects occurring within the sample. Furthermore, optical filters in each of these beams and a near-infrared camera attached to the spectrometer enable measurements at longer wavelengths.

Additionally, the software had to be adapted several times in collaboration with *Newport* to account for the mentioned new features. Thanks to these changes it is now also possible to directly determine the linear absorption with the TAS system.

3.3.3 Photoluminescence

After having studied absorption and its associated measurement techniques in detail we now turn to the processes that follow the generation of an electron-hole (e-h) pair via absorption. In particular, this subsection deals with the detection of radiative — as opposed to nonradiative — recombination known as photoluminescence (PL). This interband relaxation mechanism already has been introduced in Figure 2.8.

Steady-State Photoluminescence

Steady-state PL spectra already contain important information on the investigated perovskite NCs. In this context it is important to note that — similar to when measuring absorption — usually thousands of NCs are examined simultaneously such that the measured properties are associated with an ensemble of NCs rather than an individual NC (cf. Subsection 2.2.3). At any rate, the accessible wavelength range may be learnt from emission spectra. Moreover, an emission spectrum will usually show one or more dominant peaks. The width of single peaks or the presence of multiple peaks in itself may serve as an indicator for the homogeneity of the NCs. In general, a strong PL signal hints at a direct band gap semiconductor material, which is the case for lead-halide perovskite NCs. However, the strength of the signal is also influenced by the number of defects within the NCs. Further information on the potential band structure can be gained by evaluating the Stokes shift of the emission compared to the absorption onset.[175]

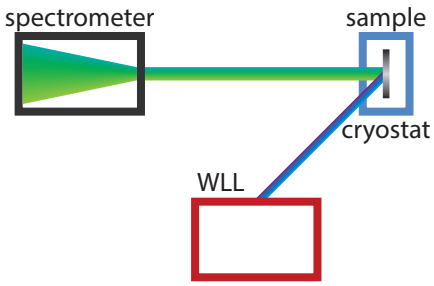

Figure 3.9: Scheme of the PL Setup. With its remarkable tunability and precise power control, the WLL serves as a reliable source for pulsed excitation of the NC sample mounted within a cryostat. Optical filtering before and after the sample ensures that only the PL generated in the sample actually enters the spectrometer where the corresponding PL spectra are recorded.

For this thesis, two devices were used to measure PL spectra, the commercial system *Fluorolog-3 FL 3-22* by *Horiba* and a custom, more versatile setup. The latter can be used in different operation modes, and in the passages accompanying Figure 3.7 it was already described how this was used to determine absorption spectra. Figure 3.9 shows a different configuration of this setup with which PL spectra were recorded. The wavelength of the WLL was set to excite the NCs above the band gap, with the excitation spectrum not overlapping with the PL emission of the sample. The geometry of the setup is devised to illuminate the sample at an angle, which prevents reflections of the excitation beam from reaching the spectrometer. Moreover, filtering before and after the sample helps to isolate the

PL signal which is collected by an objective (*Olympus*, *SLCPLFL 40x/0.55*) in proximate distance to the sample surface. The collimated PL signal was guided through a telescope and focused onto the entrance slit of the spectrometer whose width in turn controls the spectral resolution of the system. An appropriate grating was chosen to fill the whole area given by the bins of the peltier-element cooled CCD camera inside the spectrometer.

Depending on the purpose of a spectroscopic study either the wavelength or the photon energy is the proper choice for the x-axis in the evaluation process. By default, the saved spectra recorded with CCD cameras consisting of equally spaced bins are in the format "intensity versus wavelength". When plotting PL data on an energy scale, this intensity $I(\lambda)$ of the emission spectra has to be transformed due to the inverse relation of energy E to wavelength λ and the energy conservation of the energy incident on one bin of the camera

$$I(E)\mathrm{d}E = I(\lambda)\mathrm{d}\lambda\,. \tag{3.6}$$

Plugging the photon energy $E = hc/\lambda$ into this equation leads to the formula for the correct conversion to the format "intensity versus photon energy".[173]

$$I(E) = I(\lambda)\frac{\mathrm{d}\lambda}{\mathrm{d}E} = I(\lambda)\frac{\mathrm{d}}{\mathrm{d}E}\left(\frac{hc}{E}\right) = -I(\lambda)\frac{hc}{E^2} \tag{3.7}$$

In contrast, there is no need to do so for absorption spectra, since the correction term cancels out in the definition of optical density (cf. Equation 3.3). The algebraic sign in Equation 3.7 may simply be neglected, as it only reflects the different directions of integration in wavelength and photon energy. Parameterizing spectra in this way in combination with cryogenic measurments enabled studies on the influence of the temperature on the emission linewidth. Cooling down to temperatures around 10 K using the liquid helium cooled cryostat reduces homogeneous broadening, thereby rendering the inhomogeneous broadening dominant. Measurements at several temperatures between this low end and room temperature enabled the examination of exciton-phonon interactions. For this purpose, a *MATLAB* script was programmed for the plotting, fitting and evaluation of this data. As in the absorption data, also temperature-dependent shifts of the emission peak can be detected and depending on the perovskite composition, phase transitions may be observed as well.

Photoluminescence Quantum Yield

The photoluminescence quantum yield (PLQY) indicates the efficiency at which a sample re-emits absorbed photons, or more generally speaking to which degree a sample tends to perform radiative recombination. A high PLQY value is of substantial interest for the active layer material within LEDs, where the overall energy conversion efficiency η_{total} is directly proportional to the PLQY η_{PLQY}.[176]

$$\eta_{\mathrm{total}} = \eta_{\mathrm{feed}} \overbrace{\underbrace{\eta_{\mathrm{inj}}\,\eta_{\mathrm{PLQY}}}_{\eta_{\mathrm{IQE}}}\,\eta_{\mathrm{extr}}}^{\eta_{\mathrm{EQE}}} \tag{3.8}$$

The total efficiency η_{total} of an LED determines the optical output power of the device relative to the electrical input power (this is also referred to as the wall-plug efficiency). It differs from the external

quantum efficiency (EQE ≙ # of photons emitted by the LED / # of electrons passing through the LED) by the factor η_{feed} which is in turn determined by the voltage drop due to the series resistance of the device. The EQE is given by the product of the three factors of the injection efficiency η_{inj} (≙ # of electrons injected into the active region / # of electrons passing through the LED), the PLQY η_{PLQY} (≙ # of photons generated in the active region / # of electrons injected into the active region) and the extraction efficiency η_{extr} (≙ # of photons emitted from the LED / # of photons generated in the active region). The first two factors denote the so-called internal quantum efficiency (IQE). The quantities η_{feed}, η_{inj} and η_{extr} are largely dictated by the device architecture. In contrast, η_{PLQY} is only dependent on processes occurring in the active layer, thus being a good indicator of the suitability and quality of the active layer material. Accordingly, one goal of our research was to synthesize an active layer made of perovskite NCs with the highest possible PLQY.

The charm about this is that the active layer simply can be deposited onto a substrate all by itself in order to study the PLQY independently. In this scenario electrons and holes are "injected" into the NC layer by light absorption. For this measurement the *Fluorolog-3 FL 3-22* spectrometer in combination with an integrating sphere was used. The excitation photon energy is set to be above the band gap and spectrally well separated from the PL peak. The integrating sphere collects all of the light trapped inside of it and collectively sends it to a monochromator that scans the whole spectral range of interest in order to record a spectrum. The spectrum of a substrate with the NC layer is compared to a spectrum of a completely empty substrate. Subtracting the latter from the former allows for the calculation of the PLQY via

$$\eta_{\text{PLQY}} = \frac{\#\text{ of emitted photons}}{\#\text{ of absorbed photons}} = \frac{\int N_{\text{em}}(\lambda)\,\mathrm{d}\lambda}{\int N_{\text{abs}}(\lambda')\,\mathrm{d}\lambda'} \tag{3.9}$$

since the absorption and emission occur in two different non-overlapping wavelength regions.

Alternatively, in contrast to this absolute measurement there is a second approach to determine the PLQY by a relative comparison to known fluorescent dye solutions like Coumarin 47 or Coumarin 102.

Time-resolved Photoluminescence

Finally, we turn to a third and last configuration of the previously mentioned self-built spectroscopy setup. An expansion of the PL setup enables time-resolved PL measurements based on the principle of time-correlated single photon counting (TCSPC).[177,178]

To this end, and as shown schematically in Figure 3.10, there is an additional avalanche photodiode (APD) as well as a computer, which receives the APD signal and a trigger signal coming from the WLL excitation source. This further modified system (*PicoQuant, TimeHarp 260 pico*) enables the measurement of the population decay of excited e-h pairs by counting events of single photons. Therein, the spectrometer actually acts as a monochromator. Instead of measuring the full PL emission signal with help of a CCD, it permits only a narrow wavelength band — usually corresponding to the center of the PL peak — to exit the device and hence be detected on the adjacent APD. Put simply, the computer and the corresponding electronics act like a stop watch. Every time the WLL sends an excitation pulse to the sample, it simultaneously transmits a trigger signal to the computer representing the "start" of the stopwatch. This laser pulse then generates excited e-h pairs in the sample, which in turn may recombine radiatively. The APD can then detect photons produced by recombination and

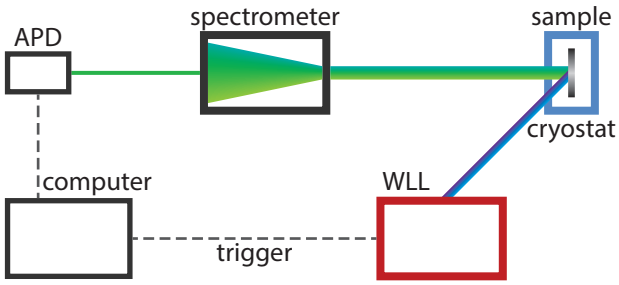

Figure 3.10: Scheme of the TCSPC Setup. In this specific configuration of the more general PL setup discussed earlier, a computer measures the lifetime of excited e-h pairs by measuring the duration between the point in time when the excitation pulse is sent out and the point in time when a PL signal caused by this excitation is detected by the avalanche photodiode (APD). Given sufficient time between two subsequent pulses and low excitation powers, a histogram of numerous measured lifetimes reflects the actual decay of the excited e-h pair population.

accordingly tell the computer to "stop" the clock. The timespan between "start" and "stop" is recorded. This process is repeated for a large number of events and a histogram of events versus this measured time is created.

Two conditions must be met in order for this histogram to represent the actual excited population decay dynamics of the investigated sample. Firstly, the time between two subsequent excitation pulses must be sufficiently long to make it very likely for an eventually excited e-h pair to return to its ground state before the second of the two pulses reaches the sample. This may be controlled using the tunable repetition rate of the WLL. Secondly, it is crucial to avoid high excitation powers that would effectively lead to two or even more detected photons per excitation pulse. In this case, only the first pulse would be detected and the others would be lost leading to an undesired overrepresentation of events at shorter times, i.e., the actual process would not be represented truthfully. Since excitation is a probabilistic process, the laser power needs to be reduced to a level at which for most excitation pulses actually nothing is detected at all — a photon should only be detected in 1–5 % of all excitation events. In return, chances are high that such detected signals indeed correspond to single photon processes.[177]

The overall timing precision of a TCSPC system is also known as the instrument response function (IRF). With infinitely short excitation pulses and an infinitely accurate detector as well as infinitely fast electronics, the IRF would be vanishingly small. However, exactly these factors induce a broadening of the IRF and thus limit the temporal resolution of the measurement as a whole. In the case at hand, mainly the pulse length of the WLL (80–100 ps) and the response of the electronics limit the resolution of the TCSPC setup, thus excluding its use for the study and observation of ultrafast processes happening almost instantaneously after the excitation. Higher temporal resolutions in PL measurements can be achieved with streak cameras or setups based on fluorescence upconversion. These could also resolve ultrafast processes like exciton-exciton annihilation. However, in this thesis the TAS and the four-wave mixing setups were used for the observation of ultrafast processes with a temporal resolution in the femtosecond region.

3.3.4 Four-Wave Mixing

Section 2.4 covered the quasi-instantaneous excitation of a NC ensemble with an ultrashort laser pulse. This leads to a coherently oscillating polarization of e-h pairs within the excited volume. Due to scattering — mainly either with phonons or with other excited e-h pairs — individual e-h pairs can get out of phase leading to a decay of the overall coherence of the oscillations. This loss of coherence is referred to as dephasing and it can be measured via degenerate transient four-wave mixing (FWM).[76]

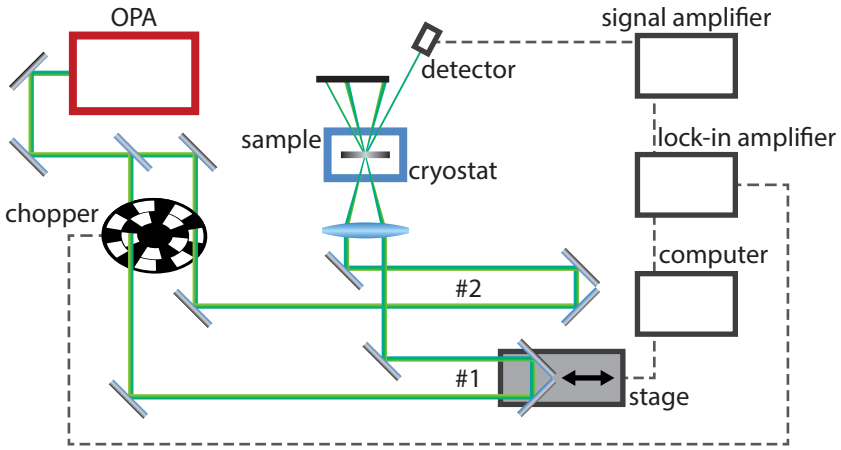

Figure 3.11: Scheme of the Four-Wave Mixing Setup. Two femtosecond pulses originating from the same tunable OPA are focused onto a perovskite NC film mounted in a cryostat. One of these pulses is guided through a motorized linear delay stage which enables the control of the time delay between the two pulses in the focal spot on the sample. If spatial and temporal overlap of the two pulses is achieved, FWM can be detected and recorded as a function of this time delay between pulse #1 and #2. A signal amplifier in combination with a lock-in amplifier connected to a chopper helps to enhance the weak FWM signal.

A FWM setup was built from scratch in order to run this experiment and to determine the dephasing time of excitons. A schematic of this setup is shown in Figure 3.11. Depending on the excitation wavelength, either excitons, free e-h pairs or both simultaneously can be excited. Therefore, the amplifier system in combination with the OPA was used as a laser source, allowing for tunable ultrashort excitation pulses. As explained in Figure 2.17, the technique itself relies on a spatial and temporal overlap of two pulses with wave vectors $\mathbf{k}_1$ and $\mathbf{k}_2$, respectively, on the sample. There, a FWM signal is created and travels in the directions of $2\,\mathbf{k}_2 - \mathbf{k}_1$ and $2\,\mathbf{k}_1 - \mathbf{k}_2$.[179,180] To achieve this, a 50:50 beam splitter is employed, splitting every initial pulse from the OPA into two. From there, pulses #1 and #2 travel separate paths and coincide again when being focused through the same lens (f = 200 mm) onto the examined sample at an angle of 6.8° between the two beams (see Figure 3.11). For the adjustment of the spatial overlap a flip mirror is placed in close proximity to the sample in front of the cryostat. When using it the two beams are directed onto a beam profiler (*DataRay, WinCamD-UCD12-1310*) that helps to find the exact overlap of the two Gaussian-shaped beams. Then, temporal overlap of both pulses is tuned by the computer-controlled linear stage with a retroreflector mounted on top of it, changing the path length for one of the pulses as the stage moves. Depending on the excitation power even higher orders of the FWM signal may be observed, but this lies beyond the scope of the present study. Here, only the signals at $2\,\mathbf{k}_2 - \mathbf{k}_1$ or $2\,\mathbf{k}_1 - \mathbf{k}_2$ were accounted for. In principle, the polarization of the pulses matters also,[181–183] but in these studies s-polarization for both beams was used exclusively.

The samples comprised ensembles of various lead halide perovskite NCs. That being said, the main results stem from experiments on $MAPbI_3$ NPls. These NCs were deposited on a sapphire substrate and the amplitude of the FWM signal was recorded as a function of the time delay t_{delay} between the two pulses #1 and #2. The exact temporal overlap of the two pulses is defined as the time delay $t_{\mathrm{delay}} = 0$. In case $t_{\mathrm{delay}} > 0$ pulse #1 hits the deposited NCs before pulse #2. Conversely, for $t_{\mathrm{delay}} < 0$, it is the other way around. In order to determine the stage position for which $t_{\mathrm{delay}} = 0$ accurately, the FWM signals in the directions of $2\,\mathbf{k}_2 - \mathbf{k}_1$ and $2\,\mathbf{k}_1 - \mathbf{k}_2$ were compared as their dephasing behavior has to be symmetric in relation to this position.

As mentioned above, the decay of the measured FWM signal is caused by scattering events. Thus, reducing the amount of scattering events can significantly increase the dephasing time. Consequently, compared to other quantities, the dephasing time T_2 is not a material constant, but a function of temperature and excitation density. In the FWM experiments carried out for this thesis the dephasing times turned out to be extremely short. In order to detect and resolve the dephasing signal at all, the three following measures needed to be implemented:

- **Reducing the Temperature**
  The extent of scattering with acoustic and optical phonons depends on the sample temperature. Therefore, reducing the temperature leads to longer dephasing times. To this end, the sample on its substrate was inserted into a liquid helium cooled cryostat and most transients were recorded in the low temperature regime of $T \leq 25\,\mathrm{K}$.

- **Reducing the Excitation Density**
  Mathematically speaking, the detected FWM signals are based on a third-order nonlinear process. Thus, the amplitude of the signal strongly depends on the pulse energy of the two interacting pulses such that using more power makes it easier to find the FWM signal and the correct spatial and temporal overlap. Moreover, the signal-to-noise ratio (SNR) benefits from higher pulse energies, as well. At the same time, this also leads to increased excitation densities and thus more scattering between the excited e-h pairs, thereby effectively shortening the dephasing time. Additionally, too strong excitation may harm or even destroy the NCs at some point. Furthermore, nonlinear effects of even higher order become more prominent at higher powers, altering the detected transient signal. Consequently, this effect should be avoided.

  The relevant excitation density not only relies on the input power, but also on the excitation volume of the beams inside the sample. Depending on the excitation wavelength, the focal spot has a diameter of around 100 µm and the thickness of the deposited NC film lies in the range of several hundreds of nanometers, as determined by a *Dektak* profilometer. To control the laser intensity, a variable ND filter wheel is placed in each of the beam paths to reduce the excitation density to values of $\leq 10^{17}\,\mathrm{cm}^{-3}$. This range results in a reduced SNR, but makes the FWM decay long enough to be temporally resolvable while avoiding higher order nonlinear processes. Summing up, the adjustment of the excitation density is a delicate procedure. The right balance between a sufficiently strong signal and a low enough excitation density has to be found to avoid the temporal resolution being too coarse to capture the dephasing process.

- **Reducing the Pulse Length**
  This brings us to the last point which is the temporal resolution of the FWM setup. As described before, low temperatures and excitation densities lead to longer dephasing times. However, even

in this case it is important that the temporal resolution is small enough to resolve the ultrafast processes that occur in the system. In principle, this resolution depends on two factors, the smallest step size of the linear motorized stage and the pulse length of the two identical pulses #1 and #2. The linear stepper stage (*Newport*, *FCL 100*) has a minimum incremental motion of only 150 nm which translates to a time difference for the traveling light pulse of less than 1 fs. Thus, effectively only the pulse length determines the temporal resolution of the setup and should consequently be kept as short as possible. An optical autocorrelator (*pulseCheck*, *A·P·E*) was employed to determine the pulse length at several positions within the setup. At the exit of the OPA, the pulse has a length of about 90 fs, but each transmissive optical element contributes to the overall group delay dispersion of the pulse such that the pulse gets longer and longer on its way to the sample. Accordingly, in order to keep the pulses as short as possible, the number and thickness of transmissive optical elements were reduced wherever possible. This way, at the critical position, i.e., on the sample surface, the pulse length could be minimized to a value of about 115 fs. This optimization process was supported by dispersion simulations with the *LabVIEW* add-on *Lab2* for calculations with femtosecond pulses.

All of the three measures detailed above were taken to achieve a sufficiently long, resolvable FWM signal. To record this trace of the FWM signal versus time delay, a time-integrated detection scheme was employed.[180] Therein, the beam in the direction of $2\,\mathbf{k}_2 - \mathbf{k}_1$ is guided onto a photo detector (*Thorlabs*, *DET210*) and the electric signal outputted by this detector is amplified (*Stanford Research Systems*, *SR570*). An optical chopper (*Newport*, *Optical Chopper Model 3501*) modulates each beam path with a different frequency. Eventually, a lock-in amplifier (*Stanford Research Systems*, *SR830*) further amplifies the signal at the difference frequency of these modulations, guaranteeing that the observed signal stems from both pulses and is not just representative of some scattering effects of one single pulse.[184] In all of this, a crucial part is to choose the parameters for the lock-in amplifier appropriately since wrong integration settings can change the whole shape of the detected curve.

In addition, the communication between all of these individual parts has to be well synchronized and controlled. For this purpose a *LabVIEW* program was developed that helped in finding the signal, changing the measurement parameters, observing the running measurement, recording and saving the data as well as the documentation.

3.3.5 Diffusion

In the final part of this thesis the diffusion of excitons in NC arrangements is studied. Information on charge carrier diffusion processes was gained using two different setups. The first one is the TAS setup that was already explained above. Therewith, layer-by-layer structures consisting of a $CsPbBr_3$ NC layer of varying thickness adjacent to a fullerene-based layer of strong electron acceptors were studied upon excitation with femtosecond pulses at 400 nm. The transients of the differential signal corresponding to the electron-hole pair population within the perovskite NC layer exhibit different decay behaviors for a decreasing NC layer thickness due to the reduced distance to the fullerene layer, where the excited electron can be extracted from the NC layer.

At the end of this chapter the second setup that was used to measure diffusion processes is introduced. I worked with this system during my research stay in the *Molecular Foundry* at the *Lawrence Berkeley National Laboratory*. Different from the TAS setup, this setup relies on the observation and mapping

of PL. The underlying working principle is described in simple terms in Figure 3.12. One of the key factors in this setup is to focus the excitation beam accurately in order to achieve a Gaussian shaped diffraction-limited spot on the sample. Actually, the intensity profile is an airy disk function with most of the intensity in the center which can be approximated by a Gaussian profile. Three different laser sources can be applied: a CW source, a pulsed source or a WLL similar to the one described in Subsection 3.2.3. The CW source has a fixed wavelength of 450 nm and is only used for steady-state PL measurements. A pulsed source with a wavelength of 405 nm and a tunable repetition rate (*Thorlabs, NPL41B*) additionally enables time-resolved measurements in combination with an APD and integrated TCSPC setup (*PicoQuant*), however, the pulse length of 6 ns strongly limits the time-resolution of the measurement. Finally, the WLL offers a tunable wavelength with pulse lengths in the picosecond regime, but with a fixed repetition rate of 40 MHz.

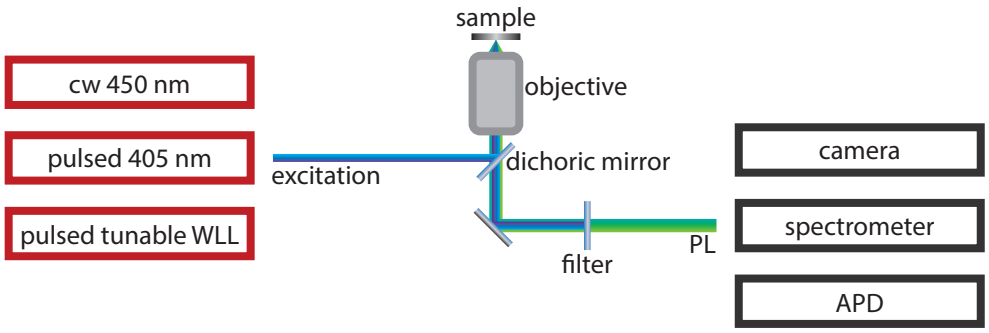

Figure 3.12: Scheme of the Exciton Diffusion Setup. The shown PL setup relies on excitations induced by a diffraction-limited spot on the sample for which various excitation laser sources can be chosen. As the excited e-h pairs diffuse before they recombine, the resulting PL profile is larger than the (approximately) Gaussian excitation. The PL profile may be recorded as an intensity map using a camera. Alternatively, the PL spectrum or the temporal decay of the e-h pair population can be measured with a spectrometer or an APD, respectively.

Upon excitation the e-h pairs can diffuse within a NC or hop to adjacent NCs. The lifetime of the excitations determines the time scale of this process and when an e-h pair recombines radiatively, the setup can detect where it ended up. Of course, this is done with many photons simultaneously such that corresponding statistics provide insights on the diffusion process in the investigated NC system. We refer to this setup as the exciton diffusion setup .

In the actual experiments, a 100x objective in combination with a suitable dichroic mirror was used simultaneously for both, the excitation of e-h pairs and the collection of the PL signal. The sample with the NCs was mounted on a computer-controlled xyz-stage. The z-direction was used for the fine adjustment of the focus and the xy-plane was scanned in order to reduce the potential damage of the laser on the sample . Along the detection path either a shortpass or a longpass filter was placed depending on whether the excitation spot or the resulting PL signal was supposed to be observed. Right behind the filters, flip mirrors guided the signal either to a high-resolution CCD camera, a spectrometer or an APD. The sensitive camera saved an image of the whole sample surface close to the excitation spot, wherein one pixel corresponded to 8.6 nm. In this general mode of operation, the spectrometer or the APD can give access to the overall spectrum of all pixels or to the respective e-h pair population decay. Alternatively, there is a specialized mode in which a fiber scans the image plane of the optical system. The end of this fiber can either be connected directly to the spectrometer or to the APD, yielding insights into the respective properties of only a certain, quite small portion of the sample (corresponding to an area of only a few pixels of the camera).

4

Recombination

The following chapter contains those results of the research conducted for this thesis that may be subsumed under the term recombination. The corresponding interband relaxation of e-h pairs and excitons in particular was studied for the case of quantum-confined $CsPbBr_3$ nanoplatelets with a tunable thickness. First and foremost, this material was characterized and specifically modified in order to obtain an efficient blue emitter suitable for the use in LEDs. To this end, nonradiative recombination within the NCs had to be suppressed and, moreover, a precise thickness control of the platelets opened the door for emission wavelength tunability. For the subsequent second section exciton-exciton annihilation as well as monomolecular recombination of excitons was studied by means of time-resolved spectroscopy.

4.1 Boosting Tunable Blue Luminescence

Shortly after the introduction of LHPS as promising material for solar cells,[8–10] NCs of the same perovskite structure began to garner strong interest for light-emitting applications due to their high photoluminescence quantum yields (PLQYs) and their emission wavelength tunability via halide ion exchange.[11,17,185]

In general, one of the most decisive breakthroughs in the development of LEDs came with the controlled epitaxial growth and p-type doping of GaN in the late 1980s.[186,187] This technique paved the way for the large scale production of blue LEDs and also enabled the first commercial white LEDs after red and green LEDs already had been established years before that.[188] As a consequence, the Nobel Prize in Physics 2014 was awarded "for the invention of efficient blue light-emitting diodes which has enabled bright and energy-saving white light sources".[189]

Interestingly, the development of LEDs based on LHP NCs seems to follow a similar trajectory in the sense that long-term colloidal stability and high quantum yields have already been achieved for NCs emitting in the red and green spectral range. However, the blue region has lagged behind due to insufficient colloidal stability, low quantum yields, and broad emission profiles.[20] Generally, a suitable material for the active layer in LEDs should feature the following properties: (i) low priced and easy synthesis routine, (ii) emission wavelength tunability, (iii) efficiency and (iv) stability.

The following section is mainly based on the work presented in Reference [20] and is intended to address the challenges of improving blue light-emitting LHP NCs. Therefore, the aforementioned four properties will be addressed one by one.

4.1.1 Photoluminescence and Linear Absorption

Generally speaking, there are two ways to achieve blue emission using LHP NCs. The first option involves halide ion exchange based on Cl, such that for example $CsPbCl_3$ or mixed $CsPbBr_xCl_{(3-x)}$ may be obtained starting from non- or only weakly confined $CsPbBr_3$ NCs.[21] On the other hand, blue emission of LHP NCs may also be achieved via quantum confinement of NCs, generally leading to blue-shifted emission and absorption (cf. Subsection 2.1.4).[19]

The first approach via halide ion exchange with Cl results in poor performance in the blue spectral range and mixed-halide perovskites $CsPbBr_xCl_{(3-x)}$ tend to undergo phase segregation such that the emission wavelength broadens and shifts over time.[190] Therefore, the option chosen within this work rather leverages quantum confinement starting from $CsPbBr_3$ NCs which in their bulk form emit green light. To this end $CsPbBr_3$ nanoplatelets (NPls) with a variable thickness were synthesized, as explained in Subsection 3.1.1. These NPls already fulfill the first requirement, i.e. property (i), for a promising LED material since colloidal synthesis of NCs enables a low priced and easy synthesis compared to other semiconductor emitters that for example rely on expensive epitaxial growth techniques. STEM studies on these $CsPbBr_3$ NPls revealed their uniform thickness, controllable via the Cs/Pb ratio given by the amounts of precursors (see Figure 3.1). This kind of characterization using electron microscopy already led to the assumption that the thickness of these NPls may be controlled with atomic precision such that each sample of NPls dispersed in a cuvette only contains NPls with the same number of monolayers (MLs).

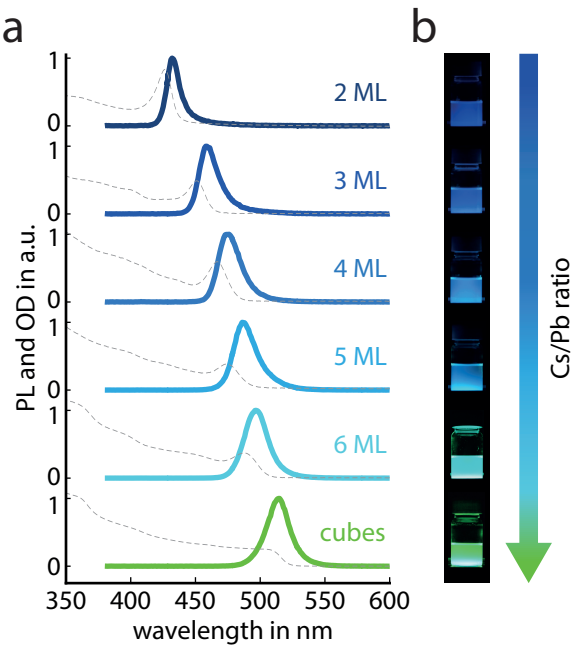

Figure 4.1: Photoluminescence of $CsPbBr_3$ Nanoplatelets. (a) Normalized PL spectra (solid lines) of $CsPbBr_3$ NPls for varying NPl thickness. Absorption spectra (dashed lines) are plotted as well to illustrate the small Stokes shift of the PL. The respective plots for weakly confined $CsPbBr_3$ nanocubes are also shown for comparison. **(b)** Photographs of cuvettes containing the colloidal NPl dispersions illuminated with UV light. A steady redshift with increasing Cs/Pb ratio can be observed, i.e., the thinnest NPls exhibit dark blue emission while the cubes emit green light.

In order to confirm this assumption, optical linear spectroscopy was employed to probe the PL and absorption spectra of each NPl dispersion at room temperature. The respective PL spectra for the NPls (2–6 ML) as well as, for comparison, that of weakly confined nanocubes are plotted in Figure 4.1 a. There are no indications of double peaks or shoulders within these plots and each of the PL spectra exhibits only a single narrow peak with FWHM values as low as 11 nm. Therefore, this confirms the hypothesis that the synthesis routine results in NPls of uniform thickness. The central PL emission peak position blueshifts from 515 nm (cubes) to 432 nm (2 ML) with decreasing NPl thickness which also may be observed in the photographs of these NPls dispersions under UV light exposure (see Figure 4.1 b). The absorption spectra have been included in Figure 4.1 a as grey dashed lines and follow the same trend regarding the blueshift. The Stokes shift of the PL compared to the absorption onset lies in the range of 6–10 nm. Moreover, it can be observed that the excitonic peak at the absorption onset grows more dominant for thinner NPls.

In order to take a more detailed look at the absorption spectra, they have been plotted in Figure 4.2 a normalized with respect to this exciton peak. Since the spectra were acquired at room temperature, the emergence of the excitonic peak signifies that the exciton binding energy E_B increases with decreasing NPl thickness. The thinner the NPls, the smaller the probability that the thermal energy suffices to dissociate excitons. The figure also reveals additional shoulders in the absorption spectra emerging at higher energies within the continuum. These originate from transitions between energetically higher (lower) bands for the electrons (holes) in the CB (VB), respectively. Interestingly, however, the absorption plots clearly show the trend that for energies above the continuum onset the spectra get flatter and flatter when reducing the NPl thickness. This shows the smooth transition from a 3D material to a 2D material and can be compared to the theoretical density of states for such cases (cf. Figure 2.3 c). However, in the following we solely focus on the absorption onset with the excitonic

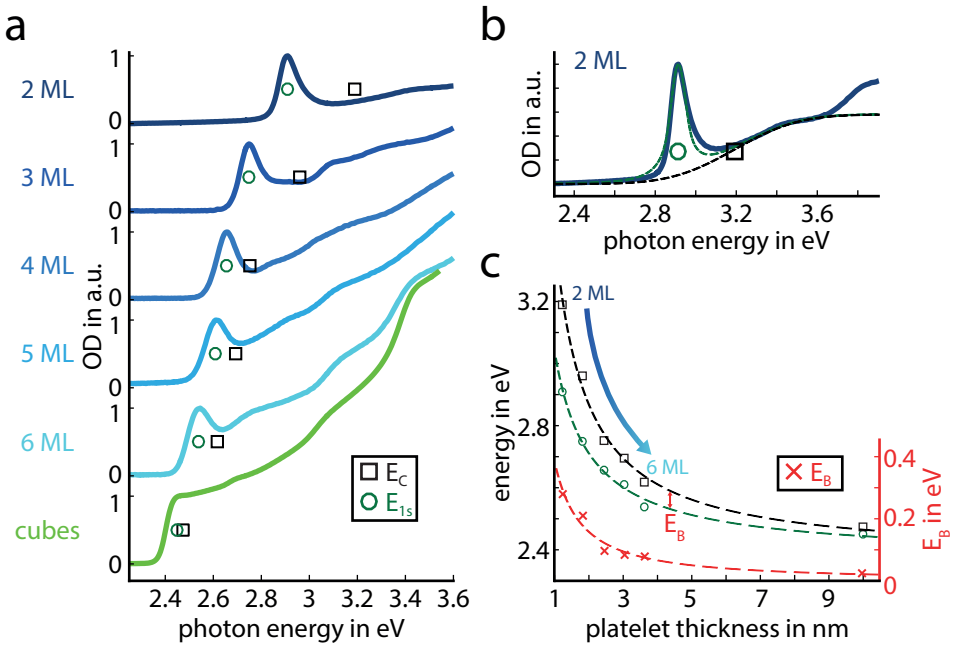

Figure 4.2: Absorption of $CsPbBr_3$ Nanoplatelets. (a) The absorption spectra normalized with respect to the exciton peak reveal how this very peak gains in dominance for thinner NPls. Black squares indicate the continuum onset E_C, whereas green circles show the corresponding energetic position of the exciton transition E_{1s} for each sample. **(b)** Modification of the Elliott model (dashed green line) applied to extract the positions E_C and E_{1s} from the experimental data (solid curve, in this case 2 ML). The dashed black line shows the contribution of the continuum states. **(c)** The respective values obtained in this manner versus the NPl thickness. The difference $E_C - E_{1s}$ corresponds to the exciton binding energy E_B (red crosses), which increases significantly with decreasing NPl thickness. Dashed lines serve as guides to the eye.

resonance and the continuum onset and these energetically higher transitions are not considered further.

As mentioned before, quantum confinement causes the observed blueshift for thinner NPls. In Subsection 2.1.4 it was already explained how this effect leads to an increase — and therefore blueshift — of the continuum onset E_C as both the electron and the hole are confined within the NC, i.e., $E_C = E_G + E_e + E_h$. At the same time, the exciton binding energy E_B increases, basically inducing a shift in the opposite direction for the exciton peak and the PL. However, since a blueshift is observed eventually, the increase of E_B must be smaller than the decrease of E_C.

To gain a deeper insight into this behavior, the experimentally measured absorption onset was fitted with a theoretical model closely related to the Elliot model as introduced in Subsection 2.1.3.[26,191] Figure 4.2 b shows how this model enables the extraction of the dominant exciton transition energy E_{1s} (green circles) and the continuum absorption onset E_C (black squares) for the 2 ML case. Accordingly, these values could be obtained for all samples. They are also plotted with their respective markers in Figure 4.2 a and c.

In Chapter 2, we learned that these values are needed to calculate the exciton binding energy $E_B = E_C - E_{1s}$. This difference is also added to Figure 4.2 c, marked by red crosses. Here, one observes an increase of E_C, E_{1s} as well as of E_B with reduced NPl thickness. For the thinnest NPls, E_B reaches a value of 280 meV, which is almost ten times the value for nanocubes of the same composition ($CsPbBr_3$). To understand this significant change, one has to take a look at the exciton Bohr radius a_{ex}, for which a value of 7 nm has been reported for bulk $CsPbBr_3$.[192] As shown in Figure 4.2 c, the NPls (2–6 ML) are thinner than the exciton Bohr radius and therefore fall into the so-called strong

quantum confinement regime, whereas the cubes with a larger edge length are assigned to the weak confinement regime.[192] Previous works have reported that the extraction of the exciton binding energy E_B from absorption data is prone to fitting errors in the case of bulk LHPs.[53] However, since the examined NPls fall into the region of strong confinement, a clearly separated excitonic peak may be observed even at room temperature. This leads to significantly more reliable values obtained through the fitting procedure.

High exciton binding energies leading to the presence of excitons instead of free e-h pairs may also be beneficial for radiative recombination within the LHP NPls since electrons and holes have to stay together for this type of interband relaxation. Summing up, the above mentioned criterion (ii) — emission wavelength tunability — can be achieved through employing confined LHP NPls.

4.1.2 Photoluminescence Quantum Yield and Trap Repair

This brings us to property (iii), efficiency. As already shown, the NPl dispersions exhibit narrow emission spectra, however, their emission intensity seemed to be relatively low, especially for the thinnest NPls. To study this quantitatively, the PLQYs were determined experimentally for all NPl samples (see open black squares in Figure 4.3 c). As a matter of fact, the obtained PLQY values for the 2 ML and 3 ML samples only amount to (7 ± 1) % and (9 ± 1) %, respectively. The PLQY values increase with NPl thickness, but only the thicker 6 ML NPls possess a value above 40 %. Clearly, these PLQY values are not satisfactory for the use of LHPs as efficient emitters. Low PLQY values like these are probably the result of surface trap states lowering the rate for radiative recombination and have been observed before.[193] This would also explain why the thinnest NPls with the highest surface-to-volume ratio exhibit the lowest PLQYs.

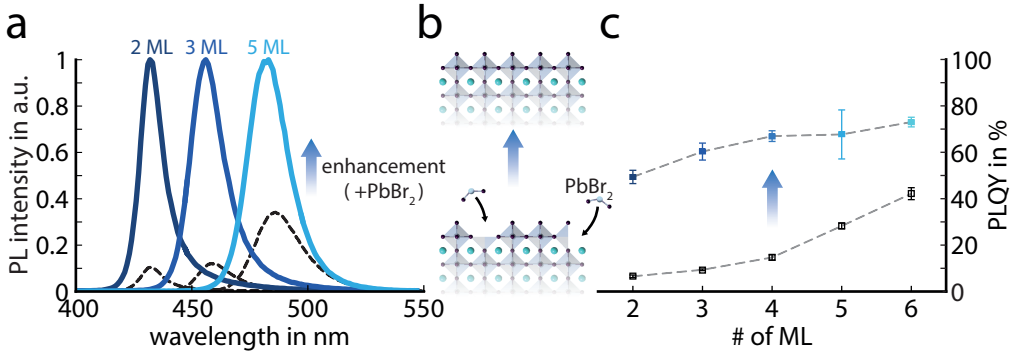

Figure 4.3: Photoluminescence Enhancement Through Surface Trap Repair. **(a)** PL spectra of initial NPl dispersions (black dashed lines) and the respective enhanced samples (normalized, solid lines). **(b)** A chemical post-treatment with a $PbBr_2$ solution initiates the repair process of surface defects on the $CsPbBr_3$ crystals. **(c)** PLQYs of the initial NPl ensembles (open black squares) and the respective dispersions after the enhancement process (full blue squares). For each data point $n \geq 6$ values have been averaged. Dashed lines are added as guides to the eye.

One of the main results of this research project is the discovery that the addition of a $PbBr_2$-ligand (oleic acid and oleylamine) hexane solution to the previously prepared NPl dispersions leads to a dramatic increase of the PLQYs. When initiating this postsynthetic treatment of the colloidal NPls, the PL signal immediately gets much stronger, which is shown in Figure 4.3 a where PL spectra before and after such enhancement process are compared to each other.

What happens on the microscopic level is illustrated in Figure 4.3 b. The added enhancement solution containing $PbBr_2$ has the potential to repair Br and Pb vacancies at the surface of the NPls. Thereby, the surface becomes uniform and the common ligands form a homogeneous passivation layer around the NPl. Defects usually create channels for nonradiative recombination of e-h pairs. Therefore, the repair process, reducing the total amount of defects, suppresses nonradiative recombination, enhancing radiative recombination.

The mentioned repair process with the concomitant enhancement of the PL is effective for all NPl samples. The PLQY measured after the treatment reaches values between (49 ± 3) % (2 ML) and (73 ± 2) % (6 ML) as it is shown by the full blue squares in Figure 4.3 c. The anticorrelation of PLQY and NPl thickness is maintained, however, for an emission wavelength below 470 nm, the respective values for the 2 ML and 3 ML samples belong to the highest reported PLQYs for any LHP material so far.

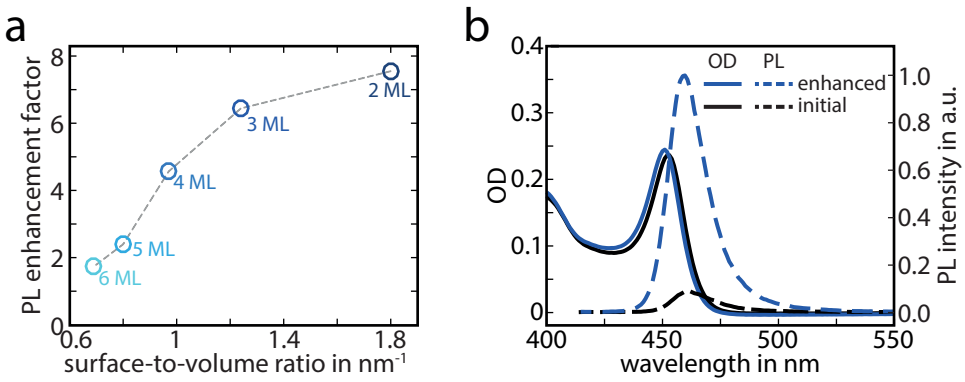

Figure 4.4: Effects of Surface Trap Repair. (a) The clear correlation between the PL enhancement factor and the surface-to-volume ratio of a NPl with given thickness indicates that the repair process probably mainly involves surface defects. **(b)** PL (dashed lines) and absorption (solid lines) spectra of an initial NPl dispersion (black) and an enhanced NPl dispersion (blue) containing the same amount of 3 ML NPls. The PL intensity is strongly boosted after the enhancement process. While the general shape of the PL spectrum is maintained, the amplitude is increased by the factor given in (a). In contrast, the absorption spectra are almost identical before and after the enhancement process.

In the following, the enhancement process will be elucidated in more detail. The observation that the relative PL enhancement is strongest for the thinnest NPls can be illustrated very clearly when plotting the PL enhancement factor (= $PLQY_{\text{enhanced}}/PLQY_{\text{initial}}$) versus the surface-to-volume ratio of the respective NPls (see Figure 4.4 a). The shown strong, monotonically increasing dependence further substantiates our previous proposition that the repair process mainly acts on the surface of the NPls. Moreover, linear spectroscopy before and after enhancement hints that the absorption process is unaffected (see Figure 4.4 b). The shape of the PL spectra also stays almost identical, only their magnitude is enhanced. This shows that the NPls do not grow thicker through the addition of $PbBr_2$; only defects on their surfaces are filled. This has also been confirmed by ADF-STEM imaging, atomic force microscopy (AFM) and XRD measurements.[20] Additionally, electron diffraction measurements revealed an increased crystallinity of the NPls after the treatment, while EDX spectroscopy showed that the ratio Br/Pb and Pb/Cs grew at the same time. In a final test, different bromide-salt-ligand solutions ($SnBr_2$, KBr, NaBr) were used as replacements for the $PbBr_2$-solution. All of them led to increased PL intensity, however, none of them could compete with the enhancement induced by the $PbBr_2$-solution — it seems that both constituents Pb and Br are needed for the repair process on the NPl surface. All in all, the results listed above imply that Br and Pb vacancies at the surface of

the NPls are filled by the enhancement solution, while the ligands serve for the passivation of any uncoordinated surface atoms.

Overall, the enhancement process led to increased PLQY values of above 50 % for all NPl samples. Even if there is still room for further improvements, the addition of the $PbBr_2$ solution to the NPl dispersions helped to tackle the problem of having PLQYs below 10 %. This represents a big step towards more efficient emission in this wavelength region and therefore addresses property (iii) mentioned at the beginning of this section.

4.1.3 Long-Term Stability

Last but not least, property (iv) — the stability — shall be discussed. Semiconductor NCs are generally known to be highly prone to surface traps which is detrimental to their long-term stability. This also applies to the NPls utilized in this work. Atoms/ions sitting at the NPl edges or at defects are often undercoordinated, resulting in dangling bonds.[194] In these positions, this might lead to the decomposition or a further thickness growth of the NPl, two effects undesired for the long-term stability. However, it turns out that the enhancement process is also beneficial for the stability of the NPls. The passivated uniform NPl surface achieved via this repair process reduces the probability for decomposition or further growth of the crystal. Surfaces with many defects exhibit the tendency to lead to more nonradiative recombination or a broadened PL spectrum over time. However, this behavior may be suppressed by surface trap repair.

In order to measure the effect of the enhancement process on long-term stability, a comparison between two NPl dispersions was conducted. The first cuvette contained unmodified 3 ML NPls, whereas the second cuvette contained the same type of NPls that underwent the enhancement procedure. The PL spectrum of both samples was measured twice each, once directly after their synthesis and then ten days later. On the one hand, the sample of the first cuvette containing the non-enhanced NPls already exhibits a lower PL signal from the beginning. However, its PL intensity further declines over the ten day period losing around 30 % of its initial strength. Moreover, the emission spectrum broadens

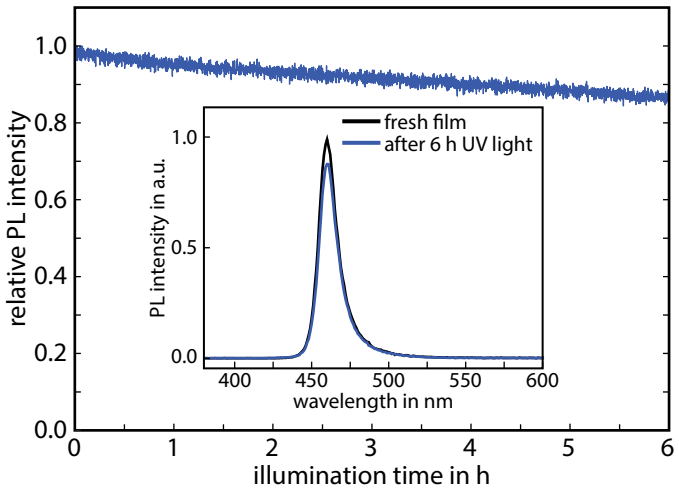

Figure 4.5: Stability Under UV Light Exposure. The photostability of a spin-coated, enhanced 3 ML NPl film was probed by illumination with a UV light source. Even after six hours, the sample maintained 85 % of its original PL intensity. The inset shows the PL spectra of this film obtained before and after illumination. While peak position and shape are retained, merely a slight drop in the PL intensity is observed.

slightly towards longer wavelengths which might indicate an ongoing growth in thickness for these crystals. Compared to that, the second sample containing enhanced NPls only loses around 10 % of its initial PL strength during ten days and its spectrum maintains the same central wavelength and shape. This proves the positive influence of the enhancement process on long-term stability.

In a second test the stability of a film of enhanced 3 ML NPls was probed over six hours. During this time period, the film was continuously exposed to UV light while its PL was monitored. Figure 4.5 shows the recorded signal over time as well as the PL spectra before and after the measurement identified in the inset. Even after six hours of such strong radiation, the NPl film still maintained 85 % of its original PL intensity. In this context it is important to note that the NPl film was spin-coated without relying on any additional protection layer. Hence, the measured stability is the one of the pure NPls. However, recent studies have shown that protecting layers lead to a significant enhancement of long-term stability against any influence from the environment. To this end, polymer films[195] as well as micelles[196] or thin aluminum oxide depositions[197] have shown promise as protection coatings for further improved stability.

4.1.4 Light-Emitting Diode

Recapitulatory, it can be stated that $CsPbBr_3$ NPls, when being enhanced through the postsynthetic treatment, represent an interesting material for the active layer in blue LEDs. In a proof-of-concept experiment, an LED based on 3 ML NPls was fabricated and characterized. Figure 4.6 a shows the electroluminescence (EL) spectrum of this LED and in the inset a photo of the working device. Its EL exhibits a single, narrow peak at 464 nm (FWHM <20 nm) close to the position of the PL.

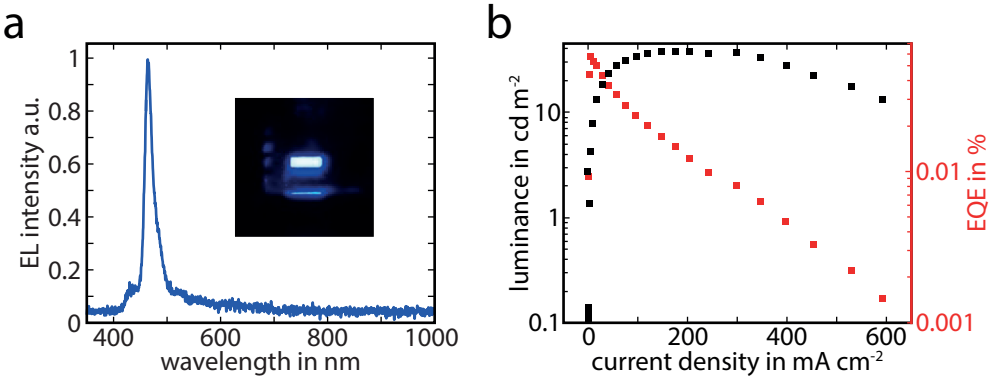

Figure 4.6: LED Based on $CsPbBr_3$ Nanoplatelets. (a) Electroluminescence (EL) spectrum of an LED with the structure ITO/PEDOT/Poly-TPD/3 ML $CsPbBr_3$/TPBi/Ca/Ag. The inset shows a photo of the working LED. **(b)** Luminance and external quantum efficiency (EQE) plotted versus current density. The device reaches a maximum luminance of 38.0 cd m^{-2} at operating voltage 6 V. At a current density of 4.95 mA cm^{-2} the highest external quantum efficiency (EQE) is reached at a value of 0.057 %. The corresponding luminance at the maximum EQE amounts to 4.26 cd m^{-2}.

Moreover, the luminance and external quantum efficiency (EQE) of this device are presented in Figure 4.6 b. The maximum EQE only amounts to 0.057 %, making it very clear that a material with a high PLQY (η_{PLQY}) does not automatically result in a highly efficient LED (η_{total}). LEDs are heterostructures and as shown in Equation 3.8 the choice of materials strongly influences the efficiencies of injecting electrons η_{inj} and of extracting photons η_{extr}. Important challenges that need to be tackled include the balanced injection of electrons and holes as well as the problem of internal reflection of the generated photons.[190]

Recently, the LED presented in Figure 4.6 a was optimized and an EQE of 0.30 % could be achieved for a device based on 3 ML NPls (blue emission at 464 nm) as well as an EQE of 0.55 % for a device based on 5 ML NPls (sky blue emission at 489 nm).[198] All in all, the LED within this work as well as the recent increase in EQE values demonstrate the potential of $CsPbBr_3$ NPls for the use as active layer within blue LEDs. This study opens the door to further optimizations and eventually all-perovskite white LEDs.

4.2 Recombination Dynamics

In Subsection 2.3.2 the recombination of excitons via radiative or nonradiative processes was described. This context can be expressed by an equation involving the respective recombination rates where the overall recombination rate is the sum of both aforementioned contributions, i.e.,

$$\begin{aligned} k_{\text{total}} &= k_{\text{r}} + k_{\text{nr}} \\ &= k_{1,\text{r}} + k_{1,\text{nr}} + \sum_{i=2}^{N_{\text{total}}} k_{\text{i,nr}} \,. \end{aligned} \tag{4.1}$$

As per the lower line of the above equation, radiative recombination is labeled $k_{1,\text{r}}$ since it involves only one exciton. Nonradiative decay channels are named in a similar fashion, i.e., with $k_{1,\text{nr}}$ describing trap-assisted decay involving one exciton only, while the remaining term sums up all exciton-exciton annihilation processes that may occur in NPls initially containing more than one exciton. Therefore, the latter contribution can be suppressed by using low excitation densities. In terms of population lifetimes Equation 4.1 may be rewritten as

$$\frac{1}{T_1} = \underbrace{\frac{1}{\tau_{1,\text{r}}} + \frac{1}{\tau_{1,\text{nr}}}}_{\text{monomolecular recombination}} + \underbrace{\sum_{i=2}^{N_{\text{total}}} \frac{1}{\tau_{\text{i}}}}_{\text{exciton-exciton annihilation}} \,, \tag{4.2}$$

wherein T_1 is the lifetime of the exciton population. Importantly, Equation 4.1 and Equation 4.2, as presented here, are not an exact mathematical model in order to describe the complete exciton population decay in a NC ensemble. They rather represent all processes through which the respective population might decay. For a more accurate analysis, the homogeneity of the NCs, the NC arrangement as well as the excitation density have to be considered. For example, for the previous determination of PLQY values in Subsection 4.1.2, exciton-exciton annihilation may be completely neglected since the used excitation density is too low. The previous section already showed how the trap repair process leads to an effective suppression of nonradiative recombination within the NPls. In the following section, it shall be examined how this additional surface trap repair procedure influences the time-resolved recombination behavior of excitons within the NPls. Based thereon, the recombination processes of exciton-exciton annihilation and monomolecular recombination were studied.

4.2.1 Exciton Recombination and Influence of Trap Repair

The observations on trap repair lead to the assumption that NPls within a given dispersion are split into two subensembles (see Figure 4.7). In this model, one subensemble is said to be without surface defects and thus exhibits a high PLQY (light-colored platelet), whereas the second subensemble contains surface defects and therefore tends to exhibit strongly reduced or even no emission (dark platelet). Surface trap repair renders a larger fraction of all NPls emissive. Thus, the overall population of excited e-h pairs dominantly recombines radiatively after the enhancement.

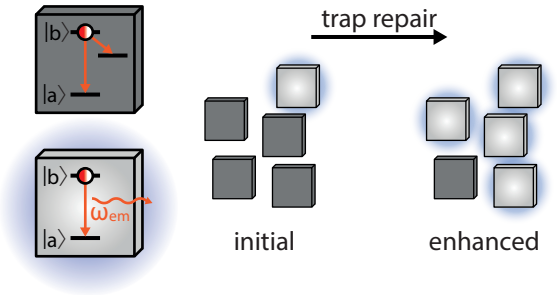

Figure 4.7: Scheme of Nanoplatelet Subensembles. Illustration of the whole NPl ensemble before and after the postsynthetic trap repair process. Two subensembles are involved in this picture: defect-containing dark NPls with a strong tendency towards nonradiative recombination and defect-free bright NPls which predominantly undergo radiative recombination.

For the purpose of validating this theoretical model, transient absorption spectroscopy (TAS) was employed. As shown in Equation 3.4 and Equation 3.5, the measured data obtained with the help of this time-resolved technique may either be presented as $\Delta OD(\lambda)$ or as $\Delta T(\lambda)/T_0(\lambda)$, respectively. Therefore, as mentioned in Subsection 3.3.2, the measurement technique may also be referred to as differential transmission spectroscopy (DTS) instead of TAS.

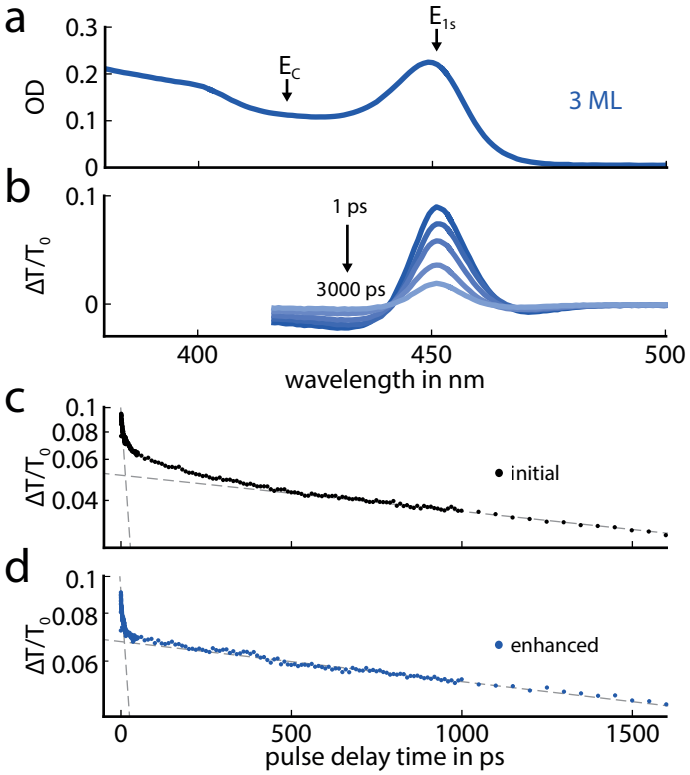

Figure 4.8: Differential Transmission Spectroscopy on $CsPbBr_3$ Nanoplatelets. (a) Steady-state absorption spectrum of a 3 ML $CsPbBr_3$ NPl dispersion. **(b)** Differential transmission spectra of the same sample at delay times ranging from 1–3000 ps. **(c)** Transient of the differential transmission at the energetic position of the exciton E_{1s}, as shown in (a), for a dispersion that has not been treated with the enhancement step. **(d)** The respective DTS transient for a NPl dispersion that underwent the trap repair process.

Figure 4.8 a shows the steady-state absorption spectrum of the dispersion containing 3 ML NPls. As discussed before for Figure 4.4 b, the absorption spectra before and after the trap repair are basically identical. For the examination of the time-resolved absorption, a pump pulse excitation wavelength of 400 nm (≈ 3.1 eV) was applied. The corresponding DTS spectra for the nonenhanced dispersion are

plotted in Figure 4.8 b. The dominant bleaching peak at around 452 nm within these spectra reveals that already 1 ps after excitation the main population of excited e-h pairs is energetically located at the exciton peak (arrow E_{1s} in Figure 4.8 a). This shows that excitons predominantly determine the behavior of these strongly confined NPls, since the bleaching peak appears well below the continuum onset E_C.[199]

To study exciton recombination dynamics, we observe two DTS transients at the position of this population E_{1s}: one before enhancement (initial) shown in Figure 4.8 c and one after enhancement (enhanced) plotted in Figure 4.8 d. The NPls in dispersion are spaced far apart with respect to each other and are hence considered to be independent, i.e., there is no charge or energy transfer between them. If one of these independent NPls is photoexcited, it may contain one or even several e-h pairs (cf. Subsection 2.3.3). A fast initial signal drop may be observed for both curves in Figure 4.8 c and d, also highlighted by a steep dashed grey line. This process relates to nonradiative exciton-exciton annihilation, dominantly occurring when a NPl initially contains more than one exciton. Its magnitude is strongly dependent on the excitation density and it dominates the temporal evolution of the exciton decay until only one exciton per photoexcited NPl remains.[200] This will be discussed in greater detail within the next subsection.

Another dashed line in both plots indicates that the remaining decay (t_{delay} > 100 ps) may be described by a single monoexponential function for the enhanced NPl dispersion in Figure 4.8 d, whereas this is not possible for the initial sample represented in Figure 4.8 c. The model proposed above in Figure 4.7 considers an overall ensemble of NPls consisting of two subensembles. Consequently, the transients in Figure 4.8 c and d should be a superposition of the DTS signals stemming from the two subensembles. On the long time scale for t_{delay} > 100 ps, the measured curve for the initial sample actually requires the sum of two exponential functions for a proper representation, indicating a well-balanced presence of both subensembles. However, the curve for the enhanced sample may be described by a single exponential function within the same time range. This behavior is typical for excitonic recombination and indicates that the overall sample consists predominantly of the subensemble representing NPls which are considered to be defect-free after the repair process. All in all, this observation is further proof for the efficiency of the trap repair process within the NPls.[20]

A similar behavior may also be observed in time-resolved PL spectra obtained with TCSPC. Figure 4.9 shows the respective data before and after enhancement for all NPl dispersions and also for two films comprising 3 ML NPls. Compared to TAS, TCSPC offers the opportunity to access longer delay times with the drawback of a worse temporal resolution (cf. Section 3.3). Therefore, fast processes like exciton-exciton annihilation cannot be determined accurately as they are superimposed and smeared out by the broader instrument response function. Hence, this data should be interpreted with caution, especially for very short time delays.

Similar to the results presented above, the enhanced samples (blue curves) shown in Figure 4.9 may be described by a monoexponential function, delivering further proof that only the subensemble with repaired NPls plays a role after the enhancement. On a short timescale, lifetimes seem to extend when repairing the NPl surface. Only when the population already dropped to a few percent, it seems as if some trap states might cause long-lived excitons in the initial samples (this can be observed best for the black curves in Figure 4.9 b and d). Interestingly, the graphs in Figure 4.9 c show the general trend for NPl films to show faster decay rates as compared to the NPls in dispersion which are represented in the other panels. This trend is rooted in the possibility of interaction between the NPls in films

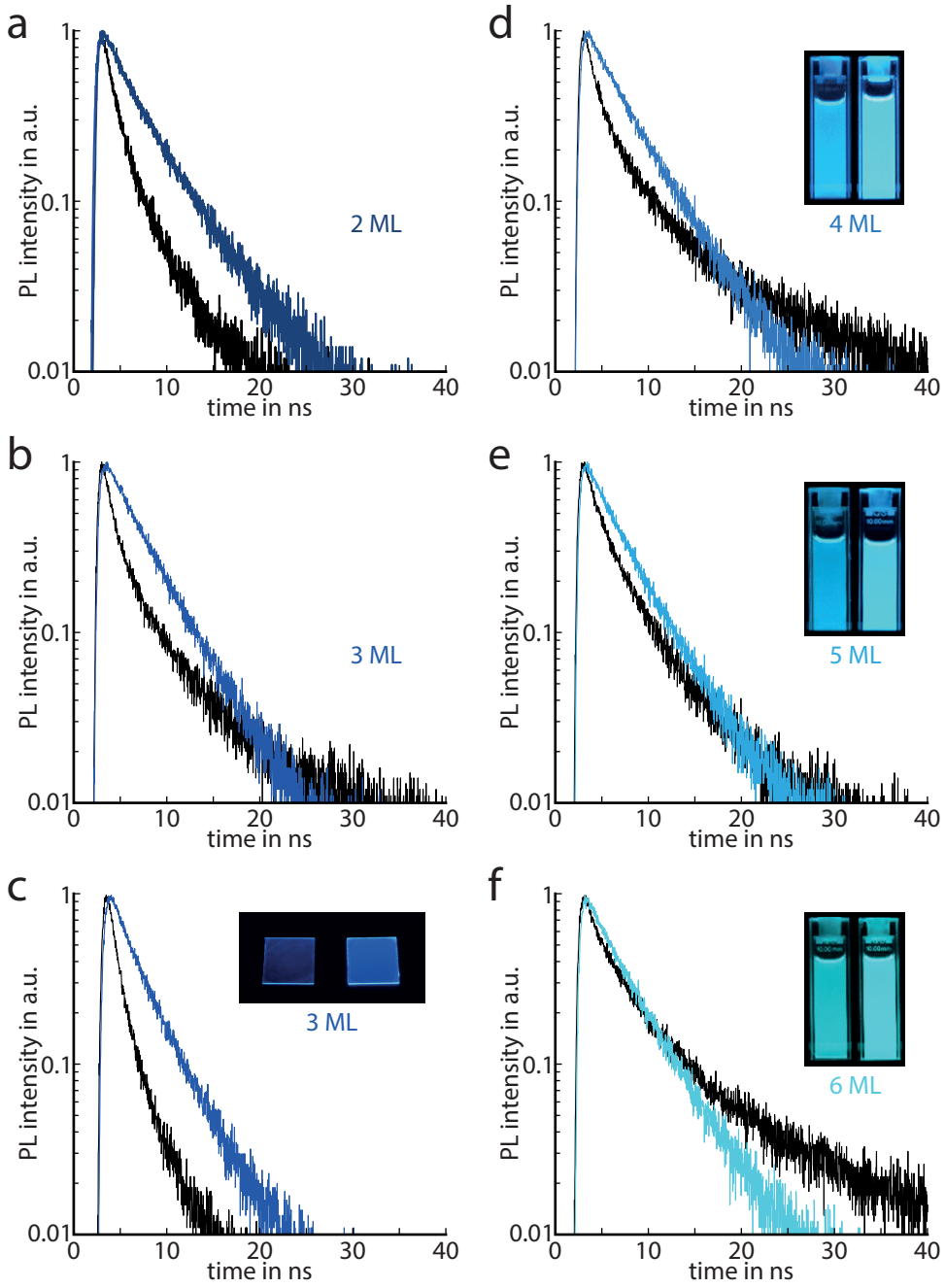

Figure 4.9: Time-Resolved PL of $CsPbBr_3$ Nanoplatelets. **(a)**,**(b)**,**(d)**,**(e)**, and **(f)** PL decay curves of initial (black lines) and enhanced (blue lines) NPl dispersions of 2–6 ML NPls, respectively. **(c)** The corresponding curves for films of the 3 ML sample. The insets present photos of initial (left) and enhanced (right) NPl samples under UV-light illumination.

and shows that the assumption of independent individual NPls — as introduced for dispersions — is not valid in this case. Moreover, it is always important to keep in mind that time-resolved TAS and PL do not necessarily exhibit the same decay curves. TAS represents the sum of electron and hole populations, whereas TCSPC is a representative of the product of these populations.

4.2.2 Exciton-Exciton Annihilation

Next, the influence of the NPl thickness on exciton-exciton annihilation shall be studied. Figure 4.8 c and d already gave an impression on how this effect has an impact on the decay curves recorded with DTS. In the following, this fast process will be studied for the nonenhanced NPls only. The lifetime τ_2 shall be extracted for dispersions of such samples (cf. Figure 2.11 and Equation 4.2). Exemplarily, the DTS data is illustrated for the 2 ML dispersion in Figure 4.10 a for which different pump pulse energies, i.e., different excitation densities, were employed. The respective decay curves of the exciton population exhibit a fast decay component within the first tens of picoseconds, the amplitude of which shows a strong correlation to the excitation density. This strong dependence and the total absence of this effect at very low excitation densities are clear indications for a multi-exciton process, namely exciton-exciton annihilation.

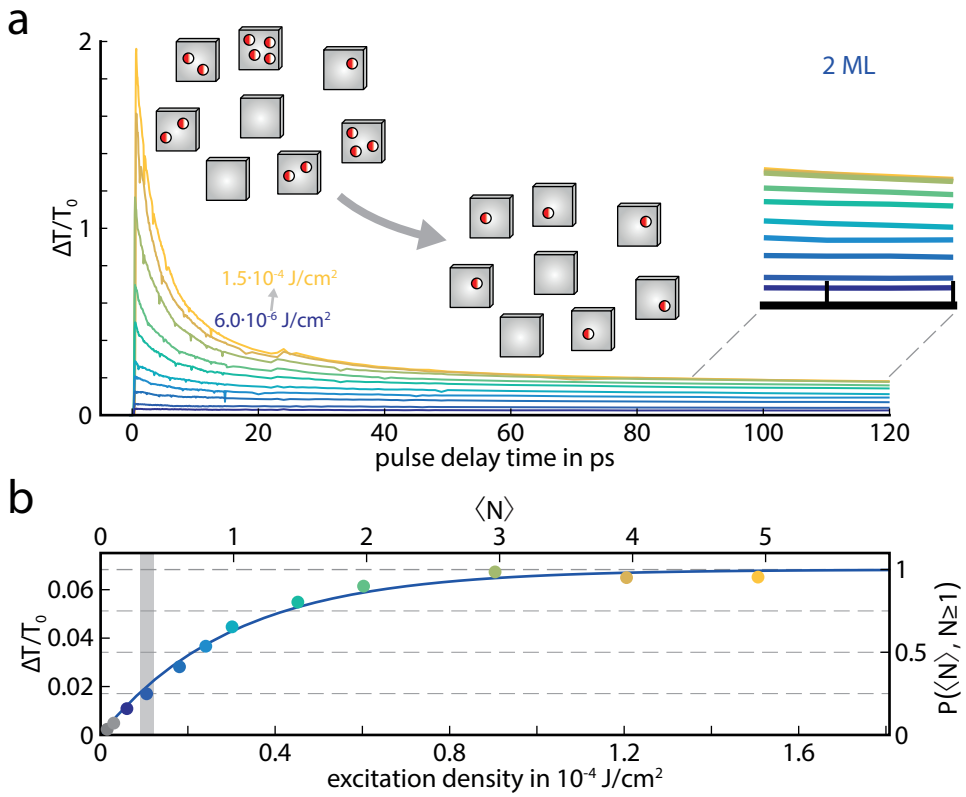

Figure 4.10: Excitation-Density Dependence of the Exciton Decay in Nanoplatelets. (a) Exciton population decay at the bleaching peak for 2 ML NPls at different excitation densities. Inset left: After the fast decay via exciton-exciton annihilation an initially excited NPl contains at most one exciton. Inset right: Above a certain excitation density the DTS signal saturates, meaning that almost every NPl was initially excited with at least one exciton. **(b)** Saturation behavior of the DTS curves from (a) averaged over longer pulse delay times 1 ns ≤ t_{delay} ≤ 3 ns. The blue curve is fitted in accordance with Poisson statistics and allows for the determination of the exact proportionality between the excitation density J_{ex} and the initial average number of excitons per NPl after excitation $\langle N \rangle$. The shaded grey area highlights the range $0.3 < \langle N \rangle < 0.4$ chosen to analyze the exciton-exciton annihilation lifetime τ_2.

As indicated in the left inset of this figure, this effect subsides after some tens of picoseconds. It may be assumed that by far the largest proportion of all initially excited NPls contains only one remaining exciton at most at this point in time which already has been introduced in Figure 2.12 and is referred to as t_1 in this model. For the measurement presented in Figure 4.10 a a value of around 100 ps is determined for t_1. After this time, in the confines of this assumption, only monomolecular recombination of single excitons — via radiative or non-radiative channels — is possible.

Since the rates for exciton-exciton annihilation and for monomolecular recombination differ strongly (cf. Figure 2.11), the following assumption may be made and based thereon a simpler function is derived from Poisson statistics.

$$\begin{aligned} P(\langle N\rangle, N = 1, t = t_1) &\approx P(\langle N\rangle, N \geq 1, t = 0) \\ &= 1 - P(\langle N\rangle, N = 0, t = 0) \\ &= 1 - \frac{\langle N\rangle^0}{0!} e^{-\langle N\rangle} \\ &= 1 - e^{-\langle N\rangle} \end{aligned} \tag{4.3}$$

Therefore, the fraction of NPls containing exactly one exciton at time t_1 may be estimated via a function $f(\langle N\rangle) = 1 - e^{-\langle N\rangle}$ only dependent on $\langle N\rangle$ as demonstrated in Equation 4.3.

As mentioned above, exciton-exciton annihilation processes can effectively be assumed to be over at around t_1. Accordingly, the overall decay behavior, i.e., the shape of the decay curve, should be excitation density independent after this point in time. The excitation density only determines how many NPls are excited with at least one exciton at $t = 0$ or, put in other words, how many NPls are excited with exactly one exciton at $t = t_1$ (cf. Equation 4.3). Naturally, there is a maximum amount of NPls that can be excited and this is the total number of observed NPls n_{total} as introduced in Subsection 2.3.3. Therefore, the $\Delta T/T_0$ intensity at $t = t_1$ is expected to converge against a saturation limit with increasing excitation density J_{ex}. This limit represents the case that each of the n_{total} observed NPls contains exactly one remaining exciton at $t = t_1$. This saturation behavior is actually shown in the right inset in Figure 4.10 a. Since the decay curves follow the same trend, the values of the transients may be averaged and plotted versus the excitation density as shown in Figure 4.10 b. As indicated by the solid blue curve, these data points may be fitted by a function $g(J_{\text{ex}}) = a\left(1 - e^{-b \cdot J_{\text{ex}}}\right)$. The fitting parameters a and b may be used to add a new pair of axes on the top and the right

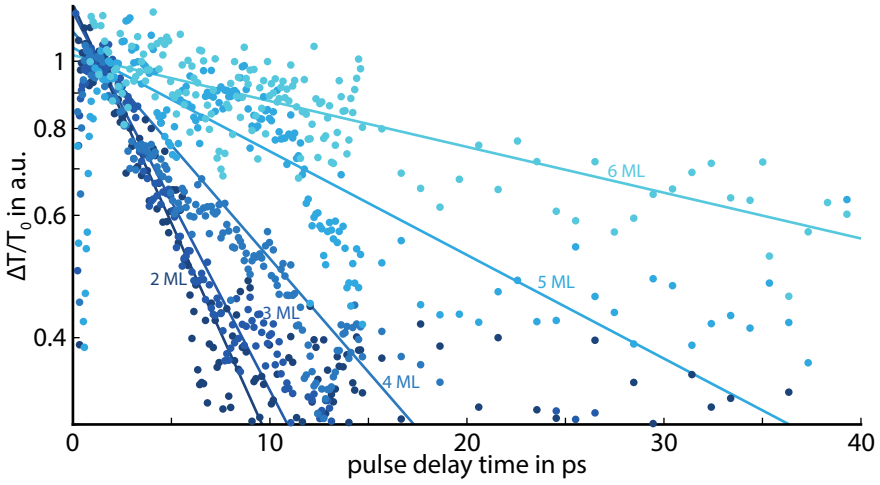

Figure 4.11: Exciton-Exciton Annihilation Lifetime Analysis for All Nanoplatelets. DTS decay curves at the excitonic peak for all samples 2–6 ML with an excitation density corresponding to $0.3 < \langle N\rangle < 0.4$ (marked by dots). Solid lines represent exponential fit functions. For better comparison the graphs have been normalized with respect to these fit functions.

side of Figure 4.10 b. In relation to these axes the fitted blue curve then represents the function $f(\langle N \rangle) = 1 - e^{-\langle N \rangle}$ as given in Equation 4.3. Consequently, the proportionality factor between $\langle N \rangle$ and J_{ex} is determined and the fraction of initially optically excited NPls $P(N \geq 1)$ may be extracted from the plot either versus J_{ex} or $\langle N \rangle$. In Subsection 2.3.3 we stated that $\langle N \rangle$ should be in the range of 0.3 – 0.4 in order to determine τ_2. This range is shaded in light grey within Figure 4.10 b and thereby it is revealed that exactly one of the initial DTS measurements fulfills this requirement. This procedure was repeated for all NPl samples. The corresponding initial decay curves attributed to exciton-exciton annihilation are plotted in Figure 4.11 where the condition $0.3 < \langle N \rangle < 0.4$ holds true for all data.

A clear trend is observable in this graph. The decay becomes faster for thinner NPls which is even easier to observe in the highlighted exponential fits. The lifetimes τ_2 can be extracted therefrom and are presented in Table 4.1.

Table 4.1: Exciton-Exciton Annihilation Lifetimes. The exciton-exciton annihilation lifetimes τ_2 are extracted from Figure 4.11 for all NPl samples.

	2 ML	3 ML	4 ML	5 ML	6 ML
τ_2 in ps	6.9 ± 0.2	8.0 ± 0.2	13.3 ± 0.2	29.1 ± 0.7	65.9 ± 1.4

The so-called "universal volume scaling law"[123] suggests a linear dependence between the lifetime τ_2 and the volume of small NCs.[201] Therein, τ_2 also denotes the lifetime via which the amount of e-h pairs in a NC is reduced from two to one. Due to their small size such NCs are also often referred to as quantum dots (QDs), even for the case of weak confinement only. Mostly, this law is confirmed for the case of spherical or cubic NCs.[202] However, the trend observed in our case does not reflect this dependence. For the $CsPbBr_3$ NPls presented here, the volume is directly proportional to the thickness since the lateral size is not changed. Clearly, there is no linear dependence between τ_2 and NPl thickness in Table 4.1 which suggests that the "universal volume scaling law" should not be applied to strongly confined LHP NPls.

It has also been suggested that the "universal volume scaling law" is not valid for CdSe NPls.[203] Li et al. derived that the size tuning of a weakly confined lateral dimension mainly influences the collision frequency of excitons, whereas the size tuning of the strongly quantum confined thickness mostly influences the interaction probability during a collision. They extracted a dependence of the exciton-exciton annihilation lifetime τ_2 on the NPl thickness which scales to the power of seven. The data presented in Table 4.1 for $CsPbBr_3$ NPls exhibit a respective dependence to the power of five. Generally, the τ_2 values for $CsPbBr_3$ NPls are short and amount to less than 70 ps even for the thickest NPls. The lifetimes are similar to the values reported for spherical CdSe QDs[123] and even faster than the ones reported for CdSe NPls.[203]

Lateral size-tuning of NPls would be beneficial to learn more about the exact influence of the NPl geometry on the lifetime τ_2. However, this is unfortunately outside the scope of this study. Nevertheless, even without this additional information, the trend presented in Table 4.1 suggests a strong deviation from the "universal volume scaling law" for perovskite NPls. Combining these results on $CsPbBr_3$ NPls with the ones of Li et al. on CdSe NPls leads to the assumption that the law might only be applicable to spherical or cubic NCs, where all dimensions exhibit a similar degree of quantum confinement.

4.2.3 Monomolecular Recombination

In the previous subsection the exciton-exciton annihilation lifetime was deduced to lie in the range of tens of picoseconds. In contrast, lifetimes for monomolecular recombination within LHP NCs usually lie in the nanosecond range. Due to this significant difference of around two orders of magnitude it may safely be assumed that the two processes happen subsequently as already illustrated in the scheme of Figure 2.12. In this subsection the exciton recombination dynamics following the exciton-exciton annihilation process will be studied for nonenhanced NPls in dispersions.

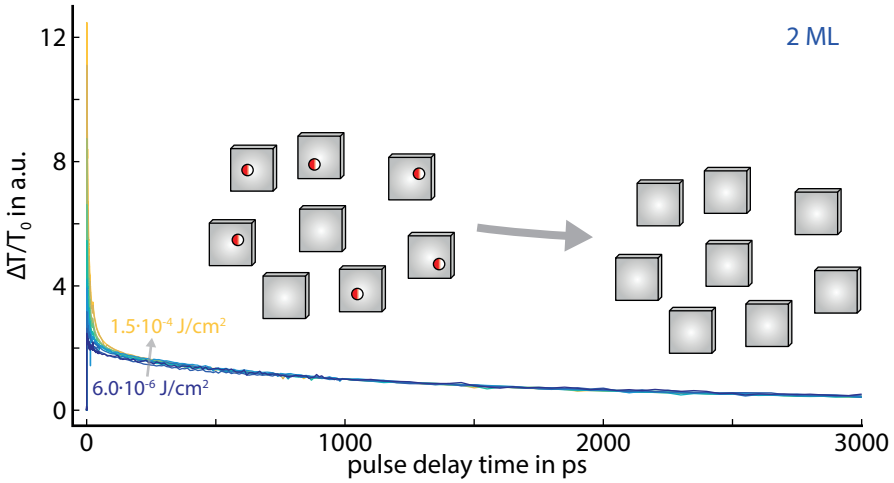

Figure 4.12: Differential Transmission Spectroscopy on 2 ML Nanoplatelets. DTS decay curves at the excitonic peak for the 2 ML sample without postsynthetic trap repair. Different excitation densities were applied ($6.0 \cdot 10^{-6}$–$1.5 \cdot 10^{-4}$ J/cm^2) and all curves have been normalized to unity at $t_{\mathrm{delay}} = 1000$ ps. Illustrating the data this way clearly shows that all curves exhibit the same shape and decay for pulse delay times longer than a few hundreds of picoseconds. This means that monomolecular exciton recombination within the NPl ensemble is an excitation density-independent process, contrary to exciton-exciton annihilation. The inset depicts the process of monomolecular recombination schematically, helping to understand this relation. Higher excitation densities only lead to a larger number of involved NPls, but the decay within each individual independent NPl — and therefore, also the decay behavior of the whole NPl ensemble — is not influenced.

Figure 4.12 shows DTS transients at the 1s exciton position that are based on the same measurement series as Figure 4.10 a. However, since the slower process of monomolecular recombination shall be studied, a larger time delay range up to 3000 ps is presented here. The curves for different excitation densities are normalized at $t_{\mathrm{delay}} = 1000$ ps revealing that all graphs exhibit the same decay behavior for longer delay times $t_{\mathrm{delay}} \geq 200$ ps. This proves that the monomolecular exciton population decay behavior of the ensemble is not influenced by the excitation density.

Long-term recombination is investigated for all different NPl thicknesses in Figure 4.13. Since the preceding exciton annihilation processes are of no importance for this investigation, the graphs are only plotted for $t_{\mathrm{delay}} \geq 200$ ps. As shown above, the excitation density J_{ex} does not influence the decay behavior, however, larger J_{ex} lead to an enhanced SNR of the DTS signal. Therefore, values $J_{\mathrm{ex}} \geq 0.5 \cdot 10^{-4}$ J/cm^2 were chosen for all samples. Looking at the plots within Figure 4.13 carefully, one recognizes that the decay curves are not entirely monoexponential. A slight deviation from the exact monoexponential decay occurs since nonenhanced NPls are examined in this case, therefore, leaving the potential for the presence of two subensembles (see Figure 4.7).

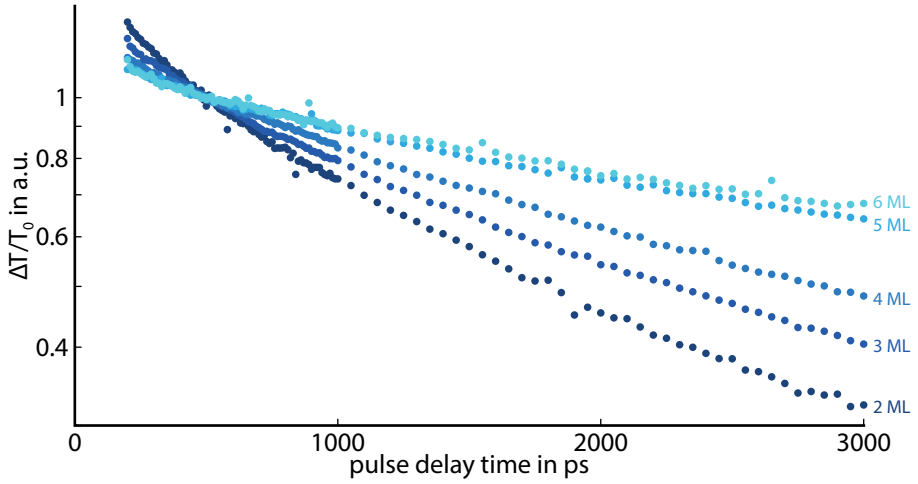

Figure 4.13: Recombination Lifetime Analysis for all Nanoplatelets. DTS decay curves for all NPl samples at the respective 1s excitonic peak. In order to focus on the monomolecular exciton recombination, all graphs are plotted for $t_{\text{delay}} \geq 200$ ps only. The decay curves are normalized at $t_{\text{delay}} = 500$ ps and a clear trend towards shorter recombination lifetimes τ_1 may be observed for thinner NPls.

Nevertheless, the quantity to be extracted from Figure 4.13 for all NPl thicknesses is the monomolecular exciton recombination lifetime

$$\tau_1 = \left(\frac{1}{\tau_{1,\text{r}}} + \frac{1}{\tau_{1,\text{nr}}} \right)^{-1} . \tag{4.4}$$

Here, in this approximation τ_1 simply represents a lifetime for each NPl ensemble without going further into detail on the role of the subensembles. As illustrated in the inset of Figure 4.12, Equation 4.4 takes into account all processes in which an exciton decays radiatively ($\tau_{1,\text{r}}$) or nonradiatively ($\tau_{1,\text{nr}}$) without interacting with another exciton. The lifetime τ_1 should not be confused with the population lifetime T_1 of the exciton ensemble as it has been introduced in Section 2.4. Equation 4.2 shows that the approximation $T_1 \approx \tau_1$ may only be made in the absence of exciton-exciton annihilation.

The lifetime values τ_1 were extracted in the pulse delay time region 1500 ps $\leq t_{\text{delay}} \leq$ 3000 ps for all graphs of Figure 4.13. The results are presented in Table 4.2.

Table 4.2: Monomolecular Recombination Lifetimes. The Monomolecular Recombination Lifetimes τ_1 are extracted from Figure 4.13 for all NPl samples.

	2 ML	3 ML	4 ML	5 ML	6 ML
τ_1 in ns	2.45 ± 0.08	2.95 ± 0.09	3.92 ± 0.19	6.05 ± 0.17	6.69 ± 0.14

The values for τ_1 exhibit a clear trend, i.e., they decrease with decreasing NPl thickness. Similar observations have been made in other two-dimensional structures as well, e.g., in GaAs/AlGaAs quantum wells, for which the relation $\tau_1 \propto E_{\text{B}}^{-1}$ was derived.[78] The thickness dependence of E_{B} for $CsPbBr_3$ NPls has been studied in Figure 4.2 c. In keeping with that, it makes sense that τ_1 decreases for thinner NPls. Recently, a similar observation was made for $MAPbI_3$ NPls.[12] Another effect that could lead to faster decay, is that a larger surface-to-volume ratio likely increases the possibility for an electron to encounter a surface trap, consequently leading to additional nonradiative decay channels.

Compared to the study on GaAs/AlGaAs quantum wells, the lifetimes τ_1 reported here for $CsPbBr_3$ NPls are about one order of magnitude larger.[78] However, compared to $MAPbI_3$ NPls, they are a factor of two smaller.[12] Overall, the values given in Table 4.2 are already reasonably long lifetimes τ_1. However, as previously indicated, in the time-resolved PL data of Figure 4.9, surface trap repair of NPls leads to even longer lifetimes, since nonradiative recombination is suppressed by this new PL enhancement procedure.[20] This may in turn, also be beneficial for LHP applications relying on exciton diffusion as longer lifetimes have a direct impact on the exciton diffusion length (see Equation 2.60).

5

Dephasing

In recent years, LHPs have experienced a boom in research activity. However, some of their fundamental properties remain largely unexplored. For example, studies so far rarely distinguish between homogeneous and inhomogeneous transition broadening. This may be of particular interest for NCs, as inhomogeneous broadening may also serve as an indicator for the homogeneity of an ensemble of NCs. In this chapter, first, the total transition broadening will be studied as a function of the sample temperature for three different LHP NC ensembles: $CsPbBr_3$ nanocubes, $CsPbBr_3$ nanowires, and $MAPbI_3$ nanoplatelets. Based thereon, the fastest relaxation regime, i.e., the coherent regime, will be examined via four-wave mixing spectroscopy, yielding the time scale for exciton dephasing in $MAPbI_3$ nanoplatelets. These results build a bridge between the ultrafast polarization decay of exciton ensembles and the respective homogeneous broadening of the exciton transition. Moreover, it will be shown that exciton wave packets may be generated within these NCs, leading to quantum beating in the polarization decay signal which can be explained with help of a three-level system.

5.1 Total Broadening of Exciton Transitions

Primarily, this section will study and explain how the total broadening of a transition is influenced by the sample's temperature. This objective is pursued by means of linear spectroscopy in the form of absorption and PL measurements. Three samples are investigated, namely $CsPbBr_3$ nanocubes,[22] $CsPbBr_3$ nanowires,[21] and $MAPbI_3$ nanoplatelets.[76] Thanks to this variety, insight is gained into the influence of the NC composition and morphology on the optical properties of the whole NC ensemble.

5.1.1 Cesium Lead Bromide Nanocubes

$CsPbBr_3$ nanocubes are known for their strong PL in the green spectral region[204,205] and high PLQY values above 80 % can be achieved for these NCs.[23] Figure 5.1 a shows the PL spectra of a film of $CsPbBr_3$ nanocubes deposited on a sapphire substrate for temperatures in the range 10–290 K. The yellow curve represents the data at room temperature. The emission spectrum of this NC ensemble is centered around 2.4 eV, corresponding to a wavelength of 517 nm, hence the green light emission of this material. When gradually cooling the sample down to a temperature of only 10 K with the help of a cryostat, the emission spectrum is altered. The central emission wavelength is redshifted while the corresponding maximum intensity increases by a factor of 7.6. However, the overall PL signal of the ensemble is, of course, not determined by the peak value, but — figuratively speaking — by the area underneath the Gaussian shaped curve. Notably, this area only increases by a factor of 2.5 when

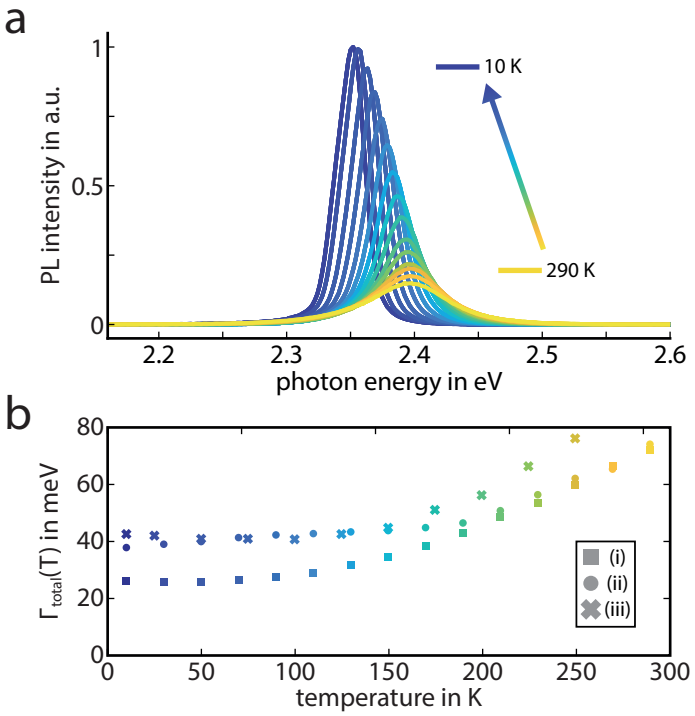

Figure 5.1: Transition Broadening Versus Temperature for $CsPbBr_3$ Nanocubes. (a) Experimentally obtained PL spectra of a spin-coated film of $CsPbBr_3$ nanocubes for temperatures in the range 10–290 K. With decreasing temperature the central emission wavelength redshifts and the signal intensity increases. **(b)** Total transition broadening $\Gamma_{total}(T)$ for three different films made of $CsPbBr_3$ nanocubes. The respectively colored squares representing sample (i) are the values extracted from the data set shown in (a). The values for sample (ii) are also based on PL spectra within the same temperature range. In contrast, the broadening for sample (iii) is based on absorption data and $\Gamma_{total}(T)$ has been determined as the FWHM at the absorption onset.

cooling the sample to 10 K. Consequentially, the PL distribution not only shifts, it also gets narrower with decreasing temperature. When cooling down the NC ensemble, phonon-assisted nonradiative recombination channels are strongly suppressed, leading to overall stronger radiative recombination, i.e., to an increased PL signal as shown in Figure 5.1 a.

In this section the main focus lies on the broadening of the distribution which is changed by the temperature. To this end, three spin-coated films of $CsPbBr_3$ nanocubes were prepared and examined via temperature-dependent spectroscopy in order to study the broadening of the exciton transition within these samples. All three samples have been synthesized on different days and therefore this comparison also reveals information about the reproducibility of the NC synthesis routine. Figure 5.1 b presents the total broadening of the exciton transition $\Gamma_{\text{total}}(T)$ versus temperature as obtained for these three samples, which are named (i), (ii) and (iii) for the sake of simplicity.

For sample (i) each square symbol in Figure 5.1 b represents a total broadening $\Gamma_{\text{total}}(T)$ as extracted from the corresponding spectrum in Figure 5.1 a relying on the FWHM of the PL peaks. At room temperature, the total broadening is about 72 meV, ($\Gamma_{\text{total}}(290\,\text{K}) = 72\,\text{meV}$), but for the lowest measured temperature, this value is reduced to 26 meV ($\Gamma_{\text{total}}(10\,\text{K}) = 26\,\text{meV}$). Note that this trend will be examined in greater detail in Subsection 5.1.4. The respective data for sample (ii) is added to the plot in Figure 5.1 b using circle symbols. These values are also obtained from PL data, i.e., from a data set similar to the one shown in Figure 5.1 a. At room temperature, the total broadening is similar as in the first sample, however, at low temperatures, $\Gamma_{\text{total}}(T)$ converges to a value of around 40 meV, a higher value compared to the first sample. This serves as an indication that the overall inhomogeneous broadening of the NC ensemble in sample (ii), represented by circle symbols, is larger than the one of sample (i), denoted by squares. Finally, sample (iii) is represented by crosses. There, the broadening data is extracted by means of the absorption onset from which the FWHM ($\Gamma_{\text{total}}(T)$) may be obtained as well. The data set indicated by crosses follows a similar trend as the data of sample (i), however, an offset in y-direction again indicates a comparatively larger inhomogeneous broadening. All in all, these measurements show that the size distribution of the NCs within the measured ensemble may vary from synthesis to synthesis. Therefore, even NC samples of identical composition may exhibit a different extent of inhomogeneous broadening.

5.1.2 Cesium Lead Iodide Nanowires

This subsection may be said to be quite similar to the previous one in the sense that the same measurements and analyses are performed once again, however, for a different NC morphology, namely for $CsPbBr_3$ nanowires (NWs) instead of nanocubes. The PL spectra of a NW ensemble as a function of the temperature are depicted in Figure 5.2 a. The most striking observation compared to the respective plot for nanocubes previously presented in Figure 5.1 a is the significantly stronger enhancement in the PL signal when cooling down. Here, the area underneath the PL peak increases by a factor of 19 when cooling down the sample from room temperature to 10 K. This increase is rooted in the significantly lower PLQY of the NWs at room temperature and the much stronger suppression of nonradiative decay at low temperatures. The low PL of the NWs is a consequence of their formation mechanism. Therein, the NWs are created through oriented attachment of nanocubes, leading to wires with similar cross sections as the cubes, but lengths of up to 2 µm corresponding to more than one hundred nanocubes.[21] With this in mind, it can be understood why NWs exhibit a very poor PLQY

of usually below 5 % at room temperature. Exciton diffusion along the wire leads to larger diffusion lengths compared to the diffusion from wire to wire or cube to cube, i.e., the exciton hopping process. Exemplary, assume a NW consisting of 98 perfect nanocubes and 2 nanocubes with many defects that lead to nonradiative recombination only. If an exciton is generated at a random position along the NW, it may easily diffuse along the longitudinal direction, eventually ending up at one of the 2 defect nanocubes where it encounters a trap and recombines nonradiatively. Equation 2.60 shows that the diffusion length L_D depends on the sample's temperature T. Thus, when cooling down the NW ensemble, exciton diffusion is suppressed reducing the likelihood that excitons will reach a region with a defect. Thus, the overall PL signal (the PLQY) is much larger at low temperatures as shown in Figure 5.2 a. This is a clear demonstration of the temperature's influence on exciton diffusion. Chapter 6 will deliver a deeper insight into the diffusion process for various morphologies at room temperature.

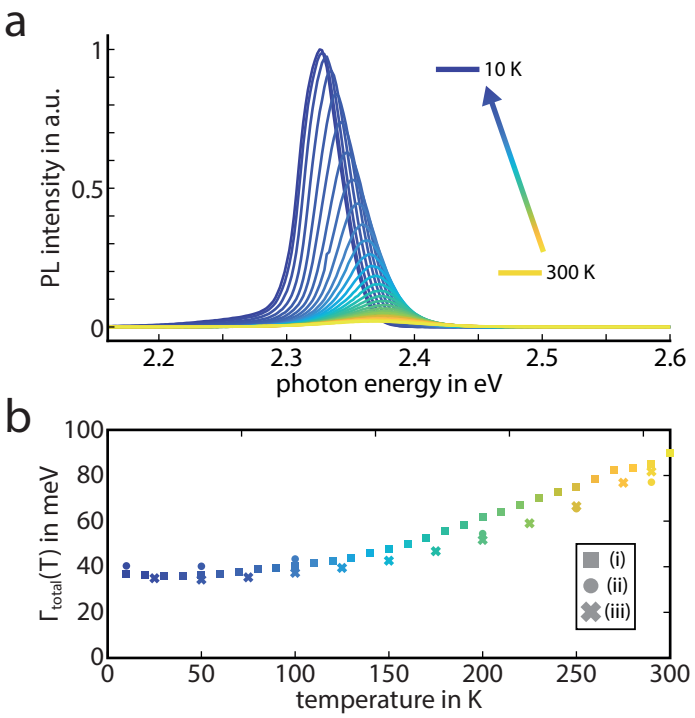

Figure 5.2: Transition Broadening Versus Temperature for $CsPbBr_3$ Nanowires. (a) Experimentally obtained PL spectra of a spin-coated film of $CsPbBr_3$ nanowires for temperatures in the range 10–300 K. With decreasing temperature, the central emission wavelength redshifts, similar as in the case shown in Figure 5.1 a for nanocubes of identical LHP composition. The increase in PL intensity with decreasing temperature is even more significant for nanowires. **(b)** Total transition broadening $\Gamma_{total}(T)$ for three different films made of $CsPbBr_3$ nanowires. The respectively colored squares representing sample (i) are the values extracted from the data set shown in (a). The values for sample (ii) are also based on PL spectra within the same temperature range. In contrast, the broadening for sample (iii) is based on absorption data and $\Gamma_{total}(T)$ has been determined as the FWHM at the absorption onset.

When comparing the PL spectra for nanocubes and nanowires in Figure 5.1 a and Figure 5.2 a, another interesting observation may be made. While the overall redshift caused by the cooling process is very similar for both NC types, the emission maximum at room temperature appears at slightly different central positions, i.e., 30 meV lower for the NWs than for the nanocubes. Figure 4.2 c showed that $CsPbBr_3$ cubes fall in the weak confinement regime along three dimensions. In contrast, NWs are only weakly confined along two dimensions. The emission maxima at room temperature accordingly reflect how a missing dimension of weak confinement may already cause a detectable redshift.

As for the nanocubes, three spin-coated films were investigated for the NWs in order to determine the temperature-dependent broadening of the exciton transition $\Gamma_{\text{total}}(T)$ (see Figure 5.2 b). Again, the obtained values for sample (i) and (ii) are based on PL spectra, whereas the broadening of sample (iii) was extracted from the onset of absorption spectra. Here, the samples (i)-(iii) exhibit very similar values indicating that the synthesis routine for $CsPbBr_3$ NWs results in good reproducibility.

5.1.3 Methylammonium Lead Iodide Nanoplatelets

Last but not least, $MAPbI_3$ nanoplatelets like the ones shown in Figure 2.7 a were investigated. Their thicknesses lie in the range of 20–100 nm with varying lateral dimensions of up to 500 nm. Previously, it had already been shown that such NPls exhibit bulk-like behavior.[12] It is known that iodide-based LHPs exhibit an emission and absorption onset in the red to NIR spectral region. Moreover, the exciton binding energy is reported to be smaller than that of other halide compositions.[11,76] For $MAPbI_3$, values in the broad range 2–62 meV have been reported so far, mostly agreeing that the exciton binding energy E_B increases for decreasing temperature.[53]

For the NPls examined for this thesis, temperature-dependent absorption spectra are shown in Figure 5.3 a. At room temperature, all excitonic features are completely invisible in the respective yellow curve due to the large total transition broadening and the low exciton binding energy. As observed before for $CsPbBr_3$ NCs, the absorption onset (and with it the emission spectrum) redshifts when cooling down the NC ensemble. This may be considered a more general behavior that is observed for

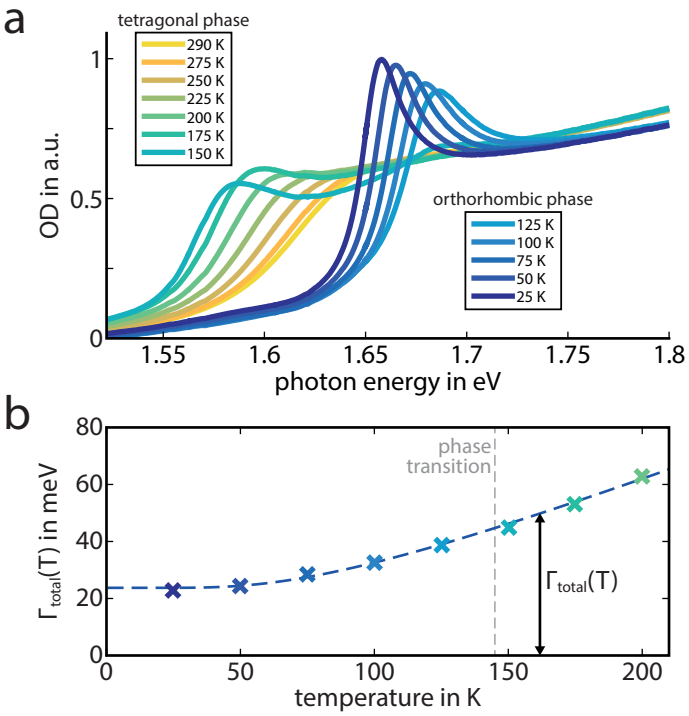

Figure 5.3: Transition Broadening Versus Temperature for $MAPbI_3$ Nanoplatelets. (a) Experimentally obtained absorption spectra for temperatures in the range 25–290 K. With decreasing temperature, the absorption onset bearing the peak of the excitonic transition experiences an ongoing redshift which is only disrupted by the phase transition from the tetragonal to the orthorhombic phase occurring at around 150 K. **(b)** Total broadening of the exciton transition $\Gamma_{\text{total}}(T)$ (i.e., the FWHM of the absorption onset for $T \leq 200$ K) versus temperature as obtained from the data shown in (a) and denoted by crosses in the respective color. The dashed blue line represents a theoretical model fitted to the experimental broadening values of $\Gamma_{\text{total}}(T)$.

LHPs, purportedly occurring due to the p-type character of the CB.[95] At the same time, the absorption onset becomes steeper due to the decreasing homogeneous broadening $\Gamma_{\mathrm{hom}}(T)$, effectively the temperature-dependent part of $\Gamma_{\mathrm{total}}(T)$. For $T \leq 200\,\mathrm{K}$ this total broadening is sufficiently reduced for the exciton peak to become distinguishable at the absorption onset. At around 150 K, there occurs a sharp jump by approximately 100 meV of the absorption onset, leading to an absorption edge at higher energies for temperatures $T < 150\,\mathrm{K}$. This signifies the phase transition from the tetragonal to the orthorhombic crystal structure, which has been reported to occur at around 150 K for bulk $MAPbI_3$ perovskites.[98] Reducing the temperature further leads to a continued redshift of the absorption edge as observed before the phase transition. Simultaneously, the exciton peak grows more pronounced at the absorption onset. Such a phase transition was not observed for the $CsPbBr_3$ NCs in Figure 5.1 a and Figure 5.2 a as cesium-based LHPs already assume the orthorhombic phase at room temperature.[94]

Similar to the previous temperature-dependent linear spectroscopy measurements presented in this section, the total broadening for the 1s exciton transition $\Gamma_{\mathrm{total}}(T)$ was extracted from the data shown in Figure 5.3 a. As mentioned above, the excitonic peak is barely discernable from the continuum onset for temperatures above 200 K. Therefore, the FWHM at the absorption onset is only extracted for spectra with $T \leq 200\,\mathrm{K}$ and it may be assumed that this FWHM value is a reasonable representation of $\Gamma_{\mathrm{total}}(T)$ as the excitonic signature may be observed in all of these cases at the onset. The obtained data is plotted in Figure 5.3 b. As could already be expected from Figure 5.3 a, the steeper onset at lower temperatures corresponds to a narrower exciton transition. Interestingly, this experimentally obtained data for $\Gamma_{\mathrm{total}}(T)$ does not seem to be affected by the phase transition occurring at around 150 K. When cooling down from 200 K, the trend of a decreasing total broadening persists without any noticeable discontinuity at the phase transition temperature. In Figure 5.3 b a fitted curve is added to the experimental data in accordance with Equation 2.30 and Equation 2.31 such that the change in total broadening is effectively attributed to the interaction of excitons with phonons. Since there is no discontinuity at the phase transition temperature, this suggests similar exciton-phonon scattering rates for the tetragonal and the orthorhombic phases in $MAPbI_3$ LHPs. The values and logical conclusions that might be drawn therefrom will be explained in detail in the following subsection together with a comparison to the other two NC types.

5.1.4 Broadening Comparison for Different Nanocrystals

First, we turn to the experimental data for $\Gamma_{\mathrm{total}}(T)$ as obtained for $MAPbI_3$ NPls and as presented in Figure 5.3 b. For the analysis of the total broadening Equation 2.30 and Equation 2.31 are combined, leading to

$$\Gamma_{\mathrm{total}}(T) = \underbrace{\Gamma_{\mathrm{inhom}} + \Gamma_{\mathrm{hom,rest}}}_{=\Gamma_0} + \gamma_{\mathrm{ac}} T + \frac{\gamma_{\mathrm{op}}}{\exp\left(E_{\mathrm{op}}/k_{\mathrm{B}}T\right) - 1}\,. \tag{5.1}$$

As already introduced in Subsection 2.1.5, γ_{ac} and γ_{op} denote the coupling constants for acoustic and optical phonons, respectively. Moreover, E_{op} represents the average LO phonon energy. The total broadening at 0 K amounts to $\Gamma_{\mathrm{total}}(0\,\mathrm{K}) = \Gamma_{\mathrm{inhom}} + \Gamma_{\mathrm{hom,rest}} = \Gamma_0$. Generally, acoustic phonons play an important role at low temperatures $T \leq 50\,\mathrm{K}$. Especially, intensive laser excitation with excess energy compared to the exciton transition (or even at the resonant condition) may lead to the generation of acoustic phonons at low temperatures due to intraband relaxation processes.[78] However, in the

absorption measurements presented in Figure 5.3 a less intense xenon lamp is applied as the light source. When fitting the data in Figure 5.3 b based on Equation 5.1, it turned out that the contribution of acoustic phonons would be rather small having no significant influence on the other fitting parameters over the broad temperature range. This has been observed by others as well,[72] and, therefore, this term has been neglected in the theoretical model for the fitting procedure in this case.[76] The consequential evaluation of the data for $MAPbI_3$ NPls presented in Figure 5.3 b leads to the fitting parameters shown in Table 5.1. The obtained values agree very well with the ones reported by Wu et al., who stated $\gamma_{op} = (92 \pm 24)$ meV and $E_{op} = (25 \pm 5)$ meV by measuring the excitonic photoluminescence of bulk $MAPbI_3$ films.[206]

Table 5.1: Exciton-Phonon Scattering Analysis. Total broadening Γ_0 at 0 K, coupling strength for acoustic phonons γ_{ac}, Fröhlich coupling constant γ_{op}, and average LO phonon energy E_{op} as extracted from Figure 5.1 b ($CsPbBr_3$ nanocubes), Figure 5.2 b ($CsPbBr_3$ nanowires), and Figure 5.3 b ($MAPbI_3$ nanoplatelets).

	$CsPbBr_3$ nanocubes	$CsPbBr_3$ nanowires	$MAPbI_3$ nanoplatelets
Γ_0 in meV	34 ± 8	37 ± 3	24 ± 1
γ_{ac} in meV/K	0.08 ± 0.01	0.02 ± 0.01	—
γ_{op} in meV	333 ± 116	270 ± 134	95 ± 28
E_{op} in meV	54 ± 12	51 ± 16	21 ± 3

The respective values for the $CsPbBr_3$ nanocubes and nanowires presented in Figure 5.1 b and Figure 5.2 b, respectively, are also added in Table 5.1. For these LHP NCs the acoustic phonons have been considered as well in the fitted theoretical model, i.e., Equation 5.1 has been applied without any modification. The three data sets for each sample have firstly been fitted individually. Then, in a next step, the average values of the fitting parameters were calculated (see Table 5.1). The results for $CsPbBr_3$ nanocubes and nanowires are quite similar and also comparable to the values obtained by Saran et al. who determined $\Gamma_0 = (40 \pm 1)$ meV, $\gamma_{ac} = (0.03 \pm 0.01)$ meV/K, $\gamma_{op} = (87 \pm 31)$ meV, and $E_{op} = (44 \pm 10)$ meV for $CsPbBr_3$ nanocubes.[73]

When comparing both $CsPbBr_3$ NCs and the $MAPbI_3$ NPls, it becomes apparent that the scattering of optical phonons is different in $MAPbI_3$ LHPs, where smaller average LO phonon energies are observed. The fundamentally different morphology of the NCs also influences the quantum confinement. $MAPbI_3$ NPls are bulk-like, whereas $CsPbBr_3$ NWs are weakly confined in two dimensions and $CsPbBr_3$ nanocubes are weakly confined in all three dimensions. The weakly confined $CsPbBr_3$ NCs exhibit a similar value for Γ_0 in the range of around 35–40 meV, whereas the bulk-like $MAPbI_3$ NPls exhibit a smaller value of only 24 meV. Sometimes literature states $\Gamma_{inhom} = \Gamma_0$,[72,73] but as shown in Equation 5.1 a more precise definition is used within this work, such that $\Gamma_{inhom} < \Gamma_0$. Nevertheless, from the large Γ_0 values presented in Table 5.1 it can be assumed that inhomogeneous broadening plays a significant role in these LHP NCs at low temperatures. The difference in Γ_0 between $MAPbI_3$ the $CsPbBr_3$ NCs suggests that inhomogeneous broadening is an effect probably gaining importance for smaller NCs in an ensemble since slight variations in the overall size of these NCs have a higher relative impact in such cases. However, an exact differentiation between homogeneous and inhomogeneous broadening will be demonstrated in the following section.

5.2 Four-Wave Mixing

Out of the three LHP NC types presented in the previous section, only $MAPbI_3$ NPls are further investigated in this section for a demonstration of four-wave mixing (FWM) spectroscopy. As shown in Figure 5.3, linear absorption spectroscopy on these NPls has already revealed two of the main quantities of the 1s exciton transition, namely, its energetic position and its total broadening as a function of temperature, i.e., $E_{1s}(T \leq 200\,\mathrm{K})$ and $\Gamma_{total}(T \leq 200\,\mathrm{K})$, respectively. Yet, the actual values of $\Gamma_{hom}(T)$ and Γ_{inhom} remain unknown and cannot be assigned exactly since only their sum $\Gamma_{total}(T)$ is known. Even for temperatures close to 0 K, $\Gamma_{hom}(T)$ does not converge to zero, i.e., $\Gamma_{total}(0\,\mathrm{K}) \neq \Gamma_{inhom}$. To tackle this issue, we rely on FWM. This technique enables a direct measurement of the exciton dephasing time T_2, thereby giving access to the homogeneous broadening via $\Gamma_{hom} = 2\,\hbar/T_2$.[131] The dephasing time T_2 for excitons, as discussed in Section 2.4, is determined by scattering processes within the investigated material.[128] Since the probability of such scattering events depends on the excitation density J_{ex} and the temperature T of the sample, the dephasing time T_2 is not a material constant, but rather a function $T_2(J_{ex}, T)$. Consequently, reducing the excitation density as well as lowering the temperature should lead to less scattering, thereby increasing the dephasing time T_2.

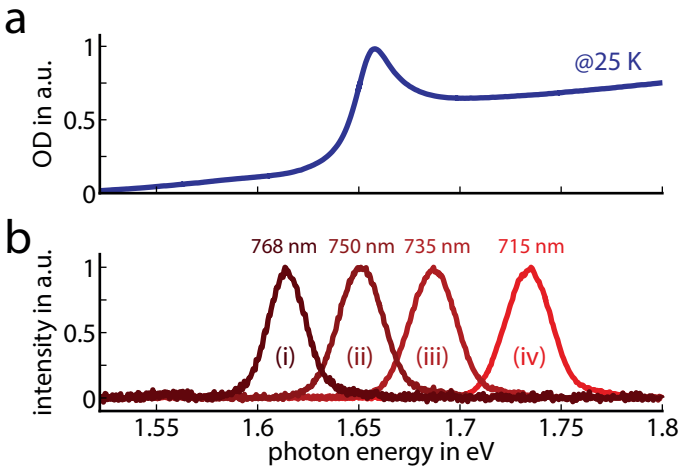

Figure 5.4: Excitation Spectra for Four-Wave Mixing Experiments. **(a)** Absorption spectrum of $MAPbI_3$ NPls at 25 K with the excitonic peak at the continuum onset. **(b)** The OPA was employed as excitation light source for the FWM experiments. Its output spectrum was adjusted such that it allows for (i) only 1s exciton excitation, (ii), (iii) simultaneous excitation of excitons and free e–h pair transitions, or (iv) excitation of free e–h pair transitions only.

The $MAPbI_3$ NPls investigated here can be seen in the SEM image shown in Figure 2.7 a. As opposed to the $CsPbBr_3$ NPls studied in Chapter 4, these $MAPbI_3$ NPls are considered to be bulk-like without any considerable quantum confinement.[12] Generally, a certain size distribution is inherent to NCs. The electron microscopy image shown in Figure 2.7 a confirms this with the NPls featuring different sizes and shapes. Here, the NC dimensions lie well above the exciton Bohr radius. However, as explained in Subsection 2.2.3, such size deviations within the NC ensemble may influence the respective absorption and PL spectra in the form of inhomogeneous broadening.

The details of the FWM setup have already been covered in Subsection 3.3.4, such that the section at hand may only discuss the most important experimental parameters. The length of the involved laser pulses amounts to 115 fs. As indicated in Table 2.4, dephasing occurs in the fastest of all relaxation regimes, the coherent regime. Therefore, in order to minimize scattering of excitons within the NPls,

all FWM measurements presented here have been performed at the low temperature of 25 K and with an excitation density resulting in merely 10^{17} cm^{-3} excitons. This results in increased dephasing times which is crucial for making this ultrafast process temporally resolvable at all.

The absorption spectrum recorded for the $MAPbI_3$ NPl ensemble at said temperature is shown in Figure 5.4 a. At 25 K the excitonic peak is well observable next to the continuum onset. Each laser pulse originating from the OPA is divided into two pulses by a beam splitter. These are the two laser pulses needed in the degenerate time-integrated FWM experiments. Accordingly, the temporal and spectral profiles of pulse #1 and #2 are identical. Both exhibit a Gaussian-shaped spectrum when plotted against photon energy and a FWHM of around 27 meV. Their central wavelength can be shifted by tuning the OPA. Four different scenarios for the excitation wavelength are represented in Figure 5.4 b. In case (i) the tails of the exciton peak and the excitation spectrum overlap such that only the 1s exciton may be excited since the continuum transitions may not be reached by the excitation wavelength centered at 768 nm. Case (iv), entailing a central wavelength of 715 nm, is the exact opposite to case (i) in the sense that the excitation spectrum has no overlap with the exciton transition and exclusively excites free e-h pairs in the continuum. The remaining cases (ii) and (iii) are located in between both aforementioned scenarios and lead to a simultaneous excitation of exciton and continuum transitions.

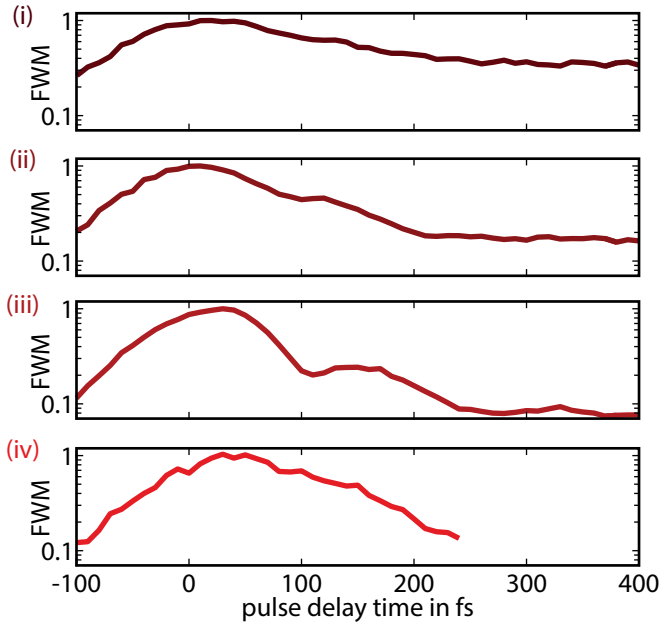

Figure 5.5: Time-Integrated Four-Wave Mixing on $MAPbI_3$ Nanoplatelets. FWM decay curves for the excitation spectra shown in Figure 5.4 for a charge carrier density of 10^{17} cm^{-3} at a temperature of 25 K. The central excitation wavelength set by the OPA has a significant influence on the shape and decay behavior of the time-integrated FWM signal. Panel (i) shows dephasing of the exciton ensemble only, whereas (ii) and (iii) additionally involve the continuum states with free e-h pairs such that quantum beating may be observed. Finally, panel (iv) depicts the dephasing process for free e-h pairs which is too fast to be temporally resolved by the laser pulses.

Figure 5.5 shows that the central excitation wavelength significantly affects the appearance of the FWM decay curves, i.e., the FWM signal plotted against the pulse delay time t_{delay} between pulses #1 and #2. The first panel, concerning case (i), shows an exponential decay related to the dephasing of excitons. This will be analyzed and discussed further in the following Subsection 5.2.1. When increasing the photon energy of the OPA as to reach a wavelength of 750 nm, i.e., case (ii), the excitation pulse spectrally overlaps slightly with the continuum transitions while still mainly exciting the exciton

transition. Compared to case (i) a shoulder appears in the FWM signal which is shown in the second panel of Figure 5.5. At an even higher photon energy, i.e., in case (iii), this shoulder turns into a clear beating behavior of the signal which will be the subject of Subsection 5.2.2. Finally, the FWM curve shown in the fourth panel (iv) in Figure 5.5 indicates that, even at low temperatures, the dephasing of free e–h pairs is too fast to perform a reasonable data deconvolution for the purpose of extracting the dephasing time T_2 for free e-h pairs.

5.2.1 Dephasing of Excitons

As mentioned above, the first panel in Figure 5.5 represents case (i) in which only the 1s exciton is excited such that the decay of coherence for this energetic transition may be observed. For further analysis, this graph is plotted again in Figure 5.6 a on a linear scale. A fast initial rise of the FWM signal is observed and after the signal maximum is reached a slower decay takes place. An estimated decay time of $T_{\mathrm{decay}} \approx 200\,\mathrm{fs}$ may be extracted from the exponential decay of this curve. As demonstrated in Equation 2.52 and Equation 2.53 this decay time T_{decay} is related to the dephasing time T_2 via $T_2 = g \cdot T_{\mathrm{decay}}$, with $g = 2$ for the case of a purely homogeneously broadened transition, whereas $g = 4$ applies for the case of inhomogeneous broadening.[130,144] Without making any assumption, the $\Gamma_{\mathrm{hom}}(25\,\mathrm{K})$ value can be calculated for both scenarios using Equation 2.40. For an inhomogeneously broadened sample $\Gamma_{\mathrm{hom}}(25\,\mathrm{K}) = 1.7\,\mathrm{meV}$ is obtained and for an homogeneously broadened sample $\Gamma_{\mathrm{hom}}(25\,\mathrm{K}) = 3.4\,\mathrm{meV}$ is obtained. The total broadening has been studied in the previous section and amounts to $\Gamma_{\mathrm{total}}(25\,\mathrm{K}) = 24\,\mathrm{meV}$ for the $MAPbI_3$ NPls. Obviously, $\Gamma_{\mathrm{total}}(25\,\mathrm{K}) > \Gamma_{\mathrm{hom}}(25\,\mathrm{K})$ for both examined scenarios and $\Gamma_{\mathrm{total}}(25\,\mathrm{K})$ is at least a factor of 7 larger than the homogeneous broadening $\Gamma_{\mathrm{hom}}(25\,\mathrm{K})$. This estimate confirms our previous conjecture that inhomogeneous broadening plays an important role within the NPl ensemble, especially at low temperatures. Therefore, the recorded FWM signal may safely be deemed a photon echo and accordingly $g = 4$ has to be applied, i.e., $T_2 = 4 \cdot T_{\mathrm{decay}}$.

Moreover, this case legitimates the use of Equation 2.54 in modeling the FWM signal. As it is much larger as compared to T_2, the influence of the lifetime T_1 is negligible in this formula. However, it is helpful to consider the pulse length of 115 fs since the theoretical model assumes infinitesimally short, delta function-like laser pulses. To this end, the fitting function of Equation 2.54 was convoluted with the respective temporal pulse profile. As shown in Figure 5.6 a, the overall theoretical model given by the dashed blue line agrees very well with the experimentally obtained curve for the FWM signal. For case (i), in which excitation occurs at the low energy side of the excitonic peak, it is likely that less present defect-bound excitons are observed as well (see Figure 5.4). For these excitons, less scattering — and therefore, a slightly increased dephasing time — may be expected, possibly explaining why the slope of the experimentally obtained curve in Figure 5.6 a is not explicitly monoexponential.[207] Still, the theoretical model allows for extracting an exciton dephasing time of $T_2(25\,\mathrm{K}) = (800 \pm 20)\,\mathrm{fs}$ for the studied $MAPbI_3$ NPls. Consequently, the homogeneous broadening at 25 K may be obtained via $\Gamma_{\mathrm{hom}}(25\,\mathrm{K}) = 2\,\hbar/T_2(25\,\mathrm{K}) = (1.7 \pm 0.1)\,\mathrm{meV}$, yielding an inhomogeneous broadening of $\Gamma_{\mathrm{inhom}} = (22 \pm 1)\,\mathrm{meV}$. Since the latter is temperature-independent, it may be indicated in the plot of $\Gamma_{\mathrm{total}}(T)$ in Figure 5.6 b as a horizontal line. This in turn helps to distinguish between homogeneous and inhomogeneous broadening for all temperatures. This graphical representation reveals that inhomogeneous broadening is the main cause for transition broadening at low temperatures $T < 100\,\mathrm{K}$. At around $T = 150\,\mathrm{K}$ homogeneous and inhomogeneous broadening exhibit a similar

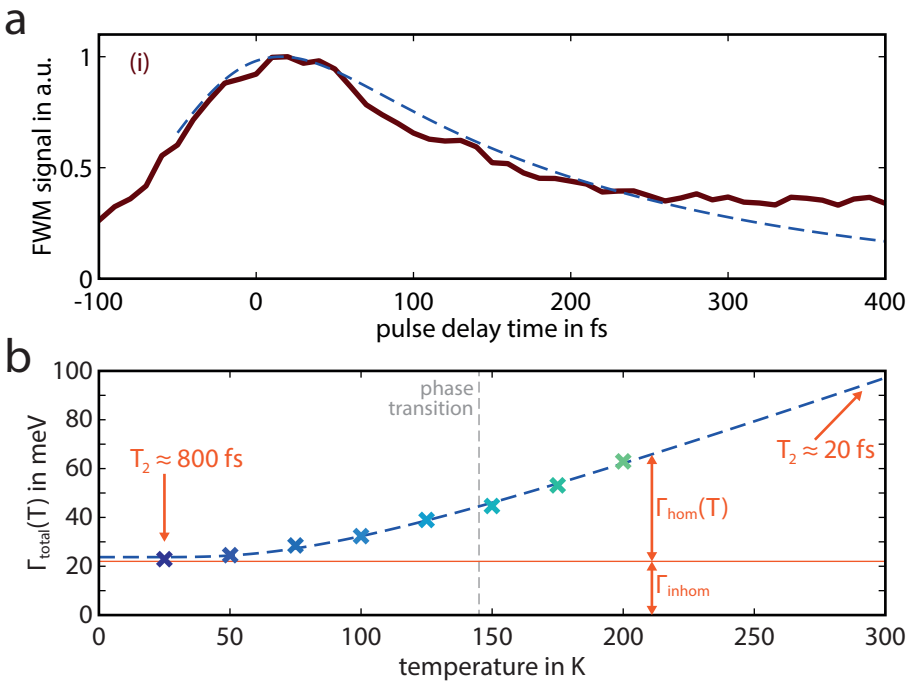

Figure 5.6: Dephasing of the Exciton Ensemble. **(a)** FWM signal decay curve for the excitation spectrum given by case (i). As shown in Figure 5.4, only the 1s exciton is excited in this case. Consequently, the decaying FWM signal (dark red curve) represents the dephasing of the exciton ensemble, thereby giving access to the dephasing time $T_2 = (800 \pm 20)$ fs. The dashed blue curve represents the respective theoretical model given by Equation 2.54 and agrees well with the experimental data when taking into account pulse length of 115 fs. **(b)** Total broadening of the exciton transition versus temperature as already presented in Figure 5.3 b, but for an extended temperature range. Using the dephasing time $T_2 = (800 \pm 20)$ fs obtained at 25 K, the homogeneous broadening at this temperature may be calculated, i.e., $\Gamma_{\mathrm{hom}}(25\,\mathrm{K}) = 2\,\hbar/T_2(25\,\mathrm{K}) = (1.7 \pm 0.1)$ meV. Based thereon, the temperature-independent inhomogeneous broadening may be extracted via $\Gamma_{\mathrm{inhom}} = \Gamma_{\mathrm{total}}(25\,\mathrm{K}) - \Gamma_{\mathrm{hom}}(25\,\mathrm{K}) = (22 \pm 1)$ meV. Consequently, the homogeneous and inhomogeneous contributions to the total broadening of the excitonic level can be distinguished for all temperatures.

magnitude and for temperatures above this region homogeneous broadening is the main contributor to the total broadening.

Moreover, using Equation 2.40, the dephasing time T_2 may be calculated for the whole temperature range up to 300 K. The underlying calculation is based on the assumption that the total broadening $\Gamma_{\mathrm{total}}(T)$ follows the fitted trend as obtained in Figure 5.3 also for $T \geq 200$ K. This approach predicts a fast exciton dephasing time T_2 of only 20 fs for $MAPbI_3$ NPls at room temperature, showing that this process cannot possibly be resolved by the laser pulses of the OPA. This value is far shorter than the pulse length of the used OPA, implying that the cooling of the sample was a crucial step in order to resolve the FWM signal at all. Just recently, Jha et al. determined the dephasing time of excitons in bulk $MAPbI_3$ films at room temperature using two-dimensional electronic spectroscopy.[208] They obtained a value of 50 fs which is in good agreement with the results of this thesis, especially considering that bulk LHP films are not identical to LHP NPls.

Finally, $\Gamma_{\mathrm{hom,rest}}$ may be calculated via

$$\Gamma_{\mathrm{hom,rest}} = \Gamma_0 - \Gamma_{\mathrm{inhom}} = \Gamma_{\mathrm{total}}(0\,\mathrm{K}) - \Gamma_{\mathrm{inhom}}\,. \tag{5.2}$$

Therefore, in the investigated $MAPbI_3$ NPl sample $\Gamma_{\mathrm{hom,rest}} < 2$ meV is obtained at an excitation density of 10^{17} cm^{-3}. This low value confirms that the excitation density has been chosen reasonably

and moreover it shows, that the total exciton transition broadening in this LHP NC is dominated by exciton-phonon interactions at higher temperatures.

5.2.2 Quantum Beating

As already demonstrated in Figure 5.5, cases (ii) and (iii), entailing a simultaneous coherent excitation of excitons and continuum transitions, exhibit no strictly monotonous decay. Rather, a beating behavior is observed in their FWM signals. Naturally, this is only possible if the spectral width of the excitation pulse is broad enough to cover both transitions. Such types of excitations are also referred to as exciton wave packets in which the excited transitions may interfere with each other.[142]

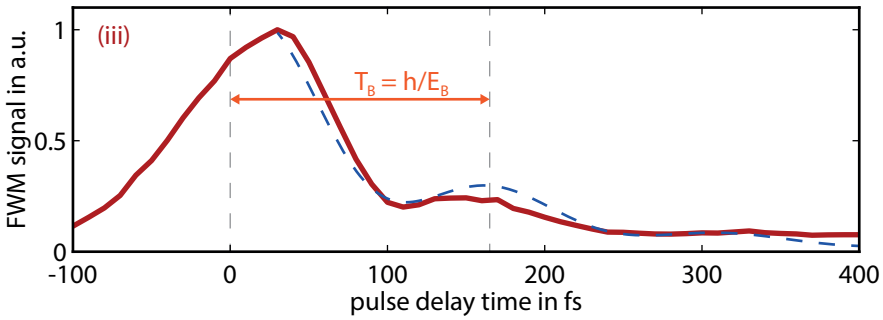

Figure 5.7: Quantum Beating in the Four-Wave Mixing Signal. FWM signal decay curve for the excitation spectrum given by case (iii). As shown in Figure 5.4, the spectrum of the excitation pulse overlaps with the exciton and the continuum transitions to a similar extent. This results in the generation of a so-called exciton wave packet in which these transitions are excited simultaneously, leading to a quantum beating behavior of the FWM signal (red curve). A periodicity of $T_B = (165 \pm 10)$ fs may be extracted from the quantum beats. Eventually, the exciton binding energy of the $MAPbI_3$ NPls may be accessed via $E_B = h/T_B$. Here, it amounts to (25 ± 2) meV. The dashed blue curve represents a theoretical model for this behavior which is rooted in Equation 2.55, i.e., it is based on the concept of a three-level system in which both excited states are superimposed.

In case (iii) as discussed here the central wavelength of the excitation pulse lies at 735 nm, such that the 1s exciton and continuum transition are excited to a similar extent (cf. Figure 5.4). The respective decay of the FWM signal is presented in Figure 5.7. The curve represents a behavior commonly referred to as quantum beating, exhibiting a clear signal drop between the first two peaks. This implies that the excitation pulse originating from the OPA is indeed broad enough to generate an excitonic wave packet. Under this condition, so-called quantum beat spectroscopy (QBS) may be performed in order to gain information on the energy spacing between the excited transitions. As shown in Figure 2.19, the simplified concept of a three-level system may be relied on here, such that one of the two excited states represents the 1s exciton and the other is given by the continuum onset. Now, the eponymous beating arises from alternating constructive and destructive inference in the respective polarization components. Based thereon, Equation 2.56 determines the relation between the beating period of the FWM signal and the energy spacing between the excited states which is actually the exciton binding energy E_B within this system. The signal decay for this three-level system is modeled in accordance with Equation 2.55 and represented by a dashed blue line in Figure 5.7. Even though this approximation neglects higher order excitons and treats the continuum onset as a single transition, the theoretical model proves to be suitable for approximating the experimentally obtained FWM signal. The beating time T_B, which is defined as the time between the 0 fs delay position and the first beat after the main peak,[142] can be obtained from the experimental and theoretical curves and amounts to (165 ± 10) fs. Consequently, a value of $E_B = h/T_B = (25 \pm 2)$ meV is obtained for the

exciton binding energy, fitting well into the range 2–50 meV of previously reported values for $MAPbI_3$ that relied on different experimental approaches at low temperature.[53] Since this technique is not strongly influenced by inhomogeneous broadening effects, QBS is an especially convenient approach for inhomogeneously broadened materials with low exciton binding energies. Due to the inverse relation between E_B and T_B, small values for E_B lead to long beating times T_B which are easier to detect given that the FWM signal decays sufficiently slowly. Another advantage of QBS is that the energy spacing is measured directly as a difference between two transitions, rendering an error-prone assumption of the absolute continuum onset E_C unnecessary.

As explained in Subsection 2.1.3 and demonstrated in Subsection 4.1.1, the Elliott model may also be used to extract exciton binding energies from linear absorption data. However, this is effectively more practical for cases in which inhomogeneous broadening does not hinder the distinction of the exciton transition from the continuum states. This has been the case for the strongly quantum confined $CsPbBr_3$ NPls with large exciton binding energies (see Figure 4.2). Summing up, QBS offers a promising technique for the calculation of small exciton binding energies E_B and supplements the Elliott model in cases where the excited transitions are difficult to distinguish in linear absorption spectroscopy due to inhomogeneous broadening.

6

Diffusion

In the preceding chapters, the recombination dynamics and the dephasing behavior of excitons in LHP NCs have been studied extensively. Therein, the generation of excitons was driven by external light sources and the excitons stayed within the LHPs. For the most part, however, conventional semiconductor devices rely on charge transport between various layers of different materials, also involving injection or extraction of e-h pairs. Therefore, the topic of exciton diffusion is a crucial one when it comes to the applicability of LHP NCs in future devices. To date, large electron-hole diffusion lengths of approximately one micrometer have already been reported for bulk films of $MAPbI_{3-x}Cl_x$.[156,158] Here, it shall be studied which diffusion lengths may be achieved for exciton transport in films of fully inorganic $CsPbBr_3$ NCs, i.e., the exciton diffusion length for $CsPbBr_3$ nanocubes and nanowires shall be studied, using two different experimental approaches.

6.1 Photoluminescence Mapping

This section focuses on PL mapping, which was already explained on a theoretical level in Subsection 2.5.3. Here, this experimental technique is employed in order to visualize exciton diffusion in LHP NC assemblies. To this end, two samples were investigated.

6.1.1 Cesium Lead Bromide Nanocubes

The first sample comprises a thin film of $CsPbBr_3$ nanocubes, which was prepared by spin-coating the respective NCs onto a polished silicon substrate. This results in an arrangement of densely packed nanocubes on the substrate surface which might be compared to the TEM image in Figure 3.2 b. The NCs exhibit an edge length of about (12 ± 1) nm. As explained before, the exciton transport between such NCs is referred to as exciton hopping. In the following, exactly this will be examined for the lateral directions within the NC film.

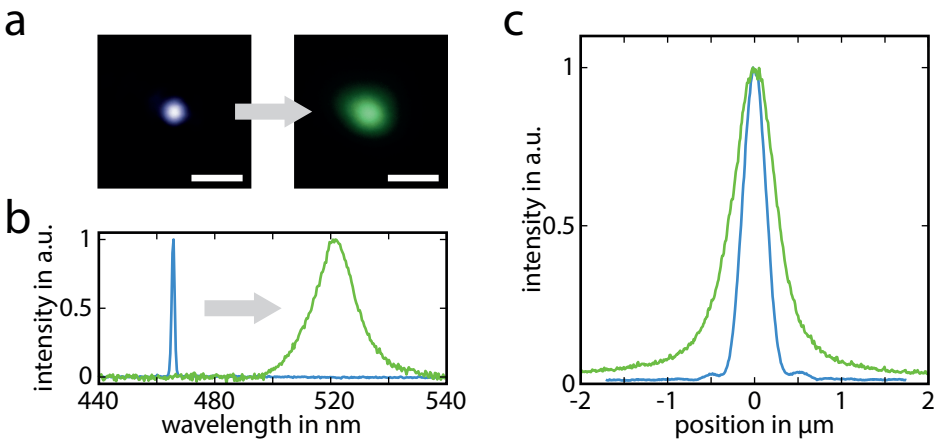

Figure 6.1: Exciton Diffusion via Photoluminescence Mapping for $CsPbBr_3$ Nanocubes. (a) 2D intensity maps in false color for the tightly focused excitation laser beam (blue) and the resulting PL profile (green) as obtained from a film of closely packed $CsPbBr_3$ nanocubes. Both scale bars represent 1 µm. **(b)** Respective, normalized spectra for the sharp laser excitation beam and the redshifted, broadened PL. **(c)** Normalized intensity profiles extracted from (a) revealing a FWHM of 313 nm for the excitation and 601 nm for the PL.

To excite the nanocubes, a blue laser light source is focused onto a diffraction-limited spot on the sample surface. Depending on the filter that is used in the exciton diffusion setup, either the excitation or the resulting PL is observed and an intensity map is recorded by the camera attached to the microscope (see Figure 3.12). Both images for the laser excitation and the PL spot are shown in Figure 6.1 a, wherein false coloring is used for a clear assignment. Already in this simple intensity map one sees at first glance that the PL is distributed over a larger area than the excitation laser spot. As depicted by the spectra in Figure 6.1 b, the sharp laser excitation (λ_{Laser} = 466 nm) and the broad PL (λ_{PL} = 522 nm) are spectrally well separated, making the aforementioned filtering for the intensity maps feasible. The intensity profiles extracted from the 2D maps shown in Figure 6.1 a are plotted in Figure 6.1 c. The latter confirms the previous observation that exciton diffusion leads to a spread-out PL profile as compared to the excitation spot. FWHM values of 313 nm and 601 nm are obtained for the blue and green curves, respectively. Equation 2.61 is exploited to calculate the standard deviation for both Gaussian profiles. Based thereon, the exciton diffusion length is calculated using Equation 2.62, in

turn yielding a value of L_D = 218 nm. Notably, the PL map in Figure 6.1 a does not exhibit perfect radial symmetry and, consequently, the profile in Figure 6.1 c is not perfectly symmetric, either. Only analyzing the left or right half of the distribution in isolation leads to an exciton diffusion length of 227 nm or 208 nm, respectively. This slight deviation demonstrates that properties like the uniformity and thickness of the NC film influence exciton diffusion. Moreover, the tilting between adjacent cubes may also play a role for the dipole interaction that is prerequisite for exciton hopping via FRET. Still, the obtained values for the exciton diffusion length in such films imply that an exciton may hop from one NC to another ten times or even more often along one direction before its extinction.

6.1.2 Cesium Lead Bromide Nanowires

Next, we turn to the sample made of $CsPbBr_3$ NWs for which the same experiment was conducted analogously. Figure 6.2 a shows the corresponding 2D intensity maps for this case. Taking into account Figure 6.2 b, it may be understood why the intensity maps differ significantly from those relating to the previously examined film consisting of nanocubes of the same LHP composition. Generally, as shown in the left panel of Figure 6.2 b, the overall orientation of the NWs in this spin-coated sample is random. However, on length scales of approximately 1 µm, neighboring NWs tend to align, thereby forming bundles in which the NWs are mainly oriented in the same direction. This effect may also be observed with the NWs in the TEM image presented in Figure 3.2 d. Due to the diffraction limit and the laser wavelength, the optical microscope being part of the exciton diffusion setup cannot resolve single NWs. However, comparisons to TEM images lead to believe that the inset shown in Figure 6.2 b is such a bundle of parallel NWs. This inset and both maps in Figure 6.2 a are all representing the identical section on the sample surface and based thereon the x-axis is defined as the direction parallel to the wire direction. The left panel in Figure 6.2 a already reveals some interesting behavior. In fact, the thin wires seem to act like a diffraction grating for the incident laser beam and an interference

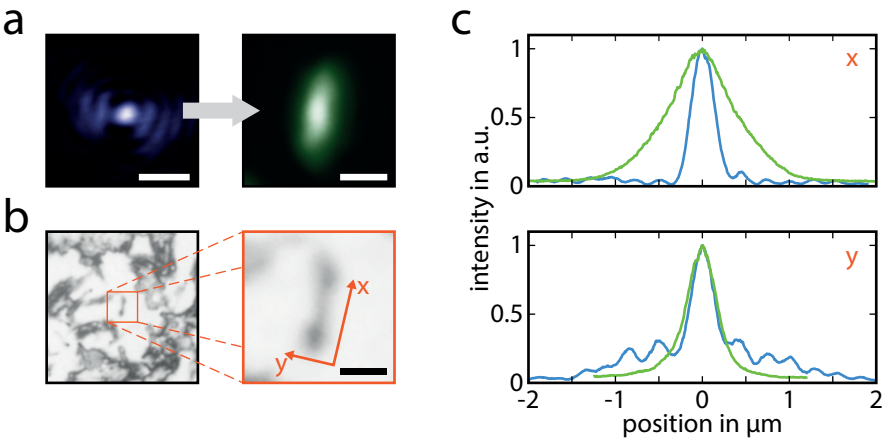

Figure 6.2: Exciton Diffusion via Photoluminescence Mapping for $CsPbBr_3$ Nanowires. (a) 2D intensity maps in false color for the tightly focused excitation laser beam (blue) and the resulting PL profile (green) as obtained from a bundle of parallel-aligned $CsPbBr_3$ nanowires. **(b)** Optical microscopy image of randomly oriented NWs on a substrate. The inset shows the exact sample position underlying the intensity maps presented in (a). As shown here, NWs tend to form bundles of parallel-aligned NWs on such small areas. Based thereon, the x-axis is defined as the direction parallel to the wire orientation, while the y-axis is oriented perpendicular thereto. All three scale bars in (a) and (b) represent 1 µm. **(c)** The center of the excitation spot shown in (a) exhibits a round shape with respective FWHM values of 312 nm and 337 nm for the x- and y-direction (blue curves). However, the normalized PL intensity profiles (green curves) show that excitons mainly diffuse along the wires leading to a FWHM of 873 nm in the x-direction.

pattern may be observed perpendicular to the wire direction along the y-axis. The resulting PL profile in the intensity map in the right panel is ellipsoidal instead of round like the intensity distribution in the previously examined nanocube film.

The exciton diffusion is further investigated in terms of the intensity profiles along the x- and y-direction which are plotted in Figure 6.2 c. FWHM values of 312 nm and 873 nm for the excitation and PL, respectively, yield an exciton diffusion length of $L_{D,x}$ = 346 nm along the x-direction. This shows that exciton diffusion along the wires is more effective, leading to generally larger diffusion lengths. Less defects within the NWs and longer NWs in general could probably lead to even larger values for $L_{D,x}$. The finite size of the bundle itself already limits diffusion along the y-direction, and as shown in the bottom panel of Figure 6.2 c the FWHM of the PL profile basically maintains the respective value given by the laser excitation. Note that the aforementioned interference pattern may be clearly observed in the blue curve within this plot, but not in the PL profile depicted in green.

When comparing the film made of nanocubes and the bundle of nanowires, it may easily be recognized that wires yield an enhanced diffusion length along their orientation, i.e., their long axes. However, variations in the behavior of exciton diffusion might also be caused by the excitation density,[156] the exact arrangement of the NCs or effects like waveguiding or reabsorption. Nevertheless, the above experiment shows that NWs may be highly useful for controlled exciton transport along one defined direction.

6.2 Exciton Diffusion Towards a Quenching Layer

In Subsection 6.1.1, an exciton diffusion length of $L_{D,xy} = 218\,nm$ along the lateral direction was determined for films of $CsPbBr_3$ nanocubes. Intuitively, exciton diffusion along the film thickness, i.e., $L_{D,z}$, should be of similar strength as lateral diffusion. In this final section, a second experimental approach is discussed that was used to determine the exciton diffusion length — this time in z-direction, i.e., perpendicular to the surface of the $CsPbBr_3$ nanocubes film.

As already explained earlier in Subsection 2.5.3, the applied experimental technique relies on a layer-by-layer structure in which a strong electron acceptor material is adjacent to the LHP NC film. A scheme of such a heterostructure as used in this experiment is shown in Figure 6.3 a. The actual samples for the experiments were prepared by first spin-coating a 15 nm film of the strong electron acceptor PCBM onto a glass substrate. In a second step, the spin-coater was employed again to add a layer of $CsPbBr_3$ nanocubes, the thickness of which is tunable such that film thicknesses in the range 25–65 nm could be applied for the experiments.[22] The thickness for each film was determined employing atomic force microscopy (AFM). The energy band diagram shown in Figure 6.3 b elucidates that these layer-by-layer

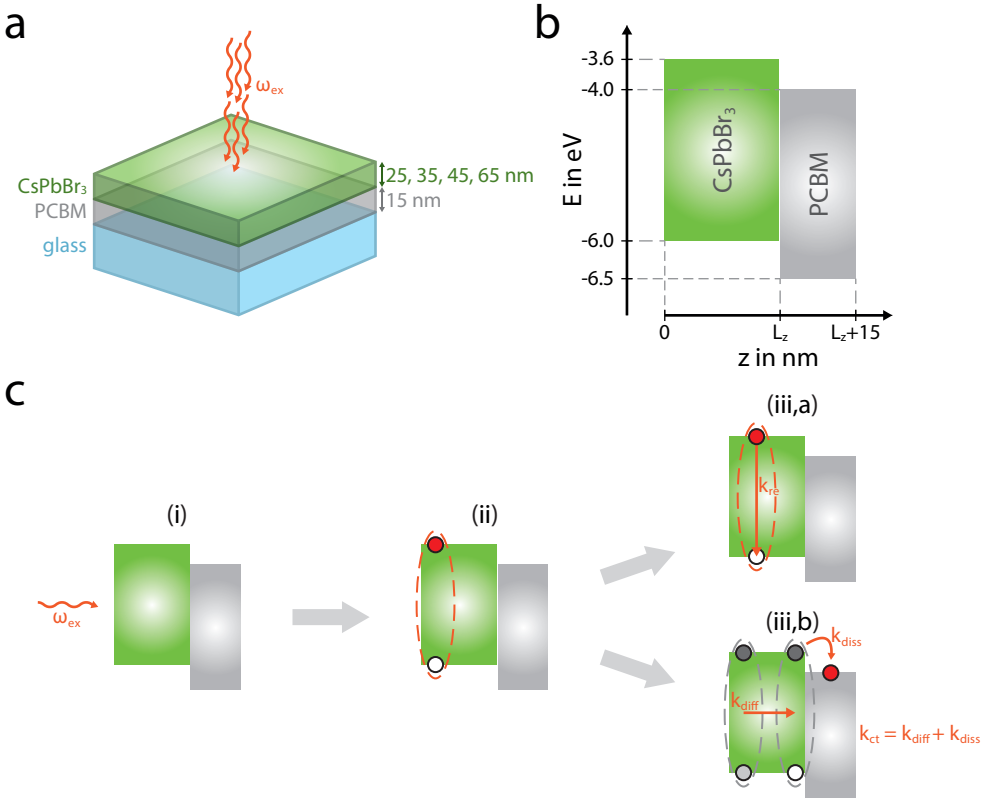

Figure 6.3: Exciton Diffusion in a $CsPbBr_3$ NC/PCBM Layer-by-Layer Heterostructure. **(a)** Scheme of a $CsPbBr_3$ NC/PCBM layer-by-layer heterostructure on a glass substrate. Excitation light is incident perpendicularly to the NC layer for which four different layer thicknesses in the range 25–65 nm were investigated. **(b)** Energy band diagram for the $CsPbBr_3$/PCBM type-II heterostructures shown in (a). L_z denotes the respective thickness of the $CsPbBr_3$ NC layer and energy values are given with respect to the vacuum level. **(c)** Temporal sequence of the experiment: (i) A photon with sufficient energy arrives at the surface of the $CsPbBr_3$ NC layer. (ii) An exciton is generated in this layer via absorption of the photon. (iii,a) From there on, the first option includes all cases in which this exciton recombines within the $CsPbBr_3$ NC layer, either radiatively or nonradiatively. Overall, this process is described by the rate k_{re}. (iii,b) Alternatively, the exciton may diffuse to the interface with the PCBM layer with a rate of k_{diff}, where it may dissociate with a rate of k_{diss}. Taken together, this is considered the so-called charge transfer process occurring at rate k_{ct} which grows more probable with decreasing $CsPbBr_3$ NC layer thickness L_z.

heterostructures exhibit a type-II heterojunction, whereas Figure 6.3 c explains how the shown band alignment enables dissociation of an exciton at the interface between both layers. As depicted in panels (i) and (ii), photoinduced exciton generation takes place in the NC film. Such an exciton then faces either of the following. The first option, illustrated in panel (iii,a), encompasses all processes in which the exciton recombines within the LHP NC film, effectively at a rate k_{re}. The second option, illustrated in panel (iii,b), represents the so-called charge transfer process described by an overall rate k_{ct} at which the exciton reaches the interface towards the PCBM layer via diffusion and subsequently dissociates when the electron is transferred into the PCBM layer, thereby spatially separating electron and hole. For thicker films, the process described by panel (iii,a) is more likely, since excitons might not reach the interface towards the PCBM during their limited lifetime. In contrast, with decreasing NC film thickness, the probability shifts towards the charge transfer process depicted in panel (iii,b). The latter case also forms the basis for PL quenching in the NC layer as this is caused by the charge transfer. This effect has been examined for four samples of different NC layer thicknesses.

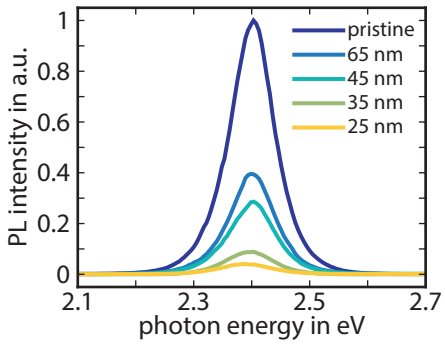

Figure 6.4: Photoluminescence Quenching. PL spectra of $CsPbBr_3$ NC layers with different thicknesses adjacent to a PCBM layer, causing quenching of the PL signal. For comparison, the spectrum for a pristine NC layer, i.e., a sample without any PCBM layer, was recorded as well. The excitation photon energy was 3.1 eV for all spectra.

The PL spectra obtained from these samples are shown in Figure 6.4. The sample labeled "pristine" is a pure $CsPbBr_3$ nanocube film on a glass substrate without a PCBM layer and serves as a reference showing the maximum PL signal emitted from the unperturbed NC layer. Clearly, the PL intensity is effectively quenched by the PCBM. As presumed, the quenching efficiency increases with decreasing NC layer thickness. For the thinnest NC layer (25 nm), the PL intensity is reduced by more than 94 % as compared to the pristine sample. This significant PL quenching is due to the exciton dissociation occurring at the $CsPbBr_3$/PCBM interface.

This constitutes the static limit of the sample and so to investigate the dynamics of these processes, femtosecond pump-probe spectroscopy (see Subsection 3.3.2) was employed to measure the time-resolved DT spectra for these heterostructures. In order to minimize the influence of effects like exciton-exciton annihilation on the DT spectra, a low excitation density of only 3.0 µJ/cm^2 at a wavelength of 400 nm (3.1 eV) was applied. The red curve of Figure 6.5 a represents the steady state absorption of the pristine film and exhibits a clear excitonic peak at its onset. All measurements were conducted at room temperature. With the average thermal energy of the electrons E_{th} being in the range of the exciton binding energy E_{B}, there is a thermal equilibrium of excitons and free e–h pairs after photoexcitation in the NC film. However, the bleaching peak of the DT spectra of this NC film at 2.41 eV due to phase space filling corresponds well to the energetic position of the exciton observed in the linear absorption spectrum.[22] The strong positive symmetric peak lacking any observable shoulder

as well as the presence of a second peak at the high-energy side suggests a predominant contribution of excitons relative to free e-h pairs in thermal equilibrium. As before, for the sake of simplicity, we mostly use the term exciton diffusion which should also include a smaller fraction of free e–h pairs.

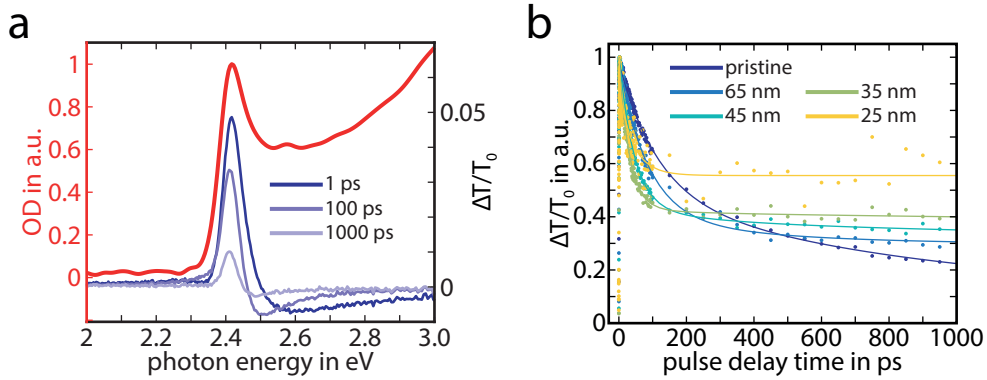

Figure 6.5: Optical Spectroscopy on $CsPbBr_3$/PCBM Heterostructures. **(a)** Absorption spectrum (red, left axis) and corresponding DT transient spectra of a pristine $CsPbBr_3$ NCs film at different pulse delay times (right axis). As in the respective PL measurements, the pump photon energy was set to 3.1 eV (400 nm). **(b)** Normalized DT decay profiles at the energetic position of the excitonic signal (peak in (a)) for the pristine $CsPbBr_3$ NC film and for different thicknesses L_z in the $CsPbBr_3$ NC/PCBM layer-by-layer heterostructure. Solid lines are added to the experimental data (colored circles) as guide to the eyes.

The intensity of the bleaching peak $\Delta T/T_0$ at the excitonic energy is assumed to be proportional to the magnitude of the exciton population in the NC film.[209] The DT spectra of layer-by-layer $CsPbBr_3$/PCBM heterostructures are very similar to the ones of the pristine film and, therefore, this assumption applies for all measurements. The transients describing the exciton dynamics for the respective samples as well as the pristine NC film are plotted in Figure 6.5 b. Especially the initial decay for short pulse delay times $t_{\text{delay}} < 200$ ps is important for the diffusion study. Only the blue curve referring to the pristine sample may be described by a single exponential decay function. In contrast, the transients of the heterostructures exhibit a faster initial decay which grows shorter with decreasing $CsPbBr_3$ NC layer thickness. This faster initial decay is mainly attributed to the electron transfer process from the $CsPbBr_3$ to the PCBM layer.[22] Therefore, the fast initial decay fades out once all photoinduced excitons are either dissociated at the interface towards the PCBM layer or recombined directly within the NC film. On the long end of the timescale $t_{\text{delay}} > 200$ ps, these transients exhibit much slower decay as compared to the pristine NC film. This may be attributed to excess holes remaining in the $CsPbBr_3$ layer after the electron transferred to the PCBM, i.e., after exciton dissociation. Eventually, electrons and holes recombine across the interface, but the limited slope of the transients at long pulse delay times suggests that this is a slow process.

As explained earlier, Figure 6.3 c gives an overview over the two main processes excitons may undergo after their photoexcitation at the NC layer surface. In the pristine film sample, solely the first process is possible, i.e., exciton recombination described by the rate k_{re} including radiative and nonradiative recombination. It fits well into the picture that the transient of the pristine sample is the only curve that might be approximated well by a monoexponential decay (solid dark blue curve in Figure 6.5 b), thereby confirming the model presented in Figure 6.3 c. Therefrom, an exciton lifetime $T_1 = 1/k_{\text{re}} = 350$ ps may be extracted for the pristine film. In contrast, photoinduced excitons in the $CsPbBr_3$/PCBM heterostructures not only undergo recombination within the film at rate k_{re}, but they may also experience charge transfer to the adjacent PCBM layer at rate k_{ct}.[155] Therefore, Equation 2.63 may be employed to describe the overall rate $k_{\text{total}} = k_{\text{re}} + k_{\text{ct}}$ within such heterostructures. The exciton

Table 6.1: Exciton Diffusion Length Analysis. Measured population decay times T_{total} in presence of a quenching layer for different $CsPbBr_3$ NC layer thicknesses L_z. T_1 = 350 ps was extracted based on the pristine NC film and with the help of Equation 2.63, the charge transfer time T_{ct} could be calculated for all samples. Moreover, the exciton diffusion length L_D was calculated using the estimate given by Equation 2.67. The average diffusion length amounts to $L_{D,avg}$ = (298 ± 22) nm.

L_z in nm	T_{total} in ps	T_{ct} in ps	L_D in nm
25	2.40	2.38	271
35	3.20	3.17	328
45	5.90	5.80	309
65	14.1	13.6	286

lifetime in the presence of the quenching layer $T_{total} = 1/k_{total}$ may be extracted from the fast initial decay of the transients shown in Figure 6.5 b for all four heterostructures. The values for T_{total} obtained this way are presented in Table 6.1. Since T_1 = 350 ps is valid for all samples, the time constants for the charge transfer process T_{ct} may be calculated and added to the table using Equation 2.63 again. Finally, the estimate of Equation 2.67 may be applied for all samples in order to calculate the respective exciton diffusion length L_D. Taking into account the individual values for L_D given in Table 6.1, an average exciton diffusion length of $L_{D,avg}$ = (298 ± 22) nm is obtained. Even for the thickest sample with L_z = 65 nm, the overall absorption of the NC film is relatively low as $\alpha L_z \approx 0.1$ in this case. In Equation 2.59 it is shown that αL_z (αz) is part of the term responsible for the exciton generation within the NC film. A small value for αL_z indicates that the initial exciton distribution is relatively homogeneously distributed along the z-direction of the NC film. Recently, it has been reported that the estimate given by Equation 2.67 only entails a small error for such low values of αL_z.[157]

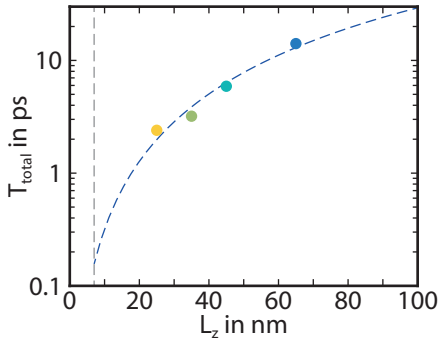

Figure 6.6: Exciton Dissociation at the $CsPbBr_3$/PCBM Interface. Experimentally obtained values for L_z and T_{total} as given in Table 6.1 (colored dots). Plugging the average exciton diffusion length $L_{D,avg}$ = 298 nm into Equation 2.66 leads to a well fitting theoretical model for the data (dashed blue line). This curve is only plotted for $L_z \geq a_{ex}$ = 7 nm as the model may only be used to describe the diffusion process which requires length scales longer than the size of the exciton given by the exciton Bohr radius a_{ex} (vertical dashed grey line). For L_z = 7 nm an exciton finds itself directly at the $CsPbBr_3$/PCBM interface and an exciton dissociation time below 200 fs may be extracted.

The experimentally determined values for T_{total} are also displayed as colored dots in Figure 6.6 for all four heterostructure samples. The fitted model in accordance with Equation 2.66 is added as a dashed blue line using the average value $L_{D,avg}$ = 298 nm for the exciton diffusion length. All experimentally measured data points lie in close proximity to this fitted curve. As indicated by the vertical dashed line in Figure 6.6, values for L_z below the exciton Bohr radius do not have to be considered for the diffusion process as the exciton already finds itself at the interface to the PCBM layer from the very beginning. However, the fitted model may be used to estimate the exciton dissociation time from the point where both dashed lines cross each other. The exact intersection reveals a value of

157 fs at 7 nm and therefore one may conclude that the exciton dissociation at the $CsPbBr_3$/PCBM interface occurs approximately within 200 fs. The value for exciton diffusion along the z-direction $L_{D,z} = L_{D,avg} = 298$ nm obtained here is slightly larger than the value $L_{D,xy} = 218$ nm extracted for the same material in the lateral directions in Subsection 6.1.1. This section focused on the exciton diffusion along the z-axis perpendicular to the NC film (cf. Figure 2.21). The different initial situation with a boundary condition for the diffusion along the z-axis may be the reason for this deviation as excitons directly at the surface may effectively only diffuse in one direction, i.e., the positive direction on the z-axis.

7

Conclusions and Outlook

All in all, the motivation of this thesis was to study exciton dynamics within lead halide perovskite (LHP) nanocrystals (NCs). In particular, three processes have been investigated: recombination, dephasing, and diffusion. Here, in this final chapter, they are addressed individually while highlighting the main findings.

Recombination

Recombination was studied based on $CsPbBr_3$ nanoplatelets (NPls), whose thickness can be controlled with atomic layer level precision. The NPl thickness ranged from 2–6 ML. After a postsynthetic surface trap repair process, high PLQYs in the range 50–75 % were achieved.[20] Linear optical spectroscopy confirmed that all of these NPls belonged to the strong quantum confinement regime. Therefore, the continuum onset was blueshifted with decreasing NPl thickness and large exciton binding energies up to 280 meV were observed. This is why e-h pairs predominantly form excitons within these NPls, even at room temperature. Moreover, tunability of the emission wavelength from dark blue (2 ML) over light blue (6 ML) to green (cubes) is enabled by taking advantage of the quantum confinement induced by variation of the NPl thickness. Overall, this places these $CsPbBr_3$ NPls among the most efficient, tunable blue-emitting perovskites to date. A proof-of-concept experiment demonstrated them to be suitable within an active layer of an LED. Recently, a follow-up study already led to higher EQEs,[198] paving the way for all-perovskite white LEDs and other light-emitting applications. The use of colloidal chemistry at room temperature allows for cost-efficient synthesis of such NPls. Eventually, it could even be possible to print perovskite LEDs when suitable electron and hole injection layers are adapted for this purpose.[210] Either way, efficient charge carrier injection remains one of the main challenges for future devices.

The considerable effect of quantum confinement within these NPls renders them a suitable material for the study of excitons and their recombination behavior. It is important to distinguish between an ensemble of individual NPls dispersed in a solvent and a densely-packed film of such NPls. The former case was chosen for investigation, as the NPls do not interact due to the large distances between them. As reported by Klimov et al., recombination rates are quantized within small NCs, such that the resulting recombination rate of an individual NPl depends on the exact number of excitons the respective NPl contains.[123] In an ensemble of NPls the average amount of excitons per NPl may be controlled via the excitation density.[203] Based thereon, two fundamentally different processes were studied: exciton-exciton annihilation ($2 \longrightarrow 1$ excitons per NPl) with lifetime τ_2 and monomolecular recombination ($1 \longrightarrow 0$ excitons per NPl) with lifetime τ_1. Similar to other reports,[123,203] it could be shown that $\tau_1 \gg \tau_2$. In fact, in this thesis, a difference of 2-3 orders of magnitude could be determined, rendering exciton-exciton annihilation by far the most dominant process occurring in NPls containing more than one exciton. Both lifetimes τ_1 and τ_2 exhibit a dependence on the NPl thickness, i.e., thinner NPls lead to shorter lifetimes. For the 2–6 ML samples the respective lifetimes were in the ranges 7–66 ps for τ_2 and 2.5–6.7 ns for τ_1. A sound knowledge on exciton-exciton annihilation is of importance for LEDs, where such nonradiative recombination generally needs to be suppressed. On the other hand, individual NPls may be interesting for the use as single-photon emitters needed for quantum communication,[211] since even for higher excitation densities usually at most one photon is emitted per NPl.

Dephasing

Dephasing of excitons after photoexcitation, i.e., the polarization decay of an exciton ensemble, was investigated within bulk-like $MAPbI_3$ NPls. Applying four-wave mixing (FWM) using ultrashort femtosecond pulses (115 fs) on such LHP NCs at 25 K enabled the measurement of a dephasing time $T_2 = 800$ fs for the 1s exciton, corresponding to a homogeneous broadening $\Gamma_{\mathrm{hom}}(T) < 2$ meV at such

low temperatures $T < 25\,\mathrm{K}$.[76] Additional temperature-dependent absorption measurements helped to determine the total broadening of the 1s exciton transition $\Gamma_{\mathrm{total}}(T)$, which appears to be unaffected by the crystal phase transition from the orthorhombic to the tetragonal phase at 150 K. The analysis of the broadening data revealed that the temperature-dependent change in $\Gamma_{\mathrm{total}}(T)$ is mainly caused by the interaction of excitons with optical phonons. FWM and absorption data combined show that the temperature-independent inhomogeneous broadening $\Gamma_{\mathrm{inhom}} = 22\,\mathrm{meV}$ is caused by size and shape variations within the NPl ensemble and dominates the total broadening at low temperatures (T<75 K). In contrast, at room temperature $\Gamma_{\mathrm{hom}}(T)$ is three times larger than Γ_{inhom}. Conversely, the dephasing time T_2 is therefore very short at room temperature due to its inverse relation to $\Gamma_{\mathrm{hom}}(T)$. A value of $T_2 \approx 20\,\mathrm{fs}$ is estimated.

Moreover, simultaneous excitation of the exciton and continuum transitions was studied in a FWM experiment, leading to a beating behavior in the FWM signal. This is related to the generation of an exciton wave packet enabling quantum beat spectroscopy (QBS), which was shown to represent an alternative approach to obtain the exciton binding energy E_{B} of the perovskite nanocrystals. A value of $E_{\mathrm{B}} = (25 \pm 2)\,\mathrm{meV}$ was extracted for $MAPbI_3$ NPls in the low temperature regime around 25 K. While there is agreement that the exciton binding energy remains largely independent of temperature, slightly smaller values may be expected with increasing temperature.[53] More recent reports narrowed down the range for E_{B} in $MAPbI_3$ LHPs and obtained values $E_{\mathrm{B}} < 20\,\mathrm{meV}$ at room temperature, which is in good agreement with the results presented here.[51,212] The low value for E_{B} as well as the strong absorption characteristics of $MAPbI_3$ in the visible spectrum are two of the main reasons for the success of this material up to date. Generally, this makes $MAPbI_3$ a promising candidate for future solar cells. However, the replacement of lead as well as the long-term stability of $MAPbI_3$ LHPs remain issues that still need to be addressed in greater detail.[213,214]

Diffusion

Exciton diffusion was examined in $CsPbBr_3$ nanocubes and nanowires (NWs) with two different experimental techniques. On the one hand, PL mapping was applied on a film of densely packed nanocubes and on a bundle of parallel NWs. The nanocube film exhibited a circularly symmetric PL profile and $L_{\mathrm{D}} = 218\,\mathrm{nm}$ was determined for the exciton hopping process. In contrast, the bundle of NWs revealed exciton diffusion to be much stronger along the wires. Here, a value of $L_{\mathrm{D}} = 346\,\mathrm{nm}$ was obtained. This demonstrates the potential use of employing NWs for directed exciton transport along a single, defined direction. On the other hand, the second technique was based on PL quenching. Exciton transport and dissociation were measured in $CsPbBr_3$ NC/PCBM layer-by-layer configurations.[22] The charge carrier dynamics under investigation in these composite structures comprised an exciton diffusion process within the NC film towards the PCBM layer preceding dissociation of the exciton at this interface. The thickness of the NC layer was modified systematically and the effect on the exciton dynamics in the heterostructures was monitored by differential transmission spectroscopy (DTS). An exciton diffusion length of $L_{\mathrm{D}} = 298\,\mathrm{nm}$ was obtained for the film of $CsPbBr_3$ nanocubes. The exciton dissociation process occurring at the $CsPbBr_3$/PCBM interface turned out to be very fast and was estimated to occur on a timescale of less than 200 fs. Notably, both experiments provide fundamental knowledge on exciton transport within and between LHP NCs, representing one of the key elements for overall efficiency of optoelectronic devices.

References

[1] Victor M. Goldschmidt. "Die Gesetze der Krystallochemie". In: *Naturwissenschaften* 14.21 (1926), pp. 477–485. DOI: 10.1007/BF01507527 (cited on pages 1, 21).

[2] A. F. Wells. "332. The crystal structure of $CsCuCl_3$ and the crystal chemistry of complex halides ABX_3". In: *Journal of the Chemical Society (Resumed)* (1947), pp. 1662–1670. DOI: 10.1039/JR9470001662 (cited on page 1).

[3] Oliver Tschauner, Chi Ma, John R. Beckett, Clemens Prescher, Vitali B. Prakapenka, and George R. Rossman. "Discovery of bridgmanite, the most abundant mineral in Earth, in a shocked meteorite". In: *Science* 346.6213 (2014), pp. 1100–1102. DOI: 10.1126/science.1259369 (cited on page 1).

[4] Alexander von Humboldt, Christian Gottfried Ehrenberg, and Gustav Rose. *Reise nach dem Ural, dem Altai und dem Kaspischen Meere*. Verlag der Sanderschen Buchhandlung, 1842 (cited on page 1).

[5] Akihiro Kojima, Kenjiro Teshima, Yasuo Shirai, and Tsutomu Miyasaka. "Organometal halide perovskites as visible-light sensitizers for photovoltaic cells". In: *Journal of the American Chemical Society* 131.17 (2009), pp. 6050–6051. DOI: 10.1021/ja809598r (cited on pages 1, 20).

[6] Constantinos C. Stoumpos and Mercouri G. Kanatzidis. "The renaissance of halide perovskites and their evolution as emerging semiconductors". In: *Accounts of Chemical Research* 48.10 (2015), pp. 2791–2802. DOI: 10.1021/acs.accounts.5b00229 (cited on pages 1, 20).

[7] National Renewable Energy Laboratory. *Best research-cell efficiencies*. URL: https://www.nrel.gov/pv/assets/pdfs/best-research-cell-efficiencies.20191106.pdf (visited on 11/08/2019) (cited on page 1).

[8] Mingzhen Liu, Michael B. Johnston, and Henry J. Snaith. "Efficient planar heterojunction perovskite solar cells by vapour deposition". In: *Nature* 501.7467 (2013), p. 395. DOI: 10.1038/nature12509 (cited on pages 2, 78).

[9] Martin A. Green, Anita Ho-Baillie, and Henry J. Snaith. "The emergence of perovskite solar cells". In: *Nature Photonics* 8.7 (2014), p. 506. DOI: 10.1038/nphoton.2014.134 (cited on pages 2, 78).

[10] Michiel L. Petrus, Johannes Schlipf, Cheng Li, Tanaji P. Gujar, Nadja Giesbrecht, Peter Müller-Buschbaum, Mukundan Thelakkat, Thomas Bein, Sven Hüttner, and Pablo Docampo. "Capturing the sun: A review of the challenges and perspectives of perovskite solar cells". In: *Advanced Energy Materials* 7.16 (2017), p. 1700264. DOI: 10.1002/aenm.201700264 (cited on pages 2, 78).

[11] Loredana Protesescu, Sergii Yakunin, Maryna I. Bodnarchuk, Franziska Krieg, Riccarda Caputo, Christopher H. Hendon, Ruo Xi Yang, Aron Walsh, and Maksym V. Kovalenko. "Nanocrystals of cesium lead halide perovskites ($CsPbX_3$, X = Cl, Br, and I): Novel optoelectronic materials showing bright emission with wide color gamut". In: *Nano Letters* 15.6 (2015), pp. 3692–3696. DOI: 10.1021/nl5048779 (cited on pages 2, 52, 78, 101).

[12] Verena A. Hintermayr, Alexander F. Richter, Florian Ehrat, Markus Döblinger, Willem Vanderlinden, Jasmina A. Sichert, Yu Tong, Lakshminarayana Polavarapu, Jochen Feldmann, and Alexander S. Urban. "Tuning the optical properties of perovskite nanoplatelets through composition and thickness by ligand-assisted exfoliation". In: *Advanced Materials* 28.43 (2016), pp. 9478–9485. DOI: 10.1002/adma.201602897 (cited on pages 2, 22, 94, 95, 101, 104).

[13] Maksym V. Kovalenko, Loredana Protesescu, and Maryna I. Bodnarchuk. "Properties and potential optoelectronic applications of lead halide perovskite nanocrystals". In: *Science* 358.6364 (2017), pp. 745–750. DOI: 10.1126/science.aam7093 (cited on page 2).

[14] Brandon R. Sutherland and Edward H. Sargent. "Perovskite photonic sources". In: *Nature Photonics* 10.5 (2016), p. 295. DOI: 10.1038/nphoton.2016.62 (cited on page 2).

[15] Zhengguo Xiao, Ross A. Kerner, Lianfeng Zhao, Nhu L. Tran, Kyung Min Lee, Tae-Wook Koh, Gregory D. Scholes, and Barry P. Rand. "Efficient perovskite light-emitting diodes featuring nanometre-sized crystallites". In: *Nature Photonics* 11.2 (2017), p. 108. DOI: 10.1038/nphoton.2016.269 (cited on page 2).

[16] Kebin Lin, Jun Xing, Li Na Quan, F. Pelayo García de Arquer, Xiwen Gong, Jianxun Lu, Liqiang Xie, Weijie Zhao, Di Zhang, Chuanzhong Yan, et al. "Perovskite light-emitting diodes with external quantum efficiency exceeding 20 per cent". In: *Nature* 562.7726 (2018), p. 245. DOI: 10.1038/s41586-018-0575-3 (cited on page 2).

[17] Yu Tong, Eva Bladt, Meltem F. Aygüler, Aurora Manzi, Karolina Z. Milowska, Verena A. Hintermayr, Pablo Docampo, Sara Bals, Alexander S. Urban, Lakshminarayana Polavarapu, and Jochen Feldmann. "Highly luminescent cesium lead halide perovskite nanocrystals with tunable composition and thickness by ultrasonication". In: *Angewandte Chemie International Edition* 55.44 (2016), pp. 13887–13892. DOI: 10.1002/anie.201605909 (cited on pages 2, 21, 78).

[18] Javad Shamsi, Alexander S. Urban, Muhammad Imran, Luca De Trizio, and Liberato Manna. "Metal halide perovskite nanocrystals: Synthesis, post-synthesis modifications, and their optical properties". In: *Chemical Reviews* 119.5 (2019), pp. 3296–3348. DOI: 10.1021/acs.chemrev.8b00644 (cited on pages 2, 20, 22–24, 55).

[19] Jasmina A. Sichert, Yu Tong, Niklas Mutz, Mathias Vollmer, Stefan Fischer, Karolina Z. Milowska, Ramon García Cortadella, Bert Nickel, Carlos Cardenas-Daw, Jacek K. Stolarczyk, Alexander S. Urban, and Jochen Feldmann. "Quantum size effect in organometal halide perovskite nanoplatelets". In: *Nano Letters* 15.10 (2015), pp. 6521–6527. DOI: 10.1021/acs.nanolett.5b02985 (cited on pages 2, 14, 22, 78).

[20] Bernhard J. Bohn, Yu Tong, Moritz Gramlich, May Ling Lai, Markus Döblinger, Kun Wang, Robert L. Z. Hoye, Peter Müller-Buschbaum, Samuel D. Stranks, Alexander S. Urban, Lakshminarayana Polavarapu, and Jochen Feldmann. "Boosting tunable blue luminescence of halide perovskite nanoplatelets through postsynthetic surface trap repair". In: *Nano Letters* 18.8 (2018), pp. 5231–5238. DOI: 10.1021/acs.nanolett.8b02190 (cited on pages 2, 14, 22, 30, 52, 54, 78, 82, 88, 95, 122).

[21] Yu Tong, Bernhard J. Bohn, Eva Bladt, Kun Wang, Peter Müller-Buschbaum, Sara Bals, Alexander S. Urban, Lakshminarayana Polavarapu, and Jochen Feldmann. "From precursor powders to $CsPbX_3$ perovskite nanowires: One-pot synthesis, growth mechanism, and oriented self-assembly". In: *Angewandte Chemie International Edition* 56.44 (2017), pp. 13887–13892. DOI: 10.1002/anie.201707224 (cited on pages 2, 20, 22, 54, 78, 98, 99).

[22] En-Ping Yao, Bernhard J. Bohn, Yu Tong, He Huang, Lakshminarayana Polavarapu, and Jochen Feldmann. "Exciton diffusion lengths and dissociation rates in CsPbBr3 nanocrystal-fullerene composites: Layer-by-layer versus blend structures". In: *Advanced Optical Materials* 7.8 (2019), p. 1801776. DOI: 10.1002/adom.201801776 (cited on pages 2, 11, 50, 54, 98, 115–117, 123).

[23] Yu Tong, En-Ping Yao, Aurora Manzi, Eva Bladt, Kun Wang, Markus Döblinger, Sara Bals, Peter Müller-Buschbaum, Alexander S. Urban, Lakshminarayana Polavarapu, and Jochen Feldmann. "Spontaneous self-assembly of perovskite nanocrystals into electronically coupled supercrystals: Toward filling the green gap". In: *Advanced Materials* 30.29 (2018), p. 1801117. DOI: 10.1002/adma.201801117 (cited on pages 2, 54, 98).

[24] Lakshminarayana Polavarapu, Bert Nickel, Jochen Feldmann, and Alexander S. Urban. "Advances in Quantum-Confined Perovskite Nanocrystals for Optoelectronics". In: *Advanced Energy Materials* 7.16 (2017), p. 1700267. DOI: 10.1002/aenm.201700267 (cited on page 2).

[25] Yu Tong, Ming Fu, Eva Bladt, He Huang, Alexander F. Richter, Kun Wang, Peter Müller-Buschbaum, Sara Bals, Philippe Tamarat, Brahim Lounis, Jochen Feldmann, and Lakshminarayana Polavarapu. "Chemical cutting of perovskite nanowires into single-photon emissive low-aspect-ratio $CsPbX_3$ (X = Cl, Br, I) nanorods". In: *Angewandte Chemie International Edition* 130.49 (2018), pp. 16326–16330. DOI: 10.1002/anie.201810110 (cited on pages 2, 54).

[26] Roger J. Elliott. "Intensity of optical absorption by excitons". In: *Physical Review* 108.6 (1957), p. 1384. DOI: 10.1103/PhysRev.108.1384 (cited on pages 2, 11, 80).

[27] Michael Kasha, Henry R. Rawls, and M. Ashraf El-Bayoumi. "The exciton model in molecular spectroscopy". In: *Pure and Applied Chemistry* 11.3-4 (1965), pp. 371–392. DOI: 10.1351/pac196511030371 (cited on page 2).

[28] Y. Kayanuma. "Wannier exciton in microcrystals". In: *Solid State Communications* 59.6 (1986), pp. 405–408. DOI: 10.1016/0038-1098(86)90573-9 (cited on page 2).

[29] Arnold Sommerfeld. "Zur Elektronentheorie der Metalle auf Grund der fermischen Statistik". In: *Zeitschrift für Physik* 47.1-2 (1928), pp. 1–32. DOI: 10.1007/BF01391052 (cited on page 4).

[30] Felix Bloch. "Über die Quantenmechanik der Elektronen in Kristallgittern". In: *Zeitschrift für physik* 52.7-8 (1929), pp. 555–600. DOI: 10.1007/BF01339455 (cited on page 4).

[31] Alan Herries Wilson. "The theory of electronic semi-conductors". In: *Proceedings of the Royal Society of London. Series A, Containing Papers of a Mathematical and Physical Character* 133.822 (1931), pp. 458–491. DOI: 10.1098/rspa.1931.0162 (cited on pages 4, 5).

[32] Claus F. Klingshirn. *Semiconductor optics*. Springer Science & Business Media, 2012. DOI: 10.1007/978-3-642-28362-8 (cited on pages 4–6, 8, 39, 40).

[33] Russell S. Ohl. "Light-sensitive electric device". US Patent 2,402,662. June 25, 1946 (cited on page 4).

[34] John Bardeen and Walter Hauser Brattain. "The transistor, a semi-conductor triode". In: *Physical Review* 74.2 (1948), p. 230. DOI: 10.1103/PhysRev.74.230 (cited on page 4).

[35] John Singleton. *Band theory and electronic properties of solids*. Oxford University Press, 2001 (cited on pages 4, 5, 12).

[36] Erwin Schrödinger. "Quantisierung als Eigenwertproblem". In: *Annalen der Physik* 385.13 (1926), pp. 437–490. DOI: 10.1002/andp.19263851302 (cited on page 4).

[37] Feliks Aleksandrovich Berezin and M. Shubin. *The Schrödinger equation*. Springer Science + Business Media, 1991. DOI: 10.1007/978-94-011-3154-4 (cited on page 4).

[38] Hartmut Haug and Stephan W. Koch. *Quantum theory of the optical and electronic properties of semiconductors*. World Scientific Publishing Company, 2009 (cited on pages 4, 9, 12).

[39] Clarence Zener. "Non-adiabatic crossing of energy levels". In: *Proceedings of the Royal Society of London. Series A, Containing Papers of a Mathematical and Physical Character* 137.833 (1932), pp. 696–702. DOI: 10.1098/rspa.1932.0165 (cited on page 5).

[40] Charles Kittel and Ching-Yao Fong. *Quantum theory of solids*. Wiley New York, 1963 (cited on pages 5, 6, 8, 17).

[41] Thomas Ihn. *Semiconductor nanostructures: Quantum states and electronic transport*. Oxford University Press, 2010. DOI: 10.1093/acprof:oso/9780199534425.001.0001 (cited on pages 5, 10).

[42] Dieter Meschede. *Gerthsen Physik*. Springer-Verlag, 2005. DOI: 10.1007/978-3-662-45977-5 (cited on page 5).

[43] Enrico Fermi. "Eine statistische Methode zur Bestimmung einiger Eigenschaften des Atoms und ihre Anwendung auf die Theorie des periodischen Systems der Elemente". In: *Zeitschrift für Physik* 48.1-2 (1928), pp. 73–79. DOI: 10.1007/BF01351576 (cited on page 6).

[44] Paul Adrien Maurice Dirac. "On the theory of quantum mechanics". In: *Proceedings of the Royal Society of London. Series A, Containing Papers of a Mathematical and Physical Character* 112.762 (1926), pp. 661–677. DOI: 10.1098/rspa.1926.0133 (cited on page 6).

[45] Tilmann D. Märk and Gordon H. Dunn. *Electron impact ionization*. Springer Science & Business Media, 2013. DOI: 10.1007/978-3-7091-4028-4 (cited on page 7).

[46] Henry Kressel. *Semiconductor lasers and herterojunction LEDs*. Elsevier, 2012. DOI: 10.1016/b978-0-12-426250-8.x5001-5 (cited on page 7).

[47] Paul Adrien Maurice Dirac. "The quantum theory of the emission and absorption of radiation". In: *Proceedings of the Royal Society of London. Series A, Containing Papers of a Mathematical and Physical Character* 114.767 (1927), pp. 243–265. DOI: 10.1098/rspa.1927.0039 (cited on page 7).

[48] Franz Schwabl. *Quantenmechanik für Fortgeschrittene (QM II)*. Springer-Verlag, 2008. DOI: 10.1007/978-3-540-85076-2 (cited on page 7).

[49] Mehran Samiee, Siva Konduri, Balaji Ganapathy, Ranjith Kottokkaran, Hisham A. Abbas, Andrew Kitahara, Pranav Joshi, Liang Zhang, Max Noack, and Vikram Dalal. "Defect density and dielectric constant in perovskite solar cells". In: *Applied Physics Letters* 105.15 (2014), p. 153502. DOI: 10.1063/1.4897329 (cited on page 8).

[50] Emilio J Juarez-Perez, Rafael S Sanchez, Laura Badia, Germá Garcia-Belmonte, Yong Soo Kang, Ivan Mora-Sero, and Juan Bisquert. "Photoinduced giant dielectric constant in lead halide perovskite solar cells". In: *The Journal of Physical Chemistry Letters* 5.13 (2014), pp. 2390–2394. DOI: 10.1021/jz5011169 (cited on page 8).

[51] Zhuo Yang, Alessandro Surrente, Krzysztof Galkowski, Nicolas Bruyant, Duncan K. Maude, Amir Abbas Haghighirad, Henry J Snaith, Paulina Plochocka, and Robin J. Nicholas. "Unraveling the exciton binding energy and the dielectric constant in single-crystal methylammonium lead triiodide perovskite". In: *The Journal of Physical Chemistry Letters* 8.8 (2017), pp. 1851–1855. DOI: 10.1021/acs.jpclett.7b00524 (cited on pages 8, 123).

[52] Verena A. Hintermayr, Lakshminarayana Polavarapu, Alexander S. Urban, and Jochen Feldmann. "Accelerated carrier relaxation through reduced Coulomb screening in two-dimensional halide perovskite nanoplatelets". In: *ACS Nano* 12.10 (2018), pp. 10151–10158. DOI: 10.1021/acsnano.8b05029 (cited on pages 8, 15, 22, 27).

[53] Laura M. Herz. "Charge-carrier dynamics in organic-inorganic metal halide perovskites". In: *Annual Review of Physical Chemistry* 67 (2016), pp. 65–89. DOI: 10.1146/annurev-physchem-040215-112222 (cited on pages 8, 23, 44, 81, 101, 109, 123).

[54] Jenya Tilchin, Dmitry N. Dirin, Georgy I. Maikov, Aldona Sashchiuk, Maksym V. Kovalenko, and Efrat Lifshitz. "Hydrogen-like wannier–mott excitons in single crystal of methylammonium lead bromide perovskite". In: *ACS Nano* 10.6 (2016), pp. 6363–6371. DOI: 10.1021/acsnano.6b02734 (cited on page 8).

[55] Jasprit Singh. *Semiconductor optoelectronics: Physics and technology*. McGraw-Hill, 1995 (cited on page 9).

[56] Peter Y. Yu and Manuel Cardona. *Fundamentals of semiconductors: Physics and materials properties*. Springer, 2010. DOI: 10.1007/978-3-642-00710-1 (cited on pages 9, 28).

[57] B. S. Wherrett. "Scaling rules for multiphoton interband absorption in semiconductors". In: *JOSA B* 1.1 (1984), pp. 67–72. DOI: 10.1364/JOSAB.1.000067 (cited on page 10).

[58] Vaidya Nathan, Arthur H. Guenther, and Shashanka S. Mitra. "Review of multiphoton absorption in crystalline solids". In: *JOSA B* 2.2 (1985), pp. 294–316. DOI: 10.1364/JOSAB.2.000294 (cited on page 10).

[59] Aurora Manzi, Yu Tong, Julius Feucht, En-Ping Yao, Lakshminarayana Polavarapu, Alexander S. Urban, and Jochen Feldmann. "Resonantly enhanced multiple exciton generation through below-band-gap multi-photon absorption in perovskite nanocrystals". In: *Nature Communications* 9.1 (2018), p. 1518. DOI: 10.1038/s41467-018-03965-8 (cited on pages 10, 62).

[60] K. Xerxes Steirer, Philip Schulz, Glenn Teeter, Vladan Stevanovic, Mengjin Yang, Kai Zhu, and Joseph J. Berry. "Defect tolerance in methylammonium lead triiodide perovskite". In: *ACS Energy Letters* 1.2 (2016), pp. 360–366. DOI: 10.1021/acsenergylett.6b00196 (cited on page 10).

[61] He Huang, Maryna I. Bodnarchuk, Stephen V. Kershaw, Maksym V. Kovalenko, and Andrey L. Rogach. "Lead halide perovskite nanocrystals in the research spotlight: Stability and defect tolerance". In: *ACS Energy Letters* 2.9 (2017), pp. 2071–2083. DOI: 10.1021/acsenergylett.7b00547 (cited on pages 10, 24, 54).

[62] Peter Grosse. *Freie Elektronen in Festkörpern*. Springer-Verlag, 2013. DOI: 10.1007/978-3-642-95344-6 (cited on page 11).

[63] Valerio D'innocenzo, Giulia Grancini, Marcelo J. P. Alcocer, Ajay Ram Srimath Kandada, Samuel D. Stranks, Michael M. Lee, Guglielmo Lanzani, Henry J. Snaith, and Annamaria Petrozza. "Excitons versus free charges in organo-lead tri-halide perovskites". In: *Nature Communications* 5 (2014), p. 3586. DOI: 10.1038/ncomms4586 (cited on pages 11, 35).

[64] Stephan Glutsch. *Excitons in low-dimensional semiconductors: Theory numerical methods applications*. Vol. 141. Springer Science & Business Media, 2013. DOI: 10.1007/978-3-662-07150-2 (cited on page 12).

[65] Mark Fox. *Optical properties of solids*. Oxford University Press, 2002 (cited on pages 12–14, 16).

[66] Marius Fischer. *Upstream-Patente in der Nanotechnologie: Ein Vergleich zwischen Europa und den USA*. Heymanns, Carl, 2019 (cited on page 12).

[67] John H. Davies. *The physics of low-dimensional semiconductors: An introduction*. Cambridge University Press, 1998. DOI: 10.1017/CBO9780511819070 (cited on pages 12, 13).

[68] Alexey Chernikov, Timothy C. Berkelbach, Heather M. Hill, Albert Rigosi, Yilei Li, Ozgur Burak Aslan, David R. Reichman, Mark S. Hybertsen, and Tony F. Heinz. "Exciton binding energy and nonhydrogenic Rydberg series in monolayer WS_2". In: *Physical Review Letters* 113.7 (2014), p. 076802. DOI: 10.1103/PhysRevLett.113.076802 (cited on page 15).

[69] Wolfgang Demtröder. *Laserspektroskopie 1: Grundlagen*. Springer-Verlag, 2011. DOI: 10.1007/978-3-642-21306-9 (cited on pages 15, 18, 36).

[70] RP Photonics Encyclopedia. *Homogeneous broadening*. URL: https://www.rp-photonics.com/homogeneous_broadening.html (visited on 04/20/2019) (cited on page 16).

[71] Christian Wehrenfennig, Mingzhen Liu, Henry J. Snaith, Michael B. Johnston, and Laura M. Herz. "Homogeneous emission line broadening in the organo lead halide perovskite $CH_3NH_3PbI_3$–x cl x". In: *The Journal of Physical Chemistry Letters* 5.8 (2014), pp. 1300–1306. DOI: 10.1021/jz500434p (cited on page 16).

[72] Adam D. Wright, Carla Verdi, Rebecca L. Milot, Giles E. Eperon, Miguel A. Pérez-Osorio, Henry J. Snaith, Feliciano Giustino, Michael B. Johnston, and Laura M. Herz. "Electron–phonon coupling in hybrid lead halide perovskites". In: *Nature Communications* 7 (2016), p. 11755. DOI: 10.1038/ncomms11755(2016) (cited on pages 17, 20, 21, 36, 103).

[73] Rinku Saran, Amelie Heuer-Jungemann, Antonios G. Kanaras, and Richard J. Curry. "Giant bandgap renormalization and exciton–phonon scattering in perovskite nanocrystals". In: *Advanced Optical Materials* 5.17 (2017), p. 1700231. DOI: 10.1002/adom.201700231 (cited on pages 17, 103).

[74] S. Rudin, T. L. Reinecke, and B. Segall. "Temperature-dependent exciton linewidths in semiconductors". In: *Physical Review B* 42.17 (1990), p. 11218. DOI: 10.1103/PhysRevB.42.11218 (cited on page 17).

[75] L. Malikova, Wojciech Krystek, Fred H. Pollak, N. Dai, A. Cavus, and M. C. Tamargo. "Temperature dependence of the direct gaps of ZnSe and $Zn_{0.56}Cd_{0.44}Se$". In: *Physical Review B* 54.3 (1996), p. 1819. DOI: 10.1103/PhysRevB.54.1819 (cited on page 17).

[76] Bernhard J. Bohn, Thomas Simon, Moritz Gramlich, Alexander F. Richter, Lakshminarayana Polavarapu, Alexander S. Urban, and Jochen Feldmann. "Dephasing and quantum beating of excitons in methylammonium lead iodide perovskite nanoplatelets". In: *ACS Photonics* 5.2 (2017), pp. 648–654. DOI: 10.1021/acsphotonics.7b01292 (cited on pages 17, 20, 21, 25, 36, 54, 72, 98, 101, 103, 123).

[77] L. Schultheis, A. Honold, J. Kuhl, K. Köhler, and C. W. Tu. "Optical dephasing of homogeneously broadened two-dimensional exciton transitions in GaAs quantum wells". In: *Physical Review B* 34.12 (1986), p. 9027. DOI: 10.1103/PhysRevB.34.9027 (cited on page 17).

[78] Jochen Feldmann, G Peter, Ernst O. Göbel, P. Dawson, K. Moore, C. Foxon, and Roger J. Elliott. "Linewidth dependence of radiative exciton lifetimes in quantum wells". In: *Physical Review Letters* 59.20 (1987), p. 2337. DOI: 10.1103/PhysRevLett.59.2337 (cited on pages 17, 94, 95, 102).

[79] A. Paul Alivisatos, A. L. Harris, N. J. Levinos, M. L. Steigerwald, and L. E. Brus. "Electronic states of semiconductor clusters: Homogeneous and inhomogeneous broadening of the optical spectrum". In: *The Journal of Chemical Physics* 89.7 (1988), pp. 4001–4011. DOI: 10.1063/1.454833 (cited on page 17).

[80] Nathalie Perret, Denis Morris, Loic Franchomme-Fossé, René Côté, Simon Fafard, Vincent Aimez, and Jacques Beauvais. "Origin of the inhomogeneous broadening and alloy intermixing in InAs/GaAs self-assembled quantum dots". In: *Physical Review B* 62.8 (2000), p. 5092. DOI: 10.1103/PhysRevB.62.5092 (cited on page 17).

[81] T. Sakurai and T. Sugano. "Theory of continuously distributed trap states at Si-SiO2 interfaces". In: *Journal of Applied Physics* 52.4 (1981), pp. 2889–2896. DOI: 10.1063/1.329023 (cited on page 18).

[82] Handong Jin, Elke Debroye, Masoumeh Keshavarz, Ivan G. Scheblykin, Maarten B. J. Roeffaers, Johan Hofkens, and Julian A. Steele. "It's a trap! On the nature of localised states and charge trapping in lead halide perovskites". In: *Materials Horizons* (2019). DOI: 10.1039/C9MH00500E (cited on pages 18, 24, 29).

[83] Yatendra Pal Varshni. "Temperature dependence of the energy gap in semiconductors". In: *Physica* 34.1 (1967), pp. 149–154. DOI: 10.1016/0031-8914(67)90062-6 (cited on pages 18, 20).

[84] Jiping Ye, Sigeo Soeda, Yoshio Nakamura, and Osamu Nittono. "Crystal structures and phase transformation in In_2Se_3 compound semiconductor". In: *Japanese Journal of Applied Physics* 37.8 (1998), p. 4264. DOI: 10.1143/jjap.37.4264 (cited on page 19).

[85] Henry J. Snaith. "Present status and future prospects of perovskite photovoltaics". In: *Nature Materials* 17.5 (2018), p. 372. DOI: 10.1038/s41563-018-0071-z (cited on page 20).

[86] Quinten A. Akkerman, Valerio D'Innocenzo, Sara Accornero, Alice Scarpellini, Annamaria Petrozza, Mirko Prato, and Liberato Manna. "Tuning the optical properties of cesium lead halide perovskite nanocrystals by anion exchange reactions". In: *Journal of the American Chemical Society* 137.32 (2015), pp. 10276–10281. DOI: 10.1021/jacs.5b05602 (cited on page 20).

[87] Georgian Nedelcu, Loredana Protesescu, Sergii Yakunin, Maryna I. Bodnarchuk, Matthias J. Grotevent, and Maksym V. Kovalenko. "Fast anion-exchange in highly luminescent nanocrystals of cesium lead halide perovskites ($CsPbX_3$, X = Cl, Br, I)". In: *Nano Letters* 15.8 (2015), pp. 5635–5640. DOI: 10.1021/acs.nanolett.5b02404 (cited on page 20).

[88] Federico Brivio, Jarvist M. Frost, Jonathan M. Skelton, Adam J. Jackson, Oliver J. Weber, Mark T. Weller, Alejandro R. Goni, Aurélien M. A. Leguy, Piers R. F. Barnes, and Aron Walsh. "Lattice dynamics and vibrational spectra of the orthorhombic, tetragonal, and cubic phases of methylammonium lead iodide". In: *Physical Review B* 92.14 (2015), p. 144308. DOI: 10.1103/PhysRevB.92.144308 (cited on page 20).

[89] Parthiban Ramasamy, Da-Hye Lim, Bumjin Kim, Seung-Ho Lee, Min-Sang Lee, and Jong-Soo Lee. "All-inorganic cesium lead halide perovskite nanocrystals for photodetector applications". In: *Chemical Communications* 52.10 (2016), pp. 2067–2070. DOI: 10.1039/C5CC08643D (cited on page 21).

[90] Sebastian Rieger, Bernhard J. Bohn, Markus Döblinger, Alexander F. Richter, Yu Tong, Kun Wang, Peter Müller-Buschbaum, Lakshminarayana Polavarapu, Linn Leppert, Jacek K. Stolarczyk, and Jochen Feldmann. "Excitons and narrow bands determine the optical properties of cesium bismuth halides". In: *Physical Review B* 100.20 (2019), p. 201404. DOI: 10.1103/PhysRevB.100.201404 (cited on pages 21, 54).

[91] Gregor Kieslich, Shijing Sun, and Anthony K. Cheetham. "An extended tolerance factor approach for organic-inorganic perovskites". In: *Chemical Science* 6.6 (2015), pp. 3430–3433. DOI: 10.1039/C5SC00961H (cited on page 21).

[92] Wired Chemist. *Metallic, covalent and ionic radii*. URL: http://www.wiredchemist.com/chemistry/data/metallic-radii (visited on 04/20/2019) (cited on page 21).

[93] Zhen Li, Mengjin Yang, Ji-Sang Park, Su-Huai Wei, Joseph J Berry, and Kai Zhu. "Stabilizing perovskite structures by tuning tolerance factor: Formation of formamidinium and cesium lead iodide solid-state alloys". In: *Chemistry of Materials* 28.1 (2015), pp. 284–292. DOI: 10.1021/acs.chemmater.5b04107 (cited on page 21).

[94] Shunsuke Hirotsu, Jimpei Harada, Masashi Iizumi, and Kazuo Gesi. "Structural phase transitions in $CsPbBr_3$". In: *Journal of the Physical Society of Japan* 37.5 (1974), pp. 1393–1398. DOI: 10.1143/JPSJ.37.1393 (cited on pages 21, 102).

[95] Joseph S. Manser, Jeffrey A. Christians, and Prashant V. Kamat. "Intriguing optoelectronic properties of metal halide perovskites". In: *Chemical Reviews* 116.21 (2016), pp. 12956–13008. DOI: 10.1021/acs.chemrev.6b00136 (cited on pages 21, 102).

[96] Noriko Onoda-Yamamuro, Takasuke Matsuo, and Hiroshi Suga. "Calorimetric and IR spectroscopic studies of phase transitions in methylammonium trihalogenoplumbates (II)". In: *Journal of Physics and Chemistry of Solids* 51.12 (1990), pp. 1383–1395. DOI: 10.1016/0022-3697(90)90021-7 (cited on page 21).

[97] Abhishek Swarnkar, Ashley R. Marshall, Erin M. Sanehira, Boris D. Chernomordik, David T. Moore, Jeffrey A. Christians, Tamoghna Chakrabarti, and Joseph M. Luther. "Quantum dot–induced phase stabilization of α-$CsPbI_3$ perovskite for high-efficiency photovoltaics". In: *Science* 354.6308 (2016), pp. 92–95. DOI: 10.1126/science.aag2700 (cited on page 21).

[98] Dehui Li, Gongming Wang, Hung-Chieh Cheng, Chih-Yen Chen, Hao Wu, Yuan Liu, Yu Huang, and Xiangfeng Duan. "Size-dependent phase transition in methylammonium lead iodide perovskite microplate crystals". In: *Nature Communications* 7 (2016), p. 11330. DOI: 10.1038/ncomms11330 (cited on pages 21, 102).

[99] Edoardo Mosconi, Anna Amat, Md. K. Nazeeruddin, Michael Grätzel, and Filippo De Angelis. "First-principles modeling of mixed halide organometal perovskites for photovoltaic applications". In: *The Journal of Physical Chemistry C* 117.27 (2013), pp. 13902–13913. DOI: 10.1021/jp4048659 (cited on page 22).

[100] Jacky Even, Laurent Pedesseau, Jean-Marc Jancu, and Claudine Katan. "DFT and k·p modelling of the phase transitions of lead and tin halide perovskites for photovoltaic cells". In: *Physica Status Solidi (RRL) – Rapid Research Letters* 8.1 (2014), pp. 31–35. DOI: 10.1002/pssr.201308183 (cited on page 22).

[101] Federico Brivio, Keith T. Butler, Aron Walsh, and Mark Van Schilfgaarde. "Relativistic quasiparticle self-consistent electronic structure of hybrid halide perovskite photovoltaic absorbers". In: *Physical Review B* 89.15 (2014), p. 155204. DOI: 10.1103/PhysRevB.89.155204 (cited on page 22).

[102] Anna Amat, Edoardo Mosconi, Enrico Ronca, Claudio Quarti, Paolo Umari, Md. K. Nazeeruddin, Michael Grätzel, and Filippo De Angelis. "Cation-induced band-gap tuning in organohalide perovskites: Interplay of spin–orbit coupling and octahedra tilting". In: *Nano Letters* 14.6 (2014), pp. 3608–3616. DOI: 10.1021/nl5012992 (cited on page 22).

[103] Claudine Katan, Laurent Pedesseau, Mikaël Kepenekian, Alain Rolland, and Jacky Even. "Interplay of spin–orbit coupling and lattice distortion in metal substituted 3D tri-chloride hybrid perovskites". In: *Journal of Materials Chemistry A* 3.17 (2015), pp. 9232–9240. DOI: 10.1039/C4TA06418F (cited on page 22).

[104] Xingang Zhao, Gustavo M Dalpian, Zhi Wang, and Alex Zunger. "The polymorphous nature of cubic halide perovskites". In: *arXiv preprint arXiv:1905.09141* (2019) (cited on page 23).

[105] David A. Egger, Achintya Bera, David Cahen, Gary Hodes, Thomas Kirchartz, Leeor Kronik, Robert Lovrincic, Andrew M. Rappe, David R. Reichman, and Omer Yaffe. "What remains unexplained about the properties of halide perovskites?" In: *Advanced Materials* 30.20 (2018), p. 1800691. DOI: 10.1002/adma.201800691 (cited on page 23).

[106] Jacky Even, Laurent Pedesseau, and Claudine Katan. "Analysis of multivalley and multibandgap absorption and enhancement of free carriers related to exciton screening in hybrid perovskites". In: *The Journal of Physical Chemistry C* 118.22 (2014), pp. 11566–11572. DOI: 10.1021/jp503337a (cited on pages 23, 24).

[107] Jacky Even, Laurent Pedesseau, Claudine Katan, Mikaël Kepenekian, Jean-Sébastien Lauret, Daniel Sapori, and Emmanuelle Deleporte. "Solid-state physics perspective on hybrid perovskite semiconductors". In: *The Journal of Physical Chemistry C* 119.19 (2015), pp. 10161–10177. DOI: 10.1021/acs.jpcc.5b00695 (cited on pages 23, 24).

[108] T. Umebayashi, K. Asai, T. Kondo, and A. Nakao. "Electronic structures of lead iodide based low-dimensional crystals". In: *Physical Review B* 67.15 (2003), p. 155405. DOI: 10.1103/PhysRevB.67.155405 (cited on page 23).

[109] Philip Schulz, Eran Edri, Saar Kirmayer, Gary Hodes, David Cahen, and Antoine Kahn. "Interface energetics in organo-metal halide perovskite-based photovoltaic cells". In: *Energy & Environmental Science* 7.4 (2014), pp. 1377–1381. DOI: 10.1039/C4EE00168K (cited on page 23).

[110] Jacky Even, Laurent Pedesseau, Jean-Marc Jancu, and Claudine Katan. "Importance of spin–orbit coupling in hybrid organic/inorganic perovskites for photovoltaic applications". In: *The Journal of Physical Chemistry Letters* 4.17 (2013), pp. 2999–3005. DOI: 10.1021/jz401532q (cited on page 23).

[111] J. S. Blakemore. "Semiconducting and other major properties of gallium arsenide". In: *Journal of Applied Physics* 53.10 (1982), R123–R181. DOI: 10.1063/1.331665 (cited on page 23).

[112] Wan-Jian Yin, Tingting Shi, and Yanfa Yan. "Unusual defect physics in $CH_3NH_3PbI_3$ perovskite solar cell absorber". In: *Applied Physics Letters* 104.6 (2014), p. 063903. DOI: 10.1063/1.4864778 (cited on page 24).

[113] Jun Kang and Lin-Wang Wang. "High defect tolerance in lead halide perovskite $CsPbBr_3$". In: *The Journal of Physical Chemistry Letters* 8.2 (2017), pp. 489–493. DOI: 10.1021/acs.jpclett.6b02800 (cited on page 24).

[114] Ming Fu, Philippe Tamarat, He Huang, Jacky Even, Andrey L. Rogach, and Brahim Lounis. "Neutral and charged exciton fine structure in single lead halide perovskite nanocrystals revealed by magneto-optical spectroscopy". In: *Nano Letters* 17.5 (2017), pp. 2895–2901. DOI: 10.1021/acs.nanolett.7b00064 (cited on page 24).

[115] Michael A. Becker, Roman Vaxenburg, Georgian Nedelcu, Peter C. Sercel, Andrew Shabaev, Michael J. Mehl, John G. Michopoulos, Samuel G. Lambrakos, Noam Bernstein, John L. Lyons, Thilo Stöferle, Rainer F. Mahrt, Maksym V. Kovalenko, David J. Norris, Gabriele Rainò, and Alexander L. Efros. "Bright triplet excitons in caesium lead halide perovskites". In: *Nature* 553.7687 (2018), p. 189. DOI: 10.1038/nature25147 (cited on page 24).

[116] Philippe Tamarat, Maryna I. Bodnarchuk, Jean-Baptiste Trebbia, Rolf Erni, Maksym V. Kovalenko, Jacky Even, and Brahim Lounis. "The ground exciton state of formamidinium lead bromide perovskite nanocrystals is a singlet dark state". In: *Nature Materials* 18.7 (2019), pp. 717–724. DOI: 10.1038/s41563-019-0364-x (cited on page 24).

[117] Feng Zhu, Long Men, Yijun Guo, Qiaochu Zhu, Ujjal Bhattacharjee, Peter M. Goodwin, Jacob W. Petrich, Emily A. Smith, and Javier Vela. "Shape evolution and single particle luminescence of organometal halide perovskite nanocrystals". In: *ACS Nano* 9.3 (2015), pp. 2948–2959. DOI: 10.1021/nn507020s (cited on page 24).

[118] Chunyang Yin, Liyang Chen, Nan Song, Yan Lv, Fengrui Hu, Chun Sun, W. Yu William, Chunfeng Zhang, Xiaoyong Wang, Yu Zhang, and Min Xiao. "Bright-exciton fine-structure splittings in single perovskite nanocrystals". In: *Physical Review Letters* 119.2 (2017), p. 026401. DOI: 10.1103/PhysRevLett.119.026401 (cited on page 24).

[119] Fengrui Hu, Huichao Zhang, Chun Sun, Chunyang Yin, Bihu Lv, Chunfeng Zhang, William W Yu, Xiaoyong Wang, Yu Zhang, and Min Xiao. "Superior optical properties of perovskite nanocrystals as single photon emitters". In: *ACS Nano* 9.12 (2015), pp. 12410–12416. DOI: 10.1021/acsnano.5b05769 (cited on page 25).

[120] Jagdeep Shah. *Ultrafast spectroscopy of semiconductors and semiconductor nanostructures*. Springer Science & Business Media, 2013. DOI: 10.1007/978-3-662-03770-6 (cited on pages 26, 27, 35, 37–39, 44, 46).

[121] Verena Hintermayr. "Tuning the carrier dynamics in light-emitting lead halide perovskite nanoplatelets". PhD thesis. Ludwig-Maximilians-Universität München, 2018 (cited on page 27).

[122] Prasanta Kumar Basu. *Theory of optical processes in semiconductors: Bulk and microstructures*. Clarendon Press, 1997. DOI: 10.1093/acprof:oso/9780198526209.001.0001 (cited on page 30).

[123] Victor I. Klimov, Alexander A Mikhailovsky, D. W. McBranch, Catherine A. Leatherdale, and Moungi G. Bawendi. "Quantization of multiparticle Auger rates in semiconductor quantum dots". In: *Science* 287.5455 (2000), pp. 1011–1013. DOI: 10.1126/science.287.5455.1011 (cited on pages 30, 31, 33, 92, 122).

[124] A. R. Beattie and P. T. Landsberg. "Auger effect in semiconductors". In: *Proceedings of the Royal Society of London. Series A, Mathematical and Physical Sciences* 249.1256 (1959), pp. 16–29. DOI: 10.1098/rspa.1959.0003 (cited on page 30).

[125] Jeffrey A. Davis. "Ultrafast coherent dynamics in semiconductor nano-structures". PhD thesis. University of Cambridge, 2005 (cited on pages 34, 38).

[126] J. L. Skinner and D. Hsu. "Pure dephasing of a two-level system". In: *The Journal of Physical Chemistry* 90.21 (1986), pp. 4931–4938. DOI: 10.1021/j100412a013 (cited on page 35).

[127] Marlan O. Scully and M. Suhail Zubairy. *Quantum optics*. Cambridge University Press, 1997 (cited on page 35).

[128] Galan Moody, Chandriker Kavir Dass, Kai Hao, Chang-Hsiao Chen, Lain-Jong Li, Akshay Singh, Kha Tran, Genevieve Clark, Xiaodong Xu, Gunnar Berghäuser, Ermin Malic, Andreas Knorr, and Xiaoqin Li. "Intrinsic homogeneous linewidth and broadening mechanisms of excitons in monolayer transition metal dichalcogenides". In: *Nature Communications* 6 (2015), p. 8315. DOI: 10.1038/ncomms9315 (cited on pages 35, 104).

[129] William W. Parson. *Modern optical spectroscopy*. Springer, 2007. DOI: 10.1007/978-3-662-46777-0 (cited on page 36).

[130] Tatsuo Yajima and Yoichi Taira. "Spatial optical parametric coupling of picosecond light pulses and transverse relaxation effect in resonant media". In: *Journal of the Physical Society of Japan* 47.5 (1979), pp. 1620–1626. DOI: 10.1143/JPSJ.47.1620 (cited on pages 36, 41, 106).

[131] T. F. Albrecht, J. H. H. Sandmann, S. T. Cundiff, Jochen Feldmann, W. Stolz, and E. O. Göbel. "Femtosecond degenerate four-wave-mixing on unstrained (InGa) As/InP multiple-quantum-wells using an optical parametric oscillator". In: *Solid-state Electronics* 37.4-6 (1994), pp. 1327–1331. DOI: 10.1016/0038-1101(94)90418-9 (cited on pages 36, 104).

[132] Leslie Allen and Joseph H. Eberly. *Optical resonance and two-level atoms*. Courier Corporation, 1987 (cited on page 37).

[133] Martin Koch. "Quantenschwebungs-Spektroskopie an exzitonischen Übergängen in Halbleiter-Heterostrukturen". PhD thesis. Philipps-Universität Marburg, 1995 (cited on pages 37, 46).

[134] Robert W. Boyd. *Nonlinear optics*. Elsevier, 2003 (cited on pages 37–40).

[135] Slobodan Prvanović. "Quantum Liouville Equation". In: *International Journal of Theoretical Physics* 51.9 (2012), pp. 2743–2753. DOI: 10.1007/s10773-012-1149-z (cited on page 38).

[136] M. Lindberg and Stephan W. Koch. "Effective Bloch equations for semiconductors". In: *Physical Review B* 38.5 (1988), p. 3342. DOI: 10.1103/PhysRevB.38.3342 (cited on page 39).

[137] Hans Joachim Eichler, Peter Günter, and Dieter W. Pohl. *Laser-induced dynamic gratings*. Springer, 2013. DOI: 10.1007/978-3-540-39662-8 (cited on page 40).

[138] Erwin L. Hahn. "Free nuclear induction". In: *Physics Today* 6.11 (1953), pp. 4–9. DOI: 10.1063/1.3061075 (cited on page 42).

[139] N. A. Kurnit, I. D. Abella, and S. R. Hartmann. "Observation of a photon echo". In: *Physical Review Letters* 13.19 (1964), p. 567. DOI: 10.1103/PhysRevLett.13.567 (cited on page 42).

[140] M. D. Webb, S. T. Cundiff, and D. G. Steel. "Stimulated-picosecond-photon-echo studies of localized exciton relaxation and dephasing in GaAs/$Al_xGa_{1-x}As$ multiple quantum wells". In: *Physical Review B* 43.15 (1991), p. 12658. DOI: 10.1103/PhysRevB.43.12658 (cited on page 43).

[141] M. Wegener, D. S. Chemla, S. Schmitt-Rink, and W. Schäfer. "Line shape of time-resolved four-wave mixing". In: *Physical Review A* 42.9 (1990), p. 5675. DOI: 10.1103/PhysRevA.42.5675 (cited on page 44).

[142] Jochen Feldmann, T. Meier, Gero Von Plessen, Martin Koch, Ernst O. Göbel, P. Thomas, G. Bacher, C. Hartmann, H. Schweizer, W. Schäfer, and H. Nickel. "Coherent dynamics of excitonic wave packets". In: *Physical Review Letters* 70.20 (1993), p. 3027. DOI: 10.1103/PhysRevLett.70.3027 (cited on pages 45, 46, 108).

[143] Ernst O. Göbel, K. Leo, T. C. Damen, Jagdeep Shah, S. Schmitt-Rink, W. Schäfer, J. F. Müller, and K. Köhler. "Quantum beats of excitons in quantum wells". In: *Physical Review Letters* 64.15 (1990), p. 1801. DOI: 10.1103/PhysRevLett.64.1801 (cited on page 45).

[144] Martin Koch, Gero von Plessen, Jochen Feldman, and Ernst O. Göbel. "Excitonic quantum beats in semiconductor quantum-well structures". In: *Chemical Physics* 210.1-2 (1996), pp. 367–388. DOI: 10.1016/0301-0104(96)00135-8 (cited on pages 45, 106).

[145] K. Leo, E. O. Göbel, T. C. Damen, J. Shah, S. Schmitt-Rink, W. Schäfer, J. F. Müller, K. Köhler, and P. Ganser. "Subpicosecond four-wave mixing in GaAs/$Al_xGa_{1-x}As$ quantum wells". In: *Physical Review B* 44.11 (1991), p. 5726. DOI: 10.1103/PhysRevB.44.5726 (cited on pages 45, 46).

[146] Wolfgang Demtröder. *Laserspektroskopie 2: Experimentelle Techniken*. Springer-Verlag, 2013. DOI: 10.1007/978-3-642-21447-9 (cited on page 46).

[147] Jürgen Falbe, Hermann Römpp, and Manfred Regitz. *Römpp Lexikon Chemie*. Thieme, 1997. DOI: 10.1055/b-004-134464 (cited on page 47).

[148] Adolf Fick. "Ueber Diffusion". In: *Annalen der Physik* 170.1 (1855), pp. 59–86. DOI: 10.1002/andp.18551700105 (cited on page 47).

[149] Pál Révész. *Random walk in random and non-random environments*. World Scientific, 2005. DOI: 10.1142/8678 (cited on page 47).

[150] Jean-Henri Lambert. *Photometria*. Eberhard Klett Verlag, 1760 (cited on page 47).

[151] D. F. Swinehart. "The beer-lambert law". In: *Journal of Chemical Education* 39.7 (1962), p. 333. DOI: 10.1021/ed039p333 (cited on page 47).

[152] Aaron R. Clapp, Igor L. Medintz, and Hedi Mattoussi. "Förster resonance energy transfer investigations using quantum-dot fluorophores". In: *ChemPhysChem* 7.1 (2006), pp. 47–57. DOI: 10.1002/cphc.200500217 (cited on page 48).

[153] C. R. Kagan, C. B. Murray, and M. G. Bawendi. "Long-range resonance transfer of electronic excitations in close-packed CdSe quantum-dot solids". In: *Physical Review B* 54.12 (1996), p. 8633. DOI: 10.1103/PhysRevB.54.8633 (cited on page 48).

[154] S. A. Crooker, J. A. Hollingsworth, S. Tretiak, and Victor I. Klimov. "Spectrally resolved dynamics of energy transfer in quantum-dot assemblies: Towards engineered energy flows in artificial materials". In: *Physical Review Letters* 89.18 (2002), p. 186802. DOI: 10.1103/PhysRevLett.89.186802 (cited on page 48).

[155] A. Haugeneder, M. Neges, C. Kallinger, W. Spirkl, Uli Lemmer, Jochen Feldmann, Ullrich Scherf, E. Harth, A. Gügel, and Klaus Müllen. "Exciton diffusion and dissociation in conjugated polymer/fullerene blends and heterostructures". In: *Physical Review B* 59.23 (1999), p. 15346. DOI: 10.1103/PhysRevB.59.15346 (cited on pages 48, 50, 117).

[156] Christian Wehrenfennig, Giles E. Eperon, Michael B. Johnston, Henry J. Snaith, and Laura M. Herz. "High charge carrier mobilities and lifetimes in organolead trihalide perovskites". In: *Advanced Materials* 26.10 (2014), pp. 1584–1589. DOI: 10.1002/adma.201305172 (cited on pages 48, 111, 114).

[157] Elizabeth M. Y. Lee and William A. Tisdale. "Determination of exciton diffusion length by transient photoluminescence quenching and its application to quantum dot films". In: *The Journal of Physical Chemistry C* 119.17 (2015), pp. 9005–9015. DOI: 10.1021/jp512634c (cited on pages 49, 50, 118).

[158] Samuel D. Stranks, Giles E. Eperon, Giulia Grancini, Christopher Menelaou, Marcelo J. P. Alcocer, Tomas Leijtens, Laura M. Herz, Annamaria Petrozza, and Henry J. Snaith. "Electron-hole diffusion lengths exceeding 1 micrometer in an organometal trihalide perovskite absorber". In: *Science* 342.6156 (2013), pp. 341–344. DOI: 10.1126/science.1243982 (cited on pages 49, 111).

[159] Gleb M. Akselrod, Ferry Prins, Lisa V. Poulikakos, Elizabeth M. Y. Lee, Mark C. Weidman, A. Jolene Mork, Adam P. Willard, Vladimir Bulović, and William A. Tisdale. "Subdiffusive exciton transport in quantum dot solids". In: *Nano Letters* 14.6 (2014), pp. 3556–3562. DOI: 10.1021/nl501190s (cited on page 49).

[160] Dirk M. Guldi. "Fullerenes: Three dimensional electron acceptor materials". In: *Chemical Communications* 5 (2000), pp. 321–327. DOI: 10.1039/A907807J (cited on page 50).

[161] Denis E. Markov, Emiel Amsterdam, Paul W. M. Blom, Alexander B. Sieval, and Jan C. Hummelen. "Accurate measurement of the exciton diffusion length in a conjugated polymer using a heterostructure with a side-chain cross-linked fullerene layer". In: *The Journal of Physical Chemistry A* 109.24 (2005), pp. 5266–5274. DOI: 10.1021/jp0509663 (cited on page 50).

[162] Richard R. Lunt, Noel C. Giebink, Anna A. Belak, Jay B. Benziger, and Stephen R. Forrest. "Exciton diffusion lengths of organic semiconductor thin films measured by spectrally resolved photoluminescence quenching". In: *Journal of Applied Physics* 105.5 (2009), p. 053711. DOI: 10.1063/1.3079797 (cited on page 50).

[163] Ioannis Lignos, Loredana Protesescu, Dilara Börte Emiroglu, Richard Maceiczyk, Simon Schneider, Maksym V. Kovalenko, and Andrew J. DeMello. "Unveiling the shape evolution and halide-ion-segregation in blue-emitting formamidinium lead halide perovskite nanocrystals using an automated microfluidic platform". In: *Nano Letters* 18.2 (2018), pp. 1246–1252. DOI: 10.1021/acs.nanolett.7b04838 (cited on page 52).

[164] Bing Xu, Weigao Wang, Xiaoli Zhang, Wanyu Cao, Dan Wu, Sheng Liu, Haitao Dai, Shuming Chen, Kai Wang, and Xiaowei Sun. "Bright and efficient light-emitting diodes based on MA/Cs double cation perovskite nanocrystals". In: *Journal of Materials Chemistry C* 5.25 (2017), pp. 6123–6128. DOI: 10.1039/C7TC01300K (cited on page 54).

[165] Norman Pellet, Joël Teuscher, Joachim Maier, and Michael Grätzel. "Transforming hybrid organic inorganic perovskites by rapid halide exchange". In: *Chemistry of Materials* 27.6 (2015), pp. 2181–2188. DOI: 10.1021/acs.chemmater.5b00281 (cited on page 54).

[166] Yu Tong. "Controlling the optical properties of colloidal lead halide perovskite nanocrystals by shape, size and dimensionality". PhD thesis. Ludwig-Maximilians-Universität München, 2018 (cited on page 55).

[167] Constantinos C. Stoumpos, Duyen H. Cao, Daniel J. Clark, Joshua Young, James M. Rondinelli, Joon I. Jang, Joseph T. Hupp, and Mercouri G. Kanatzidis. "Ruddlesden–Popper hybrid lead iodide perovskite 2D homologous semiconductors". In: *Chemistry of Materials* 28.8 (2016), pp. 2852–2867. DOI: 10.1021/acs.chemmater.6b00847 (cited on page 55).

[168] Hsinhan Tsai, Wanyi Nie, Jean-Christophe Blancon, Constantinos C. Stoumpos, Reza Asadpour, Boris Harutyunyan, Amanda J. Neukirch, Rafael Verduzco, Jared J. Crochet, Sergei Tretiak, Laurent Pedesseau, Jacky Even, Muhammad A. Alam, Gautam Gupta, Jun Lou, Pulickel M. Ajayan, Michael J. Bedzyk, Mercouri G. Kanatzidis, and Aditya D. Mohite. "High-efficiency two-dimensional Ruddlesden–Popper perovskite solar cells". In: *Nature* 536.7616 (2016), p. 312. DOI: 10.1038/nature18306 (cited on page 55).

[169] Bai-Sheng Zhu, Zhen He, Ji-Song Yao, Chen Chen, Kun-Hua Wang, Hong-Bin Yao, Jian-Wei Liu, and Shu-Hong Yu. "Potassium ion assisted synthesis of organic–inorganic hybrid perovskite nanobelts for stable and flexible photodetectors". In: *Advanced Optical Materials* 6.3 (2018), p. 1701029. DOI: 10.1002/adom.201701029 (cited on page 55).

[170] Melanie T. Asaki, Chung-Po Huang, Dennis Garvey, Jianping Zhou, Henry C. Kapteyn, and Margaret M. Murnane. "Generation of 11-fs pulses from a self-mode-locked Ti:sapphire laser". In: *Optics Letters* 18.12 (1993), pp. 977–979. DOI: 10.1364/OL.18.000977 (cited on page 56).

[171] John M. Dudley, Goëry Genty, and Stéphane Coen. "Supercontinuum generation in photonic crystal fiber". In: *Reviews of Modern Physics* 78.4 (2006), pp. 1135–1184. DOI: 10.1103/RevModPhys.78.1135 (cited on page 58).

[172] Nicolaas Bloembergen. "Conservation laws in nonlinear optics". In: *Journal of the Optical Society of America* 70.12 (1980), pp. 1429–1436. DOI: 10.1364/JOSA.70.001429 (cited on page 58).

[173] Jonathan Mooney and Patanjali Kambhampati. "Get the basics right: Jacobian conversion of wavelength and energy scales for quantitative analysis of emission spectra". In: *The Journal of Physical Chemistry Letters* 4.19 (2013), pp. 3316–3318. DOI: 10.1021/jz401508t (cited on pages 63, 69).

[174] Alexander F. Richter, Michael Binder, Bernhard J. Bohn, Nathan Grumbach, Shany Neyshtadt, Alexander S. Urban, and Jochen Feldmann. "Fast electron and slow hole relaxation in InP-based colloidal quantum dots". In: *ACS Nano* 13.12 (2019), pp. 14408–14415. DOI: 10.1021/acsnano.9b07969 (cited on page 64).

[175] Fang Yang, Michael Wilkinson, Elizabeth J. Austin, and Kevin P. O'Donnell. "Origin of the Stokes shift: A geometrical model of exciton spectra in 2D semiconductors". In: *Physical Review Letters* 70.3 (1993), p. 323. DOI: 10.1103/PhysRevLett.70.323 (cited on page 68).

[176] Tae-Yeon Seong, Jung Han, Hiroshi Amano, and Hadis Morkoç. *III-Nitride based light emitting diodes and applications*. Springer, 2013, pp. 121–152. DOI: 10.1007/978-981-10-3755-9 (cited on page 69).

[177] Desmond O'Connor. *Time-correlated single photon counting*. Academic Press, 2012. DOI: 10.1016/B978-0-12-524140-3.X5001-1 (cited on pages 70, 71).

[178] Wolfgang Becker. *Advanced time-correlated single photon counting techniques*. Springer, 2005. DOI: 10.1007/3-540-28882-1 (cited on page 70).

[179] Peixian Ye and Y. R. Shen. "Transient four-wave mixing and coherent transient optical phenomena". In: *Physical Review A* 25.4 (1982), p. 2183. DOI: 10.1103/PhysRevA.25.2183 (cited on page 72).

[180] Martin Koch, D. Weber, Jochen Feldmann, Ernst O. Göbel, Torsten Meier, A. Schulze, P. Thomas, Stefan Schmitt-Rink, and Klaus Ploog. "Subpicosecond photon-echo spectroscopy on GaAs/AlAs short-period superlattices". In: *Physical Review B* 47.3 (1993), p. 1532. DOI: 10.1103/PhysRevB.47.1532 (cited on pages 72, 74).

[181] Tallis Y. Chang, Arthur E. Chiou, and Pochi Yeh. "Cross-polarization photorefractive two-beam coupling in gallium arsenide". In: *Journal of the Optical Society of America B* 5.8 (1988), pp. 1724–1729. DOI: 10.1364/JOSAB.5.001724 (cited on page 72).

[182] Y. Z. Hu, Rudolf Binder, Stephan W. Koch, Steven T. Cundiff, Hailin Wang, and Duncan G. Steel. "Excitation and polarization effects in semiconductor four-wave-mixing spectroscopy". In: *Physical Review B* 49.20 (1994), p. 14382. DOI: 10.1103/PhysRevB.49.14382 (cited on page 72).

[183] Changbiao Li, Yanpeng Zhang, Zhiqiang Nie, Yigang Du, Ruimin Wang, Jianping Song, and Min Xiao. "Controlling enhancement and suppression of four-wave mixing via polarized light". In: *Physical Review A* 81.3 (2010), p. 033801. DOI: 10.1103/PhysRevA.81.033801 (cited on page 72).

[184] M. L. Meade. "Advances in lock-in amplifiers". In: *Journal of Physics E: Scientific Instruments* 15.4 (1982), p. 395. DOI: 10.1088/0022-3735/15/4/001 (cited on page 74).

[185] Luciana C. Schmidt, Antonio Pertegás, Soranyel González-Carrero, Olga Malinkiewicz, Said Agouram, Guillermo Minguez Espallargas, Henk J. Bolink, Raquel E. Galian, and Julia Pérez-Prieto. "Nontemplate synthesis of $CH_3NH_3PbBr_3$ perovskite nanoparticles". In: *Journal of the American Chemical Society* 136.3 (2014), pp. 850–853. DOI: 10.1021/ja4109209 (cited on page 78).

[186] Hi Amano, N. Sawaki, I. Akasaki, and Y. Toyoda. "Metalorganic vapor phase epitaxial growth of a high quality GaN film using an AlN buffer layer". In: *Applied Physics Letters* 48.5 (1986), pp. 353–355. DOI: 10.1063/1.96549@apl.2019.APLCLASS2019.issue-1 (cited on page 78).

[187] Shuji Nakamura, Stephen Pearton, and Gerhard Fasol. *The blue laser diode: The complete story*. Springer Science & Business Media, 2000. DOI: 10.1007/978-3-662-04156-7 (cited on page 78).

[188] Shuji Nakamura, Masayuki Senoh, Naruhito Iwasa, and Shin-ichi Nagahama. "High-brightness InGaN blue, green and yellow light-emitting diodes with quantum well structures". In: *Japanese Journal of Applied Physics* 34.7A (1995), p. L797. DOI: 10.1143/jjap.34.l797 (cited on page 78).

[189] Yasushi Nanishi. "Nobel Prize in Physics: The birth of the blue LED". In: *Nature Photonics* 8.12 (2014), p. 884. DOI: 10.1038/nphoton.2014.291 (cited on page 78).

[190] Guangru Li, Michael Price, and Felix Deschler. "Research Update: Challenges for high-efficiency hybrid lead-halide perovskite LEDs and the path towards electrically pumped lasing". In: *APL Materials* 4.9 (2016), p. 091507. DOI: 10.1063/1.4962351 (cited on pages 78, 84).

[191] Ali Naeem, Francesco Masia, Sotirios Christodoulou, Iwan Moreels, Paola Borri, and Wolfgang Langbein. "Giant exciton oscillator strength and radiatively limited dephasing in two-dimensional platelets". In: *Physical Review B* 91.12 (2015), p. 121302. DOI: 10.1103/PhysRevB.91.121302 (cited on page 80).

[192] Justinas Butkus, Parth Vashishtha, Kai Chen, Joseph K. Gallaher, Shyamal KK Prasad, Dani Z. Metin, Geoffry Laufersky, Nicola Gaston, Jonathan E. Halpert, and Justin M. Hodgkiss. "The evolution of quantum confinement in $CsPbBr_3$ perovskite nanocrystals". In: *Chemistry of Materials* 29.8 (2017), pp. 3644–3652. DOI: 10.1021/acs.chemmater.7b00478 (cited on pages 80, 81).

[193] Quinten A. Akkerman, Silvia Genaro Motti, Ajay Ram Srimath Kandada, Edoardo Mosconi, Valerio D'Innocenzo, Giovanni Bertoni, Sergio Marras, Brett A. Kamino, Laura Miranda, Filippo De Angelis, Annamaria Petrozza, Mirko Prato, and Liberato Manna. "Solution synthesis approach to colloidal cesium lead halide perovskite nanoplatelets with monolayer-level thickness control". In: *Journal of the American Chemical Society* 138.3 (2016), pp. 1010–1016. DOI: 10.1021/jacs.5b12124 (cited on page 81).

[194] Carlo Giansante and Ivan Infante. "Surface traps in colloidal quantum dots: A combined experimental and theoretical perspective". In: *The Journal of Physical Chemistry Letters* 8.20 (2017), pp. 5209–5215. DOI: 10.1021/acs.jpclett.7b02193 (cited on page 83).

[195] Federico Bella, Gianmarco Griffini, Juan-Pablo Correa-Baena, Guido Saracco, Michael Grätzel, Anders Hagfeldt, Stefano Turri, and Claudio Gerbaldi. "Improving efficiency and stability of perovskite solar cells with photocurable fluoropolymers". In: *Science* 354.6309 (2016), pp. 203–206. DOI: 10.1126/science.aah4046 (cited on page 84).

[196] Verena A. Hintermayr, Carola Lampe, Maximilian Löw, Janina Roemer, Willem Vanderlinden, Moritz Gramlich, Anton X. Böhm, Cornelia Sattler, Bert Nickel, Theobald Lohmüller, and Alexander S. Urban. "Polymer nanoreactors shield perovskite nanocrystals from degradation". In: *Nano Letters* 19.8 (2019), pp. 4928–4933. DOI: 10.1021/acs.nanolett.9b00982 (cited on page 84).

[197] Anna Loiudice, Seryio Saris, Emad Oveisi, Duncan T. L. Alexander, and Raffaella Buonsanti. "$CsPbBr_3$ QD/AlOx inorganic nanocomposites with exceptional stability in water, light, and heat". In: *Angewandte Chemie International Edition* 56.36 (2017), pp. 10696–10701. DOI: 10.1002/anie.201703703 (cited on page 84).

[198] Robert L. Z. Hoye, May-Ling Lai, Miguel Anaya, Yu Tong, Krzysztof Galkowski, Tiarnan Doherty, Weiwei Li, Tahmida N. Huq, Sebastian Mackowski, Lakshminarayana Polavarapu, Jochen Feldmann, Judith L. MacManus-Driscoll, Richard H. Friend, Alexander S. Urban, and Samuel D. Stranks. "Identifying and reducing interfacial losses to enhance color-pure electroluminescence in blue-emitting perovskite nanoplatelet light-emitting diodes". In: *ACS Energy Letters* 4.5 (2019), pp. 1181–1188. DOI: 10.1021/acsenergylett.9b00571 (cited on pages 85, 122).

[199] C. Weber, C. Klingshirn, D. S. Chemla, D. A. B. Miller, J. Cunningham, and C. Ell. "Gain measurements and band-gap renormalization in $GaAs/Al_xGa_{1-x}As$ multiple-quantum-well structures". In: *Physical Review B* 38.17 (1988), p. 12748. DOI: 10.1103/PhysRevB.38.12748 (cited on page 88).

[200] J. Aneesh, Abhishek Swarnkar, Vikash Kumar Ravi, Rituraj Sharma, Angshuman Nag, and K. V. Adarsh. "Ultrafast exciton dynamics in colloidal $CsPbBr_3$ perovskite nanocrystals: Biexciton effect and Auger recombination". In: *The Journal of Physical Chemistry C* 121.8 (2017), pp. 4734–4739. DOI: 10.1021/acs.jpcc.7b00762 (cited on page 88).

[201] Lazaro A. Padilha, John T. Stewart, Richard L. Sandberg, Wan Ki Bae, Weon-Kyu Koh, Jeffrey M. Pietryga, and Victor I. Klimov. "Aspect ratio dependence of auger recombination and carrier multiplication in PbSe nanorods". In: *Nano Letters* 13.3 (2013), pp. 1092–1099. DOI: 10.1021/nl304426y (cited on page 92).

[202] Yulu Li, Tao Ding, Xiao Luo, Zongwei Chen, Xue Liu, Xin Lu, and Kaifeng Wu. "Biexciton Auger recombination in mono-dispersed, quantum-confined $CsPbBr_3$ perovskite nanocrystals obeys universal volume-scaling". In: *Nano Research* 12.3 (2019), pp. 619–623. DOI: 10.1007/s12274-018-2266-7 (cited on page 92).

[203] Qiuyang Li and Tianquan Lian. "Area-and thickness-dependent biexciton Auger recombination in colloidal CdSe nanoplatelets: Breaking the "universal volume scaling law"". In: *Nano Letters* 17.5 (2017), pp. 3152–3158. DOI: 10.1021/acs.nanolett.7b00587 (cited on pages 92, 122).

[204] Yehonadav Bekenstein, Brent A. Koscher, Samuel W. Eaton, Peidong Yang, and A. Paul Alivisatos. "Highly luminescent colloidal nanoplates of perovskite cesium lead halide and their oriented assemblies". In: *Journal of the American Chemical Society* 137.51 (2015), pp. 16008–16011. DOI: 10.1021/jacs.5b11199 (cited on page 98).

[205] He Huang, Lakshminarayana Polavarapu, Jasmina A. Sichert, Andrei S. Susha, Alexander S. Urban, and Andrey L. Rogach. "Colloidal lead halide perovskite nanocrystals: Synthesis, optical properties and applications". In: *NPG Asia Materials* 8.11 (2016), e328. DOI: 10.1038/am.2016.167 (cited on page 98).

[206] Kewei Wu, Ashok Bera, Chun Ma, Yuanmin Du, Yang Yang, Liang Li, and Tom Wu. "Temperature-dependent excitonic photoluminescence of hybrid organometal halide perovskite films". In: *Physical Chemistry Chemical Physics* 16.41 (2014), pp. 22476–22481. DOI: 10.1039/C4CP03573A (cited on page 103).

[207] B. Lummer, R. Heitz, V. Kutzer, J.-M. Wagner, A. Hoffmann, and I. Broser. "Dephasing of acceptor bound excitons in II–VI semiconductors". In: *Physica Status Solidi (B)* 188.1 (1995), pp. 493–505. DOI: 10.1002/pssb.2221880147 (cited on page 106).

[208] Ajay Jha, Hong-Guang Duan, Vandana Tiwari, Pabitra K. Nayak, Henry J. Snaith, Michael Thorwart, and R. J. Dwayne Miller. "Direct observation of ultrafast exciton dissociation in lead iodide perovskite by 2D electronic spectroscopy". In: *ACS Photonics* 5.3 (2017), pp. 852–860. DOI: 10.1021/acsphotonics.7b01025 (cited on page 107).

[209] Jianhui Fu, Qiang Xu, Guifang Han, Bo Wu, Cheng Hon Alfred Huan, Meng Lee Leek, and Tze Chien Sum. "Hot carrier cooling mechanisms in halide perovskites". In: *Nature Communications* 8.1 (2017), p. 1300. DOI: 10.1038/s41467-017-01360-3 (cited on page 117).

[210] Tsuyoshi Sekitani, Hiroyoshi Nakajima, Hiroki Maeda, Takanori Fukushima, Takuzo Aida, Kenji Hata, and Takao Someya. "Stretchable active-matrix organic light-emitting diode display using printable elastic conductors". In: *Nature Materials* 8.6 (2009), p. 494. DOI: 10.1038/nmat2459 (cited on page 122).

[211] Nicolas Gisin and Rob Thew. "Quantum communication". In: *Nature Photonics* 1.3 (2007), p. 165. DOI: 10.1038/nphoton.2007.22 (cited on page 122).

[212] Paolo Umari, Edoardo Mosconi, and Filippo De Angelis. "Infrared dielectric screening determines the low exciton binding energy of metal-halide perovskites". In: *The Journal of Physical Chemistry Letters* 9.3 (2018), pp. 620–627. DOI: 10.1021/acs.jpclett.7b03286 (cited on page 123).

[213] Juan-Pablo Correa-Baena, Michael Saliba, Tonio Buonassisi, Michael Grätzel, Antonio Abate, Wolfgang Tress, and Anders Hagfeldt. "Promises and challenges of perovskite solar cells". In: *Science* 358.6364 (2017), pp. 739–744. DOI: 10.1126/science.aam6323 (cited on page 123).

[214] Yaoguang Rong, Yue Hu, Anyi Mei, Hairen Tan, Makhsud I. Saidaminov, Sang Il Seok, Michael D. McGehee, Edward H. Sargent, and Hongwei Han. "Challenges for commercializing perovskite solar cells". In: *Science* 361.6408 (2018), eaat8235. DOI: 10.1126/science.aat8235 (cited on page 123).

List of Figures

List of Tables

List of Abbreviations

ADF	annular dark field
AFM	atomic force microscopy
APD	avalanche photodiode
BBO	barium borate
CB	conduction band
CBM	conduction band minimum
CW	continuous-wave
DFG	difference frequency generation
DFT	density-functional theory
DOS	density of states
DT	differential transmission
DTS	differential transmission spectroscopy
e-h	electron-hole
EDX	energy-dispersive X-ray
EQE	external quantum efficiency
FHG	fourth harmonic generation
FRET	Förster resonance energy transfer
FWHM	full width at half maximum
FWM	four-wave mixing
HE	heavy electron
I	idler
IQE	internal quantum efficiency
IR	infrared
IRF	instrument response function
JDOS	joint density of states
LE	light electron
LED	light-emitting diode
LHP	lead halide perovskite
LO	longitudinal optical
MA	methylammonium
ML	monolayer
NC	nanocrystal
ND	neutral density
NIR	near infrared
NPl	nanoplatelets
NUV	near ultraviolet
OD	optical density
OPA	optical parametric amplifier
PA	parametric amplification
PCF	photonic crystal fiber
PID	proportional–integral–derivative
PL	photoluminescence
PLQY	photoluminescence quantum yield
QBS	quantum beat spectroscopy
QD	quantum dot
S	signal
SEM	scanning electron microscopy
SFG	sum frequency generation

SHG	second harmonic generation
SNR	signal-to-noise ratio
STEM	scanning transmission electron microscopy
TAS	transient absorption spectroscopy
TCSPC	time-correlated single photon counting
TEM	transmission electron microscopy
VB	valence band
UV	ultraviolet
VB	valence band
VBM	valence band maximum
VIS	visible
WLL	white light laser
XRD	X-ray diffraction

Acknowledgments

First of all, I want to thank my "Doktorvater" **Prof. Dr. Jochen Feldmann**, whose support during the past three years I cannot value highly enough. Basically, you provided me a "new home" to conduct research not only once, but twice — first, when I joined the group in the summer of 2016 and then again this year when we moved to the new *Nano-Institute*. Your broad experience on semiconductors and time-resolved spectroscopy was always inspiring to me. The fruitful discussions we had are one of the main reasons for the success of our recent publications. Thank you for placing your trust in me and especially I would like to thank you for the possibility to participate at numerous conferences which allowed me to present my research results in front of an international audience. This also led to the circumstances that I am sitting in a hotel room in Changsha (China) at this very moment while writing these final lines of my PhD thesis.

Dr. Jacek K. Stolarczyk and **Lakshminarayana Polavarapu**, thank you for the great collaboration in all projects we had together! Lakshmi and **Dr. Yu Tong**, a special thanks goes out to you for never running out of new LHP samples which I could analyze in the laser laboratory. I highly appreciate your help on the "chemistry side" of my research!

Like Yu never runs out of samples, **PD Dr. Theobald Lohmüller** (Theobald Jones) never runs out of entertaining stories. Theo, I want to thank you for the time we had together. Theory and experiment never agreed as well as in our little study on how to move the laser labs. Your accurate planning was the main reason why the moving of these labs worked out surprisingly smoothly.

For the largest part of my time as a PhD student, **Prof. Dr. Alexander S. Urban** has been an assistant at our chair, mainly involved in the spectroscopic studies of LHP nanocrystals. While this has been a temporary position, you gained a permanent position in relation to me in the form of a good friend. Alex, thanks for your input and feedback on science, presentations and writing!

A special thanks goes to my "correction task force": **Sebastian Rieger**, **Alexander F. Richter** and **Moritz Gramlich**. You are fantastic — probably even "meganice" — colleagues. Thank you **Dr. Thomas Simon**! Working with you at the beginning of my time as PhD student was the perfect start for my research at the chair. **Aurora Manzi**, you are the best. **Dr. Verena A. Hintermayr**, you are awesome. **Nicola Kerschbaumer** (*insert eagle emoji*), you are cool cool cool. There are also others who would deserve their "own adjective", but here I simply refer to you as great colleagues: **Simone Strohmair**, **Stefanie Pritzl**, **Dr. En-Ping Yao** and **Christoph Maier**. Thank you! Also many thanks to all other former and present colleagues who supported me at the *Chair for Photonics and Optoelectronics*.

Gerlinde Adam, without you my time at the LMU would have been different and I will really miss you! Thank you for all your support throughout the last years! **Stefan Niedermaier**, to me you are one of the most memorable persons at the LMU. Danke Stefan, for your help regarding "engineering problems of all kind" and especially for "the big move" which for the most was organized by you and Theo. Due to your endless effort and endurance, even hard tasks like moving tons of scientific equipment between Amalienstraße 54 and Königinstraße 10 (only using a Volkswagen van from the early 90s) can be fun.

Moreover, I want to thank **Dr. Alexander Weber-Bargioni** and his team for the possibility to spend some months at the *Molecular Foundry* in Berkeley, USA at the West Coast, where I conducted the experiments on exciton diffusion via PL mapping. I also want to thank my previous supervisors **Prof. Dr. Federico Capasso** and **Prof. Dr. Mikhail Kats** from the East Coast. Federico, thank you for staying in touch with me and being such a great mentor who always has some good advice. Mikhail, in the end you were the one who convinced me to do a PhD and now I can tell you that it was a good decision after all!

Kathrin Mohler, **Dr. Arthur Hipke** and **Dr. Simon Holzner**: You are the ones who have been there for me during the toughest time. This will connect us forever! **Christian Schwarz**, **Bernd Kohler**, **Dr. Oliver Trinchera** and **Lea Sofia Nikiforow**: Your friendship always kept my motivation at 100 %.

Dr. Marius Fischer aka Jiggy, Wiggy, Shaggle, Wolfgang, ..., Sir Wagglesburry. Since our paths crossed for the first time during our exchange semester in Zurich, our friendship has been a huge enrichment for my life. You know that one of my favorite phrases starts with "I remember very accurately how I helped you ...". Luckily, you do not take all this nonsense too serious and we both know that I am the one who has to thank you. It is impossible to mention everything, but here I want to point out your support in proofreading this thesis and in general for having an open ear in good and bad times. Keep that attitude (and also your tires)!

More than ten years ago I was interviewed by a local newspaper and in the course of this interview I described my brother **Karl Peter Bohn** as an all-rounder and idol. Even though many things happened since then and our lives changed in many ways, I can still stick to that statement. Thank you, Peter, for your support throughout my whole life.

Most importantly and with great gratitude, I want to mention my parents **Karl Josef** and **Gerlinde Bohn** to whom I also dedicate this thesis. Not only do I want to thank you for your emotional and financial support during my "academic career", but also for raising both of your boys. This made us the persons we are, and we will always be deeply grateful for that!